UNIVERSITÉ DE LORRAINE | BIBLIOTHÈQUES UNIVERSITAIRES

AVERTISSEMENT
DROIT D'AUTEUR

Ce document est le fruit d'un long travail approuvé par le jury de soutenance et mis à disposition de l'ensemble de la communauté universitaire élargie.

Il est soumis à la propriété intellectuelle de l'auteur. Ceci implique une obligation de citation et de référencement lors de l'utilisation de ce document. Toute contrefaçon, plagiat ou reproduction illicite encourt une poursuite pénale.

Contact bibliothèque : ddoc-theses-contact@univ-lorraine.fr
(Cette adresse ne permet pas de contacter les auteurs)

Code de la Propriété Intellectuelle. articles L 122. 4
Code de la Propriété Intellectuelle. articles L 335.2- L 335.10

UNIVERSITÉ DE LORRAINE
34 COURS LÉOPOLD — CS 25233
54052 NANCY CEDEX
WWW.UNIV-LORRAINE.FR

École Doctorale BioSE (Biologie-Santé-Environnement)

Thèse

Présentée et soutenue publiquement pour l'obtention du titre de

DOCTEUR DE l'UNIVERSITE DE LORRAINE

Mention : « Sciences de la Vie et de la Santé »

Par: **Abdulrahman ALBLOWI**

Biomechanical Characteristics of Different Bovine Pericardial Patches Preserved in Glutaraldehyde Solution

Le 22 septembre 2026

Membres du jury :

Président de jury Examinateur :	**Ambroise DUPREY**	**PU-PH, CHU Reims, Hémostase et remodelage vasculaire post-ischémie (HERVI) - EA 3801, Université de Reims.**
Rapporteurs :	**Anne LEJAY**	**PU-PH, CHU Strasbourg, Research Unit 3072 Mitochondria, Oxidative Stress and Muscular Plasticity, Biomedicine Research Centre of Strasbourg, Université de Strasbourg**
	Morgane EVIN	**PU, Laboratoire de Biomécanique Appliquée (LBA) UMRT24 Université Gustave Eiffel – Aix-Marseille Université**
Directeur(s) de thèse :	**Serguei MALIKOV**	**PU-PH, CHRU Nancy, INSERM U1116, DCAC Université de Lorraine, Nancy.**
	Alain LALANDE	**MCU-PH, Université Bourgogne Europe, ICMUB CNRS UMR 6302, Dijon.**
	Nicla SETTEMBRE	**PU-PH, CHRU Nancy, INSERM U1116, DCAC Université de Lorraine, Nancy.**
Examinatrice :	**Siyu LIN**	**Ingénieure de recherche, Laboratoire SAINBIOSE, École nationale supérieure des mines de Saint-Étienne, Saint-Étienne**

UMR_S 1116, Défaillance Cardiovasculaire Aiguë et Chronique, Faculté de Médecine de Nancy, Université de Lorraine.

"The pursuit of truth is nobler than the possession of truth itself. Knowledge is not measured by the answers we hold, but by the questions we continue to ask, the challenges we dare to confront, and the humility to recognize that every discovery is only the beginning of deeper understanding."

— Inspired by Ibn Khaldun

Acknowledgements

Completing this doctoral thesis marks the culmination of a remarkable journey that has extended over many years, across several countries, institutions, and stages of my academic and professional life. This achievement would not have been possible without the support, guidance, generosity, and encouragement of many exceptional individuals, to whom I wish to express my deepest gratitude.

First and foremost, I would like to express my profound appreciation to my thesis supervisors, **Professor Serguei Malikov** and **Professor Nicla Settembre**. Since the beginning of my residency in vascular and endovascular surgery program, they have continuously placed their trust in me and provided unwavering guidance throughout my clinical training, research activities, and doctoral studies. Their scientific excellence, intellectual rigor, kindness, and dedication have profoundly influenced both my professional development and my personal growth. They taught me not only how to become a better vascular surgeon and researcher, but also the values of perseverance, integrity, and academic excellence. I consider myself truly privileged to have trained under their mentorship, and I will always remain deeply grateful for the opportunities they offered me.

I am equally indebted to my thesis co-supervisor, **Professor Alain Lalande**, whose exceptional expertise in biomechanics and cardiovascular imaging has been instrumental in shaping this work. His scientific vision, remarkable attention to detail, constant availability, and rigorous approach to research have significantly strengthened the quality of this thesis. His enthusiasm for science and his commitment to excellence have been a continuous source of inspiration throughout my doctoral journey.

My sincere gratitude goes to **Dr. Siyu Lin**, whose collaboration was fundamental to the successful completion of this research. From the earliest experimental work to biomechanical testing, data interpretation, and scientific discussions, she generously shared her expertise with remarkable patience and dedication. Beyond her invaluable scientific contribution, I am especially grateful for her kindness, encouragement, and friendship. Working alongside her has been both a privilege and a pleasure, and I sincerely thank her for the countless hours devoted to this project.

I would also like to express my heartfelt appreciation to **Professor Olivier Bouchot** for his constant encouragement, insightful discussions, and invaluable clinical perspective. His expertise in cardiovascular surgery greatly enriched the translational significance of this work and helped bridge the gap between fundamental research and clinical practice.

My sincere thanks are extended to **Dr. Jérémy Lagrange**, whose expertise in data analysis and statistical methodology substantially strengthened this research. His scientific rigor, thoughtful advice, and willingness to help at every stage of the project were invaluable. I also greatly appreciated his professionalism, generosity, and friendship.

I would like to warmly thank the members of my thesis monitoring committee, **Professor Manuela Perez** and **Professor Eric Steinmetz**, for their constructive comments, valuable recommendations, and continuous encouragement throughout my doctoral studies. Their insightful perspectives contributed significantly to the development and refinement of this work.

It is a great honor that **Professor Ambroise Duprey**, **Professor Anne Lejay**, and **Dr. Morgane Evin** kindly accepted to serve as members of my thesis jury. I sincerely thank them for their time, interest, and willingness to evaluate this work. Their expertise represents a great privilege for me, and I deeply appreciate their contribution to my doctoral defense.

To my colleagues and friends:

I would like to extend my sincere gratitude to all my colleagues at the **DCAC Laboratory**, whose professionalism, scientific curiosity, and collaborative spirit created an inspiring and stimulating research environment.

A very special acknowledgment goes to **Sara Abd Al Rahim**, who embarked on this doctoral adventure alongside me from the very first day. Beginning our PhD journey together, within the same laboratory. Throughout these years, we have experienced together the excitement of discovery, the inevitable setbacks of research, and the satisfaction of overcoming each obstacle.

I would also like to express my deepest appreciation to my dear friend **Jaber Alfaifi**. Our friendship extends far beyond this doctoral work. We began our residency together in France, continued our fellowship training in Montréal, Canada, and eventually pursued our doctoral studies at the same university. Sharing these extraordinary milestones throughout our careers has been a rare privilege. Over the years, he has been not only a trusted colleague but also a loyal friend whose integrity, perseverance, humility, and constant encouragement have inspired me continuously. Together, we have celebrated achievements, faced challenges, and supported one another through every stage of this journey. His friendship represents one of the greatest gifts that my international training has given me, and I am sincerely thankful for every moment we have shared.

My heartfelt thanks also go to my dear friends and colleagues **Charles Sadoul, Claire Di Virgilio, and Camille Panescu**. Working alongside them has been both scientifically enriching and personally rewarding. Their kindness, generosity, professionalism, and positive spirit fostered a collaborative atmosphere that made everyday work in the laboratory enjoyable and motivating. Beyond the research itself, I will always cherish the friendships we built and the many memorable moments we shared together.

More broadly, I wish to thank all my colleagues, collaborators, and friends in **Nancy, Dijon, Montréal, and Dammam**, whose support, encouragement, scientific discussions, and friendship have accompanied me throughout this journey. Each encounter, collaboration, and exchange has contributed, in one way or another, to my personal and professional development.

To my family:

Finally, and most profoundly, my deepest gratitude and love belong to my beloved family, who have been the foundation of everything I have achieved.

To my dear mother, **Hanan**, whose unconditional love, endless prayers, and quiet sacrifices have accompanied me throughout every stage of my life. Her warmth, tenderness, and unwavering belief in me have always been my greatest source of comfort and inner strength. No achievement of mine can be separated from the love she has poured into my life since my very first breath.

To my dear father, **Ghazi** (may his soul rest in peace), whose wisdom, integrity, and dedication to excellence shaped who I am as a person, a physician, and a researcher. Though he is no longer with us, his example continues to inspire me every day to pursue the highest standards in everything I do. His memory lives within every page of this work, and I carry his values and his pride with me in every step I take. I wish he could have seen this moment — I dedicate it to him with all my love, gratitude, and longing.

To my beloved wife, **Shadia**, no words can truly express how grateful I am for everything she has done throughout this long journey. She has been my constant source of strength, comfort, patience, and inspiration. She accepted every challenge that accompanied this path, every sacrifice required by years of training abroad, every long working day, every late night dedicated to research, and every moment of uncertainty — always with unwavering love and encouragement. Her unconditional support gave me the confidence to persevere through the most difficult moments, while her faith in me continually reminded me why this journey was worth pursuing. Every accomplishment reflected

in these pages is inseparable from her countless sacrifices and her unwavering belief in my dreams. This thesis is not only the culmination of my work, but also a reflection of her love, patience, and devotion. It is with immense love, admiration, and gratitude that I dedicate this thesis to her.

To my precious daughters and son — **Natalie**, **Khalid**, **Taline**, and **Talya** — you are the joy that fills every moment of my life and the reason behind every effort I make. Your smiles, your laughter, and your innocent love have been my greatest reward throughout this journey. You have grown during these years of hard work, and I hope one day you will understand that everything I have done, I have done for you and for the future I wish to build for you. You are my greatest pride, my deepest happiness, and my most beautiful achievement.

Table of Contents

Resume en Francais 12

Summry in English 18

List of Presentations and Publications 25

Presentations related to the thesis 28

List of Abbreviations 29

List of Figures 32

List of Tables 35

General Introduction 37

Chapter 1: Clinical background of the bovine pericardial patch 41

1. Anatomy of bovine pericardium 41

2. Biological structures of bovine pericardium 44

2.1. Fibrous proteins (e.g., collagen, elastin, fibrillin, and fibulin) 44

2.2. Adhesive glycoproteins (e.g., laminin, fibronectin, tenasin, thrombospondin, and integrin) 45

2.3. Glycosaminoglycans 47

3. Physiological functions of the bovine pericardium 49

3.1. Immunological function 49

3.2. Mechanical function 49

3.3. Fixation function 49

4. Clinical background of the bovine pericardium patch from the basic to implantation 51

4.1. History of the utilization of bovine pericardial patches 51

4.2. Bovine pericardial patches currently available on the market 52

4.3. Harvesting technique of bovine pericardial patches 54

4.4. Decellularization and pre-commercial technique of bovine pericardial patches 56

4.5. Clinical application of the pericardial patch 60

4.6. Biomechanical Characterization of Bovine Pericardial Patches: Insights and Perspectives 65

4.7. Histological Examination of Bovine Pericardial Patches: Insights and Observations...69
Chapter 2: The aorta and alternative methods for replacing aortic tissue....73
1. Anatomy and structure of vessels: exploring their histological properties....73
1.1. Intima....75
1.2. Media....75
1.3. Adventitia....75
2. Biomechanics of arteries: understanding their functional role....82
3. Biomechanical and Structural Alterations in Aortic Aneurysms....97
4. Alternative Techniques for Aortic Tissue Reconstruction....99
4.1. Synthetic graft....99
4.2. Xenogeneic tissue....99
4.3. Cryopreserved grafts....99
4.4. The autologous tissues....100
4.5. Tissue-engineered vascular graft (TEVG)....100
5. Biomechanical characteristics of blood vessels using Magnetic resonance imaging (MRI) 106
Chapter 3: The objective of study....111
Chapter 4: The Materials and Methods....114
1. Radiological aspect....114
2. Biomechanical aspect....125
3. Failure test....136
4. Loss of energy test....141
5. Histological observation study....146
Chapter 5: Results....151
1. Biomechanic by MRI....151
2. Failure test....155
3. Loss of Energy test....170
Chapter 6: Discussion....174
1. Biomechanic by MRI....174
2. Failure test....176

3. Loss of energy test 179
4. Future Perspectives 181
Chapter 7: Conclusion 183
References 191

Resume en Francais

Introduction Générale :

Le patch péricardique bovin (BPP) est un matériau biologique composite, non linéaire, anisotrope et multi-laminaire, obtenu à partir du péricarde d'animaux bovins, principalement des veaux et des vaches. Le péricarde est un sac fibreux avasculaire entourant le cœur, composé de deux couches principales : une couche séreuse interne constituée principalement de collagène de type IV et de laminine, et une couche fibreuse externe composée principalement de collagène de type I (Shklover et al., 2019; Xing et al., 2021a). La matrice extracellulaire (MEC) du péricarde, riche en collagène, élastine, fibrilline, fibronectine et glycosaminoglycanes, confère l'intégrité structurelle et la polyvalence biomécanique qui font des BPPs des matériaux attractifs pour les applications chirurgicales.

L'utilisation des BPPs en chirurgie cardiovasculaire remonte à 1971, lorsqu'Ionescu et al. ont réalisé le premier remplacement de valve aortique par un patch péricardique bovin chez l'homme (Ionescu et al., 1977). Depuis lors, leur utilisation s'est étendue à de nombreuses spécialités chirurgicales, notamment la chirurgie vasculaire, cardiaque, thoracique, urologique, neurochirurgicale et générale (Li et al., 2011). Leur adoption généralisée est motivée par leur fiabilité, durabilité, biocompatibilité, résistance aux infections, disponibilité immédiate et absence de dégénérescence anévrysmale (Li et al., 2011; Zouhair et al., 2020).

En chirurgie vasculaire, les BPPs sont de plus en plus utilisés sous forme de tubes sur mesure (CMBPTs) pour remplacer des segments aortiques infectés ou pathologiques, offrant une alternative biologique et économiquement avantageuse aux prothèses synthétiques et aux allogreffes cryoconservées (Belkorissat et al., 2020; Frisch et al., 2025). L'aorte fonctionne comme un réservoir élastique dynamique, stockant environ 60% du volume d'éjection systolique ventriculaire gauche pendant la systole et le libérant pendant la diastole pour maintenir le flux sanguin périphérique, phénomène connu sous le nom d'effet Windkessel (Salvi, 2017). Les matériaux de remplacement doivent donc reproduire non seulement la résistance mécanique, mais également les propriétés de stockage et de dissipation d'énergie élastique de l'aorte native.

Malgré l'utilisation clinique généralisée des BPPs de plusieurs fabricants commerciaux, aucune étude systématique comparative n'avait précédemment évalué leur équivalence biomécanique en identifiant les fournisseurs. De plus, le ratio de dissipation d'énergie (EDR) — paramètre viscoélastique reflétant la proportion d'énergie mécanique perdue par cycle de chargement-déchargement — n'avait été

évalué de manière systématique dans les BPPs commerciaux. Cette thèse comble ces lacunes à travers trois approches complémentaires : une évaluation radiologique par IRM des CMBPTs in vitro, des tests de rupture en traction uniaxiale des BPPs commerciaux, et des tests de fatigue à faible nombre de cycles avec mesure de l'EDR.

Objectifs:

Les objectifs principaux de cette thèse étaient : évaluer le comportement biomécanique des CMBPTs in vitro par IRM ; comparer les propriétés mécaniques des BPPs de quatre fabricants commerciaux par des tests de traction uniaxiale standardisés, incluant trois nouveaux paramètres de module élastique (PEM, MPEM, MEM) ; et caractériser le comportement de dissipation d'énergie des BPPs commerciaux par des tests de fatigue à faible nombre de cycles et mesure de l'EDR. Les objectifs secondaires comprenaient la quantification de la variabilité intra- et inter-échantillons, l'évaluation du comportement mécanique selon l'orientation, et la préparation histologique de tous les spécimens pour une analyse microscopique quantitative future.

L'hypothèse centrale était que les CMBPTs chimiquement modifiés ne reproduisent pas pleinement le comportement biomécanique natif de l'aorte humaine, et que les BPPs de différents fournisseurs pourraient présenter une variabilité dans leurs propriétés mécaniques attribuable à des méthodes de traitement pré-commercial différentes.

Matériaux et Méthodes:

Étude radiologique : Sept CMBPTs ont été fabriqués par l'auteur à partir de BPPs Edwards Lifesciences® suturés autour d'un mandrin de 20 mm de diamètre en Prolène 5-0. Chaque tube mesurait 20 × 130 mm. Un fantôme de flux pulsatile in vitro a été construit à l'aide d'une pompe péristaltique ISMATEC® MCP-Z délivrant 1650 ml/min à 75 pulsations/min, reproduisant les conditions de débit de l'aorte abdominale.
Les acquisitions IRM ont été réalisées sur un système Siemens Prisma 3 Tesla utilisant des séquences en contraste de phase (PC) et en précession libre à l'état stationnaire équilibré (bSSFP). La déformation circonférentielle et la distensibilité ont été calculées à partir des mesures de surface en coupe transversale en systole et en diastole. L'analyse des images a été réalisée avec le logiciel QIR-MR (CASIS, Quetigny, France).

Étude biomécanique : Quarante BPPs de quatre fabricants commerciaux ont été obtenus : Edwards Lifesciences® (n=10, 10×15 cm), Supple Peri-Guard® Baxter (n=10, 10×16 cm), Xenosure®

LeMaitre (n=10, 10×16 cm) et Invengenx® Tisgenx (n=10, 7×10 cm). Chaque patch a été découpé en dix spécimens en forme d'os de chien à l'aide d'un gabarit 3D standardisé : cinq orientés verticalement et cinq horizontalement. Les spécimens mesuraient 50×10 mm avec une longueur utile de test de 36 mm.

Les tests de rupture (pièces 1, 2, 6, 7) ont été réalisés sur un système de traction uniaxiale horizontal (LM1, TA Instruments ElectroForce®) après dix cycles de préconditionnement à 0,125 mm par moteur à 1 Hz. Trois paramètres de module élastique ont été déterminés : le module élastique physiologique (PEM, 80-140 mmHg), le module élastique physiologique maximal (MPEM, 360 mmHg) et le module élastique maximal à rupture (MEM).

Les tests de fatigue à faible nombre de cycles (pièces 3, 4, 8, 9) ont été réalisés à des amplitudes de déplacement progressives de 1.8, 3.6, 5.4 et 7.2 mm (correspondant à 10%, 20%, 30% et 40% de déformation) à 0,1 Hz, avec un cycle de chargement-déchargement par palier.

L'EDR a été calculé à partir de l'aire de la boucle d'hystérésis de la relation contrainte-déformation. Tous les tests ont été réalisés dans de l'eau distillée à 37 ± 0,1°C dans des conditions hydrothermiques contrôlées.

La préparation histologique (pièces 5, 10) comprenait la fixation en formol tamponné à 4%, la déshydratation, l'inclusion en paraffine, la coupe au microtome à 4 µm et la coloration par HES, Orcéine, Trichrome de Masson, colorant de Weigert et Bleu Alcian. Au total, 400 lames ont été préparées et numérisées pour une analyse quantitative future.

Les analyses statistiques ont été réalisées avec GraphPad Prism 7 avec test de normalité de Shapiro-Wilk, ANOVA/Tukey, Kruskal-Wallis/Dunn et t-test de Student selon les cas ($p < 0,05$).

Résultats:

Étude IRM : La déformation circonférentielle moyenne obtenue par séquence PC était de 12,1 ± 3,60% (étendue : 6,7–18,1%) et par bSSFP de 10,3 ± 3,20% (étendue : 5,5–15,5%), toutes deux dans la plage physiologique normale de l'aorte native (Redheuil et al., 2010 ; Herment et al., 2011). Les valeurs moyennes de distensibilité étaient de $1,5 \pm 0,5 \times 10^{-3}$ $mmHg^{-1}$ par PC et de $1,3 \pm 0,4 \times 10^{-3}$ $mmHg^{-1}$ par bSSFP, toutes deux inférieures aux valeurs physiologiques de l'aorte native (Redheuil et al., 2010). Aucune différence statistiquement significative n'a été trouvée entre les mesures PC et

bSSFP (p = 0,195). La vitesse systolique maximale était de 45,5 ± 11 cm/s et la vitesse moyenne de 5,73 ± 2,84 cm/s.

Test de rupture : L'épaisseur des patchs était cohérente entre les groupes, allant de 0,384 à 0,469 mm, sans différences inter-groupes significatives sauf entre Xenosure® et Invengenx® dans la sous-étude EDR. La variabilité intra-échantillon était faible pour tous les groupes (CV% allant de 13,4% à 18,7%). Aucune différence significative selon l'orientation n'a été trouvée pour le PEM, le MPEM ou le MEM dans la majorité des comparaisons, confirmant un comportement isotrope. La seule exception était Invengenx® qui montrait une différence significative dans la variance du MEM entre les orientations (p = 0,013). Supple Peri-Guard® présentait des valeurs de PEM significativement plus faibles que Xenosure® (p = 0,0035) et Invengenx® (p = 0,0396), tandis que toutes les autres comparaisons inter-groupes pour le MPEM et le MEM étaient non significatives.

Étude EDR : À 10% de déformation, les 80 spécimens ont tous atteint la déformation cible. Les valeurs moyennes d'EDR étaient : Edwards Lifesciences® 21,40 ± 7,02%, Supple Peri-Guard® 24,95 ± 6,80%, Xenosure® 24,99 ± 6,04% et Invengenx® 23,37 ± 6,12%, sans différences inter-groupes statistiquement significatives (p > 0,05). À 20% de déformation, les taux de survie des spécimens étaient : Edwards 65% (13/20), Supple Peri-Guard 50% (10/20), Xenosure 30% (6/20) et Invengenx 5% (1/20). À 30% de déformation, seuls deux spécimens Supple Peri-Guard® (10%) ont survécu, sans survie dans les autres groupes. Aucune différence selon l'orientation n'a été observée pour l'EDR.

Discussion:

Les résultats de l'IRM démontrent que les CMBPTs présentent des valeurs de déformation circonférentielle quasi-physiologiques comparables à l'aorte thoracique ascendante et descendante native (Redheuil et al., 2010). La distensibilité réduite par rapport aux valeurs aortiques natives est cohérente avec l'effet connu de la fixation au glutaraldéhyde sur la suppression de la compliance médiée par l'élastine (Tremblay et al., 2009). L'absence de différences significatives entre les séquences PC et bSSFP soutient l'utilisation des deux méthodes d'acquisition pour l'estimation de la déformation dans les modèles de tubes péricardiques, contrastant avec les résultats antérieurs d'Herment et al. dans des études sur l'aorte native (Herment et al., 2011).

Les résultats des tests de rupture confirment que les BPPs traités au glutaraldéhyde de différents fabricants présentent un comportement mécanique globalement équivalent sous des charges physiologiques et supraphysiologiques, soutenant leur utilisation interchangeable en chirurgie cardiovasculaire. L'absence de différences selon l'orientation confirme que les BPPs peuvent être

implantés dans n'importe quelle orientation sans conséquence biomécanique significative, simplifiant la pratique chirurgicale. Les concepts de PEM et de MPEM, introduits dans cette thèse comme nouveaux paramètres d'évaluation calibrés sur des plages de pression physiologique, représentent une contribution méthodologique applicable au domaine plus large de la caractérisation des biomatériaux (Duprey et al., 2010).

Les résultats de l'EDR révèlent que la réticulation au glutaraldéhyde homogénéise le comportement viscoélastique des BPPs commerciaux indépendamment des protocoles spécifiques aux fabricants, très probablement par une réticulation covalente dominante des fibres de collagène et une suppression des contributions élastiques médiées par l'élastine(Chandran et al., 2012; Peng et al., 2017). Cette convergence des valeurs d'EDR est cohérente avec l'observation bien établie que le glutaraldéhyde induit des altérations unidirectionnelles des propriétés des tissus bioprosthétiques entre différents fabricants (Chung et al., 2014). La défaillance structurelle marquée observée à des déformations supérieures à 20% met en évidence une limitation mécanique critique pertinente pour le choix du site d'implantation, en particulier dans l'aorte proximale où la déformation circonférentielle physiologique peut atteindre 29% (Herment et al., 2011).

L'EDR fournit des informations cliniquement significatives au-delà de l'analyse conventionnelle contrainte-déformation en quantifiant la composante visqueuse dissipant l'énergie du comportement tissulaire — la proportion d'énergie mécanique convertie en chaleur plutôt que récupérée comme recul élastique pendant chaque cycle cardiaque. Un EDR élevé indique une efficacité élastique réduite et un soutien diminué pour l'effet Windkessel, avec des implications potentielles pour le couplage ventriculo-aortique et la charge de travail ventriculaire gauche (Salvi, 2017; Westerhof et al., 2009).

Conclusion:

Cette thèse doctorale fournit la première caractérisation biomécanique systématique et multimodale des BPPs commerciaux traités au glutaraldéhyde et des CMBPTs. Les CMBPTs présentent une déformation circonférentielle quasi-physiologique avec une distensibilité réduite, suggérant des performances biomécaniques acceptables pour la reconstruction aortique. Les BPPs commerciaux démontrent une épaisseur constante, un comportement isotrope et des propriétés mécaniques globalement équivalentes entre fabricants sous des charges physiologiques et modérément supraphysiologiques. L'EDR est proposé comme un paramètre biomécanique cliniquement significatif et complémentaire pour l'évaluation des biomatériaux cardiovasculaires. Les travaux futurs devront intégrer des tests mécaniques biaxiaux, des modèles de flux pulsatiles, une analyse histologique quantitative et des études in vivo à long terme utilisant l'IRM 4D de flux pour caractériser

pleinement le comportement de ces matériaux et optimiser leur sélection pour des applications chirurgicales spécifiques.

Summry in English

General Introduction:

The bovine pericardial patch (BPP) is a non-linear, anisotropic, multi-laminate biological material derived from the pericardium of bovine animals, primarily calves and cows. The pericardium is an avascular fibrous sac surrounding the heart, composed of two principal layers: an inner serous layer primarily constituted of collagen type IV and laminin, and an outer fibrous layer predominantly composed of collagen type I (Shklover et al., 2019; Xing et al., 2021b). The extracellular matrix (ECM) of the pericardium, rich in collagen, elastin, fibrillin, fibronectin, and glycosaminoglycans, confers the structural integrity and biomechanical versatility that make BPPs attractive for surgical use.

BPPs have been used in cardiovascular surgery since 1971, when Ionescu et al. performed the first bovine pericardial aortic valve replacement in a human (Ionescu et al., 1977). Since then, their use has expanded across multiple surgical specialties including vascular, cardiac, thoracic, urological, neurosurgical, and general surgery (Li et al., 2011). Their widespread adoption is driven by consistent reliability, durability, biocompatibility, resistance to infection, off-the-shelf availability, and the absence of aneurysmal degeneration (Li et al., 2011; Zouhair et al., 2020).

In vascular surgery, BPPs are increasingly used as custom-made tubular grafts (CMBPTs) to replace infected or diseased aortic segments, offering a biological and cost-effective alternative to synthetic grafts and cryopreserved allografts (Belkorissat et al., 2020; Frisch et al., 2025). The aorta functions as a dynamic elastic reservoir, storing approximately 60% of the left ventricular stroke volume during systole and releasing it during diastole to maintain peripheral blood flow, a phenomenon known as the Windkessel effect (Salvi, 2017). Replacement materials must therefore reproduce not only mechanical strength but also the elastic energy storage and dissipation properties of the native aorta.

Despite the widespread clinical use of BPPs from multiple commercial manufacturers, no systematic comparative study had previously assessed their biomechanical equivalence by identifying the supplier. Furthermore, the energy dissipation ratio (EDR) — a viscoelastic parameter reflecting the proportion of mechanical energy lost per loading-unloading cycle — had never been systematically evaluated in commercial BPPs.

This thesis addresses these gaps through three complementary investigational approaches: in vitro MRI-based radiological assessment of CMBPTs, uniaxial tensile failure testing of commercial BPPs, and low-cycle fatigue testing with EDR measurement.

Objectives:

The primary objectives of this thesis were: to evaluate the biomechanical behavior of CMBPTs in vitro using MRI; to compare the mechanical properties of BPPs from four commercial manufacturers using standardized uniaxial tensile testing including three novel elastic modulus parameters (PEM, MPEM, MEM); and to characterize the energy dissipation behavior of commercial BPPs through low-cycle fatigue testing and EDR analysis. Secondary objectives included quantification of intra- and inter-sample variability, evaluation of orientation-dependent mechanical behavior, and histological preparation of all specimens for future quantitative microscopic analysis.

The central hypothesis was that chemically modified CMBPTs do not fully replicate the native biomechanical behavior of the human aorta, and that BPPs from different suppliers may exhibit variability in their mechanical properties attributable to differing pre-commercial treatment methods.

Materials and Methods:

Radiological study: Seven CMBPTs were fabricated by the author from Edwards Lifesciences® BPPs sutured around a 20 mm diameter mandrel using Prolene 5-0 suture. Each tube measured 20 × 130 mm. An in vitro pulsatile flow phantom was constructed using an ISMATEC® MCP-Z peristaltic pump delivering 1650 ml/min at 75 pulses/min, reproducing abdominal aortic flow conditions. MRI acquisitions were performed on a 3 Tesla Prisma Siemens system using both phase-contrast (PC) and balanced steady-state free precession (bSSFP) sequences. Circumferential strain and distensibility were calculated from cross-sectional area measurements at systole and diastole, and peak systolic velocity and mean velocity were measured from PC acquisitions. Image analysis was performed using QIR-MR software (CASIS, Quetigny, France).

Biomechanical study: Forty BPPs from four commercial manufacturers were obtained: Edwards Lifesciences® (n=10, 10×15 cm), Supple Peri-Guard® Baxter (n=10, 10×16 cm), Xenosure® LeMaitre (n=10, 10×16 cm), and Invengenx® Tisgenx (n=10, 7×10 cm). Each patch was sectioned into ten bone-shaped specimens using a standardized 3D-printed cutter: five vertically and five horizontally oriented. Specimens measured 50×10 mm with a 36 mm effective gauge length.

Failure testing (pieces 1, 2, 6, 7) was performed on a horizontal uniaxial tensile system (LM1, TA Instruments ElectroForce®) following ten preconditioning cycles at 0.125 mm per motor at 1 Hz. Three elastic modulus parameters were determined: the physiological elastic modulus (PEM, 80-140 mmHg), the maximum physiological elastic modulus (MPEM, 360 mmHg), and the maximum elastic modulus at failure (MEM).

Low-cycle fatigue testing (pieces 3, 4, 8, 9) was conducted at progressive displacement amplitudes of 1.8, 3.6, 5.4, and 7.2 mm (corresponding to 10%, 20%, 30%, and 40% strain) at 0.1 Hz, with one loading-unloading cycle per step. The EDR was calculated from the hysteresis loop area of the stress-strain relationship. All tests were performed in distilled water at 37 ± 0.1°C under temperature-controlled hydrated conditions.

Histological preparation (pieces 5, 10) included fixation in 4% buffered formalin, dehydration, paraffin embedding, microtome sectioning at 4 μm, and staining with HES, Orcein, Masson's Trichrome, Weigert's stain, and Alcian Blue. A total of 400 slides were prepared and digitized for future quantitative analysis.

Statistical analyses were performed using GraphPad Prism 7 with Shapiro-Wilk normality testing, ANOVA/Tukey, Kruskal-Wallis/Dunn, and Student's t-test as appropriate ($p < 0.05$).

Results:

MRI study: The mean circumferential strain obtained by PC sequence was 12.1 ± 3.60% (range: 6.7–18.1%) and by bSSFP was 10.3 ± 3.20% (range: 5.5–15.5%), both within the normal physiological range for the native aorta (Redheuil et al., 2010; Herment et al., 2011). Mean distensibility values were $1.5 \pm 0.5 \times 10^{-3}$ $mmHg^{-1}$ by PC and $1.3 \pm 0.4 \times 10^{-3}$ $mmHg^{-1}$ by bSSFP, both lower than physiological values for the native aorta (Redheuil et al., 2010). No statistically significant difference was found between PC and bSSFP measurements ($p = 0.195$). Peak systolic velocity was 45.5 ± 11 cm/s and mean velocity was 5.73 ± 2.84 cm/s.

Failure test: Patch thickness was consistent across groups ranging from 0.384 to 0.469 mm, with no significant inter-group differences except between Xenosure® and Invengenx® in the EDR substudy. Intra-sample variability was low for all groups (CV% ranging from 13.4% to 18.7%). No significant orientation-dependent differences in PEM, MPEM, or MEM were found in the majority of comparisons, confirming isotropic behavior. The only exception was Invengenx® which showed a significant difference in MEM variance between orientations ($p = 0.013$). Supple Peri-Guard®

exhibited significantly lower PEM values compared to Xenosure® ($p = 0.0035$) and Invengenx® ($p = 0.0396$), while all other intergroup comparisons for MPEM and MEM were non-significant.

EDR study: At 10% strain, all 80 specimens reached the target deformation. Mean EDR values were: Edwards Lifesciences® 21.40 ± 7.02%, Supple Peri-Guard® 24.95 ± 6.80%, Xenosure® 24.99 ± 6.04%, and Invengenx® 23.37 ± 6.12%, with no statistically significant intergroup differences ($p > 0.05$). At 20% strain, specimen survival rates were: Edwards 65% (13/20), Supple Peri-Guard 50% (10/20), Xenosure 30% (6/20), and Invengenx 5% (1/20). At 30% strain, only two Supple Peri-Guard® specimens (10%) survived, with no survival in other groups. No orientation-dependent differences in EDR were observed.

Discussion:

The MRI results demonstrate that CMBPTs exhibit near-physiological circumferential strain values comparable to the native ascending and descending thoracic aorta (Redheuil et al., 2010). The reduced distensibility relative to native aortic values is consistent with the known effect of glutaraldehyde fixation in suppressing elastin-mediated compliance (Tremblay et al., 2009). The absence of significant differences between PC and bSSFP sequences supports the use of both acquisition methods for strain estimation in pericardial tube models, contrasting with prior findings by Herment et al. in native aorta studies (Herment et al., 2011).

The failure test results confirm that glutaraldehyde-treated BPPs from different manufacturers demonstrate broadly equivalent mechanical behavior under physiological and supraphysiological loading, supporting their interchangeable use in cardiovascular surgery. The absence of orientation-dependent differences confirms that BPPs can be implanted in any orientation without significant biomechanical consequence, simplifying surgical practice. The concepts of PEM and MPEM, introduced in this thesis as novel evaluation parameters calibrated to physiological pressure ranges, represent a methodological contribution applicable to the broader field of biomaterial characterization (Duprey et al., 2010).

The EDR results reveal that glutaraldehyde cross-linking homogenizes the viscoelastic behavior of commercially available BPPs regardless of manufacturer-specific protocols, most plausibly through dominant covalent cross-linking of collagen fibers and suppression of elastin-mediated elastic contributions (Chandran et al., 2012; Peng et al., 2017). This convergence of EDR values is consistent with the well-established observation that glutaraldehyde induces unidirectional alterations in bioprosthetic tissue properties across different manufacturers (Chung et al., 2014).

The marked structural failure observed at strains above 20% highlights a critical mechanical limitation relevant to implantation site selection, particularly in the proximal aorta where physiological circumferential strain can approach 29% (Herment et al., 2011).

The EDR provides clinically meaningful information beyond conventional stress-strain analysis by quantifying the viscous energy-dissipating component of tissue behavior — the proportion of mechanical energy converted to heat rather than recovered as elastic recoil during each cardiac cycle. A higher EDR indicates impaired elastic efficiency and reduced support for the Windkessel effect, with potential implications for ventriculo-aortic coupling and left ventricular workload (Salvi, 2017; Westerhof et al., 2009).

Conclusion:

This doctoral thesis provides the first systematic, multi-modal biomechanical characterization of commercially available glutaraldehyde-treated BPPs and CMBPTs. CMBPTs exhibit near-physiological circumferential strain with reduced distensibility, suggesting acceptable biomechanical performance for aortic reconstruction. Commercial BPPs demonstrate consistent thickness, isotropic behavior, and broadly equivalent mechanical properties across manufacturers under physiological and moderate supraphysiological loading. The EDR is proposed as a clinically meaningful and complementary biomechanical parameter for cardiovascular biomaterial evaluation. Future work should incorporate biaxial mechanical testing, pulsatile flow models, quantitative histological analysis, and long-term in vivo studies using 4D flow MRI to fully characterize the behavior of these materials and optimize their selection for specific surgical applications.

List of Presentations and Publications

Publications related to my thesis:

1. **ALBLOWI Abdulrahman**, LIN Siyu, BOUCHOT Olivier, SETTEMBRE Nicla, MALIKOV Serguei, LALANDE Alain. *Biomechanical Assessment Using MRI of Custom-Made Bovine Pericardial Tubes as Potential Aortic Replacements.* **Radiology Research and Practice.** Under review.

2. **ALBLOWI Abdulrahman**, LIN Siyu, BOUCHOT Olivier, LAGRANGE Jérémy, SETTEMBRE Nicla, MALIKOV Serguei, LALANDE Alain. *Biomechanical Evaluation of Stress–Strain Behavior of Different Bovine Pericardial Patches Preserved in Glutaraldehyde Solution.* **Discover Applied Sciences.** Under review.

3. **ALBLOWI Abdulrahman**, LIN Siyu, BOUCHOT Olivier, LAGRANGE Jérémy, SETTEMBRE Nicla, LALANDE Alain, MALIKOV Serguei. *Analysis of Energy Dissipation Ratio in Commercial Bovine Pericardial Patches Treated with Glutaraldehyde Solution.* **Journal of Functional Biomaterials.** Accepted.

Other publications :

1. **ALBLOWI Abdulrahman**, SETTEMBRE Nicla, ALSADERY Humod, NABOKOV Vicotr, PEREZ Maneula, MALIKOV Serguie. **Anatomical Study of Abdominal Wall Muscle Innervation to Optimize Retroperitoneal Vascular Approach.** *Ann Vasc Surg.* 2025. doi:10.1016/j.avsg.2024.09.051.

2. **ALBLOWI Abdulrahman**, SETTEMBRE Nicla, PEREZ Manuela, MALIKOV Serguei. *The Feasibility of Using Parietal Peritoneum Aponeurotic Tissue as a Vascular Substitute in Aortic Reconstruction: An Anatomical and Histological Study.* **Scientific Reports.** Under review.

3. **ALBLOWI Abdulrahman**, ELKHOURI Stéphane. *Endovascular Retrieval of a Migrated EVAR Limb Using Flexible Biopsy Forceps: A Bail-Out Technique for Type Ib Endoleak.* **EJVES Vascular Forum.**

4. **ALBLOWI Abdulrahman**, BLITTI Comlan Mawuko, JAILLANT Noémie, LEBOFFE Mélanie, GARCIA RODRIGUES Jairo, DELPY Jean-Philippe, STEINMETZ Eric. *One-Step Bilateral Endovascular Treatment of Complex Atherosclerotic Common Femoral Artery Stenosis.* Submitted.

5. SADOUL Charles, SETTEMBRE Nicla, NABOKOV Vicotr, **ALBLOWI Abdulrahman**, BELKORISSAT Rabie Abdelhakim, MALIKOV Serguei. **A New Technique for the Treatment of Venous Popliteal Aneurysms Using the Axillary Vein: Medium and Long-Term Results.** *Ann Vasc Surg.* 2025. doi:10.1016/j.avsg.2024.10.028.

6. FRISCH Simon, SETTEMBRE Nicla, BELKORISSAT Rabie Abdelhakim, GUERCI Philippe, MANDRY Damien, **ALBLOWI Abdulrahman**, LALEVÉE Laurent, LEFEVRE Benjamin, MALIKOV Serguei. **Management of Infectious Aortic Aneurysms: Short- and Mid-Term Outcomes**. *Ann Vasc Surg*. 2025. doi:10.1016/j.avsg.2025.01.042.

7. ALSADERY Humood, ALJEHANI Yesser, ALRESHAID Farouk, ELGHONEIMY Yasser, BAMALAN Omar, **ALBLOWI Abdulrahman**, ALHELAL Jumana, ELBAZ Ayman, ABOOLLO Moustafa. **Esophageal Injury After Anterior Cervical Spine Fixation: What Can Thoracic Surgeons Offer?** *Med Arch.* 2024. doi:10.5455/medarh.2024.78.290-295.

8. NASR Ayman Omar, ALSADERY Humood, OSMAN Adel Gaafar Elbagir, **ALBLOWI Abdulrahman**, BAMALAN Omar, ALSHAIKHI Ahmed, ALOSAIMI Nader, ELGHONEIMY Yasser, NABRI Mamoun Ahmed. **Trauma-Related Pneumopericardium: A Literature Review.** *Saudi J Health Sci.* 2023. **doi:10.4103/sjhs.sjhs_146_22.**

9. ZEINULLINA Aida, MAHAMED Jad, MIKAEL Ahmed, KAZMI Fizza, ADESOYE Emmanuel, SAH Halima, **ALBLOWI Abdulrahman**, MADERA Dario. *Early versus delayed extubation after open aortic surgery: A systematic review.* **Annals of Vascular Surgery.** Under review. Manuscript ID: **AVS-D-26-01116**.

Presentations related to the thesis:

1. **ALBLOWI Abdulrahman**, Lin S, Settembre N, Bouchot O, Malikov S, Lalande A. **The Biomechanical Characteristics of Different Bovine Pericardial Patches Preserved in Glutaraldehyde Solution.** Presented at the **29th Congress of the European Society of Biomechanics (ESB 2024)**, Edinburgh, Scotland, UK, June 30–July 3, 2024. (Oral Presentation).

Other presentations:

2. **ALBLOWI Abdulrahman**, Settembre N, Nabokov V, Perez M, Malikov S. **Anatomical Study of Abdominal Wall Muscle Innervation to Optimize Retroperitoneal Vascular Approach.** Presented at the **37th Annual Congress of the Société de Chirurgie Vasculaire et Endovasculaire (SCVE 2024)**, Montpellier, France, June 26–29, 2024. (Oral Presentation).

List of Abbreviations

Abbreviations	Meaning
Δ	Delta
ε	Strain
γ	Shear strain
σ	Stress
h	Arterial wall thickness
A	Surface area or cross-sectional area
A_l	Area under the loading curve
A_u	Area under the unloading curve
Ad	Luminal surface area at diastole phase
As	Luminal surface area at systole phase
AAA	Abdominal aortic aneurysm
BPP	Bovine pericardial patch
bSSFP	Balanced steady-state free precession
CEA	Carotid endarterectomy
CAP	Central arterial pressure or pressure difference
CNBPTs	Custom-made bovine pericardial tubes
CMR	Cardiovascular magnetic resonance
CV%	Coefficient of variation
DBP	Decellularized bovine pericardium
Dd	Diameter of vessel at diastole phase
Ds	Diameter of vessel at diastole phase
E	Circumferential or physiological Young's modulus
ECs	Endothelial cells
ECM	Extra-cellular matrix
EDR	Energy dissipation ratio
EL	Energy loss
ET	Echo time
ePTFE	Expanded Polytetrafluoroethylene
F	Load
GAGs	Glycosaminoglycans
GA	Glutaraldehyde

GE	Gradient echo
GSV	Greater saphenous vein
H&E	Hematoxylin and Eosin
HES	Hematoxylin, Eosin and Safron
IQR	Interquartile rang
LCF	Low-cycle fatigue
MAA	Mycotic aortic aneurysms
Max	Maximum
Mean ± SD	Mean and standard deviation
MEM	Maximal elastic modulus
Min	Minimum
MPEM	Maximum physiological elastic modulus
MRI	Magnetic resonance imaging
NBP	Native bovine pericardium
OSR	Open surgical repair
p25, p50, p75	25th percentile, 50th percentile (median), and 75th percentile.
PC	Phase contrast
Pd	Diastolic pressure
Ps	Systolic pressure
PEM	Physiological elastic modulus
PET	Polyethylene terephthalate
PWV	Pulse wave velocity
R	Radius of artery
RF	Radiofrequency
RT	Repetition time
rPA	Right pulmonary artery
S	Strain
SAL	Sterility assurance level
SD	Standard deviation
SMC	Smooth muscle cell
SFV	Superficial femoral veins
TEVG	Tissue-engineered vascular graft
VENC	Velocity encoding
WSS	Wall shear stress
YM	Young’s modulus

List of Figures

Figure 1. Illustration of pericardium. 43

Figure 2. Major components of the extracellular matrix (ECM) 48

Figure 3. The stretch and recoil of ECM due to the presence of elastin and collagen..... 50

Figure 4. The BPP mapping shows different thickness areas depending on the location.. 55

Figure 5. The BPP mapping shows different fibers orientation depending on the location. 55

Figure 6. The process of stabilization and sterilization of pericardial scaffolds by ultraviolet and low-energy electron irradiation. 58

Figure 7. Representation of the chemical, mechanical, and immunological factors that contribute to prosthetic valve dysfunction. 67

Figure 8. Histological study using hematoxylin and eosin stain of BPPs showing different collagen bandelle caliber 70

Figure 9. Surface roughness of porcine and bovine pericardial patches. 70

Figure 10. Histological analysis conducted in NBPs and DBPs 72

Figure 11. The structure and composition of the vessel wall. 74

Figure 12. The major branches of the aorta from ascending aorta to iliac bifurcation. 78

Figure 13. The structure and composition of the vein wall. 81

Figure 14. Great saphenous vein and its tributaries. 81

Figure 15. The Windkessel phenomenon under normal and abnormal vascular distensibility conditions. 83

Figure 16. The Windkessel phenomena and diastolic pump activity. 83

Figure 17. Application of the Laplace law. 92

Figure 18. Calculation of energy loss from the stress–strain relationship…… 95

Figure 19. Overview of intrinsic and extrinsic risk factors involved in aortic aneurysm formation. 98

Figure 20. Speculative model of AAA progression.. 98

Figure 21. Design patterns of weaving/braiding/knitting.. 102

Figure 22. Application of bipolar gradients. 107

Figure 23. Two acquisitions are illustrated 110

Figure 24. Phantom material used in research.. 116

Figure 25. The CMBPTs attached to 3D-printed connectors by nylon cable ties..... 116

Figure 26. Illustration schema of the experience and pump parameter. 118

Figure 27. MRI processing interface of flux and anatomical sequences 121

Figure 28. MRI analysis using QIR-MR software 124

Figure 29. Preparation and sectioning of BPPs..... 128

Figure 30. The 3D cutter shape that was designed and printed to have an equal bone-shaped piece. 129

Figure 31. Preparation of samples for uniaxial tensile testing. 131

Figure 32. An electronic thickness micrometer 133

Figure 33. The biaxial/uniaxial tensile test machine..... 133

Figure 34. Installation of the bone-shaped piece between the metallic clamps of the uniaxial machine 135

Figure 35. Precondition: in the red box there are one cycle from ten cycles of precondition. 137

Figure 36. Precondition setup 137

Figure 37. BPP stretched until rupture during horizontal uniaxial test..... 139

Figure 38. Stress–strain curve illustrating the three defined elastic modulus regions 139

Figure 39. Configuration of the energy loss testing protocol..... 142

Figure 40. Calculation of energy loss from the stress–strain relationship 145

Figure 41. Pre-analytical preparation of bovine pericardial patches for histological analysis. 149

Figure 42. Example of histological slide coding and digitalization process..... 149

Figure 43. Box plot graph of results of the result of strain percentage, distensibility mean velocity, and peak systolic velocity. 154

Figure 44. Description of BBP samples group thickness..... 156

Figure 45. Comparative analysis of BPPs thickness according to specimen orientation..... 158

Figure 46. PEM comparative analysis of horizontal and vertical samples of BPPs. 162

Figure 47. MPEM comparative analysis of horizontal and vertical samples of bovine pericardial tissue patch.. 167

Figure 48. MEM comparative analysis of horizontal and vertical samples of bovine pericardial tissue patch 169

Figure 49. Elastic modulus comparison of BPPs. 169

Figure 50. Energy dissipation ratio (EDR, %) of BPPs from four manufacturers 171

Figure 51. Percentage of BPPs failure after EDR testing. 173

Figure 52. Graphical Abstract 185

Figure 53.Graphical Abstract of failure test.. 187

Figure 54.Graphical abstract.. 189

List of Tables

Table 1. Overview of the bovine pericardial patches currently available on the market 53

Table 2. Utilization of BPPs in the medical fields. 63

Table 3. Characterization of bovine pericardium 68

Table 4. Vessel wall characteristics of circulatory systems. 74

Table 5. Normal value of aortic strain and distensibility in descending thoracic aorta and abdominal aorta. 89

Table 6. Elasticity of aorta in relation to age in MPa. 92

Table 7. Diagnostic criteria of the mycotic aortic aneurysm 105

Table 8. Operation technique of MAA 105

Table 9. List of serial numbers and dates of Edwards Lifesciences BPP 121

Table 10. Details of Bovine pericardial patches participated in our study 127

Table 11. The utilization of each piece of BPPs 131

Table 12. Descriptive table of strain percentage, distensibility, peak systolic velocity, and mean velocity values 153

Table 13. Paired samples T-Test of strain percentage and distensibilities values. 153

Table 14. Description of BBP samples group thickness 156

Table 15. Coefficient of variation of intra-sample variability of BPPs 158

Table 16. Coefficient of variation of inter-sample variability of BPPs 160

Table 17. PEM distribution Across Four BPP Suppliers 160

Table 18. Comparisons test for PEM inter-group differences in variability among BPPs 162

Table 19. MEPM distribution Across Four BPP Suppliers. 164

Table 20. Comparisons test for MPEM inter-group differences in variability among BPPs 164

Table 21. MEM distribution Across Four BPP Suppliers 167

Table 22. Comparisons test for MEM inter-group differences in variability among BPPs 167

Table 23. Description of BPPs' thickness (in mm) from different suppliers, calculated from 10 samples. 171

General Introduction

The bovine pericardial patch (BPP) is a non-linear, anisotropic, multi-laminate composite pliable material. It can be bent and twisted into different shapes, commonly imposed in substantial deformations during its physiological function as an implant material or graft a membrane. BPP is obtained from the pericardium of animals (calves and cows). The pericardium is an avascular fibrous sac that surrounds the heart and has a variety of functions. It consists of two layers with different histological structures and compositions. The first is an inner serous layer in direct contact with the heart which is made up of endothelium and basement membrane. It is composed primarily of collagen type IV and Laminin. The second is an external fibrous layer, made up of connective tissue and mainly composed of collagen type I (Shklover et al., 2019; Xing et al., 2021b).

A complex network of collagen and elastic fibers maintains the structural integrity of the pericardial layers (Spodick, 1992; Xing et al., 2021b). BPPs are widely used in medical specialties such as vascular surgery, cardiac surgery, thoracic surgery, neurosurgery, general surgery, and dental surgery (Li et al., 2011). They are widely used due to consistent reliability, facility of utilization, long durability, strength of material, biocompatibility, reduced suture line bleeding, off-the-shelf availability, absence of aneurismal degeneration, minimal risk of stenosis, low infection rate, and low risk of fibrotic adherence (Li et al., 2011; Zouhair et al., 2020). The decellularization of BPP could be used to produce biological scaffolds with superior immune compatibility and uniform biological features comparable to original tissues (Zouhair et al., 2020).

The BPP is widely used in vascular surgery for carotid and femoral bifurcation surgeries. The risk of infection in BPP is very low in comparison to non-biological materials. The retrospective study conducted by Ho et al. on 457 patients found that the risk of infection in BPP is 0.6% and the risk of pseudoaneurysm is 0.2% (Ho et al., 2012). A more recent retrospective study of carotid endarterectomy that was conducted on 256 patients found a lower risk of infection where no patient had developed an infection in this study (Papakostas et al., 2014). The short-term and mid-term result from our service (Vascular and Endovascular Surgery Department, Nancy University Hospital, Nancy, France), shows that the custom-made bovine pericardial tube (CMBPT) provides a viable alternative with various advantages including its accessibility, simplicity of preparation, and flexibility to implant in different aortic surgery application with no short-term or mid-term risks of infection or rupture (Belkorissat et al., 2020; Frisch et al., 2025).

The utilization of the pericardial patch in cardio-vascular surgery is cost-effective in comparison to other materials such as allografts and non-biological grafts. The allograft is a suitable replacement

for the aorta or other artery in an infected environment. On the other hand, the fundamental drawbacks of allograft use are the difficulty to obtain, the complexity and length of preparation, and the risk of degradation (Lehalle et al., 1997). BPP, in contrast, overcomes these limitations, making it a suitable alternative to allografts.

In the market, many companies produce BPPs for medical uses, using different methods of decellularization, different chaotropic agents, different additional pre-commercial treatments to stabilize the patches, and different reservation methods (Gilbert et al., 2006; Iop et al., 2018). Different methods for pre-commercial treatment of BPP could change patches' histological and biomechanical properties. The presence of cells in BPP could elicit a theoretical risk of immunological response inside the extracellular matrix. This response can vary depending on donor source, recipient tissue type, and host immune activity (Yi et al., 2017). The approved standardized sterilization methods include heat and pressure (dry heat, moist heat), ionizing radiation (ultraviolet, X-ray, and E-beam), and chemical sterilant (ethylene oxide, hydrogen peroxide, peracetic acid, carbon dioxide, and ionized gas plasma). However, these sterilization techniques induce variant degrees of damage to the extracellular matrix (ECM) components of the tissues, which could change their biomechanical, physiological, and cell attachment characteristics (Fidalgo et al., 2018). The quality and efficacity of decellularization could be examined macroscopically (size, aspect, color, and thickness) and microscopically (presence of elastic fibers, high density of collagen fibers, and absence of nuclei cells).

Concerning the biomechanical properties, it is important to comprehend the physiological processes that occur under both normal and abnormal vascular biomechanical conditions. During systole, the walls of the aorta and some proximal large vessels distend to act as an elastic buffering chamber, accommodating and storing approximately 60% of the left ventricular stroke volume. This tension in the aortic wall creates a potential energy that is transformed into kinetic energy during the diastole when the aortic tube recoils to normal status. This harmonic interaction between systole and diastole results in a continuous flow of blood to the periphery in a phenomenon known as the Windkessel function (Salvi, 2017). The degree of aortic stretching during the cardiac cycle varies according to anatomical location and corresponding physiological function. The ascending aorta demonstrates the highest distensibility and circumferential strain.

This distensibility progressively decreases along the aorta, with significantly lower values observed in the abdominal segment. Reported circumferential strain values range from approximately 29% in the proximal aorta to around 5% in the abdominal aorta (Herment et al., 2011; Humphrey & Holzapfel, 2012; Santilli et al., 2002). This value is reflected by the quantity of elastin and collagen

in aortic wall. In the ascending aorta, elastin constitutes approximately 27% of the arterial wall, while collagen accounts for about 22%. In contrast, in the distal aorta, the elastin content decreases to around 17%, whereas collagen increases markedly to approximately 53% (Concannon et al., 2020).

High energy loss reflects reduced efficiency of the arterial wall in recovering stored mechanical energy, indicating that more energy is dissipated within the tissue during each cycle. The energy dissipation ratio (EDR) is defined as the normalized fraction of total mechanical energy input that is lost during a single loading–unloading cycle. In arterial mechanics, a higher EDR denotes increased internal friction and reduced elastic efficiency, indicating altered wall behavior due to structural remodeling such as elevated collagen content, elastin fragmentation, or smooth muscle disorganization. Conversely, a lower EDR reflects more efficient elastic recoil and a structurally intact, healthier arterial wall (Laurent & Boutouyrie, 2007; O′Rourke & Safar, 2005; Redheuil et al., 2010).

Biomechanical properties can be measured by radiological and mechanical methods. The radiological method, either MRI or ultrasonography, can evaluate the strain, distensibility, compliance, and a lot of properties that help to evaluate the efficacity of materials. The mechanical method of biological material such as uniaxial or biaxial tension tests can evaluate the stiffness via elastic modulus, the fatigue and failure properties of materials. A combination of radiological and bio-mechanical techniques provides a lot of information about the biomechanical properties. An MRI is an essential technique to evaluate the hemodynamic characterization of the aorta, allowing us to estimate the aortic stiffness in clinical practice. These techniques can be used in the experimental field to evaluate the competence and suitability of aortic prostheses used in the vascular surgery field.

Despite the wide use of BPPs in many surgical specialties, no studies compare the BPPs by mentioning the supplier to compare them and evaluate the biomechanical properties, knowing these properties could optimize the selection of the proper BPPs in the surgical field. We hypothesize that the BPPs had different biomechanical properties due to different methods of decellularization, chaotropic agents, additional treatments to stabilize the patches, and different methods of reservation techniques.

The primary objective of our work is to understand the behavior of the custom-made bovine pericardial tube (CMBPT) parameters in vitro using magnetic resonance imaging (MRI). Then we evaluate the strain and distensibility of CMBPT using MRI with different sequences to understand the properties of the tube under physiological conditions. The second objective is to compare the biomechanical properties of various BPPs using a uniaxial tensile testing system. Failure testing was

performed to determine the physiological elastic modulus (PEM), maximum physiological elastic modulus (MPEM), and maximum elastic modulus (MEM). In addition, low-cycle fatigue testing was conducted to assess the energy dissipation ratio (EDR), which reflects the biomechanical energy input that is lost during a single loading–unloading cardiac cycle. The next step is to quantify intra-sample and inter-sample variability in order to evaluate the consistency of the biomechanical performance among different BPPs. The last purpose is to evaluate the BPPs from different suppliers under microscopy using different stains. This method will assist clinicians and scientists in accurately determining the biomechanical properties of BPP tissues.

Chapter 1: Clinical background of the bovine pericardial patch

The English name originates from the ancient Greek prefix (*peri*; around) and the suffix (*cardion*; heart). The bovine pericardial patch is a membrane that is obtained from the pericardium of bovine. The pericardial, or pericardium, is a sac that naturally surrounds the heart of animals or humans. The pericardial sac is a fluid-filled membrane that covers the outer surface of the heart and the roots of the great vessels, namely the vena cava, aorta, and pulmonary vessels (Mansour et al., 2018a; Mantini et al., 2021). This chapter will concentrate on the fundamental anatomy and biological structures of BPPs, physiological functions of the bovine pericardium, clinical background of BPPs, clinical applications of the BPPs, and established knowledge of the biomechanical and histological features of BPPs.

1. Anatomy of bovine pericardium

The pericardium is an avascular fibro-serous sac that surrounds the heart and great vessels. In the bovines animal family, the heart lies in the middle mediastinum mostly to the left side of the median plane (Mansour et al., 2018a). The pericardium consists of two layers ; the fibrous pericardium and the serous pericardium (Ishihara et al., 1980; Mansour et al., 2018a; Rodriguez & Tan, 2017; Spodick, 1992), see **Figure 1**.

The fibrous pericardium lies between the mediastinal pleura and the serous pericardium's parietal layer. It is a robust fibrous component of the pericardium, containing variously oriented layers of collagen fibers and small elastic fibers, and attached below to the central tendon of the diaphragm. It fuses with the outer coats of the aorta, pulmonary trunk, superior and inferior vena cava, and pulmonary veins, while it is attached anteriorly to the sternum by the sterno-pericardial ligaments.

The fibrous pericardium is made of connective tissue, and multidirectional collagen layers, mainly of collagen type I, as well as glycosaminoglycans (GAGs) and glycoproteins, growth factors, cytokines, and chemokines. Elastic fiber networks are important for maintaining normal physiological processes, providing elasticity, and allowing tissues and organs to recoil. The collagen fibers are found as a wavy configuration inside a bundle. This wavy configuration form allows the pericardium for limited stretch with fluid accumulation or during cardiac cycles.

The serous pericardium is divided into parietal and visceral layers. The pericardial cavity is the space between the serous parietal and serous visceral layers. Normally, the space contains a little quantity of tissue fluid, referred to as pericardial fluid. The serous pericardium is composed primarily of

collagen type IV and laminin and consists of two continuous layers: the parietal and visceral layers. The parietal serous layer lines the inner surface of the fibrous pericardium and is reflected around the roots of the great vessels, where it becomes continuous with the visceral serous layer. The visceral serous layer, also known as the epicardium, is firmly adherent to the myocardium and the underlying adipose tissue. During the harvesting of BPPs, only the parietal pericardium is collected, whereas the visceral layer remains attached to the heart.

The pericardial cavity fluid contains a variety of components, including some mesothelial cells, lymphocytes (53%), neutrophils (31%), macrophages (12%), eosinophils (1.7%), and basophils (1.2%), (Jaworska-Wilczynska et al., 2016). The phrenic nerves supply the fibrous pericardium and the parietal layer of the serous pericardium, whereas the visceral layer of the serous pericardium is innervated by branches of the sympathetic trunks and the vagus nerves (Peebles et al., 2011; Snell, 2007). The pericardium receives its blood supply from the pericardiophrenic and musculophrenic branches of the internal thoracic artery, as well as from branches of the descending thoracic aorta. Venous drainage of the pericardium occurs through the superior intercostal veins and the internal thoracic veins, which drain into the brachiocephalic veins (Rodriguez & Tan, 2017). There are no data about a fluid component variety of bovines, and most of the studies were done in humans.

The typical human pericardial thickness measurement is less than 1 mm (0.4 mm–1 mm) in anatomical studies, while in imaging investigations is less than 2 mm. The causes of this disparity are assumed to be motion artifact and spatial resolution limitations of imaging techniques (Peebles et al., 2011).

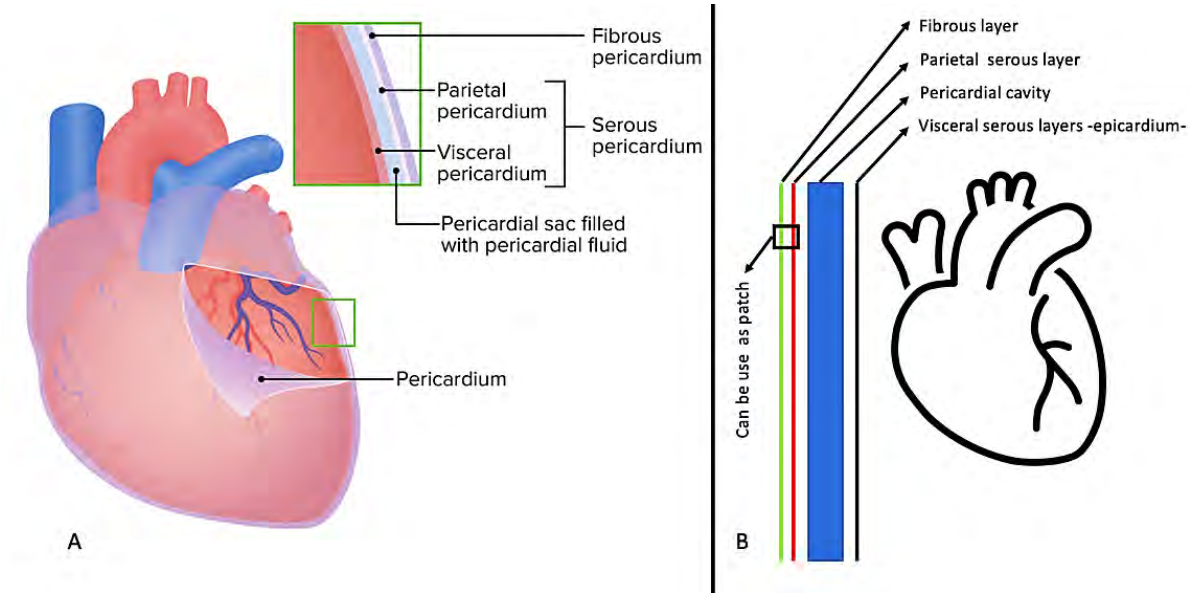


Figure 1. Illustration of pericardium. (a) Illustration of pericardium layers . (b) Schematic illustration of the layers of the pericardium.

The pericardial layers in the bovines animal family including cows, oxen, goats, sheep, bison, and buffalo, correspond with human pericardial layers and thickness (Allen et al., 1984; Mansour et al., 2018b).

The extracellular matrix (ECM) is a complex network of proteins and polysaccharides produced by resident cells within a tissue or organ. This organized structure provides mechanical support and regulates essential cellular functions. The ECM provides the physical environment and structural support necessary for cells to attach to surrounding components, develop, migrate, and respond to tissue-specific signals. Its composition determines the structural and mechanical properties of the tissue, including stiffness and elasticity, which are closely related to tissue function. In addition, the complex composition of the ECM provides bioactive cues that regulate cellular behavior and activity. The ECM also acts as a reservoir for growth factors, enhancing their biological functions and availability. Furthermore, it provides a degradable microenvironment that facilitates neovascularization and tissue remodeling in response to developmental, physiological, and pathological processes (Chan & Leong, 2008; Yi et al., 2017).

2. Biological structures of bovine pericardium

The components of ECM can be divided into three major categories (Yi et al., 2017), see

Figure *2*.

2.1. Fibrous proteins (e.g., collagen, elastin, fibrillin, and fibulin)

2.1.1. Collagen is the most common protein in the body, which makes up to 35% of the total protein mass in the body. Type I collagen, found mainly in the fibrous pericardium layer, is the most predominant protein in the body. Type I collagen is recognized as a significant structural protein because it maintains the mechanical integrity and strength of the biological structure. (Costa et al., 2017; Di Lullo et al., 2002; Yi et al., 2017). The Type IV of collagen is the most common collagen in the serous pericardium, which plays an important role in cell adhesion, migration, and differentiation of cells (Costa et al., 2017; Tanjore & Kalluri, 2006; Yi et al., 2017). The presence of collagen in the pericardium tissue is found as a wavy configuration inside a bundle, allowing for limited collagen fibers elasticity (Spodick, 1992). In addition, collagen contributes to the strength, flexibility, and hemostatic properties of tissues and constitutes the principal structural component of the extracellular matrix, thereby determining its mechanical characteristics (Yi et al., 2017).

2.1.2. Elastin is a macromolecule responsible for the elastic properties of the extracellular matrix, and it is produced and secreted as a precursor protein monomer by numerous

cells, including fibroblasts, endothelial cells, smooth muscle cells, chondrocytes, and keratinocytes (Yi et al., 2017). Elastin contributes to the extracellular matrix's biomechanical properties and gives tissues mechanical integrity. Elastic fibers give the repetitive stretch and elastic recoil quality characteristic of tissues whose physiological function demands repeated distension and relaxation during a lifetime (Muiznieks et al., 2010).

2.1.3. Fibrillins are a group of large extracellular glycoproteins that constitute the majority of the microfibril core in elastic and non-elastic extracellular matrices. Its interaction with tropoelastin and integrins contributes to the structural integrity of specific organ systems and serves as a scaffold for elastogenesis in elastic tissues such as epidermis, lung, vessels, and the pericardial sac (Wagenseil & Mecham, 2009).

2.1.4. Fibulins are extracellular matrix proteins found predominantly in elastic tissue such as lung, aorta, epidermis, and numerous additional connective tissues such as bone and cartilage. Their interactions with growth factors of the TGF- family and with enzymes that regulate the cross-linking of elastin and collagens, such as lysyl oxidases, play a crucial role in the regulation of extracellular matrix homeostasis (Hanada & Sasaki, 2018).

2.2. Adhesive glycoproteins (e.g., laminin, fibronectin, tenasin, thrombospondin, and integrin)

2.2.1. Laminins are a significant component of the basement membrane, a complex network of proteins that separates epithelium, mesothelium, and endothelium from connective tissue, and maintain tissue structure. During organ development and wound healing, laminins actively modulate cell behavior, regulate cell proliferation, differentiation, adhesion, migration, and promote re-epithelialization and angiogenesis (Yi et al., 2017).

2.2.2. Fibronectin is a widely distributed multi-domain glycoprotein. The fibronectin molecule can be classified into two distinct categories, namely soluble and insoluble fibronectin. Soluble fibronectin is primarily synthesized by hepatocytes in the liver. Insoluble fibronectin is produced by a variety of cell types, including epithelial cells, mesenchymal cells, and fibroblasts. Insoluble fibronectin is composed of multiple functionally and structurally diverse domains that possess the ability to interact with

both the cell surface and the extracellular matrix. These domains play a crucial role in facilitating the assembly of various components inside the extracellular matrix. Fibronectin has been observed to augment cellular adhesion and spreading, influence the pathways of cellular migration, and have an impact on various biological processes, including cellular morphology, organization of the cytoskeleton, phagocytosis, hemostasis, embryonic differentiation, and wound healing (Yi et al., 2017).

2.2.3. Tenascins are ECM polymorphic glycoproteins that exhibit polymorphism characteristics. They are distributed in connective and soft tissues throughout the body. Tenascin-C has temporary expression in the mesenchyme around growing organs, including the kidney, teeth, and mammary glands. The presence of this entity can be observed in several structures, including the periosteum, ligaments, tendons, myotendinous junctions, smooth muscle, and perichondrium. This presence is evident not only during embryonic development but also in adult tissues (Chiquet-Ehrismann et al., 1988).

2.2.4. Thrombospondins are a group of five glycoproteins characterized by their modular structure. The components in question have been identified as "adhesion-modulating" components of the extracellular matrix. The binding of thrombospondin serves as a molecular mechanism to facilitate the incorporation of the extracellular matrix at a molecular level. Additionally, it plays a regulatory role in the organization and metabolism of the extracellular matrix. Moreover, thrombospondin acts as a mediator for interactions between cells and the extracellular matrix, as well as between cells themselves. Its influence extends to various biological activities including cell migration, angiogenesis, tissue remodeling, and tumor growth (Lopez-Dee et al., 2012).

2.2.5. Integrin molecule is a glycoprotein consisting of two distinct subunits, forming a heterodimeric structure. The transmembrane protein, via its cytoplasmic tail, binds to ligands in the extracellular matrix and functions as a transmembrane linker, facilitating the communication and connection between the extracellular matrix and the intracellular cytoskeleton. It participates in several biological interactions, encompassing tissue development, hemostasis, angiogenesis, inflammation, and tissue regeneration (Springer & Wang, 2004; Xiong et al., 2003).

2.3. Glycosaminoglycans

Glycosaminoglycans (GAGs) are the predominant heteropolysaccharides found in the human body and are a significant category of biomolecules present in the extracellular matrix. Proteoglycans are mostly composed of glycosaminoglycans that are covalently attached to core proteins. Glycosaminoglycans and proteoglycans serve multiple functions within the extracellular matrix, including occupying interstitial spaces and exerting control over physical properties. Additionally, they play a crucial role in facilitating cell-to-cell and cell-to-matrix interactions, regulating cell proliferation and migration, and contributing to processes such as wound healing and tissue remodeling (Yi et al., 2017).

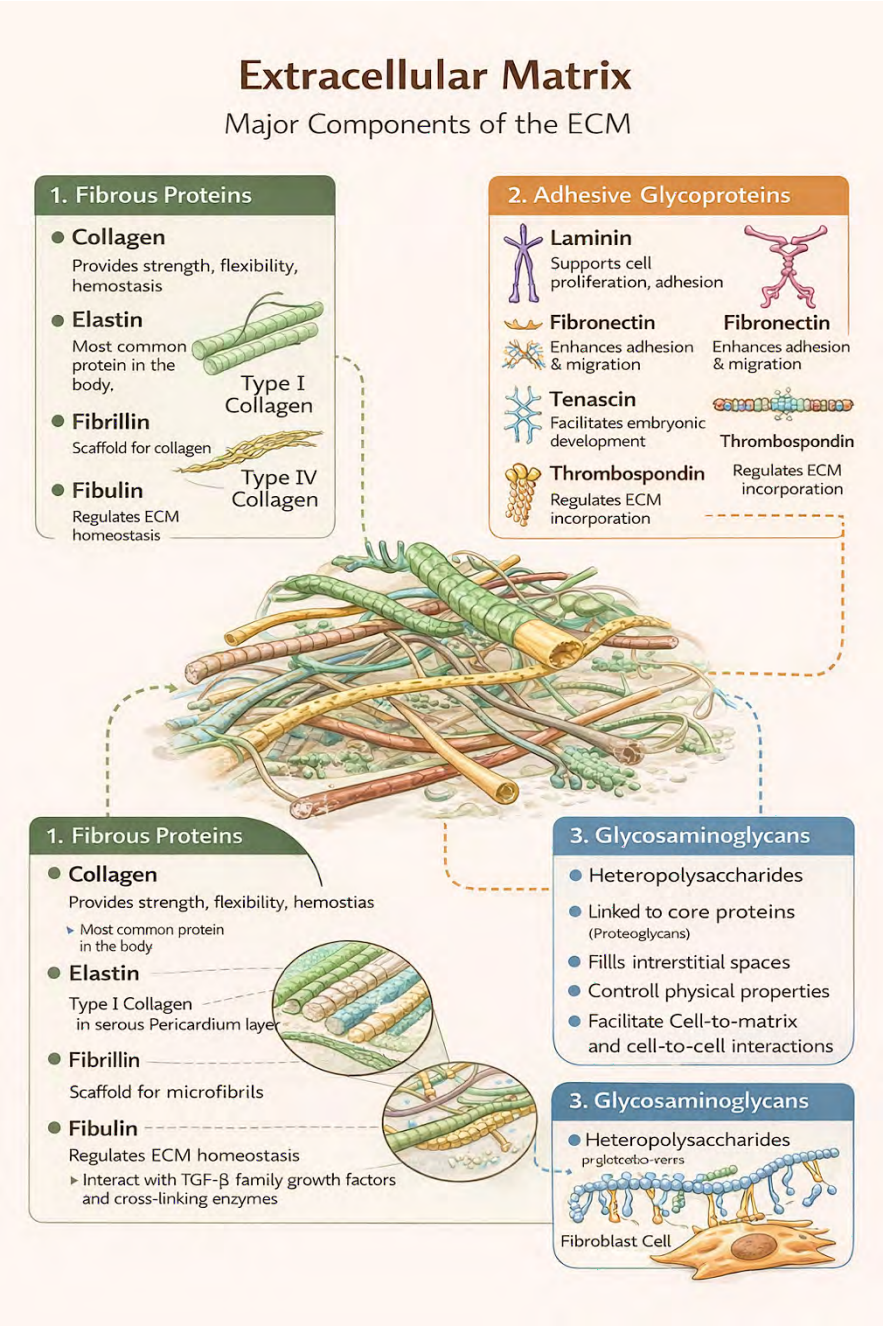


Figure 2. Major components of the extracellular matrix (ECM): The ECM is composed of three main categories: (1) Fibrous proteins (collagen, elastin, fibrillin, fibulin), which provide tensile strength, elasticity, and structural integrity; (2) Adhesive glycoproteins (laminin, fibronectin, tenascin, thrombospondin, integrins), which mediate cell–matrix interactions and regulate cell adhesion, migration, and tissue remodeling; and (3) Glycosaminoglycans (GAGs) and proteoglycans, which occupy interstitial spaces and modulate the physicochemical and biomechanical properties of the matrix. Together, these components determine the structural and functional characteristics of connective tissues, including the pericardium.

3. Physiological functions of the bovine pericardium

The function of pericardial sac is divided into three main functions:

3.1. Immunological function

The pericardium contributes to immunological defense due to the presence of mesothelial cells lining the serosal cavity. These cells participate in antigen recognition, inflammation, tissue repair, regulation of the coagulation cascade, and fibrinolytic activity, thereby limiting intrapericardial clot formation and adhesion development following hemorrhage (Jaworska-Wilczynska et al., 2016; Spodick, 1992).

3.2. Mechanical function

The pericardium surrounds the heart for mechanical protection and storing reserve fluids within the pericardium sac. This function help to lubricate the exterior wall of the heart and reduce friction. Another mechanical function of the pericardium is to assists in the prevention of overexpansion of the heart and lowering blood pressure via neuroreceptors of Vagus nerve (Jaworska-Wilczynska et al., 2016; Spodick, 1992).

The presence of collagen and elastin in the ECM of the BPP contributes to maintaining a balance between strength and elasticity under physiological pressure. This enables the BPP to stretch and accommodate changes in volume without experiencing rupture or damage during normal physiological function, see **Figure 3** (Trębacz & Barzycka, 2023).

3.3. Fixation function

The pericardium maintains the heart in its anatomical position through the pericardiophrenic and sternopericardial ligaments (Snell, 2007).

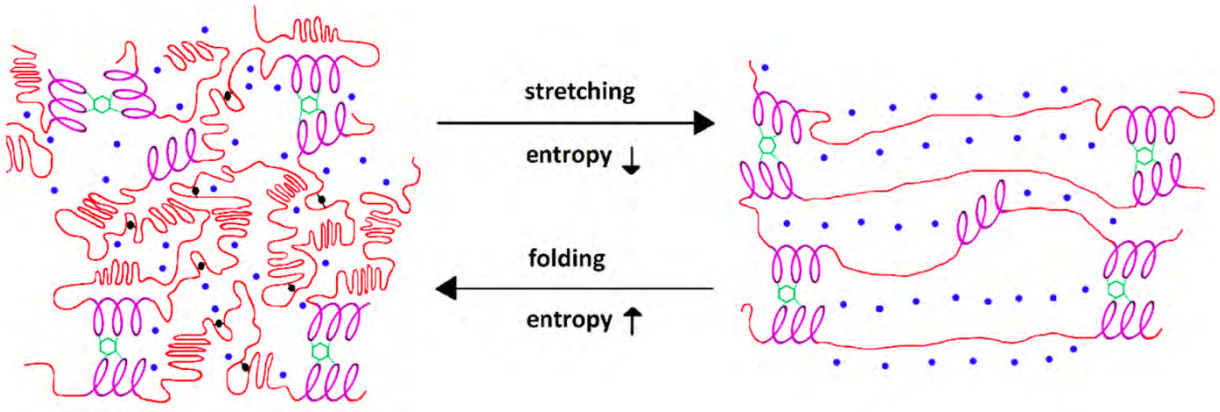


Figure 3. The stretch and recoil of ECM due to the presence of elastin and collagen (Trębacz & Barzycka, 2023).

4. Clinical background of the bovine pericardium patch from the basic to implantation

The bovine pericardial patch described mechanically as a non-linear, anisotropic, multi-laminate composite pliable material due to the presence of collagen and elastin. It can be bent and twisted into different shapes, which is commonly imposed in substantial deformations during its physiological function as an implant material or graft (Mavrilas et al., 2005). They are widely used in surgical field due to consistent reliability, facility of utilization, long durability, strength, biocompatibility, reduced suture line bleeding, off-the-shelf availability, absence of aneurismal degeneration, and decrease risk of stenosis and infection (Li et al., 2011).

4.1. History of the utilization of bovine pericardial patches

The first clinical application of BPP was performed in March 1971 by Marian I. Ionescu and colleagues, who successfully implanted the first BPP for human aortic valve replacement. This pioneering work marked a major milestone in cardiovascular surgery and was subsequently reported in their landmark publication, *Heart Valve Replacement with the Ionescu-Shiley Pericardial Xenograft* (Ionescu et al., 1977). In their landmark publication, Ionescu and colleagues described the manufacturing process of the BPPs used in their study. Sterile conditions were rigorously maintained throughout the entire manufacturing process, from harvesting the bovine pericardium from calves to the final implantation of the prosthetic valve in patients (Ionescu et al., 1977).

All xenografts BPPs are derived from calves ranging in age from 6 to 18 months. Then only thick slices of pericardium were selected, and cleaned mechanically, then washed during 3 hours in Hank's balanced salt solution. BPP are stabilized and fixed for two weeks in 0.5 percent pure glutaraldehyde buffered to pH 7.4 with 0.067 molar phosphate at 4° C. The existence of inter-molecular and intra-molecular covalent connections between the amino groups of lysine and hydroxylysine residues and various forms of glutaraldehyde irreversibly stabilizes the pericardial tissue's natural structure. Chemical immobilization and stabilization using purified glutaraldehyde markedly reduces tissue antigenicity by promoting extensive collagen cross-linking. An optimal tissue cross-link density has been reported with 0.5% purified glutaraldehyde. Following fixation, the bovine pericardial patch was stored in a solution containing 4% formaldehyde and 0.2 M acetate buffer at pH 5.4 to preserve its structural integrity and mechanical properties(Ionescu et al., 1977).

Since that time the glutaraldehyde-preserved BPPs were widely used in the cardiovascular surgery field. The utilization of glutaraldehyde results in enhanced material strength and stability and reduces

the material's antigenicity and potential susceptibility to infections (C. Lee et al., 2016; Li et al., 2011). The utilization of a combination treatment involving longer-chain alcohols exhibits potential as an effective approach for mitigating calcification in glutaraldehyde-fixed BPPs (Pathak et al., 2004). Conversely, several studies have suggested that increasing the glutaraldehyde concentration during tissue fixation is associated with a lower incidence of calcification in BPPs, potentially owing to enhanced collagen cross-linking and improved tissue stabilization (C. Lee et al., 2016).

4.2. Bovine pericardial patches currently available on the market

Worldwide, there are a several companies that produce BPPs for medical uses, using different methods of decellularization, different chaotropic agents, different additional pre-commercial treatments to stabilize the patches, and different methods of reservation (Gilbert et al., 2006; Iop et al., 2018), see
Table 1.

Table 1. Overview of the bovine pericardial patches currently available on the market (Iop et al., 2018).

N	Product Name	Manufacturer	Tissue Source	Pre-commercial Processing / Treatment
1	CardioCel®	Admedus, Malaga, Western Australia, Australia	Bovine pericardium	Decellularized, glutaraldehyde (GA)-crosslinked, and treated with proprietary ADAPT® anti-calcification technology
2	Edwards Bovine Pericardial Patch	Edwards Lifesciences, Irvine, California, USA	Bovine pericardium	GA-crosslinked and treated with proprietary XenoLogiX® anti-calcification technology
3	Peri-Guard®	Baxter International Inc., Deerfield, Illinois, USA	Bovine pericardium	GA-crosslinked
4	PhotoFix™	CryoLife Inc., Kennesaw, Georgia, USA	Bovine pericardium	Decellularized and photo-oxidized
5	SJM Biocor™ Patch	St. Jude Medical, Saint Paul, Minnesota, USA	Bovine pericardium	GA-crosslinked
6	SJM Pericardial Patch with EnCap™ AC Technology	St. Jude Medical, Saint Paul, Minnesota, USA	Bovine pericardium	GA-crosslinked and treated with proprietary EnCap™ anti-calcification technology
7	SURGIFOC®	FOC Medical, Buenos Aires, Argentina	Bovine and porcine pericardium	GA-crosslinked
8	Vascu-Guard®	Baxter International Inc., Deerfield, Illinois, USA	Bovine pericardium	GA-crosslinked

The different methods for the treatment of BPP could change patches' histological and biomechanical properties. The presence of cells in BPP could elicit a theoretical risk of immunological response inside the ECM, and enhance the degeneration of BPP (Abolhoda et al., 1996). This response can vary depending on donor source, recipient tissue type, and host immune activity. Consequently, respecting the standard quality criteria for decellularization patches is mandatory.

Although no universally accepted criteria for successful decellularization have been established, the most widely used criteria include a residual double-stranded DNA content of less than 50 ng per mg of dry extracellular matrix, a DNA fragment length of less than 200 base pairs, and the absence of visible nuclear material on histological staining (Yi et al., 2017).

The approved standardized sterilization methods include heat and pressure (dry heat, moist heat), ionizing radiation (ultraviolet, X-ray, and E-beam), and chemical sterilant (ethylene oxide, hydrogen peroxide, peracetic acid and carbon dioxide, and ionized gas plasma). However, these sterilization techniques induce variant degrees of damage to the ECM components of the tissues, which could change their biomechanical, physiological, and cell attachment characteristics (Fidalgo et al., 2018).

4.3. Harvesting technique of bovine pericardial patches

In the context of medical applications, the selected bovine animals for harvesting are limited to those aged less than two years (Ionescu et al., 1977). The pericardium utilized is the serous pericardium's parietal layer with a fibrous layer, while the epicardium is not used due to being firmly attached to the heart. Unfortunately, the manufacturer did not provide explicit details regarding the exact location of patches obtained from the bovine. Additionally, some manufacturers use the entire pericardium in order to obtain a larger size of BPP.

The behaviors of the area of bovine pericardium mapping shows different thicknesses, fiber orientation, and mechanical tests, according to Stieglmeier et al. (Stieglmeier et al., 2021). They found significant differences in thickness measurement according to the mapping in a different zone, see **Figure 4**, and different fiber directions, see **Figure 5**. The author recommends against utilizing the M area due to the significant variability in thickness over a short distance, as well as the absence of clearly identifiable fiber orientations. This study confirmed the previous studies of Simionescu et al. and Sacks et al. (Sacks et al., 1994; Simionescu et al., 1993).

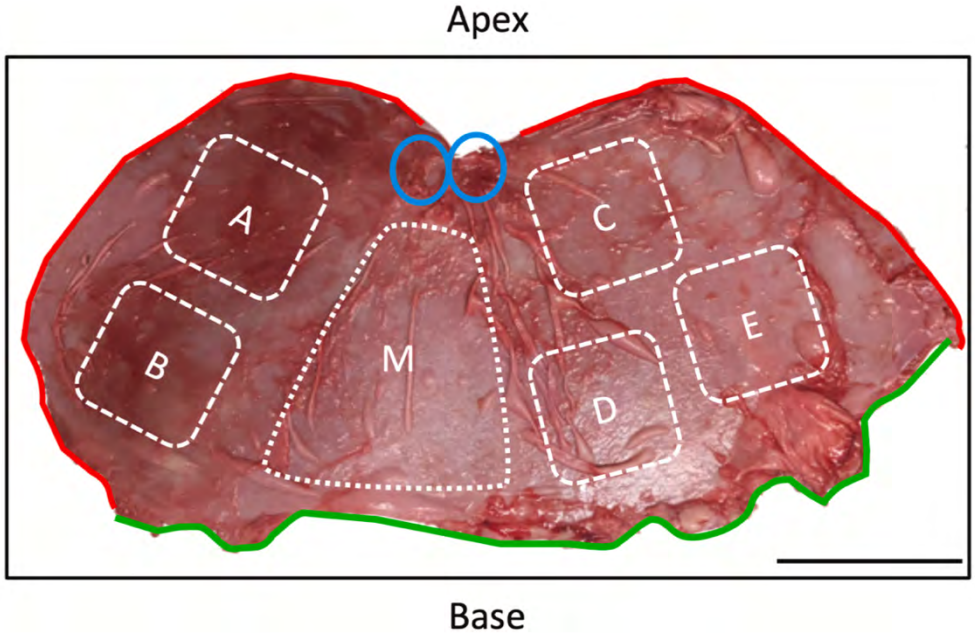


Figure 4. The BPP mapping shows different thickness areas depending on the location. Whole native flattened BPP with heart averted side on top. The circular incision shows were the pericardium was loosened from the vessels surrounding the heart (green line). The incision in axial direction was made above the middle of the left ventricle (red lines). Also marked are tendon insertions of *Ligg. Sternopericardia* (blue circles). "A" to "E" symbolize different area of pericardium, "M" indicates an unsuitable area. Scale bar: 10 cm (Stieglmeier et al., 2021).

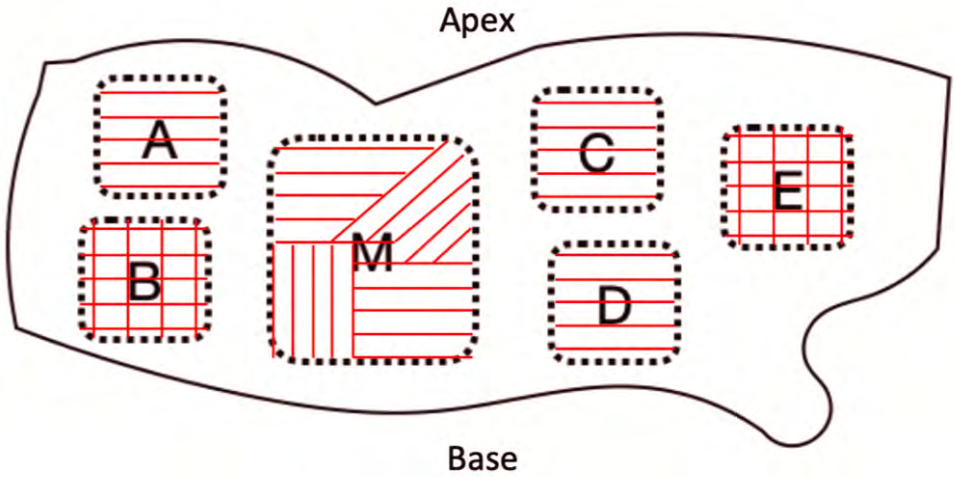


Figure 5. The BPP mapping shows different fibers orientation depending on the location. Fiber direction was mainly aligned in the circumferential direction for areas "A", "C" and "D". "B" and "E" consisted of fibers aligned in crossed direction (Stieglmeier et al., 2021).

4.4. Decellularization and pre-commercial technique of bovine pericardial patches

The process of decellularization aims to eliminate the immunological response of the host towards xenogeneic tissues and organs while preserving the ECM as a supportive structure for subsequent recellularization. Numerous methodologies have been explored in the realm of decellularization, encompassing osmotic, chemical, enzymatic, and mechanical techniques, all aimed at effectively eliminating the cellular constituents of a xenograft (Wong & Griffiths, 2014). The decellularization technique used at present of BPP are based on the decellularization technique used by Ionescu et al. (Ionescu et al., 1977).

The decellularization process described by Courtman et al. (Courtman et al., 1994) consists of four sequential steps. Following harvesting, the pericardium is mechanically cleaned to remove residual blood and immersed in a hypotonic lysis buffer (pH 8.0) containing the protease inhibitor phenylmethylsulfonyl fluoride (0.35 mL/L) for 24 hours at 4°C under continuous stirring. The tissue is subsequently incubated in a 1% octylphenoxypolyethoxyethanol solution (Triton X-100; Sigma) prepared in Tris-buffered saline with protease inhibitor for an additional 24 hours at 4°C under continuous stirring, followed by rinsing in Hanks' physiological solution. The third step involves enzymatic digestion with DNase and RNase at 37°C for 1 hour, followed by a further 24-hour extraction in Triton X-100 prepared in Tris buffer. Finally, the tissue is washed in Hanks' solution for 48 hours. The addition of 1% sodium dodecyl sulfate (SDS) has also been recommended as a final step to enhance the removal of residual cellular components.

The application of decellularization techniques to reduce the immunogenic potential of xenogeneic tissues is based on two fundamental assumptions. First, the cellular component of BPP is considered the primary source of tissue antigenicity. Second, the absence of cellular material, as demonstrated by histological assessment of residual nuclei, DNA quantification, and/or evaluation of residual cellular proteins of uncertain immunogenicity, is assumed to correlate with the effective removal of antigenic components.

However, it is important to note that there is currently no established standard for determining the success criterion of decellularization. Hence, a more thorough examination is required to assess the validity of scaffold acellularity as a criterion for evaluating residual antigenicity (Wong & Griffiths, 2014).

Glutaraldehyde treatment promotes the formation of stable cross-links between cellular and extracellular matrix proteins, thereby improving the structural integrity and durability of BPPs. This

process offers several important advantages, including a reduction in tissue immunogenicity, stabilization of matrix proteins to increase their resistance to enzymatic degradation, and effective sterilization and preservation of the tissue for long-term storage (Abolhoda et al., 1996; Courtman et al., 1994; C. Lee et al., 2016; Li et al., 2011).

The use of crosslinking in BPPs has been associated with several drawbacks, including increased susceptibility to calcification, potential cytotoxic effects due to the release of residual or depolymerized aldehydes, and significant alterations in the mechanical properties of the material (Golomb et al., 1987). On the other hand there are some studies found a proportional relationship relation between high concentrations of glutaraldehyde and a lower risk of calcification of the BPP (C. Lee et al., 2016).

High percentage of glycerol is an other reservation method of BPPs rather that Glutaraldehyde soulution. The method starting by dehydrate the BPPs and then reserved at glycerol with high perentage 99.5% to work as cross linking to stabilize the BPPs (Liao et al., 1991). This technique shows good results in animal studies, particularly shows an adaptable and biocompatible scaffold appropriate for surgical applications, less calcification rates and effective integration and remodeling. (Hafeez et al., 2004; Karrouf et al., 2017).

Dye-mediated photooxidation is another technique used for the treatment of BPPs. This method induces the formation of collagen cross-links, thereby enhancing the stability of the extracellular matrix while eliminating toxic byproducts that may serve as nucleation sites for calcium deposition. Compared with conventional glutaraldehyde cross-linking, dye-mediated photooxidation offers several advantages, including enhanced cross-link formation, improved resistance to chemical and enzymatic degradation, and a lower propensity for tissue calcification (Moore & Adams, 2001).

Stabilization and sterilization of pericardial scaffolds by ultraviolet and low-energy electron irradiation is an effective method. This method help to avoid the of glutaraldehyde utilization and uses low-energy electron irradiation as an efficient sterilization technique (Walker et al., 2018). This method involves the application of three sequential steps. First, the pericardial tissue undergoes decellularization. Second, the tissue is immersed in a riboflavin solution and subsequently exposed to ultraviolet irradiation. Finally, low-energy electron irradiation is applied to achieve stabilization and sterilization of the scaffold, see **Figure 6.**

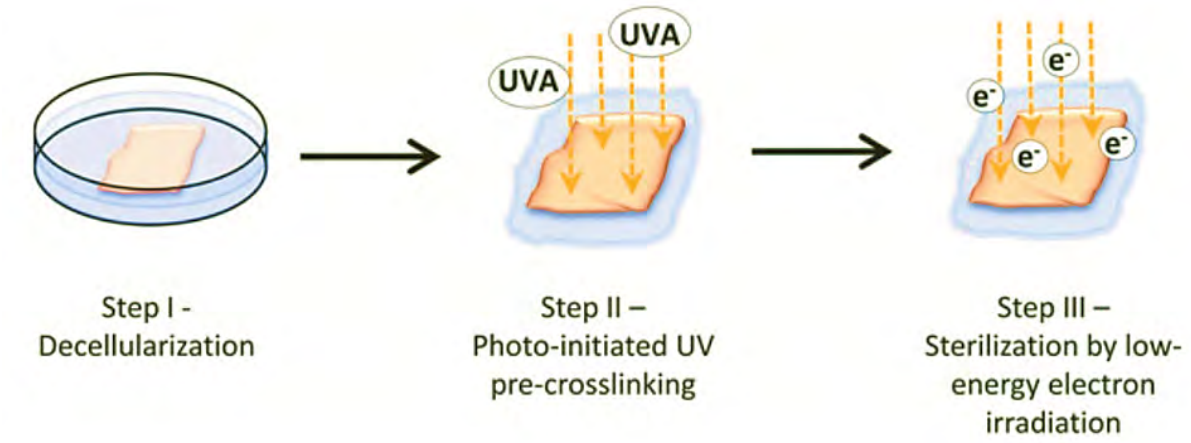


Figure 6. The process of stabilization and sterilization of pericardial scaffolds by ultraviolet and low-energy electron irradiation. Following the decellularization of pericardial tissue (step I), the pericardia were subjected to a soaking process in riboflavin and subsequently exposed to ultraviolet irradiation (step II). Finally, the pericardia were treated with low-energy electron irradiation (step III) (Walker et al., 2018).

The anti-calcification treatment is applied to BPPs to reduce the potential risk of calcification. However, the direct association between glutaraldehyde treatment and calcification in BPPs remains insufficiently supported by strong evidence. There are variable techniques of anti-calcification treatment such as a high glutaraldehyde concentration, No-React detoxification process, and glutamic acid techniques.

High glutaraldehyde concentration of 0.6% of BPPs was found to involve significantly lower risk of calcification when compared to those fixed with a 0.4% of Glutaraldehyde solution, regardless of the duration of fixation ($p = 0.030$). Additionally, the mean calcium content of the 0.6% of Glutaraldehyde solution fixed tissues showed a tendency to be lower when compared to those fixed with a 0.3% of Glutaraldehyde solution ($p = 0.083$) (C. Lee et al., 2016).

The No-React detoxification process is another treatment strategy developed by Biocor Company (Belo Horizonte, Brazil) to improve the biocompatibility of BPPs. The complete details of this proprietary method have not been fully disclosed for commercial reasons. The process involves extensive aldehyde cross-linking to enhance tissue resistance to biodegradation, followed by detoxification using solutions containing naturally occurring endogenous compounds under controlled physical conditions. Finally, the tissue is incubated with a surfactant that is believed to reduce tissue reactivity following implantation, thereby improving its in vivo biocompatibility (Abolhoda et al., 1996). The result of in vitro experimentation shows that calcification was significantly reduced in the pericardium treated with No-React Detoxification Process as compared to tissue treated with GA (p 0.001) (Abolhoda et al., 1996).

The Glutamic acid treatment with Glutaraldehyde shows also a high efficiency to reduce the calcification indexes (Braile-Sternieri et al., 2020).

There are several application of decellularization, organic solvents, and amino acid detoxification techniques on glutaraldehyde-fixed pericardial patch samples that demonstrates improved functionality and reduced calcification compared to samples treated just with glutaraldehyde (Park et al., 2017).

The advantages of BPPs using in surgical field include consistent consistency, ease of handling, durability, strength, biocompatibility, lack of suture line bleeding, off-the-shelf availability, and immediate insonation. Additionally, he has discussed the potential for anti-calcification, to decrease the risk of restenosis and infections in vascular surgery, as well as the facilitation of cellular ingrowth (Li et al., 2011).

4.5. Clinical application of the pericardial patch

The utilization of BPPs is widely used in the medical field, especially as a scaffold to replace the ECM as a biological xenograft material. The advantages of the utilization of biological materials are the resistance to infection and limited antibiotic consumption (Fullybright, 2019). For those reasons, biological materials are preferable in many surgical specialties. The first application was applied in the cardiac surgery field when Ionescu et al, performed the first bovine pericardial aortic valve replacement in a human (Ionescu et al., 1977). Since first application, the utilization of BPPs has expanded beyond the confines of aortic valve replacement and has experienced significant proliferation throughout other surgical disciplines.

In the vascular surgery field, the BPP material serves as an asset, possessing the ability to effectively resist infections while providing support for implantation inside an infectious environment. The applications of BPP in vascular surgery encompass a wide range of procedures, at different anatomical level.

For example, the carotid endarterectomy (CEA), the utilization of a prosthetic or venous patch are widely used to prevent the risk of subsequent restenosis. The BPPs are used since 1991 by Biasi et al. (Biasi, 1996), when they published their promising result about the BPP. The metanalysis published by Texakalidis et al. (Texakalidis et al., 2018), found there are no differences between the venous patch and BPP, except decrease in surgical time and the preserve of veins for more complex surgeries. Another utilization of carotid surgery is to repair the prosthetic patch infection post-CEA (Wikkeling et al., 2021).

The BPP shows good result as a patch post-femoral endarterectomy with less complications in the short-term and long-term in comparison with the autologous material (Noronen et al., 2023). Repair of the aortic arch (Patukale et al., 2022), abdominal aortic pseudoaneurysm (Nabeshima et al., 2022), Superior vena cava (Jiang et al., 2019), and Inferior vena cava (Fukushima et al., 2017) were described in several articles.

The risk of infection of BPPs post-surgical procedure is almost near to zero percent. The retrospective analysis performed by Ho et al. (Ho et al., 2012) was to determine the incidence of infection following BPPs in 456 patients over a period of 182 months. The investigation revealed that the risk of infection with BPPs was determined to be 0.6%. while the other studies published by Stone et al. (Stone et al., 2014), and Papakostas et al. (Papakostas et al., 2014), found that the percentage of infection is zero percent.

To summarize, the BPPs were used in different surgical specialties rather than cardiovascular field, see

Table 2.

Table 2. Utilization of BPPs in the medical fields.

Specialty	n	Utilizations	Authors and references
Cardiac surgery	1	Aortic valve replacement	Ionescu et al. (Ionescu et al., 1977)
	2	Mitral valve reconstruction	Handa et al. (Handa et al., 2022)
	3	Reconstruction of pulmonary valve	Shinkawa et al. (Shinkawa et al., 2010)
	4	Repair of coronary artery ostium with a ring-shaped BPP	Zhang et al. (D. Zhang et al., 2022)
	5	Pulmonary artery reconstruction	Ebert et al. (Ebert et al., 2021)
	6	Left ventricular aneurysm repair	Henry et al. (Henry et al., 2014)
	7	Closure of left atrial appendage orifice	Kuralay et al. (Kuralay, 2019)
	8	Repair ventricular septal defect	Yamasaki et al. (Yamasaki et al., 2018)
	9	Repair of tetralogy of fallot	Talwar et al. (Talwar et al., 2019)
	10	Reconstruction of the pericardial sac	Yakirevich et al. (Yakirevich et al., 1984)
	11	Reconstruction of ascending aorta	Kubota et al. (Kubota et al., 2012)
	12	Aortic arch reconstruction	Bernabei et al. (Bernabei et al., 2013)
Vascular surgery	1	First BPP for CEA surgery	Biasi et al. (Biasi, 1996)
	2	Repairer the infection of carotid artery	Wikkeling et al. (Wikkeling et al., 2021)
	3	Femoral bifurcation endarterectomy	Noronen et al. (Noronen et al., 2023)
	4	Surgical repair of femoral artery pseudoaneurysm	Huang et al. (Huang et al., 2021)
	5	Repair for abdominal aortic pseudoaneurysm	Nabeshima et al. (Nabeshima et al., 2022)
	6	Aortic and aorto bi-femroal tube reconstruction	Topel et al. (Töpel et al., 2016)
	7	Traumatic aortic dissection in a child	Mangold et al. (Mangold et al., 2022)
	8	Aortic arch repair	Patukale et al. (Patukale et al., 2022)
	9	Reconstruction of superior vena cava	Jiang et al. (Jiang et al., 2019)
	10	Reconstruction of inferior vena cava	Mehaffey et al. (Mehaffey et al., 2016)
	11	Repair of the inferior vena cava	Fukushima et al. (Fukushima et al., 2017)
	12	Reconstruction of portal vein	Leon-Takahashi et al. (Leon-Takahashi et al., 2013)
	13	Increase the maturation of arteriovenous fistulas	Grant et al. (Grant et al., 2016)
General surgery	1	Abdominal wall reconstruction	D'Ambra et al. (D'Ambra, 2012)

	2	Abdominal wall repair	Bakri et al. (Bakri et al., 2021)
	3	Abdominal wall hernia repair	Saiding et al. (Saiding et al., 2023)
	4	Wrapping intestinal anastomosis	Nabeshima et al. (Nabeshima et al., 2022)
	5	Repairer esophageal defect	Hua et al. (Hua et al., 2019)
Thoracic surgery	1	Reconstruction of the diaphragm	Bertoglio et al. (Bertoglio et al., 2021)
	2	Tracheoplasty	Fanous et al. (Fanous et al., 2010)
Urology	1	Bladder injury repair	Chee et al. (Chee et al., 2015)
	2	Reconstruction of urinary bladder	Moon et al. (Moon et al., 2011)
	3	Urethroplasty	Mandal et al. (Mandal et al., 2020)
	4	Repair of tunical defect in patients with peyronie's disease	Otero et al. (Otero et al., 2017)
	5	Corporoplasty	Zucchi et al. (Zucchi et al., 2013)
Ophthalmology	1	Tendon elongation for strabismus surgery	Hedergott et al. (Hedergott et al., 2021)
	2	Treating large corneal perforation	Khanna & Mokhtar et al. (Khanna & Mokhtar, 2008)
	3	Scleral repair	Mehta et al. (Mehta, 2002)
	4	Scleral reinforcement	Ahmed & Mohamed et al. (Ahmed & Mohamed, 2021)
Neurosurgery	1	Repair of dural tears	Epstein et al. (Epstein, 2013)
	2	Spina bifida repair	Miyabe et al. (Miyabe et al., 2022)
	3	Repair spinal cord herniation	L.Zhang et al. (L. Zhang et al., 2022)
Orthopedic surgery	1	Shoulder rotator cuff repair	Baldwin et al. (Baldwin et al., 2020)
	2	Augmentation of ligaments and tendons	Longo et al. (Longo et al., 2010)
ENT surgery	1	Vocal cords implants	Olmos-Zuniga et al. (Olmos-Zuñiga et al., 2015)

4.6. Biomechanical Characterization of Bovine Pericardial Patches: Insights and Perspectives

BPPs are commonly used in cardiovascular surgery. However, after implantation, they can undergo degeneration and calcification. This phenomenon observed in bioprosthetic heart valves. There is considerable debate surrounding the etiology of calcification in BPPs. Utilizing a combination treatment with longer-chain alcohols has been effective in reducing calcification in glutaraldehyde-fixed bovine pericardial patches (Pathak et al., 2004). Conversely, some studies suggest a correlation between higher concentrations of glutaraldehyde and reduced risk of calcification in BPPs (C. Lee et al., 2016). The expected lifespan of the bioprosthetic heart valves is 12 to 18 years before that replacement surgery is required. However, in patients with uncontrollable risk factors, this expectation decreases to 10 years (Abramov et al., 2023; Johnston et al., 2015; Kostyunin et al., 2020; S. Lee et al., 2017). Bioprosthetic heart valve degeneration is caused by multifactorial biological, chemical, and mechanical mechanisms, leading to valve failure over time (Velho et al., 2022), see **Figure 7.**

Several studies have provided evidence linking fluid shear stress on the aortic surface of aortic valve leaflets to calcification. The oscillatory and high shear stresses experienced by valve endothelial cells are considered significant factors driving initial calcification (Gomel et al., 2019; Salman et al., 2021).

A study was conducted to compare the properties of the fresh pericardial tissue versus decellularized pericardial tissue treated with varying amounts of GA. It was found that there were no significant differences in mechanical properties, as determined by mechanical testing involving uniaxial testing to failure between fresh and decellularized bovine pericardium. However, the pericardium treated with GA tended to increase stiffness (Oswal et al., 2007).

In the vascular surgery field, the utilization of BPPs as tubes to replace the aortic tissue is different from the aortic valve. The wall shear stress (WSS) in the suprarenal aortic wall is 8.6 to 10.4 dyn/cm^2, while at the infrarenal aorta, is 4.7 to 6.1 dyn/cm^2 (Osinnski et al., 1995). The WSS in the aortic surface of the valve leaflets can reach up to 20 dyn/cm^2 (Yap et al., 2012). Theoretically, the presence of calcification poses a minor risk, whereas the chance of degeneration is much lower.

A comprehensive understanding of the mechanical characteristics of biological tissue can be achieved through the utilization of a uniaxial tensile stress-relaxation test. This knowledge will enable clinicians and scientists to accurately discern the mechanical properties of both normal and pathological tissue and understand their structural behavior during mechanical testing. Young's

modulus, or elastic modulus, is a fundamental biomechanical test that quantifies a material's stiffness, defined as the ratio of stress to strain in the linear elastic region. In vascular surgery, the elastic modulus indicates the rigidity and stifness of the arterial walls. A low Young's modulus signifies less stiff arteries that can expand during systole and recoil during diastole phase, while the high stifness indicate less flexiable arteries (Gasser, 2021; Thubrikar, 2007).

For a native human pericardial patch, the modulus of elasticity is variable from 20 -80 MPa (J. M. Lee & Boughner, 1985; Pok et al., 2017), and for a human pericardial patch treated with glutaraldehyde is about 50.8 Mpa (Yamashita et al., 2012).

For the porcine pericardium, the modulus of elasticity is about 58.91 MPa (Vondrášek et al., 2018). The modulus of elasticity of donkey's pericardium is 80 MPa, with thinner pericardial patches compared with BPPs (Chen et al., 2013). Sizeland et al. conducted a study to evaluate the modulus of elasticity in neonatal bovine (age from 4- 7 days) and adult bovine (age from 18 – 24 months) individuals. The results indicated that younger individuals have a greater modulus of elasticity (80 MPa) than adults (30 MPa) (Sizeland et al., 2014).

The biomechanical investigation conducted by Walker et al. on BPPs examined the range of native, decellularized, and sterilization and cross-linking combined with ultraviolet irradiation and low energy electron irradiation treated bovine pericardial patches, which measured between 0.41 m and 0.56 mm. The elastic modulus was approximately the same in pericardial patches treated with glutaraldehyde and others, with values of 0.28 ± 0.01 and 0.28 ± 0.06 MPa, respectively. The glutaraldehyde pericardial patch exhibited the greatest Young's modulus among BPPs, measuring at 0.44 MPa (Walker et al., 2022).

Then the literature presents a diverse array of findings about the Young's modulus or modulus of elasticity of BPPs. These data suggest that there is a notable variation in the mechanical characteristics of BPPs observed in various research (Aguiari et al., 2016). see **Table 3.**

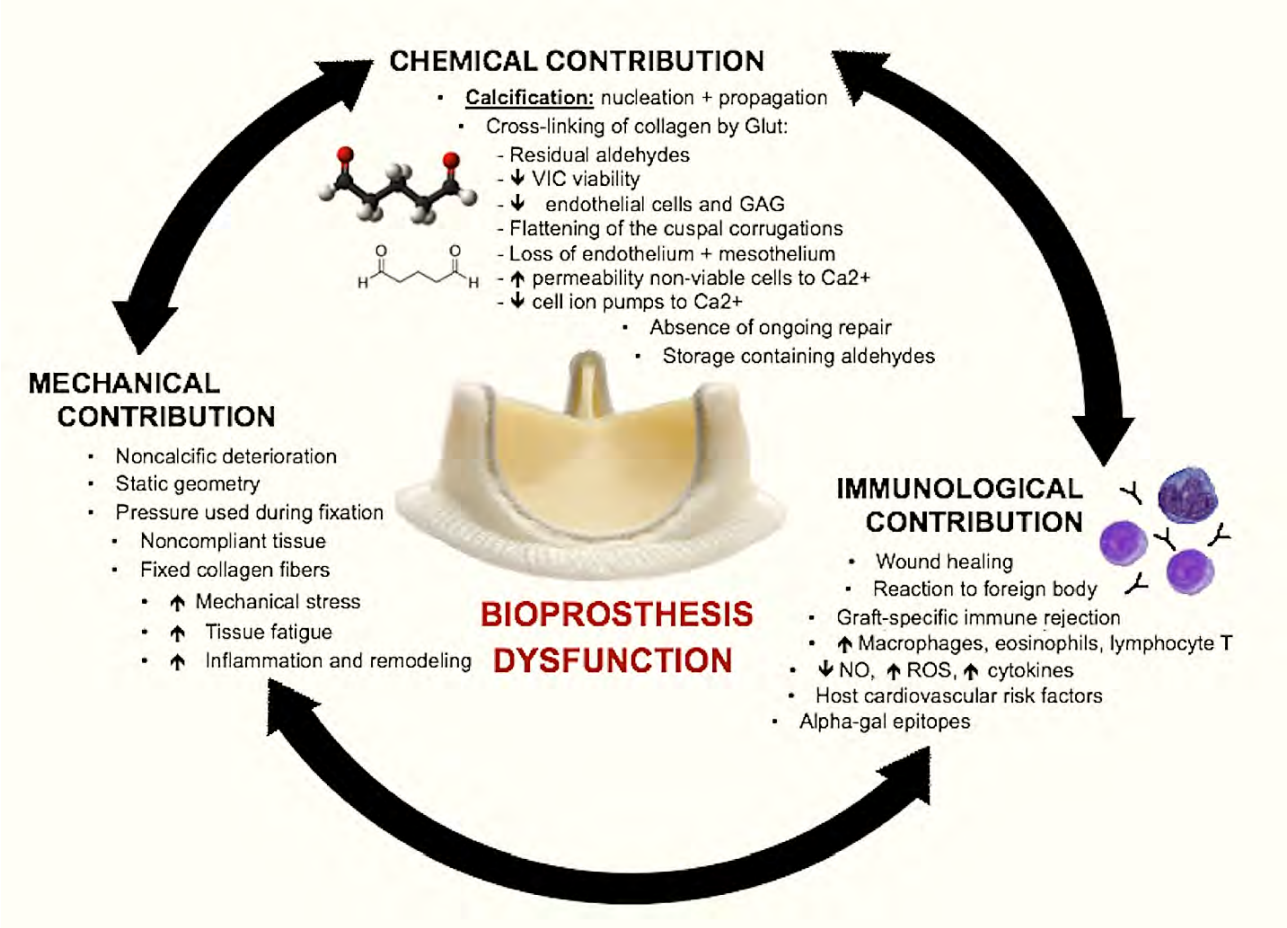


Figure 7. Representation of the chemical, mechanical, and immunological factors that contribute to prosthetic valve dysfunction. GAG: glycosaminoglycans; Glut: glutaraldehyde; NO: nitric oxide; ROS: reactive oxygen species; VIC: valvular interstitial cells (Velho et al., 2022).

Table 3. Characterization of bovine pericardium from Aguiari et al., 2016 *(Aguiari et al., 2016)*

Authors	Year	Pericardium	Preconditioning	Testing	Modulus	UTS	Strain at fracture (%)
Reece *et al.*	1982	GA-treated	–	Uniaxial loading	–	–	–
Radjeman *et al.*	1985	Native anterior	–	Uniaxial loading	1.25 ± 0.09 (10^9 dyne/cm^2)[a]	13.70 ± 0.95 (10^9 dyne/cm^2)	16.13 ± 1.16
		Native posterior			1.07 ± 0.06 (10^9 dyne/cm^2)[a]	12.85 ± 1.26 (10^9 dyne/cm^2)	15.34 ± 0.47
Trowbridge *et al.*	1985	GA-treated	Cyclic loading	Uniaxial loading, stress relaxation	–	–	–
Cohn *et al.*	1987	Native	–	Uniaxial loading	53.13 ± 3.74 MPa	8.91 ± 0.75 MPa	–
Crofts and Trowbridge	1988	Native	–	Uniaxial loading, stress relaxation	–	8.77 ± 0.77 N/mm$^{2[c]}$	27.17 ± 1.39[b]
		GA-treated				10.442 ± 0.96 N/mm$^{2[c]}$	46.05 ± 1.54[b]
Naimark *et al.*	1992	Native	Cyclic loading	Stress–strain response, stress relaxation and forced vibration	30 ± 4 MPa at 0.1 Hz	–	–
					31 ± 4 MPa at 1 Hz	–	–
					29 ± 4 MPa at 10 Hz	–	–
Zioupos *et al.*	1992	Native circumfer.	–	Inflation	46 MPa[c]	18 MPa	–
		Native root-to-apex			14 MPa[c]	2.5 MPa	–
Courtman *et al.*	1994	Native	–	Uniaxial loading	–	2.25 kN/m	30.1 kN/m
		TX100		Uniaxial loading	–	2.1 kN/m	28.7 kN/m
Pasquino *et al.*	1994	GA + GLTA	–	Uniaxial loading	–	16.8 ± 3.8 N/mm$^{2[e]}$	50.4 ± 10.4[d]
		TX100/SDS + GA + GLTA				13.3 ± 1.5 N/mm$^{2[e]}$	45.1 ± 3.6[d]
		TX100/SDS + GA				12.1 ± 2.8 N/mm$^{2[e]}$	42.3 ± 5.4[d]
		GA				12.8 ± 4.8 N/mm$^{2[e]}$	38.6 ± 9.9[d]
		Fresh				9,1 ± 5.4 N/mm$^{2[e]}$	21.9 ± 6.1[d]
Duncan and Boughner	1998	Native	Cyclic loading	Uniaxial loading, stress relaxation	17.0 ± 1.7 MPa[f]	–	–
		GA-treated (static)			11.9 ± 4.3 MPa[f]	–	–
		GA-treated (dynamic)			18.0 ± 4.9 MPa[f]	–	–
Langdon *et al.*	1999	GA-treated	Cyclic loading	Biaxial loading	250 ± 100 MPa[f]	–	–
García Páez *et al.*	2001	GA-treated right ventricle	Cyclic loading	Hydraulic simulator	–	61.18 ± 12.65 MPa[g] right	
					–	60.50 ± 13.39 MPa[g] left	–
García Páez *et al.*	2002	GA-treated right ventricle	–	Hydraulic simulator	–	49.93 ± 12.01 MPa[h]	–
		GA-treated left ventricle				71.26 ± 34.47 MPa[h]	–
Chang *et al.*	2002	GA-treated and fixed with a naturally occurring cross-linking agent	–	Hydraulic simulator, uniaxial loading	–	–	–
García Páez *et al.*	2003	GA-treated (Gore-Tex sutured)	–	Uniaxial loading	–	7.16 ± 2.97 MPa[i]	–
						6.48 ± 2.34 MPa[j]	
						11.49 ± 4.64 MPa[k]	
Sun *et al.*	2004	GA-treated	10 cycles	Uniaxial and biaxial tensile cyclic loading	–	–	–
Liao *et al.*	2005	Bovine (native and GA-treated)	–	Biaxial loading	–	–	–
Mirnajafi *et al.*	2005	Bovine (native and GA-treated)	Prestretching	Flexural loading	–	–	–
Mavrilas *et al.*	2005	Native	Manual preloading	Cyclic uniaxial loading	14 → 7 MPa[l]	–	–
		Degraded			10 → 5 MPa[l]	–	–
Maestro *et al.*	2006	GA-treated	–	Uniaxial loading	–	11.5 ± 4.6 MPa	–
Oswal *et al.*	2007	Native	–	Cyclic uniaxial loading	0.099 ± 0.038 GPa	13.862 ± 6.655 MPa	36.228 ± 9.018
		Decellularized			0.092 ± 0.037 GPa	14.3424 ± 4.437 MPa	31.769 ± 18.950
		0.05% GA-treated			0.033 ± 0.022 GPa	8.134 ± 5.019 MPa	52.293 ± 6.106
		Decell./0.05% GA			0.033 ± 0.021 GPa	7.107 ± 3.437 MPa	52.218 ± 9.661
		0.5% GA-treated			0.077 ± 0.023 GPa	9.007 ± 4.466 MPa	47.985 ± 2.689
		Decell./0.5% GA			0.049 ± 0.029 GPa	6.151 ± 3.103 MPa	42.340 ± 10.913
García Páez *et al.*	2007	Calf (GA-treated, polypropylene sutured and glued)	–	Uniaxial loading	–	34.36 ± 12.40 MPa[m]	–
						27.54 ± 10.89 MPa[n]	
						21.28 ± 6.52 MPa[o]	
						19.65 ± 5.26 MPa[p]	
Sánchez-Arévalo *et al.*	2010	GA-treated 0°	–	Uniaxial loading	105 MPa	–	–
		GA-treated 45°			70 MPa	–	–
		GA-treated 90°			63 MPa	–	–
Mendoza-Novelo *et al.*	2011	Native	–	Uniaxial loading, stress relaxation	169.1 MPa[u]	28 MPa[u]	28[u]
					102.9 MPa[v]	18 MPa[v]	20[v]
		Decell ATE			157.7 MPa[u]	21 MPa[u]	25[u]
					92.9 MPa[v]	12.5 MPa[v]	21[v]
		Decell RAS + ATE			126.9 MPa[u]	18 MPa[u]	28[u]
					94.4 MPa[v]	12 MPa[v]	22[v]
		Decell Triton X-100			139.6 MPa[u]	17 MPa[u]	26[u]
					92.9 MPa[v]	12 MPa[v]	23[v]
Pagoulatou *et al.*	2012	Fresh	Manual preloading, 10 preconditioning cycles	Uniaxial loading, cyclic uniaxial loading	48.12 ± 10.19 MPa[t]	–	–
					41.63 ± 14.65 MPa[u]		
		Triton X-100			52.67 ± 7.59 MPa[v]	–	–
					44.65 ± 19.73 MPa[u]		
		Trypsin/EDTA			36.82 ± 3.23 MPa[v]	–	–
					20.96 ± 8.17 MPa[u]		
Gauvin *et al.*	2012	GA-treated	Cyclic loading	Uniaxial loading	~190 MPa	~25 MPa	~25
Chen *et al.*	2012	Acellular GA-treated	–	Uniaxial loading	21.67 ± 11.69 MPa	15.05 ± 4.50 (kN/m) m^2	–
Bai *et al.*	2013	Native	–	Uniaxial loading	27 MPa	25 MPa	59
		Triton X-100			27 MPa	25 MPa	58
		GA-treated			21 MPa	29 MPa	60
Hülsmann *et al.*	2013	Native	–	Uniaxial loading	27 MPa	7 MPa	25
		GA-treated			10 MPa	6 MPa	50
		Decell SDS/DCA			12 MPa	7 MPa	60
		Decell SDS/DCA + GA-treated			5 MPa	4 MPa	70
		Decell Trypsin/EDTA			15 MPa	6 MPa	45

[a]Final modulus.
[b]Averaged over five different orientations.
[c]Terminal tensile modulus.
[d]Measured within 1 week after the process.
[e]At 30 mm/s.
[f]Highest value measured by authors.
[g]Best result.
[h]Biaxial stepwise.
[i]Left 45°.
[j]Right 90°.
[k]Centre.
[l]Collagen modulus calculated under middle to high-frequency cyclic loadings.
[m]Longitudinally cut control samples.
[n]Transversely cut control samples.
[o]Samples cut longitudinally and sutured.
[p]Samples cut transversely and sutured.
[q]Longitudinal samples sutured and glued with Glubran.
[r]Transverse samples sutured and glued with Glubran.
[s]Longitudinal samples sutured and glued with Loctite.
[t]Transverse samples sutured and glued with Loctite.
[u]Apex to base.
[v]Transverse samples.
GA: glutaraldehyde; UTS: ultimate tensile strength; Triton-X100: t-octylphenoxypolyethoxyethanol, SDS: sodium dodecyl sulphate; ATE: tridecyl alcohol ethoxylate; EDTA: ethylenediaminetetraacetic acid; RAS: reversible alkaline swelling; GLTA: glutamic acid; DCA: deoxycholic acid.

4.7. Histological Examination of Bovine Pericardial Patches: Insights and Observations

The main component of BPPs is a complex composition of ECM contains collagen elastin as a primary component. At physiological pressure, the ECM of the BPPs contains collagen and elastin, which contribute to the maintenance of a balanced equilibrium between stretch and return to normal status. This property allows the BPP to undergo variations in volume and elongation without encountering rupture or injury in the course of typical physiological activities (Trębacz & Barzycka, 2023).

The histological analysis conducted by Peivandi et al. on BPPs revealed collagen bundle degradation and variations in caliber among different brands. These findings may be attributed to the sterilizing and preparation processes for medical use (Peivandi et al., 2022), see **Figure 8.** The fibrous layer of BPPs exhibits more roughness compared to the serous layer, and more roughness in bovine samples when compared to porcine pericardial patches (Campion et al., 2021), see **Figure 9.**

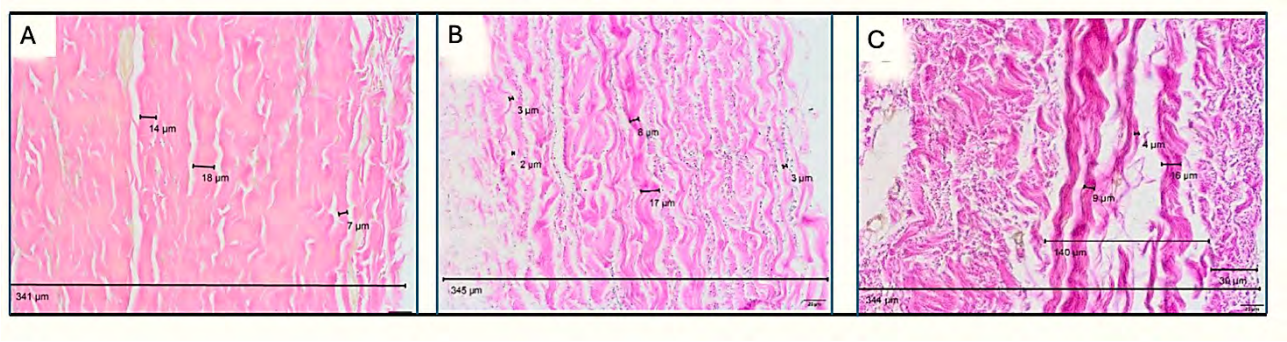


Figure 8. Histological study using hematoxylin and eosin stain of BPPs showing different collagen bandelle caliber in. A: native BPPs. B: CardioCel® patch .C: VascuGuard® patch, *(Peivandi et al., 2022)*.

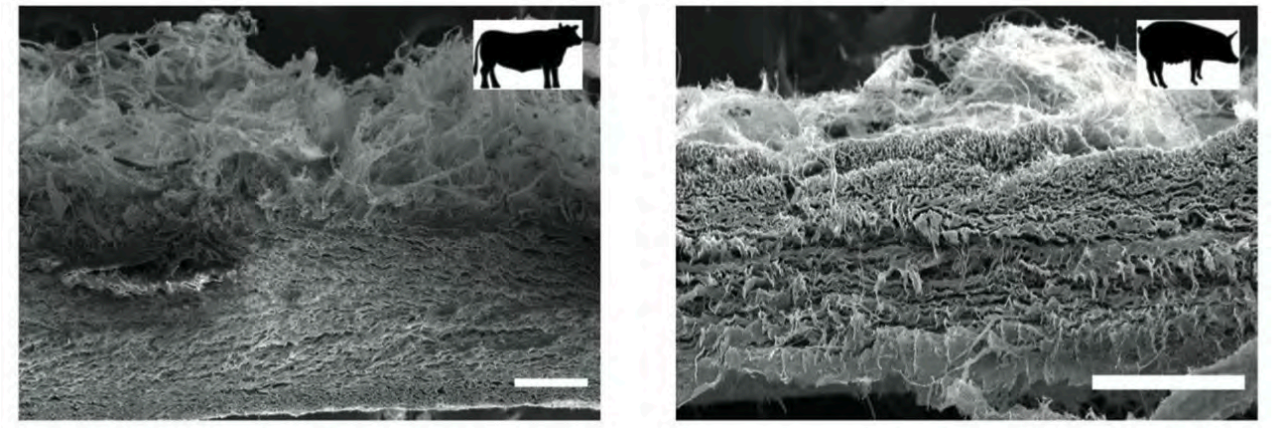


Figure 9. Surface roughness of porcine and bovine pericardial patches. The image shows a cross-section of the fibrous surface of bovine and porcine pericardium at the top, and the serous surface at the lower half. The scale bar measures 200 millimeters. Magnification: bovine = 105 times, porcine = 25 times *(Campion et al., 2021)*.

Another study that examined the characteristics of native bovine pericardium (NBP) and decellularized bovine pericardium (DBP) demonstrates the TRICOL decellularization procedure, which involves the use of Triton X-100 and cholate (TRI-COL) followed by the elimination of nucleic acids using nuclease, effectively maintained the structural integrity of the pericardium's ECM. This preservation included the distinct layers of serosa and fibrosa. The TRICOL technique did not affect the organization of elastin around the collagen bundles across the entire thickness. The presence of collagen and elastin was maintained, but the amounts of glycosaminoglycans were significantly reduced, especially in the bovine scaffolds, see

Figure 10.

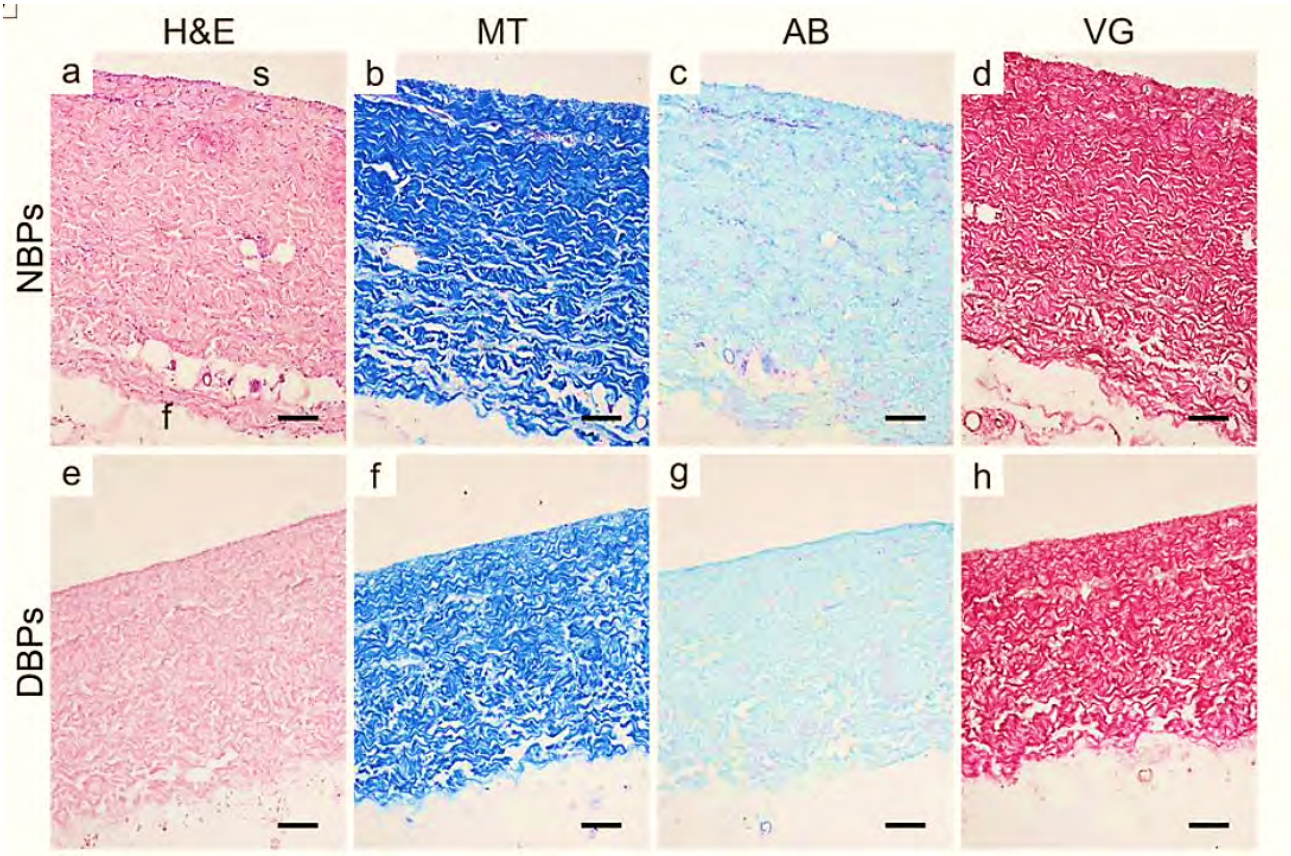


Figure 10. Histological analysis conducted in NBPs and DBPs demonstrated the presence of an intact extracellular matrix and the absence of nuclear material in the DBPs. S: serosa (inner layer of patches). F: Fibrosa (outer layer of patches). NBPs: Native bovine pericardium. DBPs: decellularized bovine pericardium. H&E: Haematoxylin and eosin stain. MT: Masson trichrome stain. AB: Alcian blue stain. VG: Van Gieson stain *(Zouhair et al., 2020)*.

Chapter 2: The aorta and alternative methods for replacing aortic tissue

To estimate the efficacy of BPPs to replace vascular tissue. It is essential to engage the previous studies of histological and biomechanical characteristics of the aorta and peripheral arteries. The vascular system contains arterial and venous systems. These systems contain different characteristics of vessel walls, see
(SIDAWY & BRUCE A, 2022).
Arterial, venous, and lymphatics systems work together as transporting tubes between various organs and tissues. A clear understanding of the differences between normal and aneurysmal aortic tissue is essential for guiding the development and selection of appropriate strategies for aortic replacement.

1. Anatomy and structure of vessels: exploring their histological properties

The artery wall exhibits a consistent organizational structure throughout the body, albeit with varied quantities of its constituent components in different anatomical regions. The structure consists of cellular components and a fibrous matrix arranged into three layers: intima, media, and adventitia, see **Figure 11**.

Table 4. Vessel wall characteristics of circulatory systems *(SIDAWY & BRUCE A, 2022)*.

	Arterial Wall	Venous Wall	Lymphatic Wall
Collagen content	Moderate	High	Mixed
Elastic fiber content	High	Moderate	Mixed
Central pressure	High	Very low	Low
Shear stress	High	Low	Low
Stretch force	High	Low	Low
Pulsatility	High	Low	Low
Compliance	Moderate	High	High
Oxygen tension	High	Low	Low
Intrinsic propulsion	None	None	Predominant
Valves	None	Some	Many

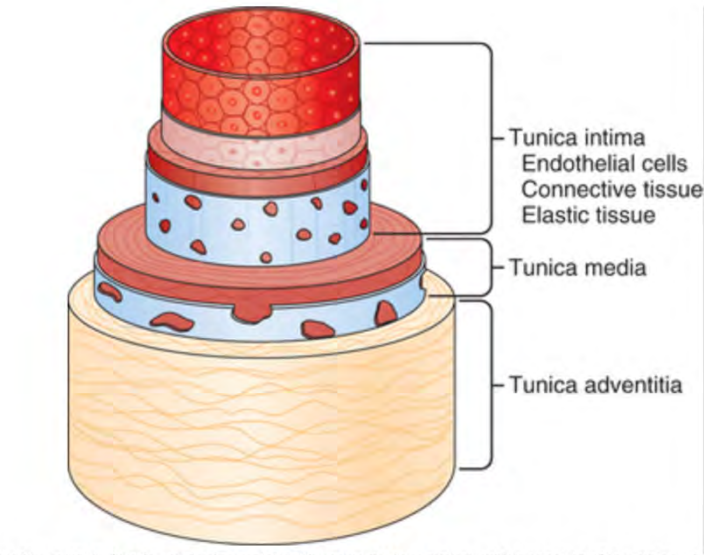


Figure 11. The structure and composition of the vessel wall. Arteries exhibit a shared fundamental structure, comprising the tunica adventitia, tunica media, and tunica intima (SIDAWY & BRUCE A, 2022).

1.1. Intima

The intima is the inter-most luminal layer, comprised of three main components: the endothelium, the connective tissue, and a basal layer of elastic tissue known as the internal elastic lamina. This lamina serves as the separation layer between the intima and the media. The endothelium is a single layer (monolayer) of cells that functions as the interface with circulating blood and the vessel, which have a direct contact with blood flow. The normal endothelium has the capacity to react to physical and chemical stimuli through the synthesis of many factors that regulate vascular tone, cellular adhesion, thromboresistance, smooth muscle cell proliferation, and vessel wall inflammation.

Endothelial dysfunctions affect directly to the endothelial activation, as it has the potential affect to contribute to the development of arterial disease under specific circumstances (Deanfield et al., 2007). Next to the endothelium there is the basement membrane, also known as the basal lamina, which serves the purpose of securely anchoring the endothelium to the underlying connective tissue.

The basement membrane exhibits both mechanical strength and flexibility of the tunica intima, while also demonstrating permeability to facilitate the passage of various materials. The outer layer of the tunica intima is composed of a limited quantity of areolar connective tissue, largely comprising elastic fibers to enhance the vessel's flexibility to dilate and construct. Additionally, it contains a proportion of collagenous fibers to augment its strength. Damage to the elastic lamina of tunica intima will increases the risk arterial stiffness (Deanfield et al., 2007; Miura, 2020; SIDAWY & BRUCE A, 2022).

1.2. Media

The media is the middle segment of arterial layers, that lie between tunica intima and tunica adventitia. The tunica media layer is a porous heterogeneous layer made up of an ECM phase with embedded SMCs (SIDAWY & BRUCE A, 2022). The composition and microarchitecture of the tunica media maintain the stability of the vascular system. The tunica media is made up of vascular SMCs, elastin, and collagen fibers that are arranged in a highly structured manner to provide the mechanical properties of arterial tissues (Dobrin, 1999).

1.3. Adventitia

The adventitia is the outer layer of arterial segments that extends from the tunica media to a boundary that is typically indistinct and often adjacent to the perivascular connective tissue. The thickness and structure of the adventitia are variable from large to small diameter depending on the arteries function and anatomy. The aorta possesses a limited amount of adventitial fibrous connective tissue, with high amounts of elastic and collagen fibers are present in aortic adventitia (SIDAWY & BRUCE A, 2022).

The distribution of collagen, elastin, and SMCs in arteries depends on the diameter of vessels. We can divide the arteries into large, medium, and small arteries. The large arteries such as the aortoiliac and pulmonary arteries have more elastin tissue than collagen and SMCs, and the largest layer is the media layer. The quantity of elastin lamellae and thickness of media layer correlate with the patient's blood pressure and age. Upon birth, the aorta has a minimal amount of elastin lamellae; nevertheless, in adult age, the aorta contains about 40 to 70 lamellae of elastin. The quantity of elastin lamellae could increase proportionally with the severity of hypertension.

For the medium-sized arteries such as brachio-cephalic trunk, femoro-poplital, and tibial arteries. They have more quantity of muscle tissue and collagen than elastin tissue, with tunica media up to 40 concentric layers of SMCs. The quantity of elastin and collagen is variable in the aortic wall, in the ascending aorta, elastin constitutes approximately 27% of the arterial wall, while collagen accounts for about 22%. In contrast, in the distal aorta, the elastin content decreases to around 17%, whereas collagen increases markedly to approximately 53% (Concannon et al., 2020).

The thickness of the tunica intima is variable and depend on multiple factors, the age of the patient is one of the most important factors that could play an important role in that. In newborn patients, it has a thin and delicate structure. For the young people, the tunica intima comprises approximately one-sixth of the overall wall thickness in the muscular arteries. while lipid deposits, commonly in the form of irregular "fatty streaks" can cause the expansion of the tunica intima in older adults. For the small arteries and arterioles, it could be differentiated based on the amount of SMCs layers in the tunica media with less than 6 concentric layers of SMCs (Ross & Pawlina, 2016).

The properties of vessels are variable depending to size and function, even for the large and vessels size such as aortic segments. For the aorta and aortic segments, it is important to understand the anatomy and the function according to the aortic segments. The aorta is the biggest artery in the human body that transports the oxygenated blood of the heart to different body organs via arterial systemic circulation. The aorta originates from the left ventricle and is divided into four major portions, see

Figure *12*.

The first portion is the ascending aorta which originates at the base of the left ventricle and extends up to form the aortic arch, with variable diameter from 28.8 mm to 33.2 mm (Rogers et al., 2013), and average length of 5 cm (SIDAWY & BRUCE A, 2022). The aortic arch is the second portion that arches superiorly, posteriorly and to the left to link the ascending and descending aorta. It has a diameter of 2.0 – 2.3 cm and a length of 4 cm (SIDAWY & BRUCE A, 2022). It begins at the level of the right brachiocephalic artery and ends at the origin of the left subclavian artery. The descending thoracic aorta is the third portion that begins at the end of the aortic arch and descends to the diaphragm, which is the point of separation between the thoracic cavity and the abdominal cavity. The descending thoracic aorta's diameter is estimated to range from 20.5 mm to 24.7 mm in middle-aged individuals under the age of 45. (Rogers et al., 2013). The last portion is the thoracoabdominal aorta, which extends from the aortic opening of the diaphragm at the level of the T12 vertebra to the lower portion of the body of the L4 vertebra, where it divides into right and left iliac arteries (Snell, Richard S, 2012).

The abdominal aorta is divided into two portions. The suprarenal portion gives rise to celiac, superior mesenteric, and renal arteries. The second portion is infrarenal and it has only one artery, the inferior mesenteric artery, which originates at its anterior aspect. The diameter of the infrarenal abdominal aorta in middle age individuals younger than 45 years is reported between 15.2 mm and 18.5 mm, while a wider diameter (17.8 mm and 22.5mm) is reported in individuals less than 65 years old (Rogers et al., 2013; SIDAWY & BRUCE A, 2022).

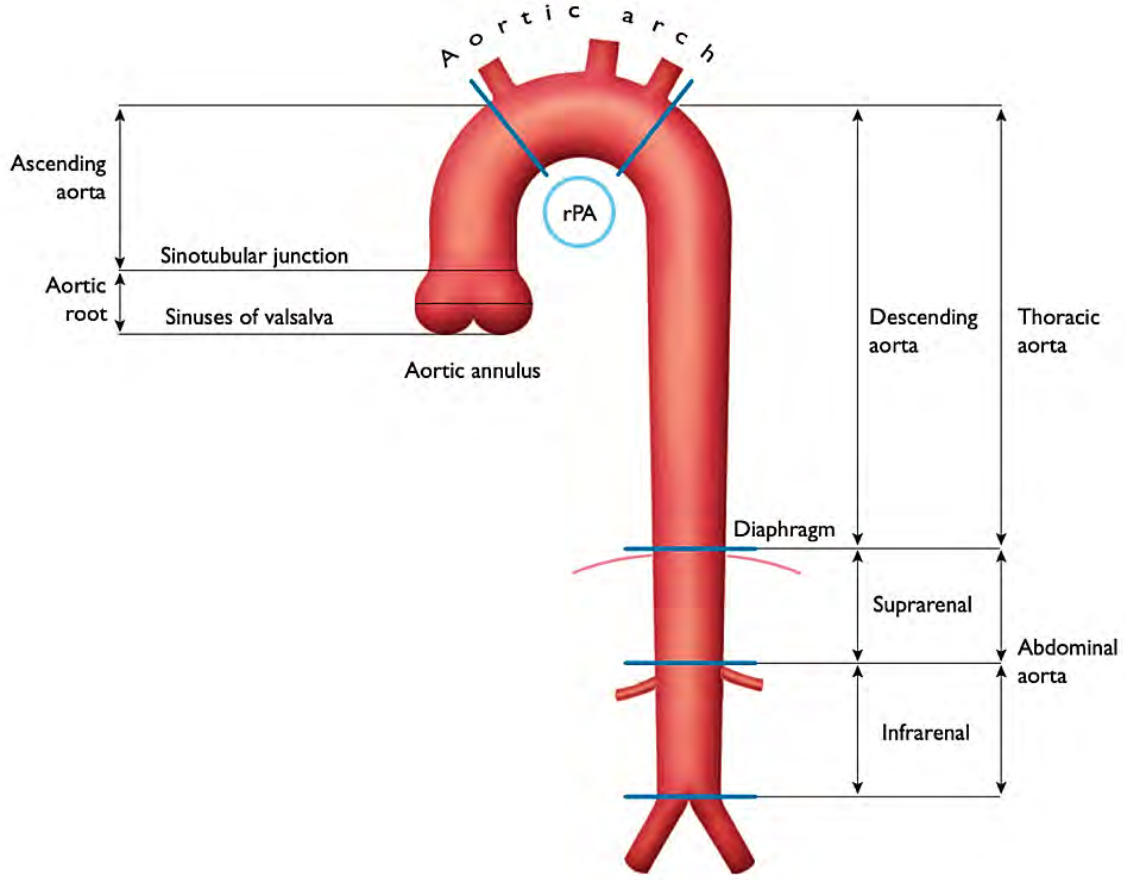


Figure 12. The major branches of the aorta from ascending aorta to iliac bifurcation. rPA: right pulmonary artery. (Erbel et al., 2014).

For the veinous wall, it comprises three fundamental layers: the tunica intima, tunica media, and tunica adventitia. This system plays a crucial role in the circulatory system, serving as vascular structures distributed throughout the body responsible for recovering oxygen-depleted blood and transporting it back to the heart. These veins cooperate with other vasculature and the cardiac system to maintain the continuous circulation of blood. The blood volume in the venous system varies from 60%-70% of the total blood amount (King & Fink, 2006; Wolff et al., 2016). The vein anatomy consists of three primary layers: the tunica intima, tunica media, and tunica adventitia, see **Figure 13**.

The intima layer is the innermost layer of the vein wall and comprises a monolayer of endothelial cells situated atop an incomplete elastic basement membrane. Under normal, healthy conditions, these endothelial cells play essential roles in preserving the integrity and functionality of the venous wall. They generate vasorelaxants and platelet inhibitors, such as PGI2 and nitric oxide. The functions of the venous intima and endothelial cells in their unaltered state are pivotal in various pathological processes, notably in the occurrence of neointimal hyperplasia, particularly when exposed to arterial pressure(Ovalle & Nahirney, 2021; SIDAWY & BRUCE A, 2022).

The media is a medial layer of the venous wall, consists of SMCs arranged circularly, and displays significant variability based on location. Generally, it is less developed than the arterial system and might contribute to the formation of varicosities in veins of the extremities (Ovalle & Nahirney, 2021; SIDAWY & BRUCE A, 2022). The regulatory process is essential as it helps maintain the normal vessel wall with low cell turnover, characterized by low rates of proliferation and apoptosis. Any injury or changes in the environment, such as exposure of veins to arterial flow, can increase rates of proliferation (intimal hyperplasia) or apoptosis (Cai et al., 2004; Wasse et al., 2012).

The adventitia is the outer layer of the venous wall, that represents the thickest layer in large veins, occasionally merging with the media. Within this layer, bundles of smooth muscle cells oriented longitudinally are interspersed with collagen and elastic fibers. Large veins may exhibit abundant collagen fibers, which can adopt either a longitudinal or helical orientation. In contrast to the vasa vasorum found in arteries, those in venous adventitia are notably more extensive and penetrate deeper regions (Ovalle & Nahirney, 2021; SIDAWY & BRUCE A, 2022).

The most common vein utilizable in the vascular surgery field is the great saphenous vein, see **Figure 14**. The Young modulus, also known as the elasticity modulus, of the great saphenous vein varies depending on the orientation of the section utilized in the study. For the longitudinal orientation, the

Young modulus ranges from 23 to 130 Mpa (Soletti et al., 2010; Stekelenburg et al., 2009). The circumferential orientation of Young's modulus varies between 2.25-43Mpa (Donovan et al., 1990; Stekelenburg et al., 2009). Venous insufficiency is one of the primary factors that might modify the biomechanical properties of the great saphenous vein. The fibrosis and decreased wall compliance are a result of the increased stiffness of collagen and elastin in both the longitudinal and circumferential orientations (Nguyen et al., 2015).

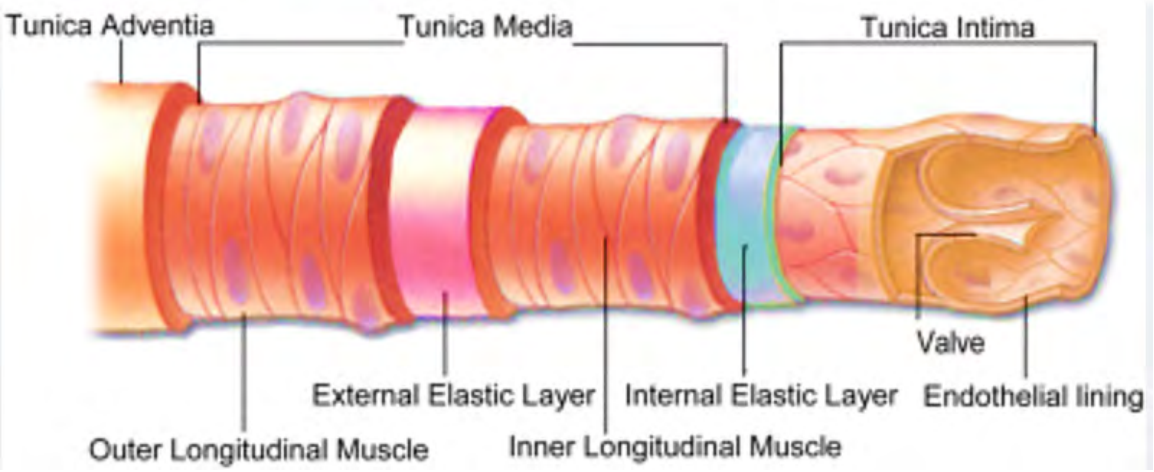


Figure 13. The structure and composition of the vein wall. The veins exhibit a shared fundamental structure, comprising the tunica adventitia, tunica media, and tunica intima (Radhakrishnan, 2022).

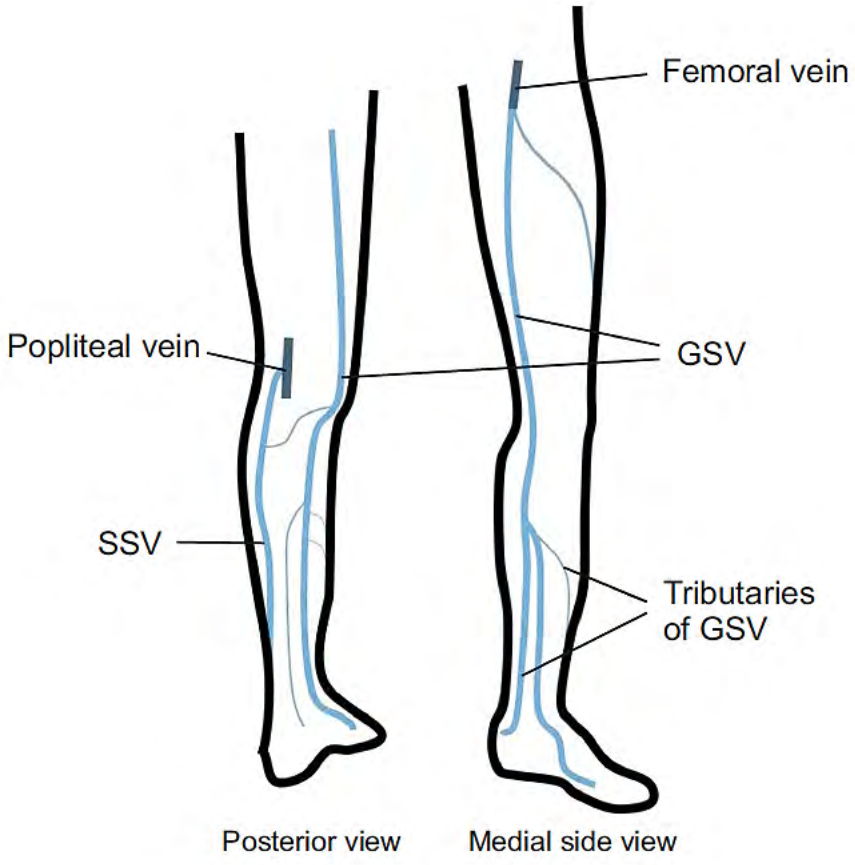


Figure 14. Great saphenous vein and its tributaries. The text describes the upward pathways of the great saphenous vein (GSV) and short saphenous vein (SSV) in the lower limbs *(H.-J. Kim et al., 2022)*.

2. Biomechanics of arteries: understanding their functional role

The aorta functions is a compliant tube that buffers and carries pulsatile cardiac output flow and pulse wave propagation to all arteries. It is able to amortize left ventricular stroke volume due to its physiological and biomechanical characteristics (Kuecherer et al., 2000). Aortic energy is a combination of kinetic energy and potential energy. The kinetic energy is the energy of high-flow motion or speed. The potential energy is the stored energy that comes from material elasticity forcing the material to return to the original status. For example, stretching or pulling a piece of rubber is kinetic energy, while returning to its original status is potential energy. The aorta is similar to this piece of rubber when it stretched and then returning to normal status.

In normal aorta, during the systolic phase, the stroke volume pumped by the heart to transfer oxygenated blood to the peripheral vascular system works as kinetic energy. This energy transfers 40% of stroke volume to the peripheral vascular system great part of portion is stored in the elastic aorta that is transferred when the potential energy is transformed into kinetic energy. This transformation of the potential energy occurs during the diastolic phase. With the closure of the aortic valves during the diastole, the ascending aorta distend as a balloon due to the remaining portion of the stroke volume, tends to return to its baseline state, causing a propelling toward the periphery. This energy stored in aortic wall makes aorta function as a diastolic pump to maintain the pumping activity of the circulatory system during the diastolic phase, this is exactly what happens in the Windkessel phenomena (Salvi, 2017), see
Figure *15* (A & B) and
Figure *16*.

There is a variety of para-physiological or pathological conditions that can affect the anatomical, structural, and functional properties of large elastic arteries. These conditions include aging, hypertension, media calcifications, atherosclerosis, chronic kidney disease, and diabetes mellitus (Millasseau et al., 2005; Redheuil et al., 2010; Salvi, 2017). Changes in the elastic characteristics of the aorta result in increased parietal stiffness and decreased aortic compliance. As a result, the stroke volume amount held by the aorta during the systolic ejection time diminishes and causes cardiac anomaly- cardiac hypertrophy- as a natural response. See
Figure *15* (C & D).

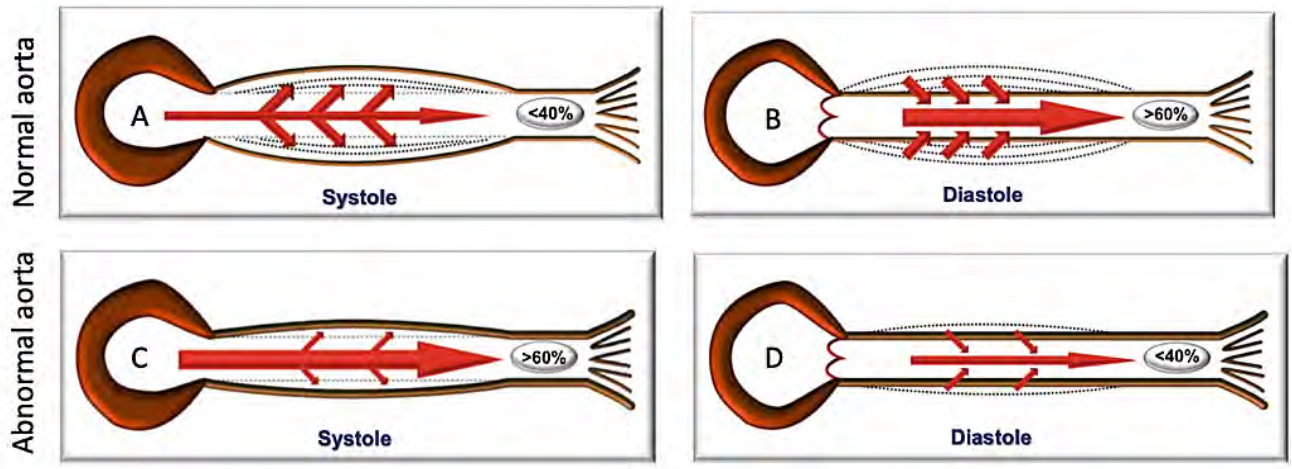


Figure 15. The Windkessel phenomenon under normal and abnormal vascular distensibility conditions. A and B: in normal aorta the volume held in elastic aorta is about 60% that pushed in circulation during the diastole. The aorta distends during each systolic phase to allow the reception of the blood stroke volume. This energy is expended during the diastolic phase when the aortic tube recoils to normal status, and the blood flow continues to the periphery. C and D: in abnormal aorta, due to alternation of aortic elasticity, the amount held in the aorta is reduced. As a sequence, the heart becomes hypertrophied (Salvi, 2017).

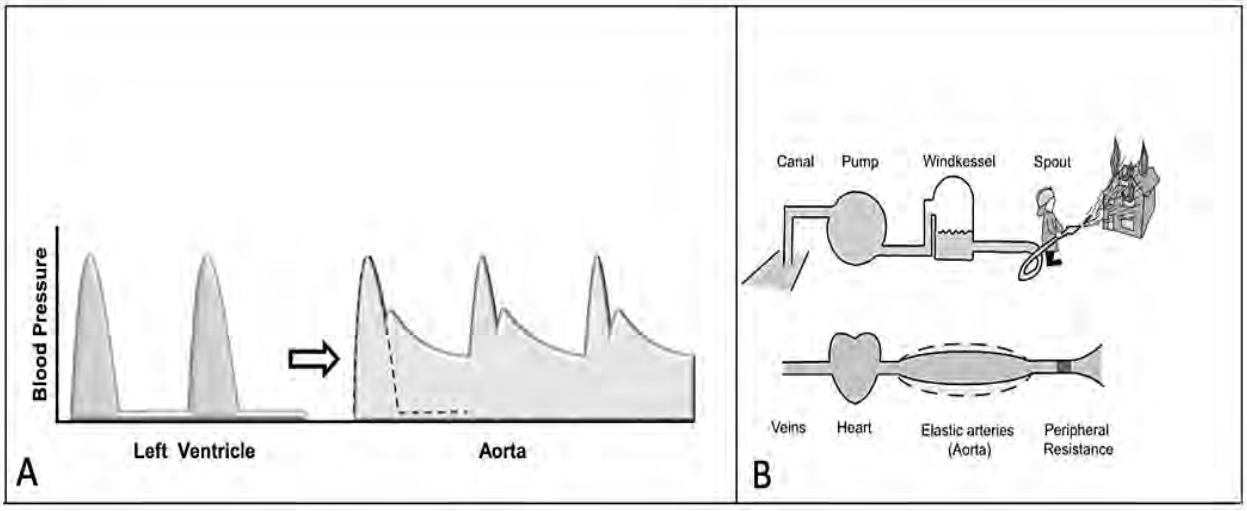


Figure 16. The Windkessel phenomena and diastolic pump activity. A: Actual blood pressure in aorta. B: The air reservoir serves as Windkessel, that converting potential energy held in the wall to kinetic energy in order to maintain blood flow. (Salvi, 2017; Westerhof et al., 2009).

Aortic stiffness can be evaluated either by measuring the velocity of a pulse wave propagating through the aorta or by calculating aortic strain and distensibility from the cross-sectional area of the aorta during cardiac cycles. Measurement of distensibility is the most sensitive marker of arterial aging in adults less than 50 years old, while aortic arch pulse wave velocity (PWV) is more sensitive in individuals more than 50 years old. These two methods can evaluate aortic stiffness regardless of gender, body size, or cardiovascular risk factors (Redheuil et al., 2010).

PWV is the wave created during the contraction of the left ventricle and the ejection of blood into the aorta. This wave will then propagate along the aorta and aortic branches at a certain speed. Pulse wave propagating through the aorta is measured by carotid-femoral PWV which is determined by the time taken for the arterial pulse to propagate from the carotid to the femoral artery (Millasseau et al., 2005). The velocity of a pulse wave propagating through the arterial system is inversely related to the viscoelastic properties of the vessel wall; thus, increased pulse wave velocity reflects reduced arterial elasticity and greater wall stiffness.

The normal range value of carotid-femoral PWV is equivalent to 8.74 ± 1.15 m/s in men and 8.31 ± 1.13 m/s in women (Baldo et al., 2018) . Since ΔT represents the time delay of the distal pulse pressure wave, the pulse wave velocity is a global parameter of aortic elasticity. The equation of PWV expressed in mm/s, is calculated by dividing the distance between two arterial segments by the transit time (ΔT) required for the pulse wave to travel between them.

The strain (S) is a unitless measure of the deformation of the length or the area of the applied force divided by the initial length or the initial area of the material. Measuring the strain is one of the biomechanical modalities to assess the aortic properties. There are two types of strain, engineering strain and aortic strain (Gasser, 2021).

First the engineering strain, that defined as the amount of deformation in the applied force divided by the initial length of the material. It can be calculated by the mechanical measurement of the axial tension test. It is divided into two subtypes of strain. First subtype is a normal strain (ε) which is the deformation in the same direction of the applied force. The second subtype is the shear strain (γ), which expresses the change in angle between two lines initially perpendicular to each other, not the same direction of applied force.

Second type of strain is the aortic strain, which is a true applied strain defined as the amount of physiological deformation in the applied force divided by the initial surface area of the aorta. It can be measured by radiological techniques such as MRI and ultrasonography. Aortic strain or true strain has a different concept from engineering strain because they measure the physiological deformation of the physiological pressure. (Duprey et al., 2010; Thubrikar, 2007).

$$Aortic\ strain\ (\%) = (As - Ad)/Ad \times 100 \quad (1)$$

Where:

- **As** = Luminal surface area at systolic phase
- **Ad** = Luminal surface area at diastolic phase

The percentage of strain which is measured from the change in the cross-sectional area of the vessel between systole and diastole phases can estimate the elasticity. In normal healthy individuals, the percentage of strain was measured for descending thoracic aorta, visceral aorta, and abdominal aorta. The results were 30% ± 11, 26% ± 70, and 29% ± 8, with a flowrate of 4094 ml ± 1600 ml, 2839 ml ± 910 ml, and 1602 ml ± 549 ml respectively (Amanuma et al., 1992). In MRI, the normalization of the local strain by the local pulse pressure provides the distensibility of the aortic wall (Herment et al., 2011), see table (2-2).

The compliance is the absolute change in vessel diameter (or area) for a given change in pressure. It is a criterion of the vascular system to measure characteristics of vascular walls, the component of the stress on the blood vessel, and to determine the pressure and flow wave configurations.
It is defined as the change in diameter or surface area of the artery in absolute values, at a given change pressure level, for a given arterial localization. In other words, compliance is the ratio between change in volume and change in pressure (Oliver & Webb, 2003; Salvi, 2017).

$$\text{Diameter compliance} = (D_s - Dd)/(P_s - Pd) = \Delta D/\Delta P \quad (2)$$

$$\text{Area compliance} = (A_s - Ad)/(P_s - Pd) = \Delta A/\Delta P \quad (3)$$

Where:

- **Ds** = systolic diameter
- **Dd** = diastolic diameter
- **As** = systolic cross-sectional area
- **Ad** = diastolic cross-sectional area
- **Ps** = systolic pressure
- **Pd** = diastolic pressure
- **ΔD** = change in diameter (Ds − Dd)
- **ΔA** = change in cross-sectional area (As − Ad)
- **ΔP** = pulse pressure (Ps − Pd)

Compliance can be measured by (different surface area / different pressure) in mm^2/mmHg unit. A highly compliant aorta or normal aorta has a lower pulse pressure for a given stroke volume than a low compliant or low stiff aorta. With aging and atherosclerosis, the aortic compliance was declined, resulting in an increase in pulse pressure (Redheuil et al., 2010).

The vascular distensibility is another dynamic crucial characteristic of the vascular system to evaluate the biomechanical characteristics of aortic wall properties. It is defined as a relative change in vessel diameter or area for a given change in pressure. It is also defined as the value of arterial compliance in relation to the initial diameter of the artery or relative change in diameter in relation to the change in pressure (see distensibility equation below, D is diameter and P is pressure) (Oliver & Webb, 2003; Salvi, 2017). The unit of distensibility is $10^{-3} \times mmHg^{-1}$.

$$\text{Diameter distensibility} = (Ds - Dd)/[(Ps - Pd) \times Dd] = \Delta D/(\Delta P \times Dd) \quad (4)$$

$$\text{Area distensibility} = (As - Ad)/[(Ps - Pd) \times Ad] = \Delta A/(\Delta P \times Ad) \quad (5)$$

$$\text{Area distensibility} = \Delta A/(CAP \times Ad) \quad (6)$$

$$\text{Volumetric distensibility} = [(Vs - Vd)/Vd]/\Delta P = (\Delta V/Vd)/\Delta P \quad (7)$$

Where:

- **Ds** = systolic diameter
- **Dd** = diastolic diameter
- **As** = systolic cross-sectional area
- **Ad** = diastolic cross-sectional area
- **Vs** = systolic volume
- **Vd** = diastolic volume
- **Ps** = systolic pressure
- **Pd** = diastolic pressure
- **CAP** = central arterial pressure
- **ΔD** = change in diameter (Ds − Dd)
- **ΔA** = change in cross-sectional area (As − Ad)
- **ΔV** = change in volume (Vs − Vd)
- **ΔP** = pulse pressure (Ps − Pd)

(CAP) is the central arterial pressure or pressure difference, while V is the volume in the artery. Peripheral resistance is one of the important factors that play a key role in holding blood in arteries during the diastolic phase. If peripheral resistance is equal to zero, the distensibility is close to zero. Measurement of distensibility is the most sensitive marker of arterial aging in adults more than 50 years of age (Redheuil et al., 2010), see

Table *5*.

Table 5. Normal value of aortic strain and distensibility in descending thoracic aorta and abdominal aorta.

Aortic strain	**Study**	**Normal value**	**Technique**	**Reference**
Unit in percentage %	Amanuma et al.	29 % ± 8	MRI FEER	(Amanuma et al., 1992)
	Herment et al.	17.8% ± 11.7	MRI SSFP	(Herment et al., 2011)
	Herment et al.	16.9% ± 8.18	MRI PC	(Herment et al., 2011)
	Redheuil et al.*	<50 y: 26% ± 9.46	MRI	(Redheuil et al., 2010)
	Redheuil et al.*	>50 y: 15.1% ± 7.29	MRI	(Redheuil et al., 2010)
Distensibility	**Study**	**Normal value**	**Technique**	**Reference**
Unit in $x10^{-3}$ $mmHg^{-1}$	Herment et al.	4.26 ±1.98	MRI SSFP	(Herment et al., 2011)
	Herment et al.	3.92 ± 2.72	MRI PC	(Herment et al., 2011)
	Redheuil et al.*	<50Y: 7.44 ± 2.54	MRI	(Redheuil et al., 2010)
	Redheuil et al.*	>50Y : 2.89 ± 1.29	MRI	(Redheuil et al., 2010)
	Voges et al.	8.3 ± 3.0	MRI GE	(Voges et al., 2012)

*Grand mean and pooled standard deviation were calculated

The elasticity is defined as the ability of a deformed material to return to its original shape and size when the forces causing the deformation are removed. Young's modulus or stress-strain curve modulus is defined as being the slope of the straight-line portion of a stress (σ) strain (ε) curve.

Focusing on the elastic component, if the slope is taken between two stress-strain points, the modulus is the change in stress divided by the change in strain. The strain was defined previously, while stress is a physical term that represents the internal forces exerted by adjacent particles of a continuous substance on one another, calculated as (load /superficial area) for engineering stress. (Thubrikar, 2007).

$$\text{Stress } (\sigma) = F/A \tag{8}$$

In the equation (8), F is the load, and A: the superficial area.

According to Pascal's principle, the pressure within a balloon or a tube must be uniform throughout at equilibrium. However, there are significant variations in wall tension over the balloon or tube surface.

The variance is characterized by the Laplace's law. Considering the physiological statutes, the force should be physiological not the maximal force, so we should apply the circumferential stress (σ) which is wall tension in Laplace law (tension or stress circumferential of the aortic wall), and longitudinal stress (σ) which is wall stress in Laplace law (internal pressure applied on the aortic wall). See **Figure 17**, (Duprey et al., 2010; Massaglia & Quaglio, 2018; Salvi, 2017):

$$\text{Circumferential stress } (\sigma) = (P \times R)/h \tag{9}$$

$$\text{Longitudinal stress } (\sigma) = (P \times R)/(2 \times h) \tag{10}$$

P: pressure, *R:* radius of the artery, and h: the thickness of the artery

$$\text{Young's modulus (E)or Elastic modulus} = \text{Stress/Strain} = \sigma/\varepsilon \tag{11}$$

Also, there is another calculation, than can measure the physiological Young's modulus by Moens-Korteweg Equation (Newman & Greenwald, 1978):

$$\text{Physiological Young's modulus (E)} = (\Delta P \times Dd)/(\Delta D \times h) \quad (12)$$

Where in equation (12):

- **E** = physiological Young's modulus (kPa or MPa)
- **ΔP** = pulse pressure (Ps − Pd)
- **Dd** = diastolic diameter
- **ΔD** = change in diameter (Ds − Dd)
- **h** = vessel wall thickness

The stiffness describes how the stress changes in response to the strain (Gasser, 2021). There is a physiological gradient of stiffness between the aorta and the distal arteries. The elasticity and the dilation of the arteries reduce gradually as one moves away from the heart, and it could change over time in response to factors such as aging and disease, see **Table 6**. (Gasser, 2021; Thubrikar, 2007).

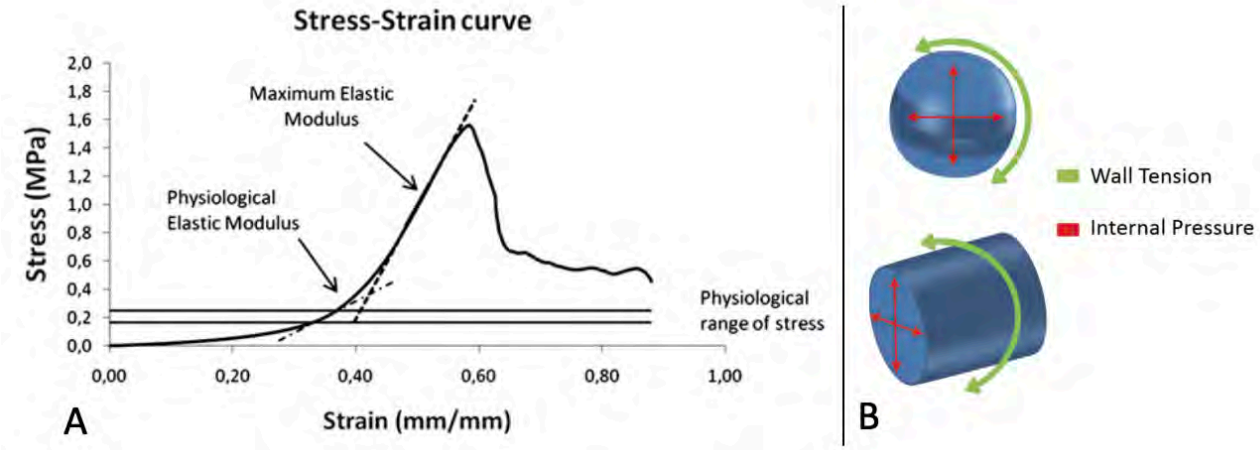


Figure 17. Application of the Laplace law. A: Principles of calculation of the physiological and maximum elastic modulus, see the difference of slop in maximum elastic modulus and physiological elastic modulus, the physiological pressure applied in the arterial wall is 80-120 mmHg (Duprey et al., 2010). B: Representation of theoretical concept of Laplace's law represents the cylindrical vessel and spherical vessel (Massaglia & Quaglio, 2018).

Table 6. Elasticity of aorta in relation to age in MPa, (Thubrikar, 2007).

Artery	Young (11–20 years)	Old (36–52 years)
Thoracic aorta	0.6	2.0
Abdominal aorta	1.0	1.2
Iliac artery	2.9	0.7
Femoral artery	3.1	1.4
Carotid artery	0.8	1.1

The loss of energy test, commonly and historically applied to solid materials, measures the energy absorbed by a material prior to fracture, serving as a critical indicator of its toughness and resistance to mechanical failure (Z. Wang & Xian, 2023). For the elastic materials, deformation occurs in response to an applied force, and they are capable of returning to their original shape upon removal of the load, reflecting their characteristic reversible mechanical behavior.

For the artery, the presence of elastin and collagen within the vascular wall imparts elasticity, allowing it to deform in response to pressure and return to its original shape upon unloading. In the normal artery, approximately 20% of mechanical energy is dissipated during each loading-unloading cycle (systole and diastole phase) due to viscoelastic nature of arterial walls, while up to 80% is temporarily stored as elastic energy within the vessel wall. This stored energy is subsequently released, facilitating arterial recoil and contributing to blood propulsion during diastole—a phenomenon known as the Windkessel effect (Camasão & Mantovani, 2021; Cocciolone et al., 2018; Mishani et al., 2021).

Greater energy loss reflects reduced efficiency in arterial function, with more energy dissipated into the aortic wall and less stored elastically. Over time, this may contribute to aortic wall remodeling and eventual failure. The energy loss parameter considers the entire stress–strain behavior throughout the entire loading–unloading cycle, providing a more consistent and reliable measure of mechanical performance (Chung et al., 2014).

For grafts or tissues used to replace the aorta, assessing energy loss is important to estimate the amount of elastic energy stored, which plays a crucial role in supporting diastolic blood flow particularly in the proximal aorta. In aortic surgery, the use of replacement materials with biomechanical properties closely resembling those of the native aorta may reduce the risk of postoperative complications such as cardiac hypertrophy and hypertension , the equation of energy loss is (Badran et al., 2015; Chung et al., 2014; Girerd et al., 1991):

$$\text{Energy loss (EL)} = A_l - A_u \quad (13)$$

Where:

- **EL** = energy loss
- $\mathbf{A_l}$ = area under the loading curve
- $\mathbf{A_u}$ = area under the unloading curve

This means:

Calculate the total energy during stretching.

Calculate the total energy recovered when relaxing.

Subtract the recovered energy from the total energy put in.

The difference is the energy lost due to heat, internal friction, or viscoelastic behavior in the tissue (Camasão & Mantovani, 2021; Cocciolone et al., 2018; Mishani et al., 2021), see **Figure 18**.

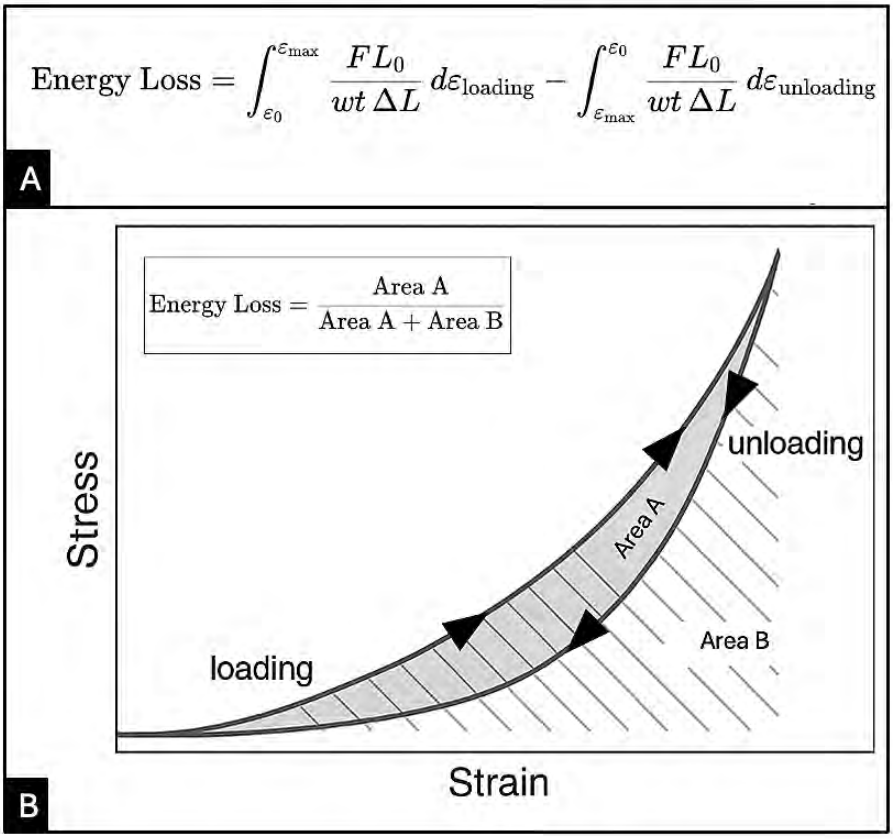


Figure 18. Calculation of energy loss from the stress–strain relationship: (A) Mathematical formulation used to calculate the biomechanical energy loss (hysteresis loss) during cyclic loading and unloading; where F : Applied force, L_0 : Initial length of the specimen, w : Width of the specimen, t : Thickness of the specimen, ΔL : Elongation under load , ε : Strain, ε_0 : Initial strain, ε max : Maximum applied strain, ε loading: Strain during loading, ε unloading : Strain during unloading phases. (B) Schematic representation of the stress–strain relationship illustrating the areas corresponding to absorbed and released energy. The shaded region between the loading and unloading curves represents the hysteresis loop with specified percentage, which quantifies the behavior of the biomaterial and indicates the mechanical energy dissipated per deformation cycle.

To summarize the properties of aortic tissue, we can say the composition and structure of the aortic wall can vary because of physiological changes caused by growth and remodeling. This varity og behavior influenced by complex mechanical and physiological factors depending to directions of the aortic tissue. The reason of this phenomenon is the repetitive application of stress on the cardiovascular system in a circular manner.

In general, when the healthy aorta is subjected to circumferential force stimulation, it results in an increase in the distribution of elastic fibers and collagen fibers along the circumferential direction. This, in turn, leads to higher stiffness of the tissue in the circumferential direction compared to the longitudinal direction (Di Giuseppe et al., 2019). The stress-strain curves of aortic tissue are typically nonlinear. This phenomenon occurs as a result of the progressive dissociation of collagen fibers under the influence of external loading (Liu et al., 2019).

3. Biomechanical and Structural Alterations in Aortic Aneurysms

Aortic aneurysm instances, particularly abdominal aortic aneurysm (AAA), are defined by the breakdown of proteins in ECM, death of SMCs in the blood vessels, infiltration of immune cells into the outer layer of the blood vessel and increasing oxidative stress in the wall of the aorta. High-throughput microarray-based genome-wide analysis have shown that AAAs exhibit a more significant adaptive immune response compared to occlusive atherothrombotic aortic disease.

Aneurysms are distinguished by a greater degree of damage to the middle layer of the blood vessel (medial injury) compared to the inner layer (intimal atheroma). This damage is mostly induced by proteolysis (breakdown of proteins) and oxidative processes (Biros et al., 2015; Sakalihasan et al., 2018).

There are several factors that induced aneurysm, that results from the cumulative effects of endothelial injury, cellular degeneration, chronic inflammation, sustained biomechanical stress, and genetic susceptibility. The interaction between intrinsic factors and extrinsic influences with the recruitment of inflammatory and immune effector cells, lead to aortic wall degeneration (Schahab et al., 2025), see **Figure 19**.

The ECM of the aortic wall consists of elastin and collagen, which provide structural support and enable the aorta to withstand severe hemodynamic loads. Degradation of ECM is the primary process responsible for the development and progression of aortic aneurysms (Michel, 2001; Sakalihasan et al., 2018), see **Figure 20**.

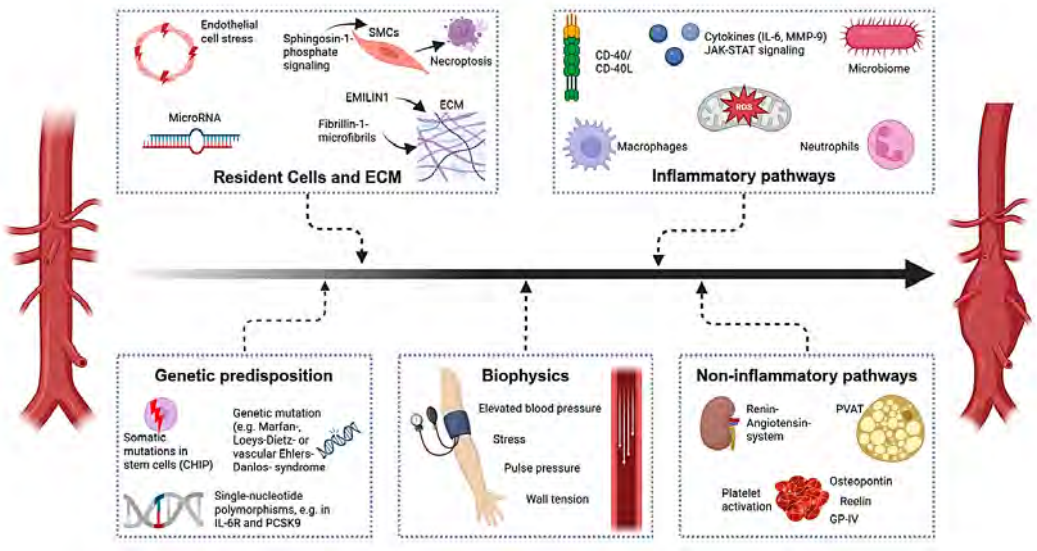


Figure 19. Overview of intrinsic and extrinsic risk factors involved in aortic aneurysm formation, including inflammatory pathways, extracellular matrix degradation, structural protein alterations, smooth muscle cell dysfunction, perivascular adipose tissue activity, and genetic factors, collectively leading to progressive weakening of the aortic wall *(Schahab et al., 2025)*.

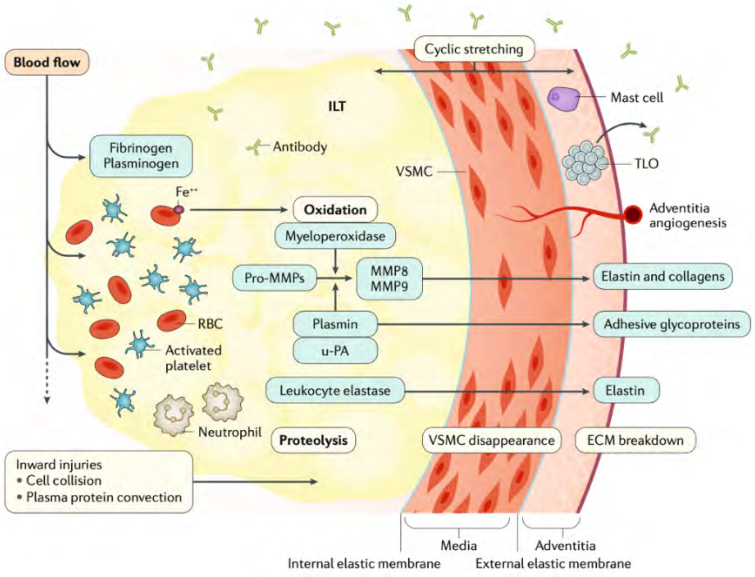


Figure 20. Speculative model of AAA progression. In aortic aneurysm progression, interactions between blood components and the aortic wall promote intraluminal thrombus formation with proteolytic and oxidative activity. This process activates plasmin and MMPs, degrades extracellular matrix, induces smooth muscle cell apoptosis, and amplifies inflammation through neutrophil and mast cell activation, leading to progressive wall weakening *(Sakalihasan et al., 2018)*.

4. Alternative Techniques for Aortic Tissue Reconstruction

The vascular grafts are conduits employed to replace diseased arterial segments or to bypass obstructed vessels in order to restore adequate distal perfusion. These grafts may be classified into five main categories (Ravi & Chaikof, 2010):

4.1. Synthetic graft

Synthetic graft is a non-degradable polymer graft, that is highly demanding because of its cost-effective manufacturing, off-the-shelf availability, ease and flexibility of tailoring, and long period of permeability. There are two main synthetic grafts used in vascular surgery specialty:

4.1.1. Expanded Polytetrafluoroethylene (e-PTFE) grafts, that have been categorized into two groups based on their porosity levels, namely low porosity (<30 μm internodal distance) and high porosity (>45 μm internodal distance). It has been observed that higher porosity allows for increased tissue ingrowth, while lower porosity results in grafts that are stiffer and less flexible, leading to reduced tissue ingrowth and endothelialization (Hytönen et al., 2019).

4.1.2. Polyethylene terephthalate (PET) or Dacron graft that presents an alternative form of synthetic non-degradable polymer conduit. Textile vascular grafts fabricated using polyethylene terephthalate fibers can be classified into two main categories: woven or knitted. Woven grafts exhibit smaller holes, resulting in reduced permeability and diminished bleeding. Conversely, knitted grafts, which are created through the interlacing of fibers, include bigger pores that facilitate enhanced tissue ingrowth and offer more compliance (Naegeli et al., 2022).

4.2. Xenogeneic tissue

ECM grafts derived from xenogeneic sources offer the advantages of readily available tissue that possesses robust mechanical properties, flexibility, and long-term durability. Vascular xenografts are obtained from many mammalian tissue sources, typically bovine or porcine in nature. The vascular xenografts currently employed in medical practice are subjected to a decellularization process, as discussed in the preceding chapter.

4.3. Cryopreserved grafts

Arterial or venous graft obtained from a donated cadaver to be transplanted into another human body to replace the infected artery or vein. One significant benefit of cryopreservation is the ability to store living vascular tissues in a structurally intact state for an indefinite period, owing to the storage at extremely low temperatures (sub-zero°C).

The techniques of cryopreservation of tissues, initially designed for the long-term storage of individual cells, face challenges due to the inherent complexity of multicellular systems. Tissues consist of numerous cell types, each with unique requirements for good preservation (Müller-Schweinitzer, 2009). The utilization of cryopreservation needs specialized storage, related planning, warming processes before utilization, and long preparation time, providing complex practical constraints on the application of these conduits (Naegeli et al., 2022).

4.4. The autologous tissues

The autologous tissues are the most common graft options using by cardiovascular surgeons. The autologous vessels demonstrate physiological properties that closely resemble those of the vasculature in need of repair, rendering them a first choice. Commonly employed options in vascular surgery encompass arteries with small diameters such as the radial artery, as well as larger vessels like the greater saphenous veins (GSV), superficial femoral veins (SFV), and internal iliac artery (Buxton & Galvin, 2013).

4.5. Tissue-engineered vascular graft (TEVG)

TEVG is a scaffold seeded with cells that can develop into functional blood vessels over time. The procedure began by cultivating confluent monolayers of fibroblasts and smooth muscle cells (SMC) for a duration of 30 days in the presence of sodium ascorbate. Subsequently, the fibroblast sheets that had merged together were physically separated from the underlying surface and then carefully wrapped around an inert mandrel, resulting in the formation of a tubular configuration. Following a period of one week of maturation, that structure underwent dehydration, resulting in the formation of an acellular inner membrane.

Multiple layers of SMC were formed in the vessel wall by wrapping an SMC sheet around the acellular inner membrane. During an 8-week maturation phase, the lumen of the tissue-engineered blood artery was subjected to periodic distension by inserting silicon tubing. Subsequently, an additional layer of fibroblasts was enveloped around the SMC layers, resulting in the formation of the adventitia. Finally, endothelial cells (ECs) were seeded into the inner surface, completing the

process. The complete process necessitated around three months. The final result was highly stiff with burst pressure greater than 2500 mmHg (Blum et al., 2022; Naegeli et al., 2022).

Reconstruction of aortic aneurysm by vascular graft is one of the most important operations in the cardiovascular surgery fields. The textile material often referred to as Dacron, which is specifically made from polyethylene terephthalate, has been the predominant choice for 70 years. Various producers utilize different types of sealing impregnation, such as gelatin or albumin, to achieve a complete absence of porosity in the graft (Wanhainen et al., 2024).

The introduction of the polyethylene terephthalate graft occurred in 1939. DuPont subsequently advanced and secured a patent for its highly recognized Dacron fiber in 1950. The initial implantation of vascular grafts constructed from Dacron occurred in 1957 by Julian and in 1958 by DeBakey (Hess, 1985; Xue & Greisler, 2003).

Dacron grafts that are now accessible for clinical use are manufactured in either woven or knitted forms. The woven grafts utilize multifilament Dacron threads arranged in an over-and-under pattern, resulting in a graft with restricted porosity and minor creep. Knitted grafts are created using a textile method where Dacron threads are looped to increase the porosity and radial distensibility. The velour technique, which involves elongating the loops of yarn on fabric surfaces, has been employed to enhance tissue integration. The crimping process is employed to enhance the flexibility, distensibility, and kink resistance of textile grafts. Prosthetic rings or coils are used on the outer surface of the grafts to provide external support and prevent kinking and potential mechanical compression (X. Wang et al., 2022; Xue & Greisler, 2003), see **Figure 21**.

The disadvantages of using a dacron graft include the loss of the natural elastomechanical properties of the aorta. This can have negative effects on the normal functioning of the aortic root complex and may present challenges in the long-term outcomes and clinical treatment of aortic replacement in medical practice (Spadaccio et al., 2016). The negative elastomechanical characteristics and the compliance mismatch between the natural aorta and the Dacron graft are believed to cause excessive stress along the suture lines, leading to the development of intimal hyperplasia, anastomotic aneurysms, or pseudoaneurysm (Baird et al., 1977; Leuprecht et al., 2002).

Another disadvantage is the lack of ability to resist infections, making it unsuitable for use in infected environments such as mycotic aortic aneurysms (MAA) or as a replacement for infected grafts (Wanhainen et al., 2024).

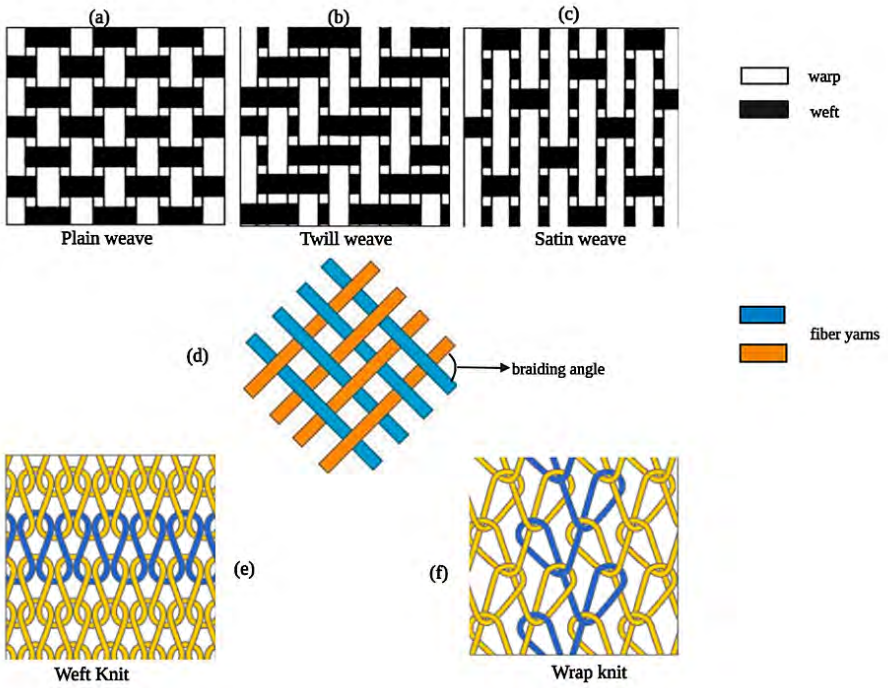


Figure 21. Design patterns of weaving/braiding/knitting. There are three varieties of weaving designs, denoted as (a–c). The regular structure of braiding is represented by (d), while (e,f) represent two forms of knitting designs. (d) The braiding has a consistent and organized structure, while (e,f) represent two distinct patterns used in knitting *(X. Wang et al., 2022)*.

Primary infected aortic aneurysms or MAA is a life-threatening disease (Sörelius et al., 2014), caused by septic emboli to the vasa vasorum resulting from homogenous spread during bacteremia or direct extension of an adjacent infection. These septic emboli lead to infectious degeneration of the aortic wall which subsequently results in the development of aneurysms. Septic emboli of the vasa vasorum are the most common cause of MAA. Osler et al. were the first to report mycotic aortic aneurysms, which occurred due to malignant endocarditis described as (mushroom-like appearance), with the misnomer term of "mycotic aortic aneurysm" (Osler, 1885).

However, this might be misleading because the majority of MAA are caused by common microorganisms including bacteria such as Gram-positive bacteria and Gram-negative bacteria, not only fungi (Wanhainen et al., 2019). Bacterial infection that causes MAA are either Gram-positive (staphylococcal, enterococcus species, Streptococcus pneumoniae, and Clostridium species) or Gram-negative bacilli (Salmonella, Coxiella burnetti, and mycobacterium). The diagnosis is based on a combination of clinical presentation, laboratory results, and imaging findings such as computed tomography, see

(Sörelius et al., 2014).

Early suspicion and detection of MAA is important. Treatment with intravenous empirical antibiotics against Staphylococcus aureus and Gram-negative rods should be initiated as soon as cultures have been obtained and should be continued in those who have negative cultures (Wanhainen et al., 2019).

Open surgical repair (OSR) is widely considered the gold standard for the treatment of MAA according to European guidelines (Wanhainen et al., 2019). Surgical treatment for aneurysms includes resection of the aneurysm and infected tissue and intensive local debridement. Revascularizations using extra-anatomical bypass or in situ repair techniques (anatomical bypass, endovascular technique) is recommended. The continuation of intravenous antibiotics and aneurysm wall culture are also recommended. In situ conduits can be obtained from autologous veins, cryopreserved arteries, or bovine pericardium. If these are not accessible, prosthetic grafts can be considered depending on the surgeon's preference.

Endovascular techniques are a less invasive alternative to traditional OSR of MAA, allowing the treatment of fragile patients or patients with significant comorbidities. In emergencies, endovascular techniques may serve as a bridge to definitive surgery later. In patients who cannot tolerate OSR,

endovascular techniques may serve as a permanent or palliative treatment (SIDAWY & BRUCE A, 2022; Sörelius et al., 2014; Wanhainen et al., 2019). There are serious concerns about endovascular techniques as we leave contaminated tissue in place, including the aneurysm itself, and the potential of recurrent and persistent infection, see **Table *8***.

There is no preference and superiority of different techniques in ORS. However, in the case of aortic graft infection, autologous vein replacement (Neo-aorto-iliac system) is recommended as a first choice, followed by antibiotic-treated prosthetic grafts (impregnated or soaked with vancomycin antibiotic) (SIDAWY & BRUCE A, 2022)Sidawy & Bruce, 2022).

Table 7. Diagnostic criteria of the mycotic aortic aneurysm by Sörelius et al.(Sörelius et al., 2014; Wanhainen et al., 2019)

The diagnosis is based on a combination:	
Clinical presentation	Pain, Fever, Sepsis, Concomitant infection, cardiovascular disease and/or Immunosuppressed state.
Laboratory results	Elevation of inflammatory markers including C-reactive protein, erythrocyte sedimentation rate, and white blood cells, Positive blood culture, and/or Positive aneurysm wall culture.
Radiological findings	Computed tomography (CT) or MRI that show rapid expansion of aneurysm, Saccular aneurysm, multi-lobular aneurysms, Eccentric aneurysms, Periaortic gas, and/or Periaortic soft tissue mass.

Table 8. Operation technique of MAA

Open surgical technique		
Extra-anatomical bypass	Autologous vein Cryopreserved arteries Bovine pericardium Prosthetic grafts	
In situ reconstruction	Autologous vein	Femoral Great saphenous vein Neo-aorto-iliac system
	Cryopreserved arteries	
	Bovine pericardium	
	Prosthetic grafts	PTFE Dacron Antibiotic-soaked Dacron grafts Silver Graft protheses Antibiotic impregnated graft
Endovascular technique		
Definitive		Antibiotic-soaked Dacron protheses Non- Antibiotic-soaked Dacron protheses
Bridging		+ suppressive antibiotics

5. Biomechanical characteristics of blood vessels using Magnetic resonance imaging (MRI)

Bloch and Purcell were awarded the Nobel Prize in physics in 1952 for their experimental descriptions of the nuclear magnetic resonance phenomena. Since then, the method has rapidly advanced, allowing the development of clinical applications. In 1980, the first clinical magnetic resonance image was created in Nottingham and Aberdeen. Currently, MRI is widely available and potent clinical technique (Grover et al., 2015).

The cine MRI of cardiovascular magnetic resonance (CMR) acquisitions is unquestionably the gold standard for assessing the anatomy, physiology, and function of the cardiovascular system. The cine MRI, also known as cine sequences, is obtained by taking a series of multiple and rapidly recorded images of the area of interest for a specific amount of time within a single slice. The images are then reconstructed and shown in a dynamic cinematic format. This technique allows analyzing the interested cross-sectional aortic area in different segments at a certain time. Data obtained from CMR provides important clinical information such as the risk of aortic rupture, assessment of aortic size over time, estimation of aortic stiffness indices, quantifying mechanical and genetic disorders, and estimation of local aortic distensibility (Bohbot et al., 2020; Herment et al., 2011).

MRI uses nuclei of hydrogen atoms that have a magnetic field (protons). In the human body, protons are commonly orientated in several directions. When the human body enters a strong magnetic field such as an MRI machine, protons transform from a scattered orientation to become aligned within the magnetic field. In this state, applying a radio frequency (RF) pulse causes the protons to deflect by 90°. When the RF pulse is applied, a loud sound characteristic of an MRI scan is produced. The energy of the RF pulse is subsequently stored by the deflected protons. When the RF pulse is interrupted, the deflected protons return to their original orientation while emitting the stored energy. The period required for these protons to return to their original orientation varies depending on the type of tissue in which the protons are linked (muscle, blood, fat, bone, etc.). This energy is received as a signal by a receiver and an image is created by evaluating this signal as well as the time duration of the return. When the patient exits the MRI machine, the protons return to their normal previous state, reoriented in various ways throughout the body, see **Figure 22** (Kagawa et al., 2017; Kramer et al., 2020; Wymer et al., 2020).

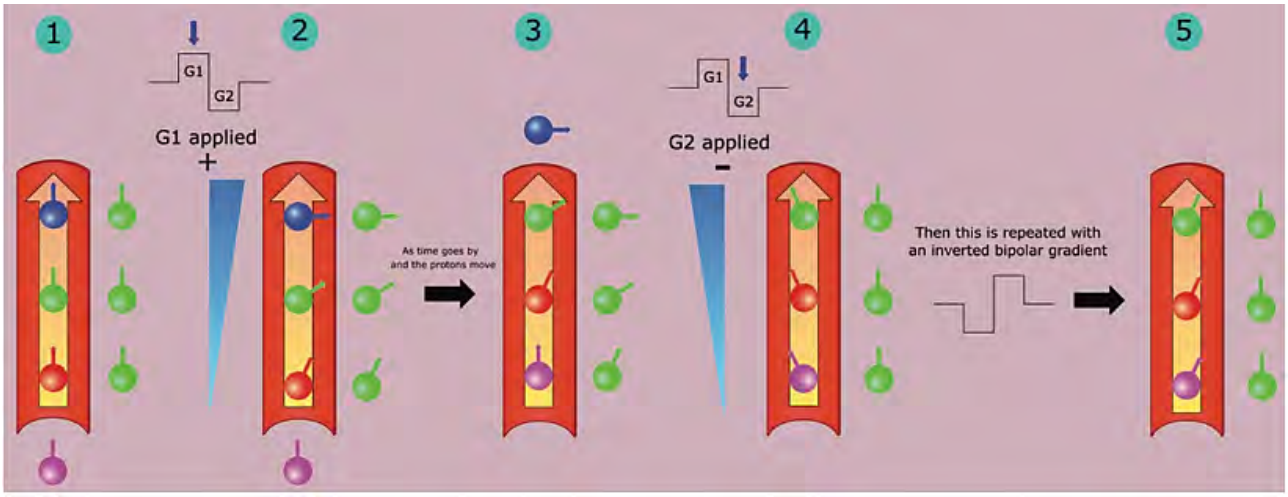


Figure 22. Application of bipolar gradients, (Wymer et al., 2020).

Different RF sequences are used to image different parts of the body. The two most common types of sequences used are known as the spin echo sequence (anatomic sequences) and the gradient echo sequence (cine MRI sequences). In an echo sequence, there are two parameters: the echo time (ET) and the repetition time (RT).

a. The spin echo sequence consists of a 90° RF pulse, followed by a 180° RF pulse of rephasing at half ET and signal readout at ET. This sequence is repeated at every interval of RT. That permits the momentary elimination of the parasitic phase shift of instrumental origin that attenuate the signal. This sequence provides anatomical images of high-quality of aorta; however, the acquisition time is exorbitant.

b. The gradient echo (GE) sequences can be used to analyze the aorta dynamically. These kinetic sequences have an excellent spatial and temporal resolution. That allows accurate determination of the aortic surface area during the cardiac cycle. It is used to determine the compliance and distensibility of the aorta. The gradient echo sequence flip angle is less than 90 degrees. This angel degree reduces magnetization. The absence of a 180° rephasing RF pulse reduces the RT between pulses. Therefore, RT and ET can be obtained in a significantly shorter time. This allows for a dynamic examination by significantly reducing the time required to acquire this type of sequence. As there is no compensation for the systematic "parasitic" phase shift caused by the 180° pulse, they are susceptible to artifacts. weighting is also challenging in this technique.

In contrast to other imaging modalities, cardio-vascular MRI has many advantages. These advantages include the absence of ionizing radiation, high spatial resolution and very high temporal resolution, and the capability to characterize tissue with clear soft-tissue contrast. It has also the ability to evaluate qualitative and quantitative blood motion and surrounding tissue movements with different acquisitions such as phase-contrast (PC), and balanced steady-state free precession (bSSFP) (Herment et al., 2011; Li et al., 2011; Lotz et al., 2002).

MRI is a proven technique for determining blood velocities and flows. The principle of phase contrast acquisitions is based on the dephasing of mobile spins subjected to a bipolar gradient. The phase shift of the mobile spins is proportional to their speed and to the intensity of the gradient for a bipolar gradient of given intensity, orientation, and duration. Phase contrast acquisition includes sequences without and with flow encoding, from which magnitude (anatomical aspect) and phase (quantitative aspect, which is a mapping of velocities in a selected direction) images are obtained. To prevent the aliasing phenomenon, the preceding selection of an appropriate encoding speed (maximum speed limit) is essential.

The maximal encoding speed for the normal aorta is typically from 100-200 cm/s. In the pathological aorta, such as in cases of aortic stenosis or coarctation, the velocities may exceed 200–400 cm/s. In aortic aneurism the velocities is about 100cm/s (Catapano et al., 2020). Aortic blood flow velocity decreases progressively from the proximal to the distal segments of the aorta. The mean blood flow velocity over the cardiac cycle is highest in the ascending aorta, ranging approximately from 60 to 80 cm/s, corresponding to about 40–50% of peak systolic velocity. It decreases to approximately 40–60 cm/s in the aortic arch and descending thoracic aorta, and further declines to about 20–40 cm/s in the abdominal aorta (Garcia et al., 2018).

Magnetic moments or spins moving along a magnetic field gradient experience a shift in rotational phase in comparison to stationary spins. In the case of linearized field gradients, the amount of this phase shift is proportional to the velocity at which the moving spin is occurring. With the assistance of a bipolar gradient, phase shifts caused by stationary tissue can be compensated. The elimination of phase shifts caused by other sequence factors can be accomplished by repeating the measurement with an inverted bipolar gradient. After subtracting data sets from one another, the phase difference that remains after subtraction of these two data sets is utilized for the voxelwise calculation of velocities.

The values of phase shifts are measured in degrees, and they should fall within a range that is between 0 and 180 degrees. Before starting the measurement of velocity, the physician or MRI technician should adjust the sequence to correspond to the peak velocity that is anticipated in the vessel of interest. The amplitudes of the flow-sensitizing gradients are calculated when this threshold value is adjusted as the encoding velocity. This ensures that the peak velocity corresponds to a phase shift of 180 degrees. The Velocity Encoding (VENC) parameters should be specified before performing PC-MRI. VENC, measured in centimeters per second, is selected to include the maximum velocities expected to be encountered within the vessel of interest (Lotz et al., 2002), see **Figure 23**.

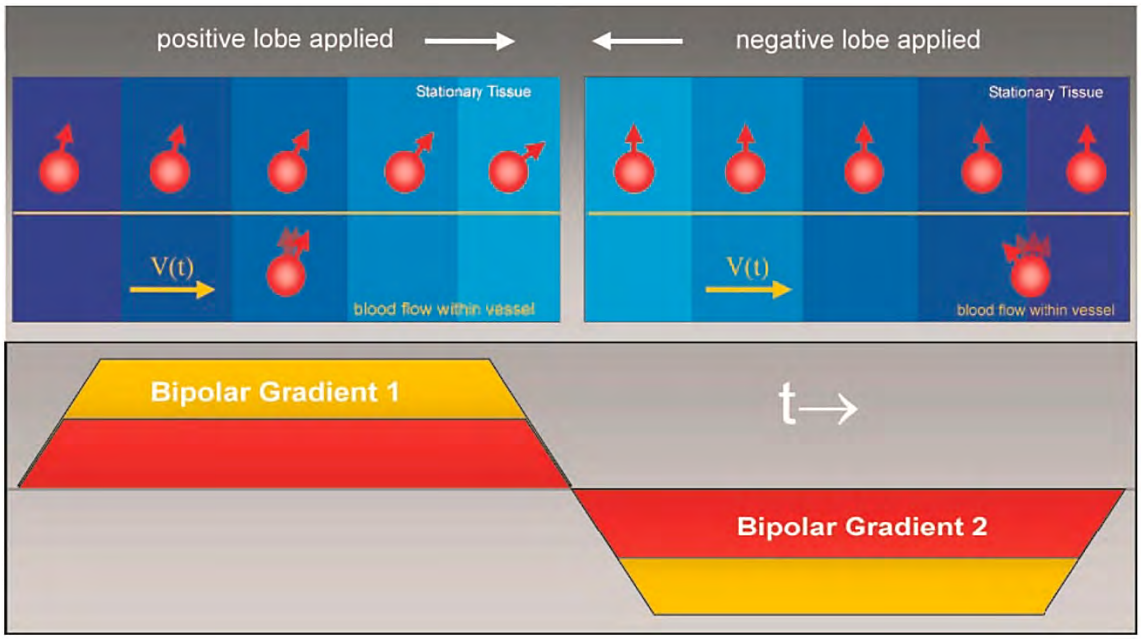


Figure 23. Two acquisitions are illustrated, each with all parameters held constant except for the flow-sensitizing bipolar gradients. The data of the two acquisitions are subtracted. The effective flow encoding is achieved using the difference in the bipolar gradients of the two acquisitions. This technique eliminates all phase shifts induced by imaging gradients. t: time, v: velocity, (Lotz et al., 2002).

Chapter 3: The objective of study

Strain, stress, distensibility, compliance, and elasticity are major properties to evaluate aortic graft including both biological and synthetic. Changes in those properties are major causes of cardiovascular mortality. The aortic elastic properties could be decreased due to aging, hypertension, atherosclerosis, chronic kidney disease, diabetes, or replacement of aortic segment by open or endovascular technique.

Decrease in aortic elasticity leads to aortic stiffness and decreased compliance (Millasseau et al., 2005; Redheuil et al., 2010; Salvi, 2017). Under these conditions, the amount of stroke volume that is held by the aorta during systolic ejection decreases. As a result, the heart compensates to overcome the backpressure, which may lead to cardiomegaly or myocardial infarction. Since this physiologic phenomenon may occur following aortic replacement surgery, it is essential to utilize an aortic graft that has biomechanical properties that are comparable to those of the healthy aorta. The bovine pericardial patch is biological xenograft which is harvested from animals and suitable to use in human begin.

Replacing the native aorta with a rigid material can alter vascular pressure and flow patterns, potentially exacerbating peripheral vascular disease (Tremblay et al., 2009). These hemodynamic changes can also affect aortic valve and left ventricular function, leading to a higher cardiac workload and increased oxygen demand, especially during physical activity (Kim et al., 1995; Salvi, 2017).

Pressure mismatch between the native aorta and a prosthetic graft is thought to promote the formation of false aneurysms (Mehigan et al., 1985) and intimal hyperplasia (Ballyk et al., 1998). This stress concentration at the junction between the native tissue and the graft can lead to structural remodeling, driven by the altered mechanical environment created by the pressure mismatch (Ballyk et al., 1998; Surovtsova, 2005).

Energy loss reflects reduced efficiency of the arterial wall in recovering stored mechanical energy, indicating that more energy is dissipated within the tissue during each cycle. In arterial mechanics, a higher EDR denotes increased internal friction and reduced elastic efficiency, indicating altered wall behavior due to structural remodeling—such as elevated collagen content, elastin fragmentation, or smooth muscle disorganization. Conversely, a lower EDR reflects more efficient elastic recoil and a structurally intact, healthier arterial wall (Laurent & Boutouyrie, 2007; O′Rourke & Safar, 2005; Redheuil et al., 2010).

Evaluating the EDR in BPPs from different suppliers is essential for estimating elastic energy storage and guiding the development of aortic substitutes that mimic aortic properties. This property plays a pivotal role in diastolic flow support, particularly within the proximal aortic segment. To our knowledge, this parameter has not been investigated in previous studies.

In the market, many companies produce BPPs for medical uses, using different methods of decellularization to stabilize the patches (Gilbert et al., 2006; Iop et al., 2018) . This different methods for pre-commercial treatment of BPP could change patches' histological and biomechanical properties. The presence of cells in BPP could elicit a theoretical risk of immunological response inside the extracellular matrix. This response can vary depending on donor source, recipient tissue type, and host immune activity (Yi et al., 2017) .However, these sterilization techniques induce variant degrees of damage to ECM components of the tissues, which could change their biomechanical, physiological, and cell attachment characteristics (Fidalgo et al., 2018). The quality and efficacity of decellularization could be examined macroscopically (size, aspect, color, and thickness) and microscopically (presence of elastic fibers, high density of collagen fibers, and absence of nuclei cells).

The ideal material for aortic replacement should possess the capacity to absorb and buffer pulsatile mechanical energy without inducing structural damage, while exhibiting limited energy dissipation to preserve efficient distal blood flow. Additionally, it should maintain an intact microscopic architecture and be free of viable cellular components.

Our hypothesis is that chemically modified CMBPT does not replicate the native biomechanical behavior of the human abdominal aorta. Furthermore, the BPPs obtained from different suppliers are expected to demonstrate variability in their biomechanical properties and may exhibit differences in structural integrity at the microscopic level.

The primary objective of this study is to understand the behavior of the CMBPT parameters in vitro using MRI. Then compare the biomechanical properties of various BPPs using a uniaxial tensile testing system. Failure testing was performed to determine the PEM, MPEM, and MEM. In addition, low-cycle fatigue testing was conducted to assess the EDR, which reflects the biomechanical energy input that is lost during a single loading–unloading cardiac cycle,

The secondary objective is to quantify intra-sample and inter-sample variability in order to evaluate the consistency of the biomechanical performance among different BPPs. The to evaluate the strain and distensibility for CMBPT by using MRI with different sequences to understand the properties of

tube under physiological condition. Last purpose is to evaluate the BPPs from different supplier under microscopy with different stains. This method will assist clinicians and scientists in accurately determining the biomechanical properties of both normal and pathological tissue

These objectives aim to provide a comprehensive understanding of the properties of BPPs from several perspectives, including radiological, biomechanical, and histological analyses, thereby supporting clinicians, surgeons, and biomedical engineers in evaluating their structural and functional performance.

Chapter 4: The Materials and Methods

1. Radiological aspect

In the initial part of this study, we developed an alternative in vitro method for evaluating the structural parameters of CMBPTs using MRI. This protocol was designed and complement before methodologies used for biomechanical studies by using uniaxial tensile test to evaluate the radiological aspect.

In the subsequent phase, biomechanical testing was conducted to assess the tensile and elastic properties of different BPPs preserved in glutaraldehyde, allowing for a comparative analysis of their mechanical behavior under multiple stress.

For the material and method for evaluating the structural parameters of CMBPTs using MRI. Experiments were conducted using a 3 Tesla Prisma Siemens MRI (Magnetom Prisma; Siemens Healthcare GmbH, Germany). With the assistance of an *ISMATEC © MCP-Z pump* connected to *ISMATEC © MI0023* pump head, see
Figure *24* (A). We were able to set a continuous constant flow with a flow rate of 7020 ml/min. The internal and external ports of the pump head had a diameter of 6mm. The flow was progressively increased using silicone tubes with luminal diameter of 6 mm, 10 mm, and 15 mm respectively, as shown in
Figure *24* (C).

The 3D printed connectors (with dimensions of 20 × 12 × 118 mm) were attached to the CMBPT inflow. For the return flow, we used 3D printed connector to create outflow resistance simulating arterial resistance in human blood circulation and to maintain diastolic volume. The outflow 3D printed connector had 6 mm diameter at the distal part,
Figure *24* (B). The outflow poured into an open container and then is absorbed by the same pump. The CMBPTs were constructed by the author using a glutaraldehyde-preserved Edwards Lifesciences Corporation, Irvine, CA, USA), BPPs of 10 × 15 cm.

The patch was sutured around 20 mm diameter syringe by Prolene 5-0 using a running suture, then a simple continuous suture was used along the running suture to have the final shape of the tube. The dimensions of CMBPT were 20 × 130 mm. The CMBPTs then were attached to 3D printed connectors by nylon cable ties, see
Figure *25*.



Figure 24. Phantom material used in research. A: ISMATEC © MCP-Z pump with pump head ISMATEC © MI0023. B: 3D printed piece - external dimension; 20 × 12 × 118 mm for in flow, 20 × 6 × 118mm for outflow. C: silicone tube with different diameters.



Figure 25. The CMBPTs attached to 3D-printed connectors by nylon cable ties. Black arrow: nylon tie.

The *ISMATEC © MCP-Z pump* was placed outside the Faraday shield. The pump was connected to a 6 mm luminal diameter silicone tube, that gradually increased up to 15 mm. Then, the tube was connected to an inflow 3D printed connector, see
Figure *24* (B), before attaching it to the CMBPT from both sides. The outflow tube was connected to an open container. The rigid tube coming out from the open container was connected to the pump to prevent negative pressure in elastic silicone tube during pump aspiration. We used a water open circulation with a pulsatile flowrate of 75 pulses/min.

The pulsatile flow rate of the pump was 1650 ml/min, which is equivalent to the abdominal aorta flow rate (1602±549 ml/min) (Amanuma et al., 1992). We could not test descending thoracic aorta flow rate due to the limited capacity of the pulsatile pump (2632ml/min). The maximum pulsatile flow rate capacity of the pump is less than the normal descending thoracic aorta flow rate (normal descending thoracic aorta flow rate is 4094±1600 ml/min)(Amanuma et al., 1992). The experience schema and pump setup are illustrated in
Figure *26*.

Inflow 3D printed connector was designed as a conical shape, with an external dimension of 20 × 12 × 118 mm to decrease turbulence flow. Outflow 3D printed connector was designed as conical shape, with external dimension different than that of inflow connector (20 × 6 × 118 mm) to attach the distal part of CMBPT to 6 mm silicone tube. We decreased the distal diameter of the outflow connector to half the diameter of the inflow connector to create distal resistance. This resistance will help to keep the flow in the CMBPT in the diastolic phase. Without changing the distal diameter of the outflow connector, the CMBPT will collapse in the diastolic phase.

Open circulation was chosen over closed circulation, so the expansion of CMBPT is not limited by the water volume in the circuit. We found open circulation circuit method is more physiological because the human body has cells, small capillaries, high compliance venous system, and lymphatic system similar to the open circulation used in the water container
Figure 26. The central tube pressure was measured by using an arterial catheter connected to 20-gauge needle, inserted at the distal part of CMBPT.

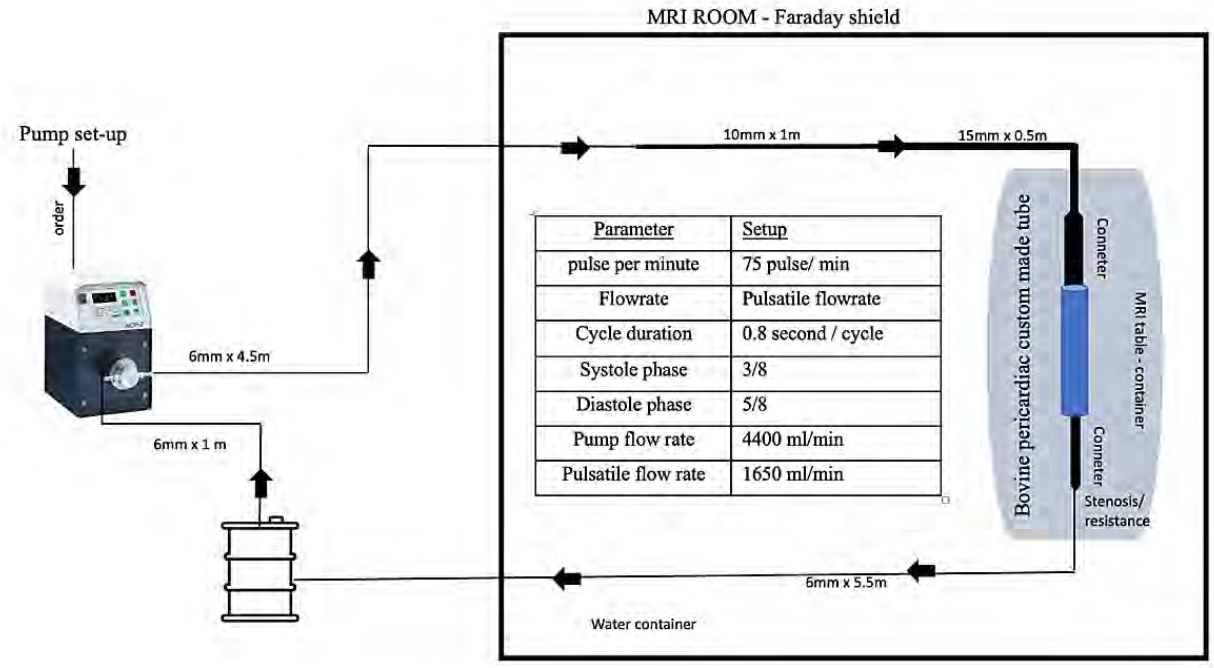


Figure 26. Illustration schema of the experience and pump parameter.

The seven CMBPT MRIs were performed at Nancy University hospital, with a 3 Tesla Prisma Siemens MRI (Magnetom Prisma; Siemens Healthcare GmbH, Germany) within the framework of the hospital protocol. The list of CMBPTs is shown in

Table *9*. The acquisitions were performed in axial, longitudinal, and transversal planes of the CMBPT model. The PC sequence and SSFP were repeated 3 times for each CMBPT, see ***Figure 26***.

The spine echo sequences (SSFP acquisitions) were performed on the phantom, allowing to obtain high-resolution anatomical sequences with programmed ECG synchronization (ECG: 800 RR) during the cardiac cycle (60 images per cycle). The acquisition settings were as follows: echo time of 1.7 msec, repetition time of 3.91 msec, acquisition matrix of 256 x 256, pixel size of 1 x 1 x 5mm, slice thickness of 5 mm. The total time of acquisition was 2.21 ms.

The gradient echo sequences (PC acquisition) with destruction of residual transverse magnetization allowed obtaining series of ultra-fast and robust images and a very good signal-to-noise ratio. We used PC acquisition because it is less susceptible to artifacts in 3 Tesla MRI. The acquisition was performed on the phantom, with programmed ECG synchronization (ECG: 800 RR) during the cardiac cycle (60 images per cycle). The acquisition settings were as follows: echo time of 3.59 msec, repetition time of 6.17 msec, flip angle of 20°, acquisition matrix of 256 x 256, pixel size of 0.8 x 0.8 x 5mm, slice thickness of 5 mm. The total time of acquisition was 6.50 ms and the encoding velocity was 100 cm/s.

Table 9. List of serial numbers and dates of Edwards Lifesciences BPP

n	Serial number	Fabrication date	Expiration date	Experimentation date
1	17250501112105021063773803	12/04/2021	11/05/2025	29/04/2022
2	17250919112109201064002437	20/09/2021	19/09/2025	17/05/2022
3	17260205112202061064214078	06/02/2022	05/02/2026	07/06/2022
4	17250831112109011063974265	01/09/2021	31/08/2025	09/06/2022
5	17250411112104121063733077	12/04/2021	11/04/2025	17/06/2022
6	17250411112104121063733073	12/04/2021	11/04/2025	01/07/2022
7	17260202112202031064214080	03/02/2022	02/02/2026	01/07/2022

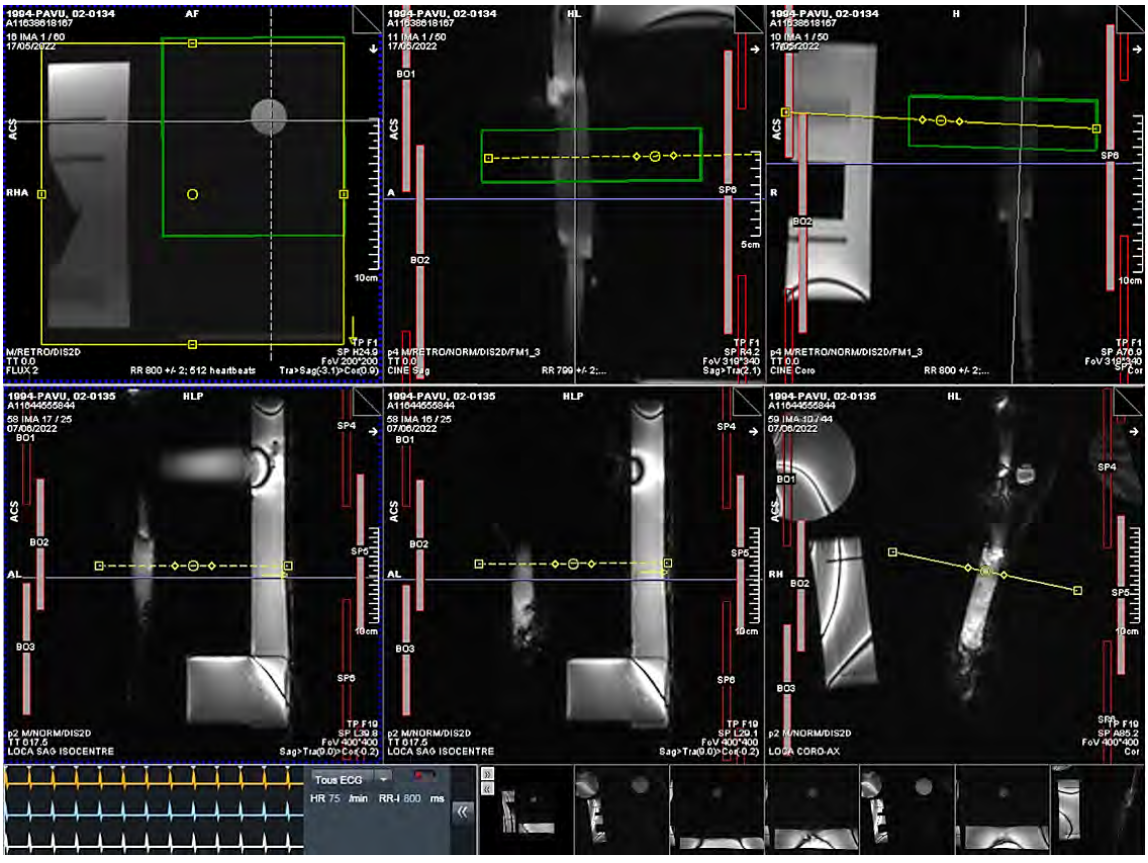


Figure 27. MRI processing interface of flux and anatomical sequences: the image shows the plane of interest, axial, coronal, and transverses axes of CMBPT from the phantom model.

For the analysis of the MRI images, the QIR-MR software (CASIS company, Quetigny, France), which allows to detect surface area, was used to calculate the velocity and distensibility. The contours of the CMBPTs were automatically detected, with the option for manual correction in both flow and anatomical sequences. The software was used to automatically identify the CMBPT contours and calculate its area during the cardiac cycle.

The PC acquisitions were used to estimate both the velocity and the CMBPT strain. An additional SSFP sequence was used to increase the accuracy of CMBPT strain estimation, see **Figure *28*.** The pressure inside the CMBPT was measured using a central line connected to the pressure transducer machine before starting the experimentation. Pressure measurements were recorded at the distal end of the CMBPT and repeated five times. The average central flow pressure was calculated to be 80 ± 7.9 mmHg. The CMBPT strain and distensibility were measured by the aortic strain equation and distensibility equation as follows:

$$Aortic\ strain\ (\%) = (As - Ad)/Ad \times 100 \quad (1)$$

$$\text{Diameter distensibility} = (Ds - Dd)/[(Ps - Pd) \times Dd] = \Delta D/(\Delta P \times Dd) \quad (4)$$

$$\text{Area distensibility} = (As - Ad)/[(Ps - Pd) \times Ad] = \Delta A/(\Delta P \times Ad) \quad (5)$$

$$\text{Area distensibility} = \Delta A/(CAP \times Ad) \quad (6)$$

$$\text{Volumetric distensibility} = [(Vs - Vd)/Vd]/\Delta P = (\Delta V/Vd)/\Delta P \quad (7)$$

Where :

- **Ds** = systolic diameter
- **Dd** = diastolic diameter
- **As** = systolic cross-sectional area
- **Ad** = diastolic cross-sectional area
- **Vs** = systolic volume
- **Vd** = diastolic volume
- **Ps** = systolic pressure
- **Pd** = diastolic pressure
- **CAP** = central arterial pressure
- **ΔD** = change in diameter (Ds − Dd)
- **ΔA** = change in cross-sectional area (As − Ad)
- **ΔV** = change in volume (Vs − Vd)
- **ΔP** = pulse pressure (Ps − Pd)

Where Ad denotes the luminal surface area during diastole and As the luminal surface area during systole. CFP refers to central flow pressure. Dd and Ds represent the vessel diameter at diastole and systole, respectively, while Pd and Ps correspond to diastolic and systolic arterial pressures.

The velocity values have been measured in the axial plane in phase-contrast images (PCp). The peak systolic velocity and mean velocity value were measured for all samples. The data obtained from the experimentation was analyzed using the Jamovi software (version 1.6.23.0, The Jamovi Project, Sydney, Australia).

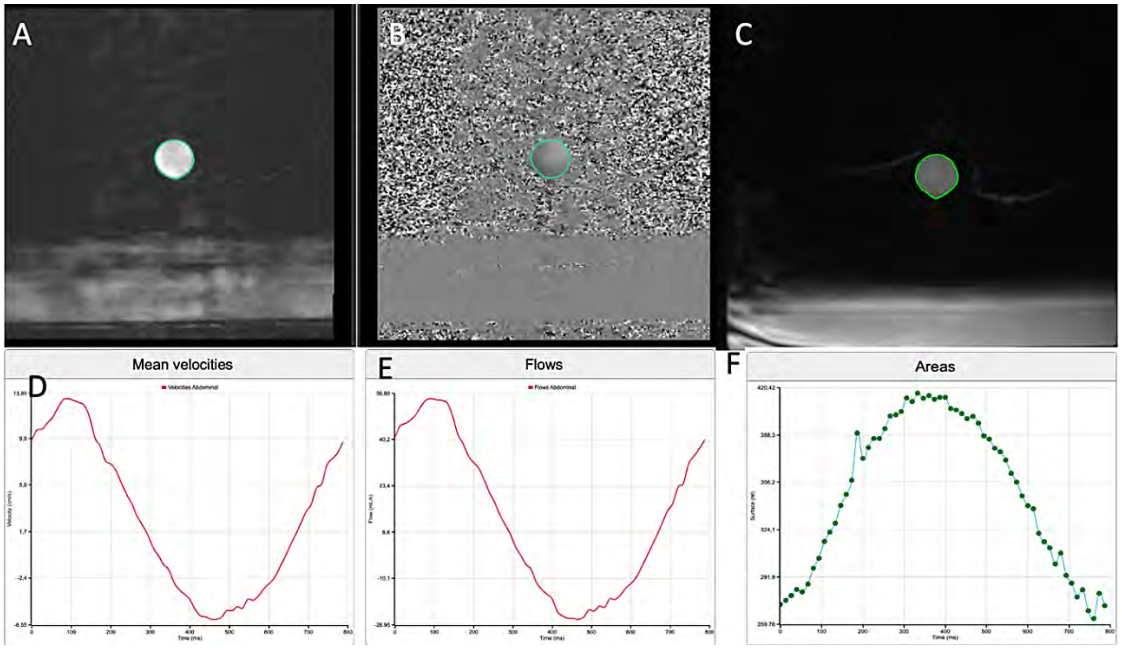


Figure 28. MRI analysis using QIR-MR software (CASIS company, Quetigny, France). (A) PCm and (B) PCp images to evaluate the aortic strain percentage and the velocity. (C) SSFP sequence to evaluate the aortic strain percentage and the distensibility. (D) Mean velocity curve in cm/s obtained from PCm. (E) Flow curve in ml/s from PCp. (F) Surface area versus time curve in mm^2 from SSFP.

2. Biomechanical aspect

For the biomechnical aspect, three BPPs suppliers based in France and one supplier from the United States agreed to participate in our research. From each supplier, ten samples of BPPs preserved in glutaraldehyde were obtained, see **Table 10**.

a. EDWARDS LIFESCIENCES®, manufactured by EDWARDS company (Edwards Lifesciences Corporation, Irvine, CA, USA), is a product made from bovine pericardium that has been cross-linked with glutaraldehyde. It undergoes chemical sterilization using ethanol and a polysorbate-80 , and is further treated with sodium hydroxide to prevent calcification. We obtained 10 patch of 10 x 15 cm (model mumber: 4700).

b. SUPPLE PERI-GUARD®, manufactured by BAXTER company (Baxter International Inc., Deerfield, IL, USA), is a product made from bovine pericardium that has been cross-linked with glutaraldehyde. It undergoes chemical sterilization using ethanol and propylene oxide, and is further treated with sodium hydroxide to prevent calcification. We obtained 10 patch of 10 x 16 cm (model mumber: PC-1016SN).

c. XENOSURE®, manufactured by LeMaitre Vascular company (LeMaitre Vascular Inc., Burlington, MA, USA), is a product made from bovine pericardium that has been cross-linked with glutaraldehyde. It undergoes chemical sterilization using the method of sterility assurance level (SAL) of 10^{-6}, indicating a probability of less than 1 in 1 million of a unit being non-sterile. We obtained 10 patch of 10 x 16 cm (model mumber: 10BV16).

d. INVENGENX®, manufactured by Tisgenx Inc company, (Tisgenx Inc., Irving, TX, USA), is a product made from bovine pericardium that has been cross-linked with glutaraldehyde. It undergoes chemical sterilization, with elixP™ tissue fixation technology that preserves the natural collagen structure and reduces antigenicity. We obtained 10 patch of 7 x 10 cm (model mumber: XM-21).

We collected the serial number, expiration date, manufacturing date, and we noted the experimentation date for each sample and thereafter conducted an examination of each. Prior to commencing the experimentation, we thoroughly examine the container and package to confirm the presence of undamaged shrink wrap and tamper-evident tape. Subsequently, we proceed to unseal the inner container in order to securely grip the edge of the patch using atraumatic forceps and extract it from the container.

We rinse surgical gloves to eliminate glove powder before coming into contact with the patch. Next, we submerge and shake a pericardial patch for at least 3 minutes in a clean container filled with 1000 ml of sterile physiologic saline (0.9% NaCI). Next, we ensure that the patch remains submerged in sterile saline until it is ready to be used for the experimentation.

Subsequently, we placed the BPP on the cutter board to verify the measurements and ensure accurate cutting during our preparation procedure, see **Figure 29 (A).** The fibrous layer on the upper side and the serous layer is in direct touch with the board. Next, cover a bovine pericardial patch with a piece of tissue briefly to soak up any residual fluid in the fibrous layer. The cutter was dipped in methylene blue ink and thereafter positioned on the lower left side of each sample, see **Figure 29(B).**

The vertical samples were sequentially numbered from 1 to 5, while the horizontal samples were sequentially numbered from 6 to 10, **Figure 29 (C).** All of the samples were divided into 10 equal pieces of using a surgical blade, **Figure 29 (D).** A 3D printer was used to design and create a 3D cutter shape that resembles a bone-shaped piece. This is shown in **Figure 30**.

In our experimentation, we cut a sample to a dog-bone shape in order to get many significant benefits. The shape of this specimen decreases the stress accumulation at the clamp by uniformly spreading tension along its length, thus assuring that failure happens in the middle of dog-bone shape. This design guarantees the uniformity of failure points, which is essential for obtaining precise data on mechanical properties, especially for samples that are small or have varying compositions. The consistent cross-sectional area in the center of dog-bone shape facilitates accurate measurement of biomechanical properties such as Young's modulus. Moreover, the dog-bone shape prevents the occurrence of clamping artifacts, such as stress concentration and shearing damage, hence improving the reliability of the test findings (Sang et al., 2018; Yoshihara & Yoshinobu, 2014).

Table 10. Details of Bovine pericardial patches participated in our study

n	Name of product	Company	Size in cm	Preservation	Reservation
1	Edwards Lifesciences	Edwards	10 x 15	Glutaraldehyde	10°C - 25°C
2	SUPPLE PERIGUARD	Baxter	10 x 16	Glutaraldehyde	20°C - 25°C
3	XENOSURE	LeMaitre	10 x 16	Glutaraldehyde	0°C - 40°C
4	INVENGENX	Tisgenx	7 x 10	Glutaraldehyde	0°C - 40°C

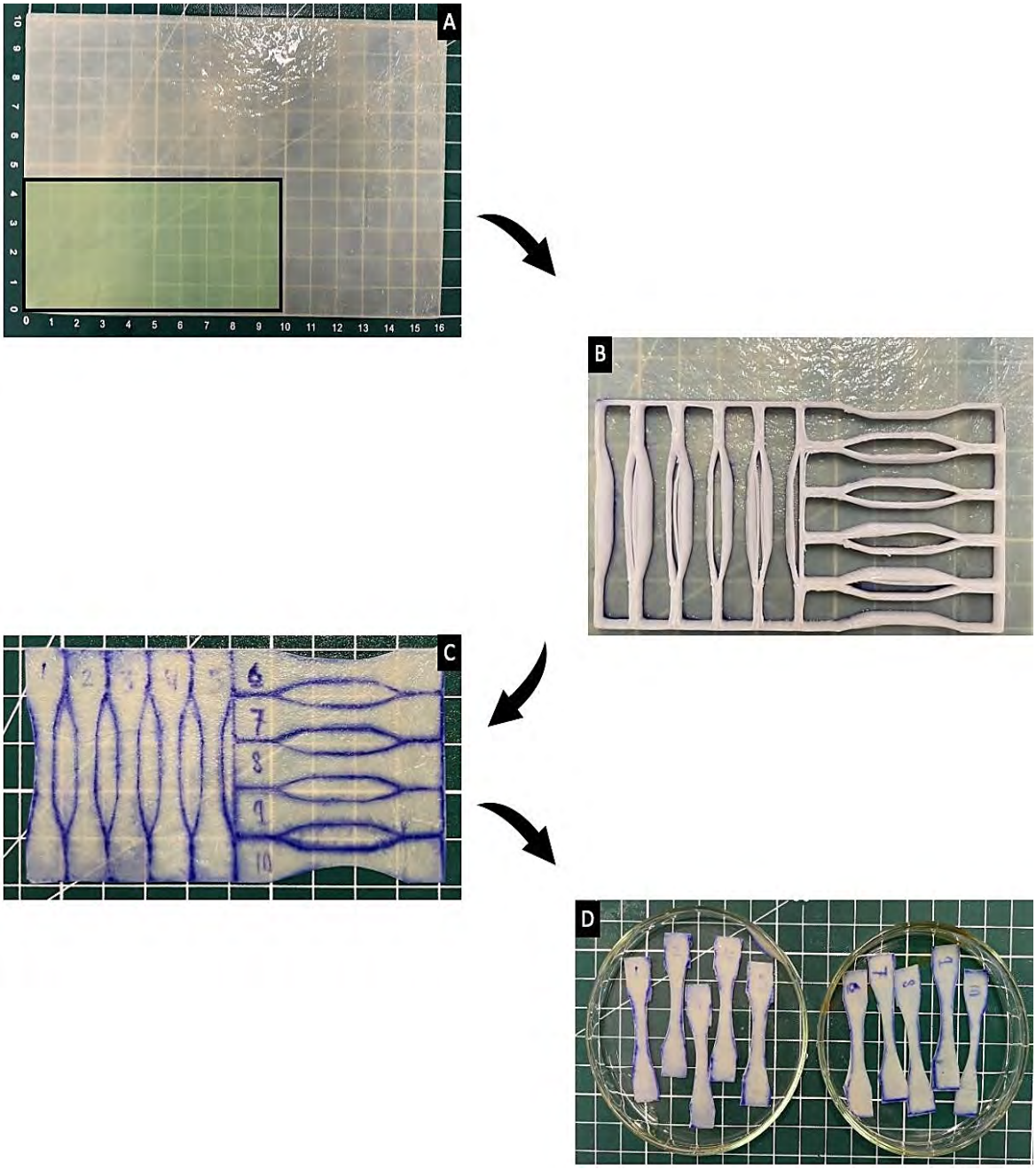


Figure 29. Preparation and sectioning of BPPs. (A) The BPP was positioned on the cutter board to verify measurements and ensure precise cutting, with the fibrous and serous layers in contact with the board. (B) The fibrous surface was gently blotted to remove residual fluid, and the cutter was marked with methylene blue and placed at the lower left corner of each sample. (C) Vertical samples were numbered 1–5 and horizontal samples 6–10. (D) Each patch was divided into ten equal segments using a surgical blade.

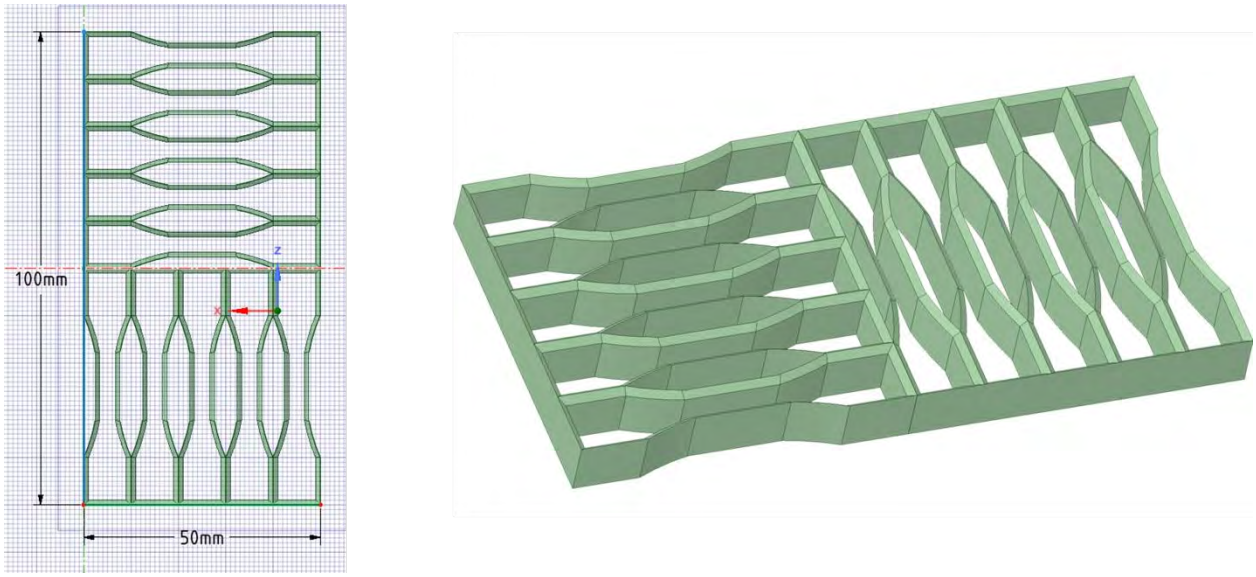


Figure 30. The 3D cutter shape that was designed and printed to have an equal bone-shaped piece.

The samples were cut for the uniaxial test into dimensions of 10 cm x 5 cm, resulting in 5 pieces for the vertical direction and 5 pieces for the horizontal direction. To provide further specificity, a total of 10 pieces were obtained from one patch sample. Each piece measures 5 cm x 1 cm, with an experimental size of 3.6 cm x 1 cm, and 1.4 cm dedicated to the portion clamped with machine clips, see
Figure *31*(A). The utilization of each piece was detailed in
Table *11*.

After the preparation of the pieces, three separate readings of each piece's thickness were taken, one on each side and one at the center of the piece
Figure *31* (B). An electronic thickness micrometer (Litematic VL-50, Mitutoyo®, Japan) was utilized throughout the course of the biomechanical studies in order to acquire accurate measurements of the sample's thickness **Figure 32**. This instrument has a resolution of 0.01 N, which contributes to its accuracy in reducing the pressure applied to the sample before the experiment. To ensure consistent values, it is important to wait between three and five seconds for each measurement record. The motor-driven plunger gives you a range of approach and retraction speeds for safe and easy operation.

Table 11. The utilization of each piece of BPPs :

Vertical pieces			Horizontal pieces		
N	Test	Laboratory	N	Test	Laboratory
1	Failure test	ICMUB	6	Failure test	ICMUB
2	Failure test	ICMUB	7	Failure test	ICMUB
3	Loss of energy	ICMUB	8	Loss of energy	ICMUB
4	Loss of energy	ICMUB	9	Loss of energy	ICMUB
5	Histology test	DCAC	10	Histology test	DCAC

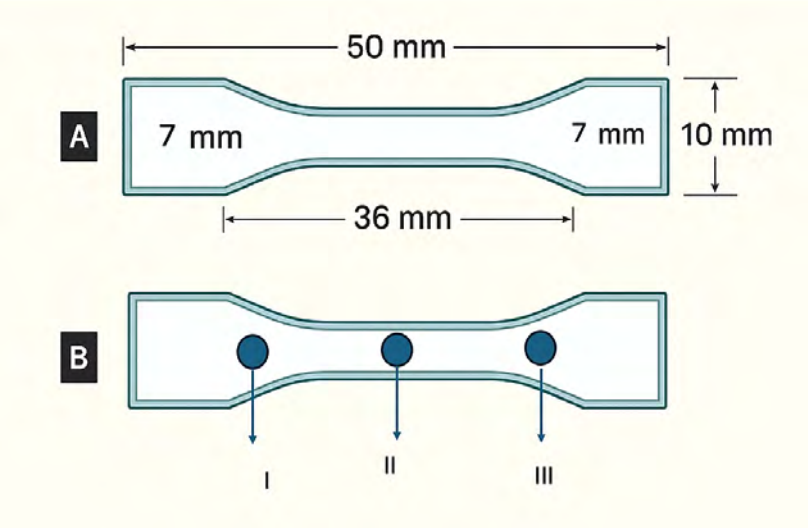


Figure 31. Preparation of samples for uniaxial tensile testing. (A) Each BPP was sectioned into dimensions of 10 × 5 cm, yielding ten specimens: five oriented in the vertical direction and five in the horizontal direction. Each specimen measured 50 × 10 mm, with an effective testing length of 36 mm and 14 mm allocated for clamping within the testing machine. (B) The thickness of each specimen was measured at three locations—both edges and the central region—to ensure accurate dimensional assessment prior to mechanical testing.

The biaxial/uniaxial tensile test machine (LM1, TA Instruments, ElectroForce® System Group, USA) was used for all the experiments. This machine has a maximum measurement capacity of 200 N and a sensitivity of 0.01 N for tension measurements. The tensile arms have a sensitivity of 0.0001 mm and a displacement range of +7 mm to -7 mm, equivalent to 14 mm of displacement. However, in our experiment, we used a reduced range from +6 mm to 6 mm, equivalent to 12 mm of displacement, to avoid reaching the machine's displacement limitation. To create conditions similar to the physiological state of the human body and minimize gravitational displacement, the bath of the biaxial/uniaxial tensile test machine was filled with 7 litres of distilled water and heated to a temperature of 37 ± 0.1 °C, see **Figure 33**.

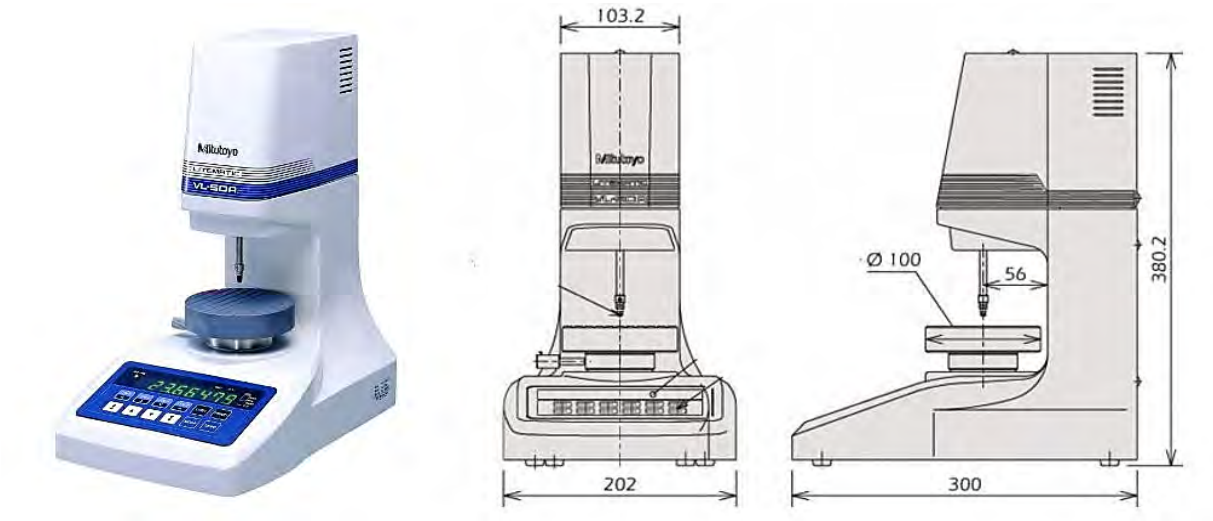


Figure 32. An electronic thickness micrometer (Litematic VL-50, Mitutoyo®, Japan).

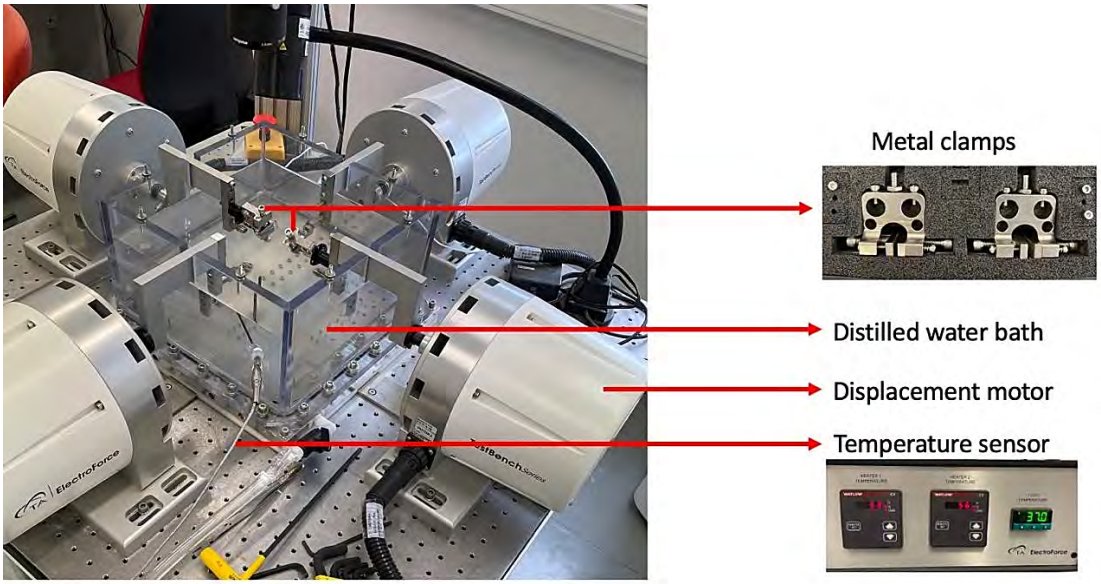


Figure 33. The biaxial/uniaxial tensile test machine (LM1, TA Instruments, ElectroForce® System Group, USA).

The pieces then were soaked with normal saline for five minutes, then installed between metal clamps of the uniaxial machine, while the serous faced to the upper side as shown in the **Figure 34**. This preparation for pieces from 1 to 4, and 6 to 8 is for biomechanical test, while the pieces 5 and 10 is preserved for histological study.

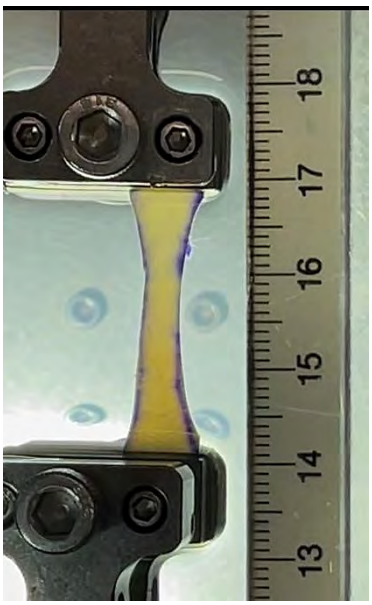


Figure 34. Installation of the bone-shaped piece between the metallic clamps of the uniaxial machine, that shows sample displacement during the uniaxial test.

3. Failure test

The uniaxial test is a mechanical testing method used to analyse the behaviour of a material under a load applied in one direction. It provides valuable information about the material's qualities, including strength, stiffness, and elasticity. In our experiment, we programmed the machine to perform ten cycles of preconditioning, applying a displacement of 0.125 mm per motor at a frequency of 1 Hz for 10 cycles, see **Figure 35**. This is equal to a displacement of 0.25 mm for two motors in the opposite direction, resulting in a total preconditioning of 0.69 %, see **Figure 35** and **Figure 36**.

From each sample, pieces numbered 1 and 2 were selected to represent the vertical orientation, while specimens numbered 6 and 7 were selected for the horizontal orientation. This selection was performed to assess potential variability in biomechanical properties between the two directional alignments.

Preconditioning in tissue testing helps to stabilize tissue properties, enabling uniform and reproducible mechanical responses. It minimizes energy dissipation (hysteresis) and the gradual distortion over time (creep), resulting in precise readings. Preconditioning, by the alignment of fibers, leads to a consistent and predictable reaction. Additionally, it sets up a baseline condition, reducing any initial flexibility for accurate property evaluation. This procedure improves the consistency and dependability of data, eliminates any bias in experimentation, and generates dependable data for the development of precise predictive models of tissue function. (Ao & International Association of Engineers, 2013; Cheng et al., 2009; Schatzmann, 1998).

This value can be calculated using the following equation. The displacement per motor multiplied by the number of motors, divided by the length of utilizable pieces in the machine, is calculated as follows:

(Displacement of each motor x number of motors)/ longer utilizable pieces in the machine
Equal to = 0.125 x 2 / 36 = 0.69 %.

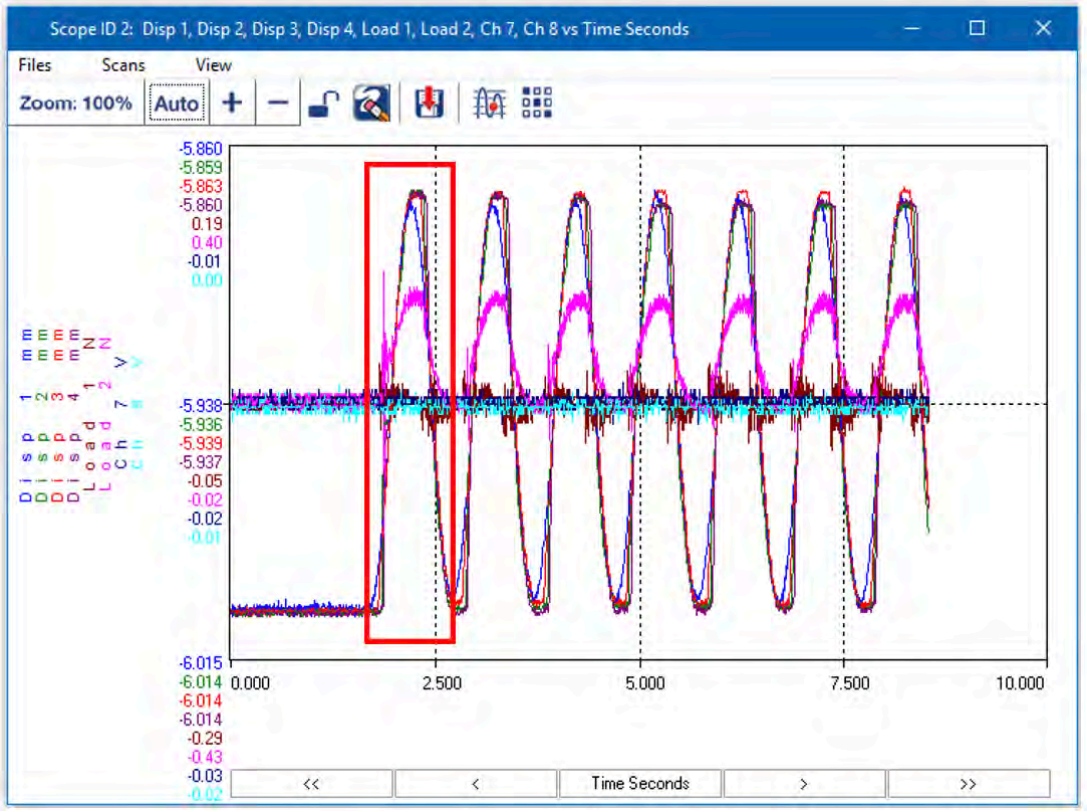


Figure 35. Precondition: in the red box there are one cycle from ten cycles of precondition.

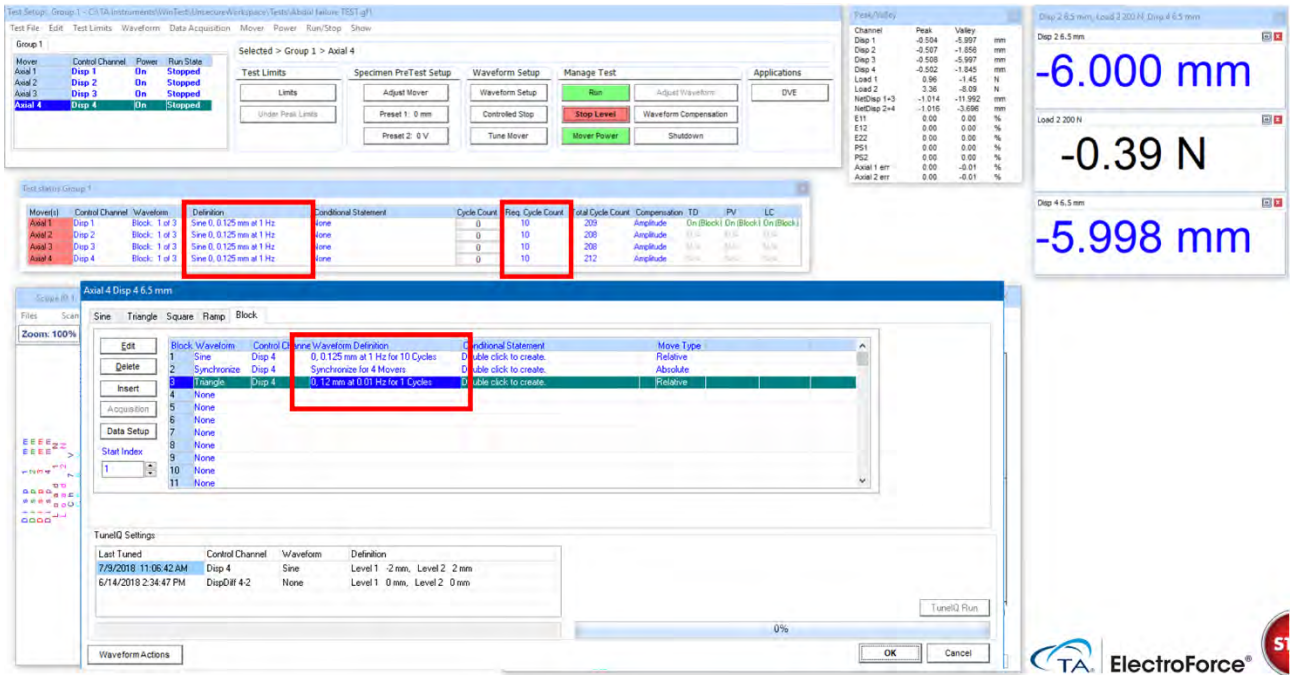


Figure 36. Precondition setup: we programmed the machine to perform ten cycles of preconditioning, applying a displacement of 0.125 mm per motor at a frequency of 1 Hz for 10 cycles.

The software utilized during the experiments was WinTest® 8 (TA Instruments, ElectroForce® System Group, Eden Prairie, MN, USA). Then, all data were analyzed to measure the elastic modulus at three different points: PEM when the pressure was between 80 and 140 mmHg, the MPEM when the pressure was 360 mmHg (Narloch & Brandstater, 1995), MEM when the pressure reached the BPPs' failure point, see **Figure 37**.

This study aims to explore the intra-variation and inter-variation of the biomechanical properties of two types of BPP, from PEM, MPEM, and MEM derived from uniaxial tensile testing, see **Figure 38**.



Figure 37. BPP stretched until rupture during horizontal uniaxial test.

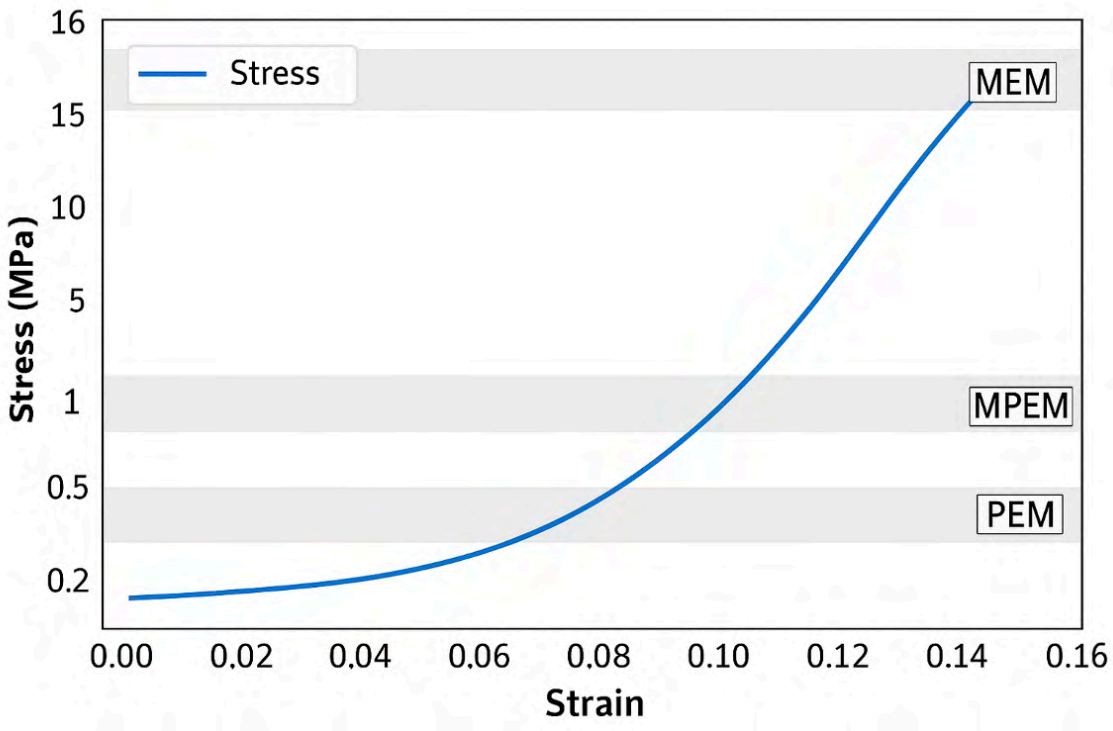


Figure 38. Stress–strain curve illustrating the three defined elastic modulus regions: PEM (physiological elastic modulus, 80–140 mmHg), MPEM (maximum physiological elastic modulus, 360 mmHg), and MEM (maximum elastic modulus at failure).

Based on the measured thickness and width of the BPPs, the initial gauge length between between the two arms of the uniaxial tensile testing machine, and the applied tensile force, a stress–strain analysis was performed to determine the elastic modulus according to Hooke's law:

$$\text{Elastic modulus (E)} = \text{Stress/Strain} = \sigma/\varepsilon = (F \times L_o)/(w \times t \times \Delta L) \quad (14)$$

Where:

- E = elastic modulus (MPa)
- σ = engineering stress (MPa)
- ε = engineering strain (dimensionless)
- F = applied tensile force (N)
- L_o = initial gauge length of the specimen (mm)
- w = initial specimen width (mm)
- t = initial specimen thickness (mm)
- ΔL = change in specimen length during tensile loading (mm)

GraphPad Prism 7 software (GraphPad Software, San Diego, California, USA) was utilized for parameter fitting and statistical analysis. Data derived from the BPPs' mechanical tests using the LM1 system (TA Instruments, ElectroForce® System Group, USA) and measured specimen thickness were used to construct stress–strain curves and to determine the failure stress and strain for each specimen.

Continuous variables are presented as means ± standard deviation (SD). For each BPP, the mean parameter values, including thickness, PEM, MPEM, and MEM, were calculated either from the four bone-shaped pieces or from the two pieces with the same orientation for specific horizontal and vertical comparison analysis. Normality was assessed using the Shapiro–Wilk test. For two-group or orientation comparisons, the Mann–Whitney U-test was used for nonparametric data and the *t*-test for parametric data. To compare more than two groups, ANOVA with Tukey's post-hoc test was applied for parametric data, and the Kruskal–Wallis test with Dunn's correction was used for nonparametric data. The coefficient of variation (CV%), defined as the ratio of the standard deviation to the mean (CV% = SD/Mean × 100), was used to assess intra-sample variability among BPPs. A *p*-value of less than 0.05 was considered statistically significant.

4. Loss of energy test

The Low-Cycle Fatigue (LCF) testing is a test to evaluate the behaviour of materials in the low-cycle fatigue regime, typically involving a few cycles to failure and higher stress amplitudes (under conditions of high strain and low cycle numbers). It is often used to assess structures' fatigue performance under dynamic loading or severe operating conditions. The study was conducted using a horizontal uniaxial tensile testing system (LM1, TA Instruments, ElectroForce® System Group, USA) to evaluate the EDR of the BPPs under conditions of high strain and low cycle counts, representative of dynamic loading and severe physiological stress.

Prior to testing, each specimen underwent 10 preconditioning cycles to minimize hysteresis and stabilize the mechanical response. All tests were performed in distilled water maintained at a physiological temperature of 37 ± 0.1 °C to replicate in vivo conditions. In our experimentation, the displacement was increased gradually. 1.8 mm at 0.1 Hz for 1 cycle per motor, 3.6 mm at 0.1 Hz for 1 cycle per motor, 5.4 mm at 0.1 Hz for 1 cycle per motor, then 10, 7.2 mm at 0.1 Hz for 1 cycle per motor. This equals 10%, 20%, 30%, and 40% respectively, see **Figure 39**.

From each sample, pieces numbered 3 and 4 were selected to represent the vertical orientation, while specimens numbered 8 and 9 were selected for the horizontal orientation. This selection was performed to assess potential variability in biomechanical properties between the two directional alignments.

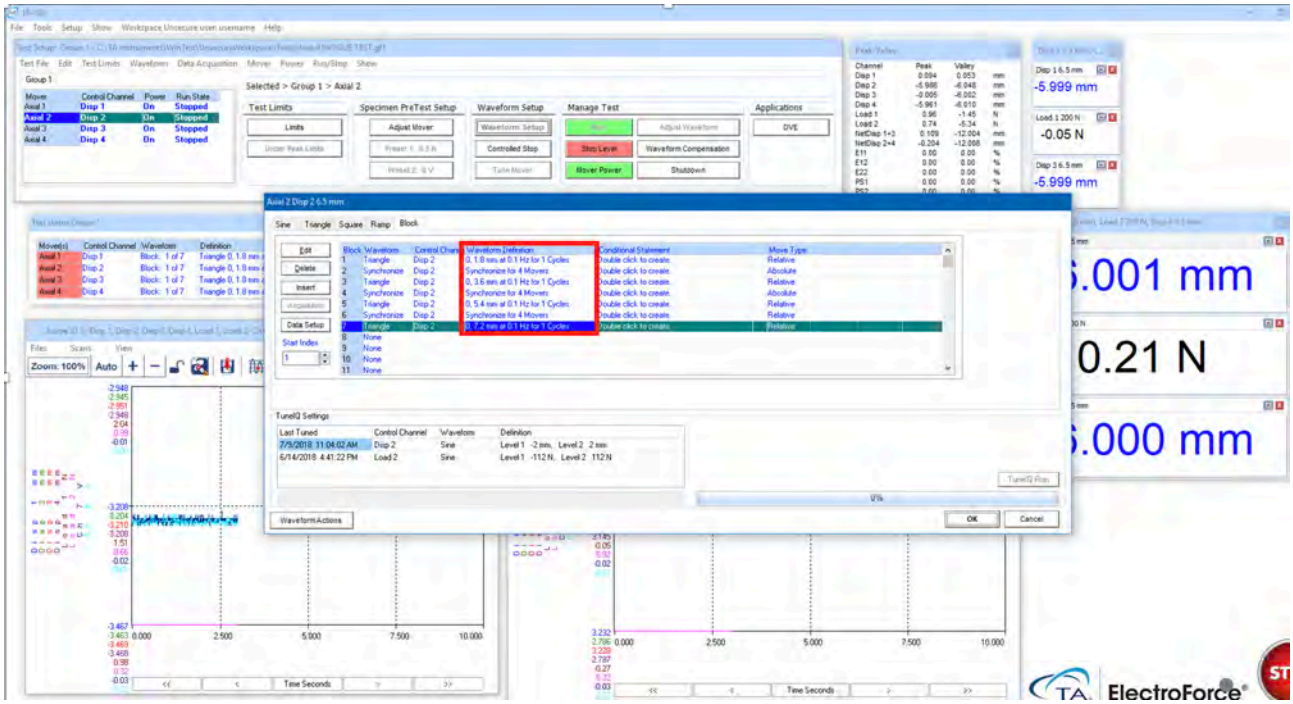


Figure 39. Configuration of the energy loss testing protocol. The displacement was progressively increased at a constant frequency of 0.1 Hz, with one cycle per motor at each step: 1.8 mm, 3.6 mm, 5.4 mm, 7.2 mm, and 10 mm, to evaluate the viscoelastic response under incremental loading conditions.

Each specimen was tested until the completion of the loading protocol or until material rupture occurred during the low-cycle fatigue testing process. All the measurements were taken within a time frame of 0.0001 seconds to ensure precise data. The software utilized during the experiments was WinTest® 8 (TA Instruments, ElectroForce® System Group, USA). The data were then analyzed to determine the energy dissipation ratio and elastic modulus at different strain percentages. Cycle affected by rupture, incomplete loading, or an unexpected reduction in the energy dissipation ratio relative to the preceding cycle—indicative of micro-damage or early failure—was excluded from the analysis.

All the measurements were taken within a time frame of 0.0001 seconds to ensure precise data. The collected data was then transferred to an Excel sheet with inputs of the computational procedure the (.csv) file for data analysis. The data analysis was performed by Spyder (Anaconda Inc., Austin, TX, USA), which is an open-source distribution of Python for scientific computing.

Based on the measured specimen thickness, the initial distance between the clamps of the uniaxial tensile testing system, and the applied force at various strain levels, the energy dissipation ratio and elastic modulus were calculated across different strain percentages using the equation in **Figure *40* (A).** To evaluate the biomechanical behavior of the BPPs, the energy loss was then calculated as the percentage of strain energy dissipated between the loading and unloading curves of the stress–strain relationship. This parameter represents material hysteresis and characterizes the viscous component of the tissue as shown in **Figure *40* (B).**

The primary endpoint is the measurement of the EDR of different BPPs at predefined percentage of strain. The secondary endpoint is the evaluation of intra-sample and inter-sample variability to determine the consistency and reliability of the biomechanical performance of BPPs.

GraphPad Prism 7 software (GraphPad Software, San Diego, California, USA) was utilized for parameter fitting and statistical analysis. Data derived from the BPPs' mechanical tests using the LM1 system (TA Instruments, ElectroForce® System Group, USA) and measured specimen thickness were used to construct stress–strain curves and to determine the EDR for each specimen.

Continuous variables are presented as means ± standard deviation (SD). For each BPPs, the mean parameter values including thickness and EDR were calculated either from the four bone-shaped pieces or from the two pieces with the same orientation for specific horizontal and vertical comparison analysis. Normality was assessed using the Shapiro-Wilk test. The four groups were compared using an ANOVA with Tukey's post-hoc test was applied for parametric data and the Kruskal Wallis test with Dunn's correction was used for non-parametric data. A p-value of less than 0.05 was considered statistically significant.

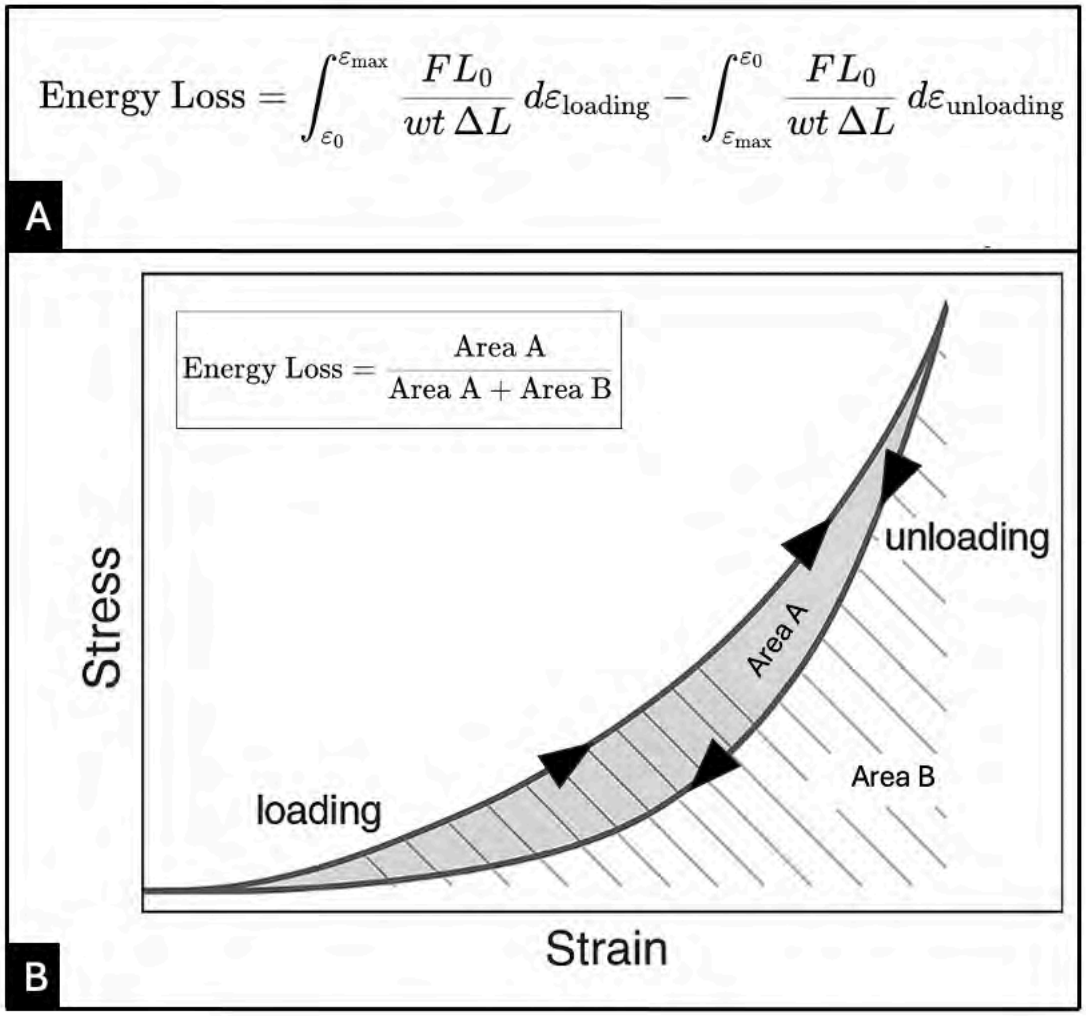


Figure 40. *Calculation of energy loss from the stress–strain relationship:* (A) Mathematical formulation used to calculate the biomechanical energy loss (hysteresis loss) during cyclic loading and unloading; where F : Applied force, L_0 : Initial length of the specimen, w : Width of the specimen, t : Thickness of the specimen, ΔL : Elongation under load , ε : Strain, ε_0 : Initial strain, ε max : Maximum applied strain, ε loading: Strain during loading, ε unloading : Strain during unloading phases. (B) Schematic representation of the stress–strain relationship illustrating the areas corresponding to absorbed and released energy. The shaded region between the loading and unloading curves represents the hysteresis loop with specified percentage, which quantifies the behavior of the biomaterial and indicates the mechanical energy dissipated per deformation cycle.

5. Histological observation study

Pre-analytical preparation: different brands of bovine pericardial patches were studied. After identifying pieces numbers 5 and 10 from each sample using the numerical data method and employing different cutting techniques at the edge of each sample in the preservation tube, each piece underwent serval steps. The fixation step, when all pieces were fixed for 24 hours in a 4% buffered formalin solution at room temperature to preserve and stabilize the natural structure of BPPs and decrease the risk of protein degradation by irreversibly cross-linking. The serous and fibrous layers were identified based on their appearance, see **Figure 41 (A).** The fibrous face was painted with Indian ink as a marker for subsequent histological study, see **Figure 41(B).** Each piece was then longitudinally cut using a histological blade and placed in cassettes with black foam and positioned at the lateral side to examine the serous and fibrous layers, see **Figure 41 (C-E).**

The second step is the dehydration step; this step is important to remove the liquid from the samples. This step was achieved by following the laboratory protocol for tissue preparation by one bath at 70% ethanol for 30 minutes. Then one bath at 80% ethanol for 30 minutes. Followed by another bath at 95% ethanol for 30 minutes to eliminate ethanol from the tissue. Then two baths at 100% ethanol for 45 minutes each. Then two baths in xylene for 45 minutes each. For the last step of dehydration, two baths in paraffin at 58/60°C (using the embedding machine), with 1 hour and a half for the first bath and 24 hours for the second bath. This entire process is automated, using the for efficient and standardized dehydration.

The third step is the embedding or Inclusion step. This process is for encapsulating a sample in paraffin wax to facilitate the extraction of cellular structures and convert the tissue into a solid form that can be easily sliced. This procedure is typically performed using an embedding machine.

The fourth step is the sectioning step by using the microtome. In this study, a thickness of 4 micrometres was used. The cut sections are then transferred to a distilled water bath at 40/45°C. Then, the sections are transferred onto histological slides and left to dry on a slide heater at 45/50°C for 24 hours. This drying process prepares the sections for staining and subsequent examination under a microscope.

The fifth step is the coloration steps; the preparation of stains was prepared according to the laboratory protocols. There is serval stains were used in this observational study. The hematoxylin-eosin-saffron (HES) staining is a commonly employed histological method that provides valuable information on the overall composition and structure of tissues. Hematoxylin imparts a purplish-blue color to cell nuclei, whereas eosin adds a pink color to the extracellular matrix and cytoplasm. Incorporating saffron into the H&E staining method referred to as haematoxylin-eosin-saffron (HES) staining, can enhance the detection of collagen fibers. Saffron, including acidic carotenoid compounds, is a natural dye that imparts a yellow-orange color to collagen fibers when applied. This aids in differentiating collagen from other constituents such as muscular tissue (Ceccopieri et al., 2021).

The orcein is a histology stain that implicated in this research, that has the ability to specifically identify elastic fibers in tissue slices. When treated with orcein, elastic fibers exhibit a mahogany brown or dark red/brown coloration. The orcein staining method functions by attaching the orcein dye to the elastin constituent of elastic fibers (Kornhauser, 1952; Nakamura et al., 1977).

The masson's trichrome staining highlights the collagen fibres. The purpose of this stain is to differentiate between collagen and muscle. The main structure that can be seen with this coloration is collagen with a green or blue coloration, Keratin or muscle tissue seen with a red to pink coloration, dark brown to black for cell nuclei, and light red or pink for cytoplasm (Foot, 1933).

Wiegert stain is a combination of stains used in histology that is useful for distinguishing and displaying elastic fibers in tissue samples since they exhibit a blue-black or blue coloration in contrast to the surrounding background.

Blue alcian stain help us to identify the degeneration tissue by identifying the Mucopolysaccharides, Tissue parts that specifically stain by this dye become blue to bluish green after staining and are called 'Alcianophilic'.

Following tissue preparation, each histological slide was systematically coded to ensure accurate identification and traceability throughout the analysis process. Each slide was labeled with a

unique reference number incorporating the sample identifier, orientation (vertical A1, or horizontal A2), specimen number, and staining method. This standardized labeling protocol was implemented to prevent misclassification and to maintain methodological rigor.

Subsequently, all slides were digitized using a high-resolution slide scanner to enable numerical archiving and facilitate detailed microscopic evaluation. Digitalization allowed standardized visualization, enhanced reproducibility of observations, and improved accessibility for comparative histological analysis, see **Figure 42**.

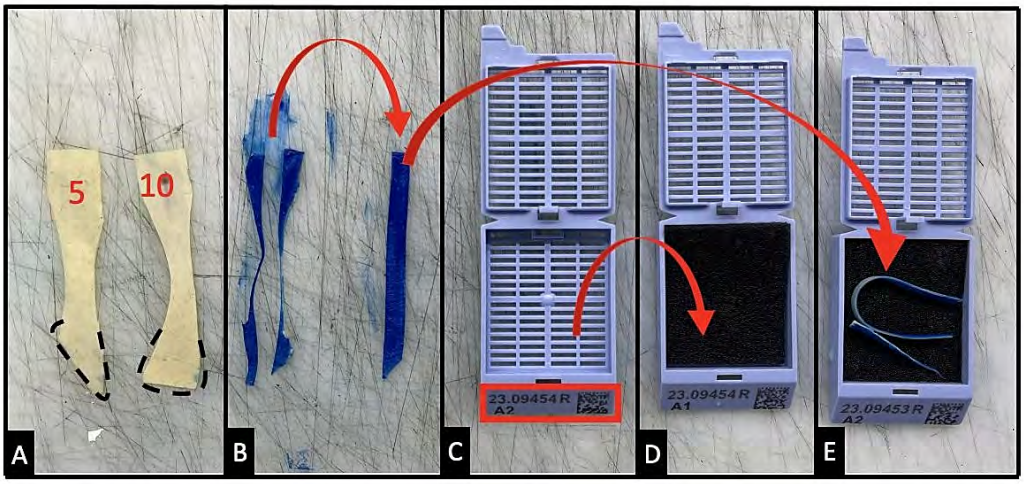


Figure 41. Pre-analytical preparation of bovine pericardial patches for histological analysis. (A) Identification of the serous and fibrous layers based on macroscopic appearance. (B) Marking of the fibrous surface with Indian ink for orientation. (C–D) Longitudinal sectioning of the specimens using a histological blade. (E) Placement of the sections in cassettes with black foam, positioned laterally to enable evaluation of both layers.



Figure 42. Example of histological slide coding and digitalization process. The slide was labeled with a unique reference code including the sample identifier, orientation, specimen number, and staining method.

To qualitatively assess the structural composition of BPPs from four different suppliers, an observational histological analysis was performed using multiple staining methods: HES, Orcein, Masson's Trichrome, Weigert's stain, and Alcian Blue.

This histological analysis facilitated a qualitative evaluation of structural characteristics among different BPPs, highlighting variations in tissue architecture, fiber composition, and staining properties. The distribution of collagen and elastic fibers, muscle components, and areas rich in mucopolysaccharides were analyzed. This visual classification, however subjective, offered a systematic approach for comparing structural attributes and fiber density among BPPs from various sources.

For each supplier, 10 vertical and 10 horizontal sections of bovine pericardial patches were obtained, resulting in a total of 80 tissue samples. Each sample underwent five different histological stainings—HES, Orcein, Masson’s Trichrome, Weigert’s stain, and Alcian Blue—producing a total of 400 stained histological slides for comparative analysis.

From these stained samples, five vertical and five horizontal slides were randomly selected per supplier (40 slides in total) to perform a detailed qualitative assessment. The histological evaluation was conducted by the lead author using the Pathomation digital pathology software (version 2.1.1.2017, Pathomation BV, Berchem, Belgium) to support standardized visualization and analysis.

Chapter 5: Results

1. Biomechanic by MRI

In this study, physiological strain was measured by two methods, the cross-sectional areas of the magnitude of phase contrast and the cross-sectional areas of steady-state free precession. The mean of the maximum cross-sectional area obtained from the magnitude of phase contrast is 419 ± 22.1 mm^2, [Min: 376.9 mm^2, Max: 450.4 mm^2], while the mean of minimum cross-sectional area is 374.5 ± 21.1 mm^2, [Min: 339.1 mm^2, Max: 408.3 mm^2]. The mean of the maximum cross-sectional area obtained from the SSFP is 438.4 ± 24.3 mm^2, [Min: 385.9 mm^2, Max: 465.7 mm^2]), while the mean of minimum cross-sectional is 397.6 ± 23.4 mm^2, [Min: 346.6 mm^2, Max: 429.4 mm^2]. Due to the small sample size, the Shapiro-Wilk-P test was used to evaluate the distribution of our results. The Shapiro-Wilk-P test of strain percentage by PC is 0.471, and for strain percentage by SSFP is 0.503. The Shapiro-Wilk-P test is more than 0.05, which proves normal distribution of our results. The mean strain percentage calculated from the PC sequence is 12.1 ± 3.60 %, [Min: 6.7%, Max: 18.1%]. While the strain value obtained from SSFP is 10.3 ± 3.20 %, [Min: 5.5%, Max: 15.5%].

The mean distensibility value obtained from the PC sequence is 1.5 ± 0.5 $10^{-3} \times mmHg^{-1}$, [Min: 0.810 $^{-3} \times mmHg^{-1}$, Max: 2.310 $^{-3} \times mmHg^{-1}$]. The distensibility value obtained from SSFP is 1.3 ± 0.410 $^{-3} \times mmHg^{-1}$, [Min: 0.710 $^{-3} \times mmHg^{-1}$, Max: 1.910 $^{-3} \times mmHg^{-1}$]. The Shapiro-Wilk-P test for distensibility measured by PC method and SSFP are 0.471 and 0.503 respectively, see **Different plane** axes were performed in our study. Only the axial plane in 2D phase contrast was able to measure the velocity values. The peak systolic velocity and mean velocity value were measured for all samples in the PC sequence. The peak systolic velocity measured in our phantom model is 45.5 ± 11 cm/sec, the maximum peak systolic velocity is 58.8 cm/sec, and the minimum peak systolic velocity is 23.1 cm/sec. The mean velocity value calculated in our study is 5.73 ± 2.84 cm/sec, while the maximum mean velocity is 10.1 cm/sec, and the minimum mean velocity is 1.0 cm/sec, see **Table 13** and **Figure 43 (C and D).** The data obtained from PC and SSFP for strain were different, as well as distensibility values, see **Figure 43 (A and B)**. Student's t-tests were used to compare the values obtained from the two sequence methods (strain percentage and distensibility). The student's t-test found non-significant difference between SSFP and PC for strain and distensibility (P-value is 0.195), see **Table 13**.

Table 12.

Different plane axes were performed in our study. Only the axial plane in 2D phase contrast was able to measure the velocity values. The peak systolic velocity and mean velocity value were measured for all samples in the PC sequence. The peak systolic velocity measured in our phantom model is 45.5 ± 11 cm/sec, the maximum peak systolic velocity is 58.8 cm/sec, and the minimum peak systolic velocity is 23.1 cm/sec. The mean velocity value calculated in our study is 5.73 ± 2.84 cm/sec, while the maximum mean velocity is 10.1 cm/sec, and the minimum mean velocity is 1.0 cm/sec, see **Table 13** and **Figure 43 (C and D).** The data obtained from PC and SSFP for strain were different, as well as distensibility values, see **Figure 43 (A and B)**. Student's t-tests were used to compare the values obtained from the two sequence methods (strain percentage and distensibility). The student's t-test found non-significant difference between SSFP and PC for strain and distensibility (P-value is 0.195), see **Table 13**.

Table 12. Descriptive table of strain percentage, distensibility, peak systolic velocity, and mean velocity values.

	Strain % PC	Strain % SSFP	Distensibility PC $10^{-3} \times mmHg^{-1}$	Distensibility SSFP $10^{-3} \times mmHg^{-1}$	Peak systolic velocity cm/sec	Mean velocity cm/sec
N	17	17	17	17	17	17
Mean	12.1	10.3	1.51	1.29	45.5	5.73
Standard deviation	3.60	3.17	0.450	0.396	11.0	2.84
Minimum	6.69	5.47	0.836	0.684	23.1	1.00
Maximum	18.1	15.5	2.26	1.93	58.8	10.1
Shapiro-Wilk p	0.471	0.503	0.471	0.503		

Table 13. Paired samples T-Test of strain percentage and distensibilities values.

			statistic	df	p
Strain percentage PC	Strain percentage SSFP	Student's t	1.35	16.0	0.195
Distensibility PC	Distensibility SSFP	Student's t	1.35	16.0	0.195

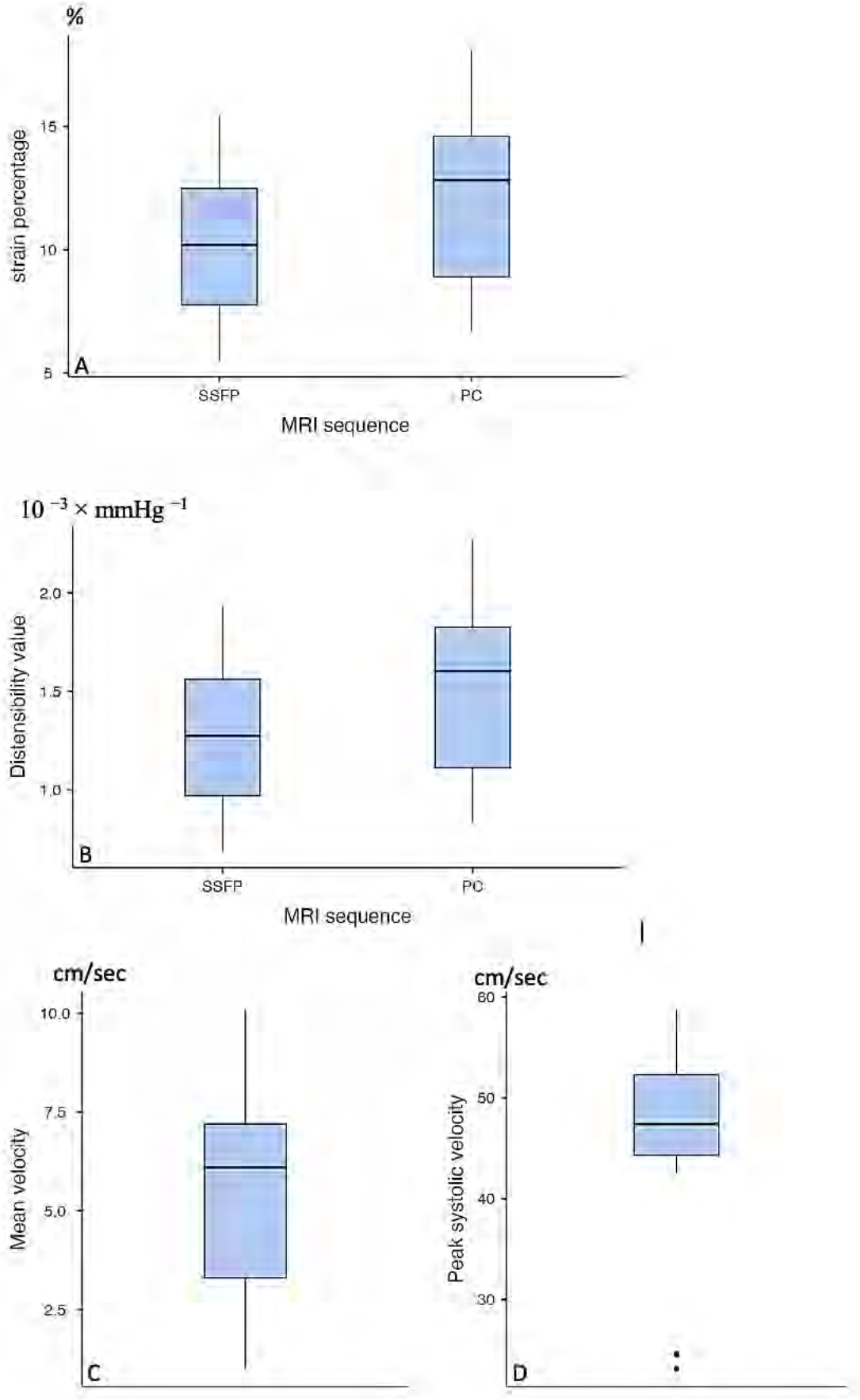


Figure 43. Box plot graph of results of the result of strain percentage, distensibility mean velocity, and peak systolic velocity. A) Box plot of strain percentage of PC and SSFP sequences. B) Box plot of distensibility value of PC and SSFP sequences. C) Box plot of mean velocity values. D) Box plot of Peak systolic velocity.

2. Failure test

Different biomechanical analyses were performed on BPPs from four different suppliers, with each supplier providing ten BPPs. Each BPP was then sectioned into four bone-shaped specimens: two oriented horizontally and two oriented vertically. The mean of thickness of BPPs from Edwards Lifesciences® (Edwards Lifesciences Corporation, Irvine, CA, USA) was 0.419 ± 0.074 mm (median 0.411; range 0.30–0.56 mm**),** while the mean of thickness of BPPs from Supple Peri-Guard® (Baxter International Inc., Deerfield, IL, USA) was 0.424 ± 0.085 mm (median 0.415; range 0.30–0.58 mm**).** The mean of thickness of BPPs from Xenosure® (LeMaitre Vascular Inc., Burlington, MA, USA) exhibited slightly lower values, with a mean of 0.384 ± 0.068 mm (median 0.377; range 0.28–0.49 mm). whereas Invengenx® (Tisgenx Inc., Irving, TX, USA) patches were the thickest, with a mean of 0.469 ± 0.084 mm (median 0.462; range 0.35–0.60 mm), see **Table 14**, and **Figure 44**.

Table 14. Description of BBP samples group thickness

n	Group	N	Mean ± SD	Median	Min – Max	p25	p75	IQR
1	Edwards Lifesciences	10	0.419 ± 0.074 mm	0.411	0.30 – 0.56	0.373	0.466	0.26
2	Supple Peri-Guard	10	0.424 ± 0.085 mm	0.415	0.30 – 0.58	0.367	0.477	0.28
3	Xenosure	10	0.384 ± 0.068 mm	0.377	0.28 – 0.49	0.332	0.446	0.21
4	Invengenx	10	0.469 ± 0.084 mm	0.462	0.35 – 0.60	0.391	0.537	0.25

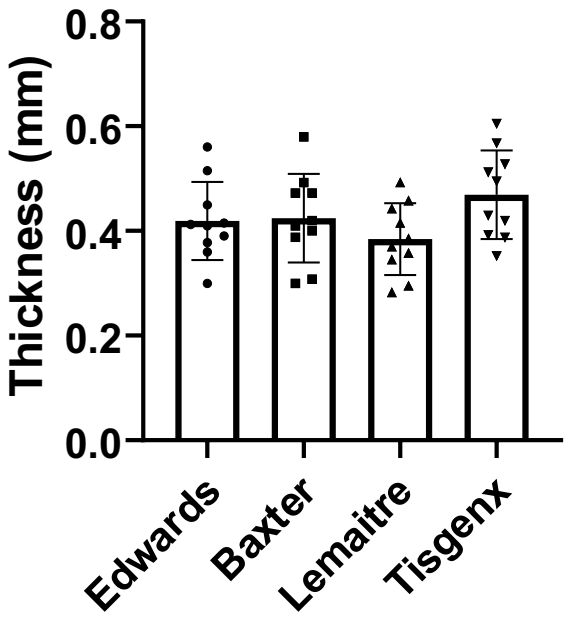


Figure 44. Description of BBP samples group thickness.

The coefficient of variation (CV%) to measure the intra-sample variability, defined as the ratio of the standard deviation to the mean (CV% = SD/Mean × 100), was used to assess the variability across BPPs. Ten independent specimens from each patch type were tested (mean of two measurements per orientation). The mean CV% values is 13.4% for Edwards Lifesciences- Edwards, 15.5% for Supple Peri-Guard-Baxter, 17.9% for Xenosure-LeMaitre, and 18.7% for Tisgenx- Invengenx. This result indicating low variability within samples. Statistical analysis revealed no significant intra-sample differences across patch types (all $p > 0.05$) as shown in the **Table 15** . These findings suggest a homogeneous mechanical behavior within each BPP group.

Paired *t*-tests were performed to assess intra-sample variability between the horizontal and vertical orientations for each patch. The results demonstrated no significant differences for Supple Peri-Guard-Baxter (P = 0.18) and Tisgenx (P = 0.20), indicating consistent thickness and homogeneity across orientations. In contrast, Edwards Lifesciences- Edwards patches showed a borderline significant difference (P = 0.048), while Xenosure-LeMaitre patches exhibited a highly significant difference ($p = 0.0006$), suggesting greater intra-sample variability in thickness. These findings imply that most BPPs display uniform structural behavior, except for Lemaitre, which presented noticeable directional variation, see **Figure *45*.**

Table 15. Coefficient of variation of intra-sample variability of BPPs

n	Group	Test	Mean Difference / Median	Mean CV%	p-value
1	Edwards	t-test	0.0150 ± 0.0365	13.4%	0.6856
2	Baxter	t-test	0.0265 ± 0.0473	15.5%	0.5823
3	Lemaitre	t-test	–0.0215 ± 0.0369	17.9%	0.5671
4	Tisgenx	Mann–Whitney	–0.0025	18.7%	0.8937

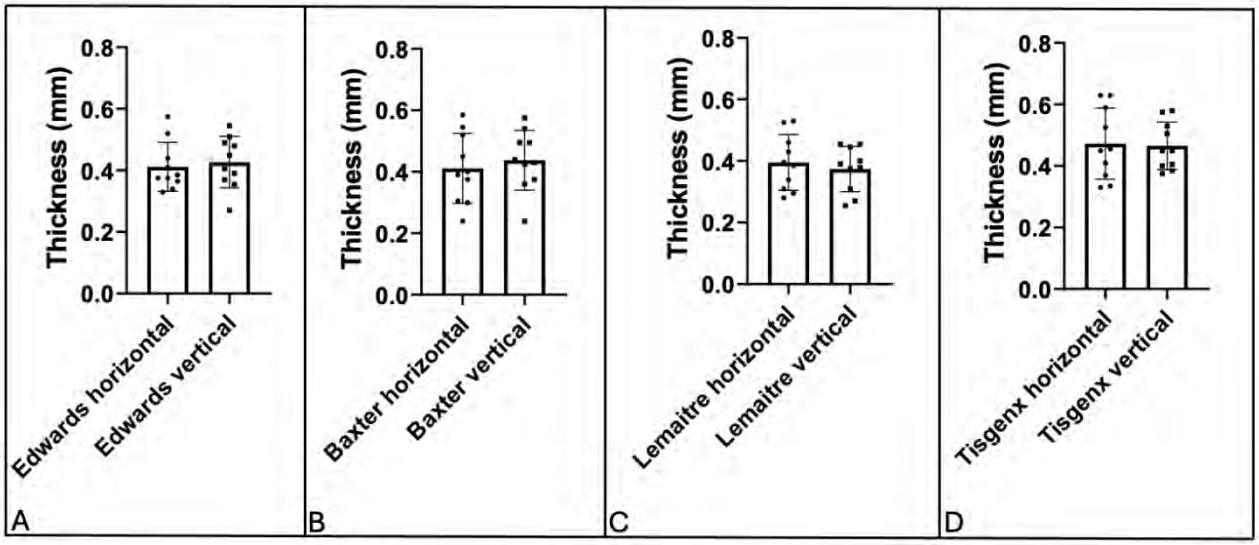


Figure 45. Comparative analysis of BPPs thickness according to specimen orientation (vertical versus horizontal).

Tukey's multiple comparisons test revealed no statistically significant differences in CV% among the four group (all adjusted $p > 0.05$), indicating comparable inter-group homogeneity. Pairwise comparisons showed that BPPs grups exhibited similar variability profiles, with no meaningful differences in mean CV% across groups. Although a borderline trend was noted between Lemaitre and Tisgenx ($p = 0.0921$), this difference did not reach statistical significance after adjustment, suggesting that the overall variability among BPPs remains consistent and not influenced by patch origin or manufacturing process, see **Table 16**.

The PEM values for the BPPs were as follows: Edwards Lifesciences- Edwards exhibited a mean of 1.931 ± 1.456 MPa (range: 0.256–6.203 MPa), Supple Peri-Guard-Baxter showed 1.392 ± 1.289 MPa (range: 0.090–5.860 MPa), Xenosure-LeMaitre recorded 4.121 ± 2.467 MPa (range: 0.775–9.391 MPa), and Tisgenx- Invengenx presented 3.985 ± 2.868 MPa (range: 0.289–11.020 MPa), see **Table 17**.

Table 16. Coefficient of variation of inter-sample variability of BPPs

Comparison	Mean Diff	95% CI of Diff	Adjusted p-value
Edwards vs. Baxter	–0.0053	–0.0997 to 0.0892	0.9988
Edwards vs. Lemaitre	0.0348	–0.0597 to 0.1292	0.7558
Edwards vs. Tisgenx	–0.0500	–0.1445 to 0.0445	0.4924
Baxter vs. Lemaitre	0.0400	–0.0545 to 0.1345	0.6676
Baxter vs. Tisgenx	–0.0448	–0.1392 to 0.0497	0.5841
Lemaitre vs. Tisgenx	–0.0848	–0.1792 to 0.0097	0.0921

Table 17. PEM distribution Across Four BPP Suppliers

n	Group – PEM	Mean (MPa)	SD	Min	Max
1	Edwards Lifesciences	1.931	1.456	0.256	6.203
2	Supple Peri-Guard	1.392	1.289	0.090	5.860
3	Xenosure	4.121	2.467	0.775	9.391
4	Invengenx	3.985	2.868	0.289	11.020

Dunn's multiple comparisons test showed that Supple Peri-Guard-Baxter patches exhibited significantly lower variability compared with Xenosure-LeMaitre with ($p = 0.0035$) and Tisgenx-Invengenx with ($p = 0.0396$). No other significant differences were observed among the remaining patch types (all adjusted $p > 0.05$), see **Table 18**.

Paired analyses comparing horizontal and vertical orientations revealed no significant intra-sample differences in the PEM across all BPPs. Mean PEM values ranged from 1.8 to 4.5 MPa among the different patches. These findings indicate that all BPPs exhibited consistent biomechanical behavior between horizontal and vertical orientations, confirming structural homogeneity and uniform stress distribution under physiological conditions, see **Figure 46** and **Figure 49 (A).**

Table 18. Comparisons test for PEM inter-group differences in variability among BPPs

Comparison	Mean Rank Diff	Adjusted p-value	Significant
Edwards vs. Baxter	+5.40	>0.9999	ns
Edwards vs. Lemaitre	–12.60	0.0957	ns
Edwards vs. Tisgenx	–8.80	0.5540	ns
Baxter vs. Lemaitre	–18.00	0.0035	** (significant)
Baxter vs. Tisgenx	–14.20	0.0396	* (significant)
Lemaitre vs. Tisgenx	+3.80	>0.9999	ns

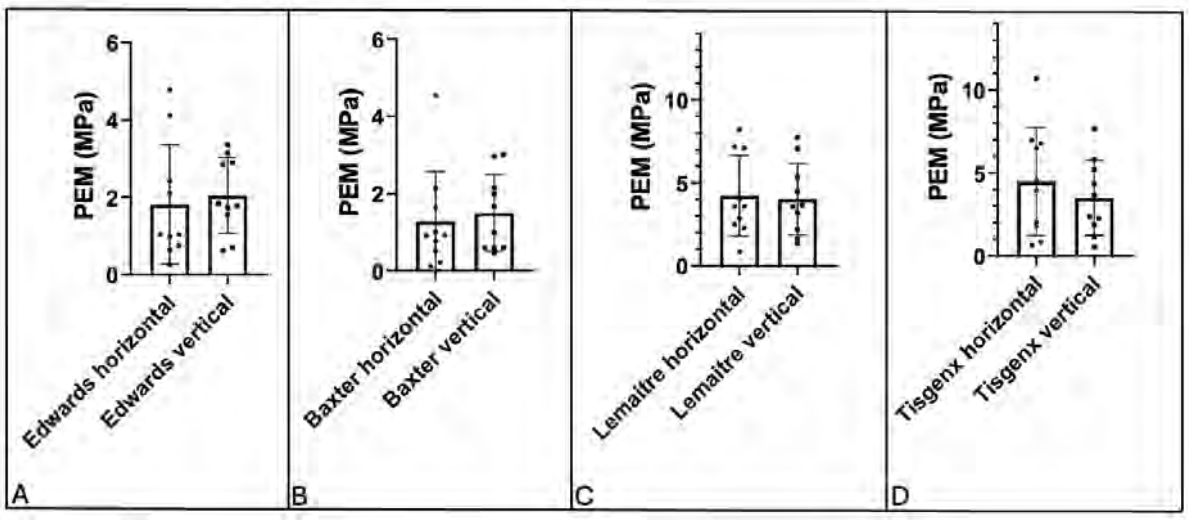


Figure 46. PEM comparative analysis of horizontal and vertical samples of BPPs. n=10 per group.

The MPEM values for the BPPs were as follows: Edwards Lifesciences–Edwards exhibited a mean of 2.928 ± 1.716 MPa (range: 0.426–7.752 MPa), Supple Peri-Guard–Baxter showed 4.608 ± 6.706 MPa (range: 0.760–35.492 MPa), Xenosure–LeMaitre recorded 6.929 ± 5.689 MPa (range: 1.255–24.669 MPa), and Tisgenx–Invengenx presented 5.560 ± 4.080 MPa (range: 0.565–16.993 MPa), see **Table 19**.

Dunn's multiple comparisons test revealed no statistically significant differences in mean rank values among the four gruops (all adjusted $p > 0.05$). The comparisons between Edwards Lifesciences–Edwards and LeMaitre–Xenosure ($p = 0.0557$) and between Baxter–Supple Peri-Guard and LeMaitre–Xenosure ($p = 0.0908$) showed borderline trends toward higher variability in the LeMaitre–Xenosure group, although these differences did not reach statistical significance. All other pairwise comparisons—including Edwards Lifesciences–Edwards vs. Baxter–Supple Peri-Guard, Edwards Lifesciences–Edwards vs. Invengenx–Tisgenx, and Baxter–Supple Peri-Guard vs. Invengenx–Tisgenx—were clearly non-significant (all adjusted $p > 0.9999$), indicating overall comparable performance among the tested materials, see **Table 20**.

Table 19. MEPM distribution Across Four BPP Suppliers.

n	Group- MEPM	Mean (MPa)	SD	Min	Max
1	Edwards Lifesciences	2.928	1.716	0.426	7.752
2	Supple Peri-Guard	4.608	6.706	0.760	35.492
3	Xenosure	6.929	5.689	1.255	24.669
4	Invengenx	5.560	4.080	0.565	16.993

Table 20. Comparisons test for MPEM inter-group differences in variability among BPPs

Comparison	Mean Rank Diff	Adjusted p-value	Significant
Edwards vs. Baxter	–0.90	>0.9999	ns
Edwards vs. Lemaitre	–13.60	0.0557	ns
Edwards vs. Tisgenx	–4.30	>0.9999	ns
Baxter vs. Lemaitre	–12.70	0.0908	ns
Baxter vs. Tisgenx	–3.40	>0.9999	ns
Lemaitre vs. Tisgenx	+9.30	0.4516	ns

No significant differences were observed between the horizontal and vertical orientations for the MPEM across BPPs. These results indicate consistent biomechanical behavior between both orientations, confirming homogeneity in material properties, see **Figure 47** and **Figure 49 (B).**

The MEM values for the BPPs were as follows: Edwards Lifesciences–Edwards demonstrated a mean of 17.724 ± 8.052 MPa (range: 5.469–44.045 MPa). Supple Peri-Guard–Baxter showed a slightly higher mean of 20.357 ± 13.226 MPa (range: 0.062–61.272 MPa**)**. Xenosure–LeMaitre presented the highest mean value of 28.603 ± 15.650 MPa (range: 9.562–74.318 MPa), while Tisgenx–Invengenx exhibited a mean of 21.230 ± 10.802 MPa (range: **7**.576–61.168 MPa), see

Dunn's multiple comparisons test demonstrated no statistically significant differences in mean rank between the tested groups (all adjusted $p > 0.05$). A borderline trend was observed between Edwards Lifesciences (Edwards) and Xenosure (LeMaitre) ($p = 0.0557$), as well as between Supple Peri-Guard (Baxter) and Xenosure (LeMaitre) ($p = 0.0908$), suggesting slightly higher variability in LeMaitre patches. However, these differences did not reach statistical significance after adjustment. All other pairwise comparisons, including Edwards vs. Baxter, Edwards vs. Invengenx (Tisgenx), Baxter vs. Invengenx, and LeMaitre vs. Invengenx, showed no significant differences, see **Table *22*** .

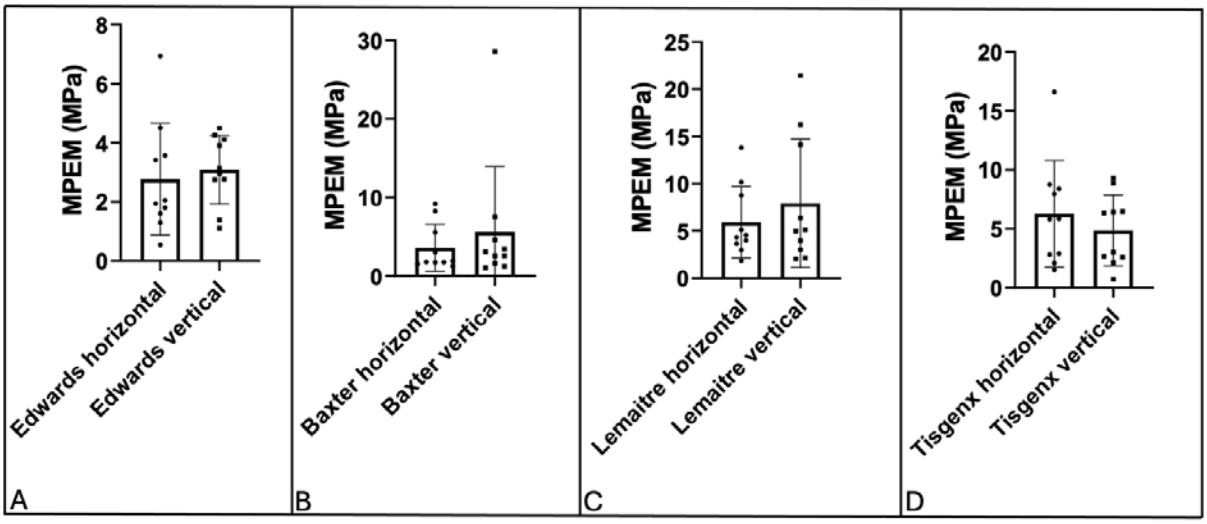


Figure 47. MPEM comparative analysis of horizontal and vertical samples of bovine pericardial tissue patch. n=10 per group.

Table *21*.

Dunn's multiple comparisons test demonstrated no statistically significant differences in mean rank between the tested groups (all adjusted $p > 0.05$). A borderline trend was observed between Edwards Lifesciences (Edwards) and Xenosure (LeMaitre) ($p = 0.0557$), as well as between Supple Peri-Guard (Baxter) and Xenosure (LeMaitre) ($p = 0.0908$), suggesting slightly higher variability in LeMaitre patches. However, these differences did not reach statistical significance after adjustment. All other pairwise comparisons, including Edwards vs. Baxter, Edwards vs. Invengenx (Tisgenx), Baxter vs. Invengenx, and LeMaitre vs. Invengenx, showed no significant differences, see **Table *22*** .

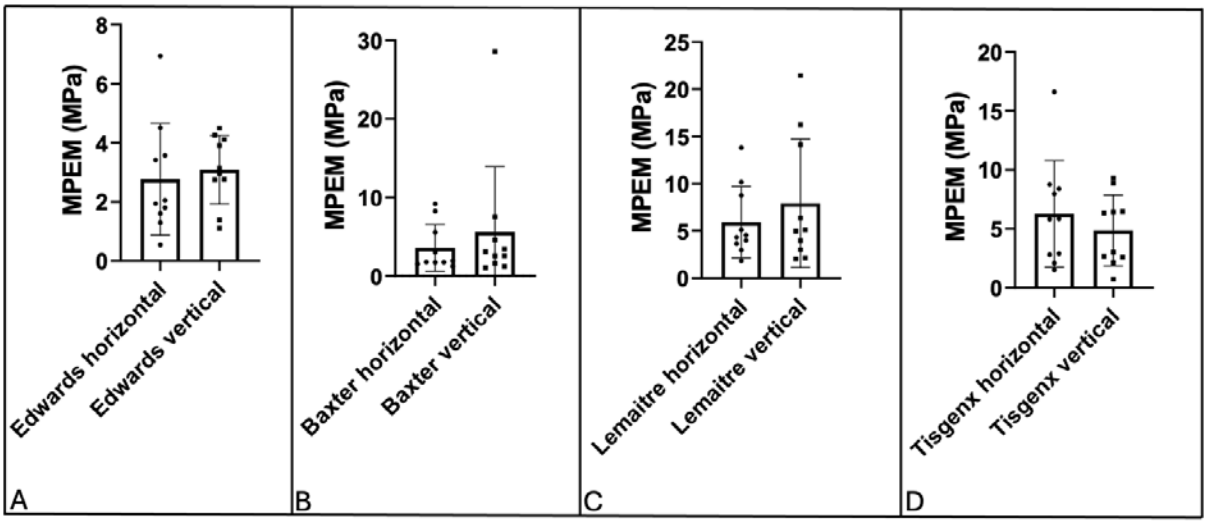


Figure 47. MPEM comparative analysis of horizontal and vertical samples of bovine pericardial tissue patch. n=10 per group.

Table 21. MEM distribution Across Four BPP Suppliers

n	Group	Mean (MPa)	SD	Min	Max
1	Edwards Lifesciences	17.724	8.052	5.469	44.045
2	SUPPLE PERI-GUARD	20.357	13.226	0.062	61.272
3	XENOSURE	28.603	15.650	9.562	74.318
4	INVENGENX	21.230	10.802	7.576	61.168

Table 22. Comparisons test for MEM inter-group differences in variability among BPPs

Comparison	Mean Rank Diff	Adjusted p-value	Significant
Edwards vs. Baxter	–0.90	>0.9999	ns
Edwards vs. Lemaitre	–13.60	0.0557	ns
Edwards vs. Tisgenx	–4.30	>0.9999	ns
Baxter vs. Lemaitre	–12.70	0.0908	ns
Baxter vs. Tisgenx	–3.40	>0.9999	ns
Lemaitre vs. Tisgenx	+9.30	0.4516	ns

No significant differences were observed between horizontal and vertical orientations for the MEM across most BPPs. Only Tisgenx showed a significant difference in variance ($P = 0.013$), suggesting slightly higher variability between orientations, while all other patches demonstrated uniform elastic behavior, see **Figure 48** and **Figure 49 (C).**

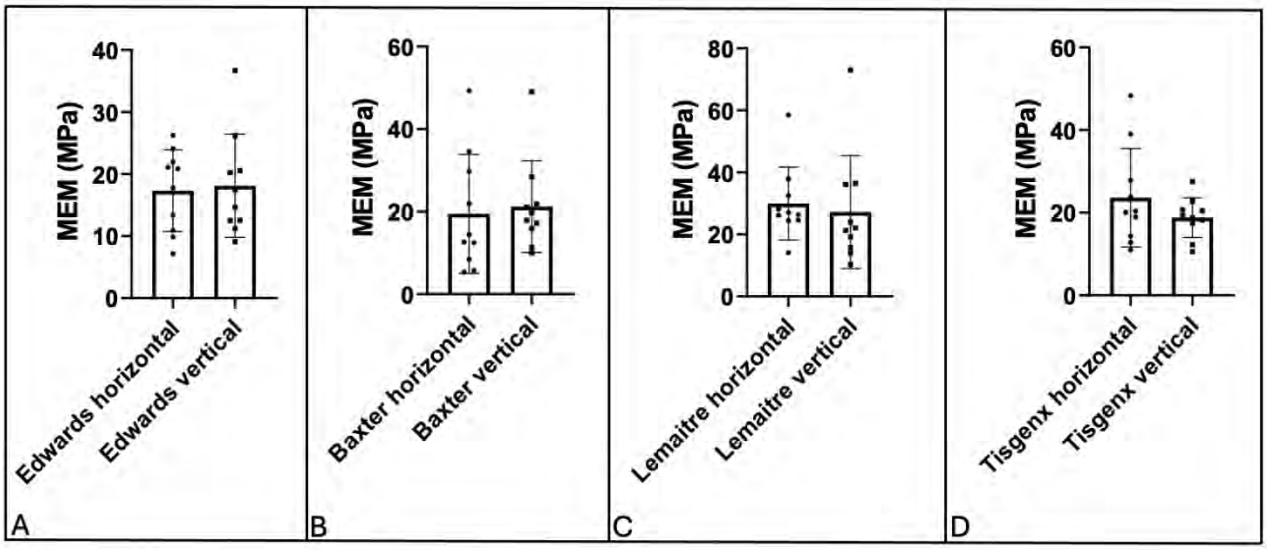


Figure 48. MEM comparative analysis of horizontal and vertical samples of bovine pericardial tissue patch. n=10 per group.

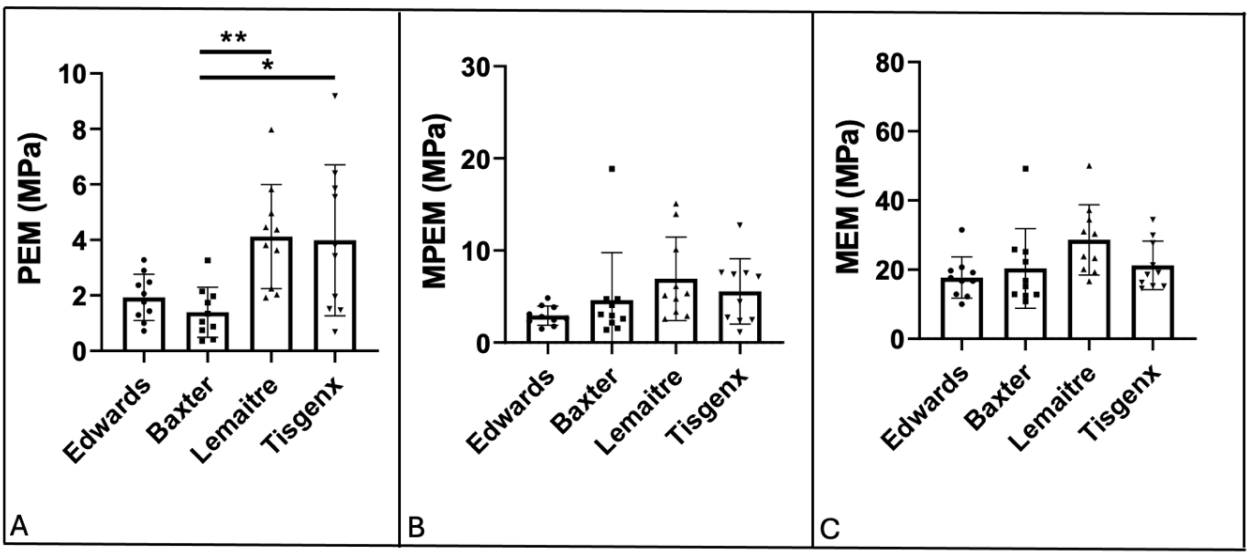


Figure 49. Elastic modulus comparison of BPPs. (A) Physiological elastic modulus (PEM); Supple Peri-Guard (Baxter) patches exhibited significantly lower values than Tisgenx (Invengenx) ($p = 0.0396$) (*) and Xenosure (LeMaitre) ($p = 0.0035$) (**). (B) Maximum physiological elastic modulus (MPEM). (C) Maximum elastic modulus (MEM).

3. Loss of Energy test

Biomechanical testing was conducted on BPPs provided from four commercial suppliers. The mean thickness of patches from Edwards Lifesciences was 0.441 ± 0.047 mm (median, 0.439 mm; range, 0.353–0.508 mm). Supple Peri-Guard (Baxter) patches demonstrated a mean thickness of 0.457 ± 0.069 mm (median, 0.453 mm; range, 0.315–0.548 mm). In comparison, Xenosure (LeMaitre) patches exhibited lower thickness values, with a mean of 0.387 ± 0.075 mm (median, 0.408 mm; range, 0.253–0.465 mm). Invengenx-Tisgenx patches were the thickest among the evaluated products, with a mean thickness of 0.484 ± 0.082 mm (median, 0.463 mm; range, 0.393–0.608 mm), see **Table 23**.

With the exception of a significant difference between the Xenosure (LeMaitre) e and Invengenx-Tisgenx groups (mean difference −0.097; 95% CI −0.181 to −0.013; p = 0.018) there were no other statistically significant differences in thickness among groups. Additionally, no significant intra-group differences in thickness were observed between vertical and horizontal directions.

For the 10% strain measurement, the mean EDR for Edwards Lifesciences patches was 21.40 ± 7.02%, with values ranging from 10.31% to 47.96%. Supple Peri-Guard (Baxter) patches demonstrated a mean EDR of 24.95 ± 6.80% (range: 16.48%–40.65%). Xenosure (LeMaitre) patches showed a mean EDR of 24.99 ± 6.04% (range: 15.73%–38.96%). Invengenx–Tisgenx patches exhibited a mean EDR of 23.37 ± 6.12%, with values ranging from 15.68% to 45.01%. There were no statistically significant differences between the groups. These results indicate comparable energy dissipation behavior at 10% strain across all tested materials, see **Figure 50 (A).**
In addition, there was no significant differences in EDR for 10% strain between vertical and horizontal orientation.

For the 20% strain measurement, the mean EDR for Edwards Lifesciences patches was 26.07 ± 6.98% (range: 21.45%–39.71%; n = 6). Supple Peri-Guard (Baxter) patches demonstrated a mean EDR of 33.73 ± 7.92% (range: 25.03%–48.66%; n = 7). The Xenosure (LeMaitre) showed a mean EDR of 28.83 ± 2.55% (range: 26.06%–32.24%; n = 4). For Invengenx–Tisgenx patches, only one specimen remained available at 20% strain, with an EDR value of 23.35% (n = 1). No statistically significant differences were observed between the groups, see **Figure 50 (B)** despite the apparent dispersion of the values.

Table 23. Description of BPPs' thickness (in mm) from different suppliers, calculated from 10 samples.

Group	Mean ± SD	Median	Min–Max	p25	p75	IQR
Edwards Lifesciences	0.441 ± 0.047	0.439	0.353–0.508	0.409	0.478	0.069
Supple Peri-Guard (Baxter)	0.457 ± 0.069	0.453	0.315–0.548	0.417	0.513	0.096
Xenosure (LeMaitre)	0.387 ± 0.075	0.408	0.253–0.465	0.326	0.460	0.134
Invengenx-Tisgenx	0.484 ± 0.082	0.463	0.393–0.608	0.406	0.575	0.169

Mean ± SD: Mean and standard deviation. p25, p50, p75: 25th percentile, median, and 75th percentile. IQR: Interquartile range.

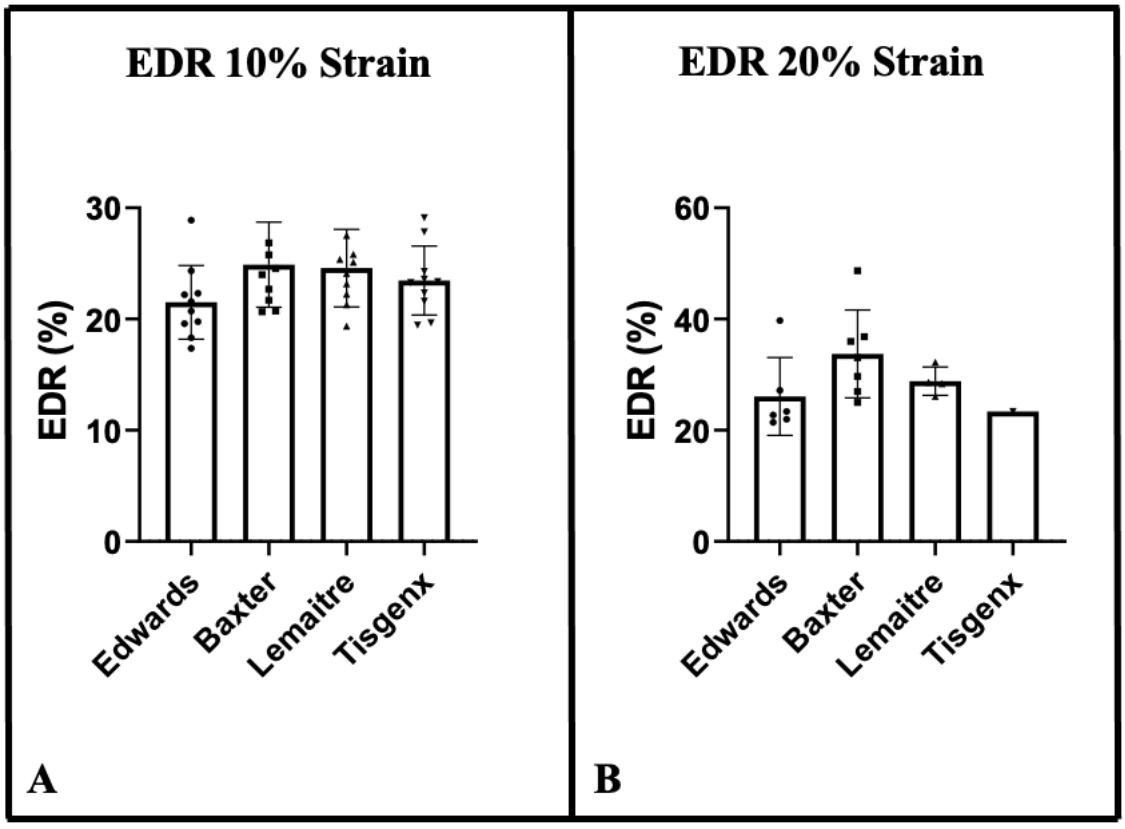


Figure 50. Energy dissipation ratio (EDR, %) of BPPs from four manufacturers (Edwards, Baxter, Lemaitre, and Tisgenx) measured at 10% strain **(A)** and 20% strain **(B)**.

All BPPs from all manufacturers successfully reached 10% strain for EDR test, allowing complete analysis at this deformation level. In contrast, 18.75% of all patches reached 20% strain for EDR test, including 13 Edwards Lifesciences patches (32.5%), 10 Supple Peri-Guard (Baxter) patches (25%), 6 Xenosure (LeMaitre) patches (15%), and 1 Invengenx-Tisgenx patch (2.5%). At 30% strain for EDR test, only 1.25% of the total samples were able to sustain deformations. Specifically, two Supple Peri-Guard (Baxter) patches (5%) reached this level, whereas no BPPs from Edwards Lifesciences, Xenosure (LeMaitre), or Invengenx-Tisgenx achieved 30% strain for EDR test, see **Figure 51**.

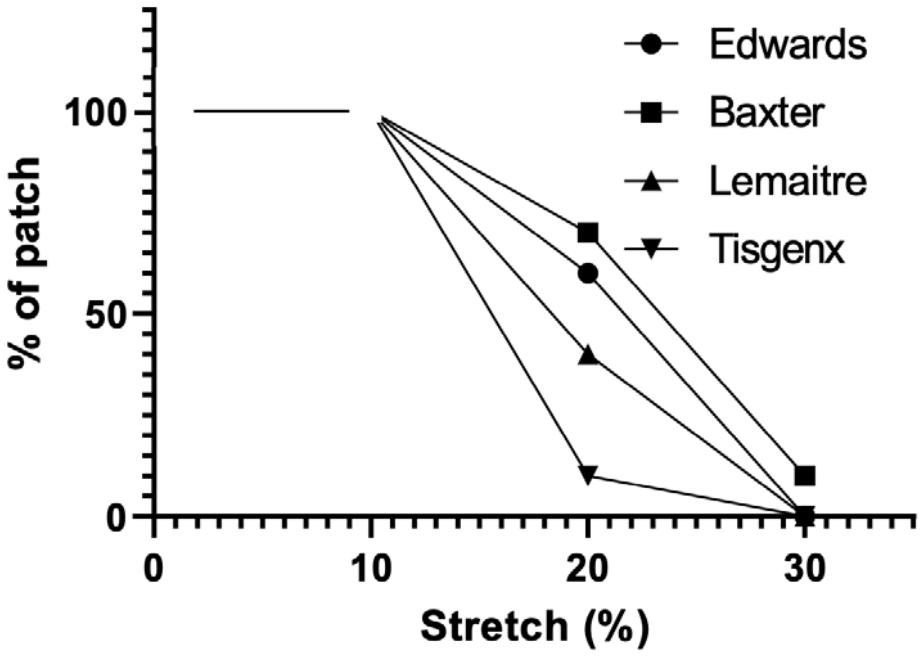


Figure 51. Percentage of BPPs failure after EDR testing. This panel shows the proportion of BBPs that underwent failure during energy dissipation ratio testing at progressive increasing strain levels.

Chapter 6: Discussion

1. Biomechanic by MRI

Our study aims to provide a better understanding of the biomechanical behavior of CMBPTs in simulated physiological conditions by providing physiological values of strain and distensibility.

The physiological strain value of the ascending and descending thoracic aorta ranges between 10% and 15%, whereas the abdominal aorta demonstrates a higher strain value ranging from 21% to 37% (Bell et al., 2014; Amanuma et al., 1992). Aortic strain decreases with age; individuals younger than 50 years exhibit strain values of 26% ± 9.46%, whereas those older than 50 years demonstrate lower values of 15.1% ± 7.29%[12]. The prosthetic grafts exhibit markedly lower strain values, approximately 1.8% for Dacron grafts and 1.2% for expanded polytetrafluoroethylene grafts (Tai et al., 2000).

In this study, the CMBPT strain value obtained is 12.1% ± 3.60% for the PCm approach and 10.3% ± 3.20% for the SSFP approach. Our results are within the normal range of the normal aortic strain measured by MRI technique (Redheuil et al., 2010). They also estimated the distensibility value by age groups: $7.44 \pm 2.54 \times 10^{-3}$ $mmHg^{-1}$ for people less than 50 years old and $2.89 \pm 1.29 \times 10^{-3}$ $mmHg^{-1}$ for people more than 50 years old.(Redheuil et al., 2010) Voges et al. found a value of $8.3 \pm 3.0 \times 10^{-3}$ $mmHg^{-1}$.(Voges et al., 2012) Rose et al. confirmed that distensibility decreases with age and found that women have higher aortic distensibility than men at the level of the descending aorta ($7.20 \pm 1.61 \times 10^{-3}$ $mmHg^{-1}$ vs. $5.05 \pm 2.40 \times 10^{-3}$ $mmHg^{-1}$).(Rose et al., 2010)

The reported strain values may vary depending on the measurement methodology, including the specific MRI sequences employed for strain assessment. Herment et al. found in their study significant differences od aortic strain value between the two methods, SSFP and PC sequences, used to estimate the strain values ($P < 0.02$). The values were 17.8% ± 11.7% for the SSFP sequence and 16.9% ± 8.18% for the PCm sequence (Herment et al., 2011). This difference is not confirmed in our study, which could be explained by the small sample size.

According to our results, the estimation of the CMBPT physiological strain can be calculated from both SSFP and PC acquisitions. Small variations across acquisition methods were approved in the study of Hermet et al., mostly as a result of poor image quality or artifacts that can impede the segmentation process(Herment et al., 2011). Therefore, when a local evaluation of aortic stiffness is required, better results were obtained from SSFP sequences compared to PC sequences. The balanced SSFP sequence provides the highest signal-to-noise ratio compared to other sequences, but it has

limited practical use for diagnostic imaging because of the mixed T2/T1 contrast behavior. However, SSFP is widely used in functional and morphological imaging in the cardiovascular field. Using the PC sequence, on the other hand, has a complementary role to the SSFP sequence, where it could provide additional flow information and the ability to precisely evaluate velocity (in particular peak wave velocity) to determine aortic stiffness segment.(Bieri & Scheffler, 2013; Herment et al., 2011)

In our study, the central CMBPT pressure was calculated by a central line inserted into the distal third of the CMBPT (80 mmHg), while the cross-sectional areas were obtained from both PC and SSFP. We found that the mean distensibility value obtained from the PCm sequence is $1.5 \pm 0.5 \times 10^{-3}$ $mmHg^{-1}$, while the distensibility value obtained from SSFP is $1.3 \pm 0.4 \times 10^{-3}$ $mmHg^{-1}$. There are no significant differences between SSFP and PCm distensibility values in our study.

The mechanical behavior of bovine pericardium is predominantly determined by its collagen-dense hierarchical microstructure, marked intrinsic anisotropy, and variability related to both the anatomical site of harvesting and the age of the animal (Aguiari et al., 2016; Sizeland et al., 2014; Stieglmeier et al., 2021).

Our findings indicate that CMBPTs may exhibit mechanical properties that are intermediate between native aortic tissue and conventional prosthetic grafts, thereby potentially mitigating the degree of compliance mismatch.

The small sample size has an impact on the measured data. These findings require further investigation in a larger cohort to have more accurate results. Performing similar experiments on different BPP brands approved in the medical field would give more accurate results for biomechanical parameters. The pump-generated flow was designed to reproduce abdominal aortic flow rates, the model does not capture the full spectrum of physiological pressure waveforms, vascular branching patterns, or dynamic interactions with surrounding tissues.

To our knowledge, no previous publication has evaluated the biomechanical properties of CMBPTs using MRI in vitro, which represents the main strength of our study.

2. Failure test

In this study, we present the biomechanical properties of BPPs widely used in cardiovascular surgery. By evaluating patches from four commercial suppliers, we aim to provide surgeons with a clearer understanding of their biomechanical behavior and the potential impact of their differences on clinical outcomes. Uniaxial tensile testing was selected instead of biaxial testing because the original cutting orientation of the supplied patches was not specified, and variations introduced during sample preparation or surgical handling could not be controlled. Given these constraints, uniaxial testing offered a more consistent and reproducible method for assessing the biomechanical performance of the materials.

In our study, the CV% analysis demonstrated minimal intra-sample variability, with no significant differences detected across the different patch types. However, thickness-related intra-sample variability was observed in the Edwards Lifesciences (Edwards) and Xenosure (LeMaitre) patches, where differences between horizontal and vertical orientations suggested reduced thickness homogeneity. This variation may be attributed to the relatively small sample size.

Inter-sample CV% analysis revealed no statistically significant differences among the four groups, confirming consistent inter-group uniformity. In terms of biomechanical performance, comparisons of PEM showed that Supple Peri-Guard (Baxter) patches exhibited significantly lower values than Xenosure (LeMaitre) ($p = 0.0035$) and Tisgenx (Invengenx) ($p = 0.0396$), while no significant intra-sample variability in PEM was observed among the BPPs.

PEM is a useful and realistic parameter (Duprey et al., 2010) for evaluating elasticity under normal physiological conditions to understand real biomechanical behaviors. To our knowledge, no study has determined PEM for bovine pericardial patches. MPEM represents a novel parameter designed to assess tissue elasticity under maximum physiological loading conditions, corresponding to the highest recorded physiological blood pressure of approximately 360–370 mmHg (Narloch & Brandstater, 1995). This new concept helped us to evaluate the biomaterials under high physiological conditions rather than under very high and abnormal conditions that could not happen in a physiological setting. This concept may be applicable to other medical disciplines for evaluating biomaterials or tissues subjected to high physiological loading conditions.

For both MPEM and MEM, no significant inter-group variability was identified in our study. The only notable exception was the Tisgenx (Invengenx) patch, which displayed a significant difference in MEM variance ($p = 0.013$), suggesting slightly higher orientation-dependent variability.

Overall, the findings indicate that thickness variability among the BPPs remained consistent and was not influenced by the supplier. The results for PEM, MPEM, and MEM collectively demonstrate uniform biomechanical behavior regardless of orientation, reflecting structural homogeneity and stable stress distribution under physiological loading conditions.

The BPP cutting orientation—whether horizontal or vertical—showed no significant differences in thickness or elastic properties, indicating comparable biomechanical performance across both directions. Therefore, the selection of orientation may be guided primarily by surgical preference and procedural requirements. Moreover, none of the suppliers specify the direction of BPPs, reinforcing the notion that BPP orientation has a limited impact on functional outcomes. In another study, BPPs exhibited minimal anisotropic behavior at low strain levels, with directional differences in mechanical response becoming apparent only at higher strain values (Tremblay et al., 2009). Our results, however, demonstrate that BPPs behave relatively isotropically, suggesting that orientation during aortic reconstruction does not significantly influence their mechanical performance.

Across the bovine family, the pericardial layers demonstrate structural organization comparable to that of the human pericardium, with a typical thickness ranging between 0.4 mm and 1 mm (Allen et al., 1984; Mansour et al., 2018b; Peebles et al., 2011). This value is slightly higher than that observed in our study, a difference that may be attributed to variations in the decellularization method and the use of glutaraldehyde for tissue preservation.

The literature presents a diverse array of findings about the Young's modulus or MEM of BPPs (Aguiari et al., 2016). These data suggest that there is a notable variation in the mechanical characteristics of BPPs observed across different studies. Reported values for uniaxial loading range widely, with the lowest modulus reaching approximately 9.9 MPa (Oswal et al., 2007), and the highest reaching 180 ± 49 MPa (Duncan & Boughner, 1998). This broad range underscores the multifactorial influence of tissue processing parameters, glutaraldehyde fixation, preconditioning protocols, and experimental testing methodologies on the mechanical behavior of BPPs. Additionally, variations in tensile testing apparatus, specimen geometry, and hydration conditions likely account for the heterogeneity observed across reported mechanical property values. In our study, all bovine

pericardial patches were preserved in glutaraldehyde, chemically sterilized, and supplied ready for clinical use, ensuring consistency and minimizing sample heterogeneity.

Unfortunately, prior studies that evaluated BPPs' biomechanical properties did not mention the suppliers' names, and they reported a wide range of elastic modulus values. Even the suppliers did not indicate the age of bovines, the harvesting site (Stieglmeier et al., 2021), or the average elastic modulus of these BPPs.

The utilization of BPPs is not limited to cardiovascular surgery; multiple studies have mentioned their utilization in abdominal wall reconstruction (D'Ambra, 2012; Saiding et al., 2023), urinary bladder reconstruction (Chee et al., 2015; Moon et al., 2011), replacing ligaments and tendons (Baldo et al., 2018; Longo et al., 2010), and spinal cord herniation repairs (L. Zhang et al., 2022). These different uses show that BPPs can adapt to tissues with different biomechanical demands and anatomical location according to the surgical application. For aortic surgery, using BPPs shows good results in the short and medium term, as confirmed by Frisch et al. (Frisch et al., 2025). Sizeland et al. (2014) conducted a study evaluating the modulus of elasticity in neonatal and adult bovines. The results indicated that younger individuals have a greater modulus of elasticity (80 MPa) than adults (30 MPa).

A clear age-related variation in arterial elasticity has been observed. In younger individuals, the femoral artery is the most elastic, with a value of 3.1 MPa, followed by the iliac artery at 2.9 MPa, the abdominal aorta at 1.0 MPa, the carotid artery at 0.8 MPa, and the descending thoracic aorta at 0.6 MPa. In contrast, older individuals demonstrate a marked reduction in arterial elasticity, with the iliac artery measuring 0.7 MPa and the femoral artery 1.4 MPa, while the descending thoracic aorta is 2.0 MPa, the abdominal aorta 1.2 MPa, and the carotid artery 1.1 MPa (Thubrikar, 2007). For cardiovascular surgery, our results confirm the possibility of using any of the tested BPPs, with no significant difference among them.

The use of rigid materials to replace the proximal aorta may increase the risk of cardiac hypertrophy. This inability to replicate the native aortic elasticity can impose additional strain on the heart, resulting in elevated left ventricular workload, increased pulse pressure, and a potential progression toward congestive heart failure over time (Sultan et al., 2022). Most studies that evaluate vascular remodeling following thoracic endovascular aneurysm repair (TEVAR) procedures focus on assessing changes in aortic wall structure, compliance, and hemodynamic adaptation over time

(Vallerio et al., 2019; van Bakel et al., 2019). The MEM of expanded polytetrafluoroethylene (e-PTFE) grafts is also variable, with results ranging from 17.4 to 55.2 MPa (Bouchet et al., 2019; Kleinstreuer et al., 2008).

To our knowledge, the potential risk of cardiac hypertrophy following the use of BPPs has not yet been investigated. Factors such as material stiffness, graft length, patch or tubular configuration, and anatomical implantation site may play a crucial role in determining postoperative cardiac sequelae.

A limitation of this study is that *in vitro* tissue testing does not replicate physiological internal pressure and involves simplified loading, typically applied in a uniaxial direction. The suppliers have provided insufficient data regarding the harvesting site and the age of the bovine sources. A histological study to evaluate the quantity of elastic and collagen would help strengthen our data.

3. Loss of energy test

This study characterized the biomechanical properties of BPPs commonly used in cardiovascular surgery. By systematically evaluating BPPs from four commercial suppliers, we aimed to provide a clearer vision of biomechanical behavior and to elucidate how inter-manufacturer differences may influence clinical performance and outcomes.

Low-cycle fatigue testing was employed to evaluate the biomechanical behavior of different BPPs under varying strain levels and limited cycle numbers, conditions that are intended to simulate physiological hemodynamic loading and intraoperative mechanical manipulation. Within this framework, the EDR quantifies the proportion of mechanical energy lost during a loading–unloading cycle. Reduced arterial compliance and impaired buffering capacity lead to adverse mechanical consequences, increasing the risk of left ventricular hypertrophy and impairing coronary perfusion and compromises coronary perfusion (Laurent & Boutouyrie, 2007; O′Rourke & Safar, 2005; Redheuil et al., 2010).

In our study, the thickness of the samples varied between 0.253 and 0.608 mm. These findings are consistent with previous studies indicating that the typical thickness of pericardial tissue generally ranges between 0.4 and 1.0 mm (Allen et al., 1984; Mansour et al., 2018b; Peebles et al., 2011). The values obtained from the different suppliers were within the normal range.

In addition, no significant differences were observed across the different patch types regarding thickness or biomechanical evaluations, and there was no thickness-related intra-sample variability indicating homogenous biomaterial. The result of EDR 10% and 20%, show no statistically significant differences among the groups.

The concept of energy loss is relatively new in the field of biomaterials and is used to assess tissue degeneration. A previous study applying this approach to ascending aortic specimens demonstrated that samples exhibiting higher energy loss also showed more pronounced medial degeneration compared with tissues of similar size but lower energy loss (Chung et al., 2014).

At present, there is no validated threshold to define material degeneration. Complementary histological assessment following repeated strain cycles would be required to characterize microscopic structural changes. Furthermore, simulating intraoperative conditions, such as clamping with a cardiovascular clamp, followed by histological reassessment could provide valuable insight into the mechanical fragility and clinical suitability of the BPPs.

The potential relationship between the use of BPPs and subsequent cardiac remodeling, including hypertrophy, remains insufficiently explored. Mechanical properties such as stiffness, as well as graft length, configuration (patch *versus* tubular reconstruction), and anatomical implantation site, may influence ventriculo–aortic coupling and long-term cardiac adaptation. These factors warrant further investigation to better understand their potential impact on postoperative hemodynamics and myocardial workload.

Several limitations should be acknowledged. The present *in vitro* mechanical assessment does not fully replicate physiological conditions, particularly pulsatile pressure and multidirectional EDR states encountered *in vivo*, as testing was performed under simplified uniaxial loading for energy loss. Moreover, incomplete information regarding the harvesting site and age of the bovine donors may have contributed to inter-sample variability.

Finally, MRI of the aorta may serve as a valuable noninvasive tool for evaluating patients treated with bovine pericardial patch or tubular graft reconstructions, particularly for assessing long-term structural and functional outcomes (thanks to conventional exam with inwithin addition 4D flow MRI). Further studies integrating histological analysis with *in vivo* imaging assessments are warranted to better characterize long-term performance and remodeling behavior.

4. Future Perspectives

The present work provides an initial framework for understanding the biomechanical behavior of bovine pericardial patches (BPPs) and custom-made bovine pericardial tubular grafts (CMBPTs). However, several aspects remain to be explored in order to fully elucidate the relationship between tissue microstructure, mechanical performance, and clinical applicability.

One of the main limitations of this study lies in the incomplete histological analysis. While a qualitative assessment of the structural organization of BPPs was successfully performed, the complexity of the histological evaluation prevented the completion of a detailed quantitative analysis. In particular, the precise quantification of collagen and elastin content remains a crucial objective. These two components play a central role in determining the mechanical behavior of biological tissues, including elasticity, compliance, and resistance to fatigue. Future work will therefore focus on implementing advanced digital image analysis techniques to quantify the relative proportions of collagen and elastin fibers within the tissue. Such quantification will allow a more objective comparison between different suppliers and may help explain the biomechanical similarities and subtle differences observed in this study.

In addition, the evaluation of residual cellular elements, particularly the presence and distribution of nuclei, represents another important direction for future research. Although glutaraldehyde-treated BPPs are generally considered acellular, the persistence of cellular remnants may influence long-term tissue degeneration, calcification, or inflammatory response. A systematic assessment of nuclear content using appropriate histological staining and image segmentation tools will provide further insight into the biological characteristics of these materials.

Beyond histology, future studies should aim to strengthen the link between microstructural findings and biomechanical properties. Establishing correlations between fiber organization, density, and parameters such as strain, distensibility, and energy loss would significantly enhance the interpretability of the results. This integrative approach would contribute to a more comprehensive understanding of how BPPs behave under physiological conditions and may improve their selection for specific surgical applications.

From a biomechanical perspective, the current study is limited by the use of uniaxial testing and simplified experimental conditions. Although these methods provide reproducible data, they do not fully replicate the complex, multidirectional stresses encountered in vivo. Future work should therefore incorporate biaxial mechanical testing and pulsatile flow models to better simulate physiological loading conditions. In particular, the evaluation of fatigue behavior under cyclic loading

and the simulation of intraoperative mechanical stresses, such as clamping, could provide valuable information regarding the durability and resilience of BPPs.

Another important perspective concerns the translation of these findings into clinical practice. In vitro results, although informative, must be validated in vivo. Long-term clinical and imaging follow-up studies will be necessary to assess graft remodeling, compliance, and hemodynamic adaptation over time. Advanced imaging techniques, such as 4D flow MRI, could play a key role in evaluating the interaction between the graft and the cardiovascular system, particularly in terms of flow dynamics and aortic stiffness.

Finally, the potential impact of BPP mechanical properties on cardiac function represents an emerging area of interest. The use of relatively stiff materials in aortic reconstruction may contribute to increased ventricular workload and subsequent cardiac remodeling. Future investigations should aim to explore the relationship between graft stiffness, ventriculo–aortic coupling, and long-term cardiac outcomes.

In conclusion, further work integrating quantitative histology, advanced biomechanical testing, and clinical evaluation will be essential to fully characterize the behavior of bovine pericardial materials and optimize their use in vascular surgery.

Chapter 7: Conclusion

The MRI study presents the biomechanical behavior of CMBPTs under physiological conditions assessed using in vitro MRI. The strain percentage was found to be within the normal range for a physiological aorta, whereas the distensibility was observed to be lower than the normal physiological values of the aorta. The use of CMBPTs in vascular surgery may be a viable alternative given their biomechanical characteristics being nearly identical to those of a normal aorta. Significant differences in strain values between SSFP and PC sequences, as found in previous studies, were not confirmed in this study. Both SSFP and PC acquisitions can be used to estimate CMBPT strain, with small variations caused by image quality or artifacts, see the graphic abstract in **Figure 52.**

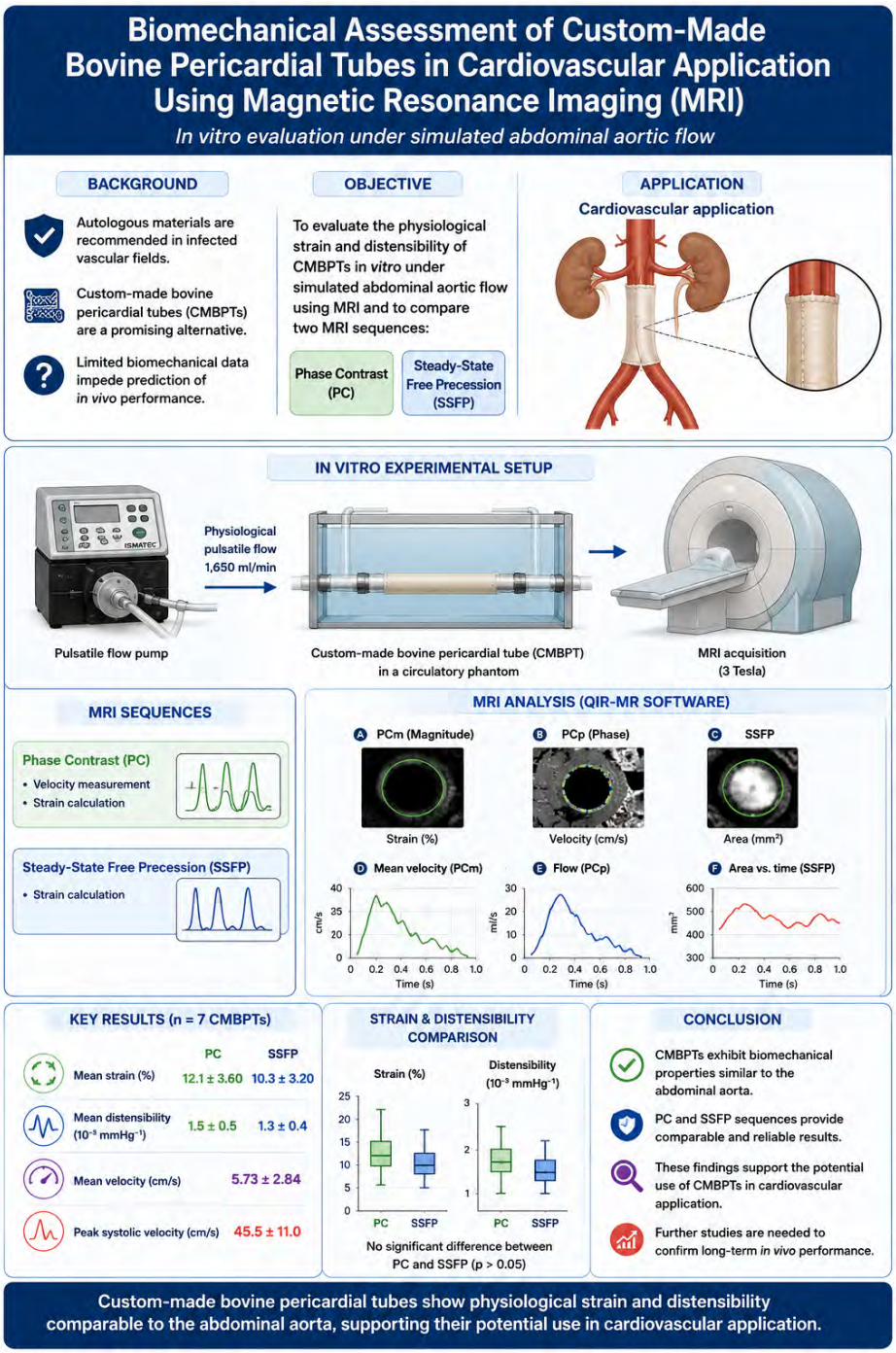


Figure 52. Graphical Abstract**.** Seven CMBPTs were evaluated in an in vitro pulsatile flow model using 3-T MRI. PC and SSFP sequences were used to quantify circumferential strain and distensibility. Both techniques produced comparable results, supporting the biomechanical suitability of CMBPTs for cardiovascular applications.

The failure test research showed that BPPs preserved in glutaraldehyde exhibit consistent thickness, with minimal intra- and inter-sample variability. No significant differences were detected between horizontal and vertical orientations in either thickness or elastic modulus, confirming structural homogeneity. BPPs exhibit relatively isotropic mechanical behavior, indicating that no specific orientation is needed during aortic reconstruction. The proposed PEM and MPEM concepts provide meaningful evaluation under realistic physiological conditions. Overall, BPPs demonstrated biomechanical properties that support their safe and effective application in cardiovascular surgery. Future studies should include *in vivo* assessments and histological analyses to evaluate remodeling behavior, long-term outcomes, and potential hemodynamic effects on cardiac and aortic tissue, see the graphic abstract in **Figure 53**.

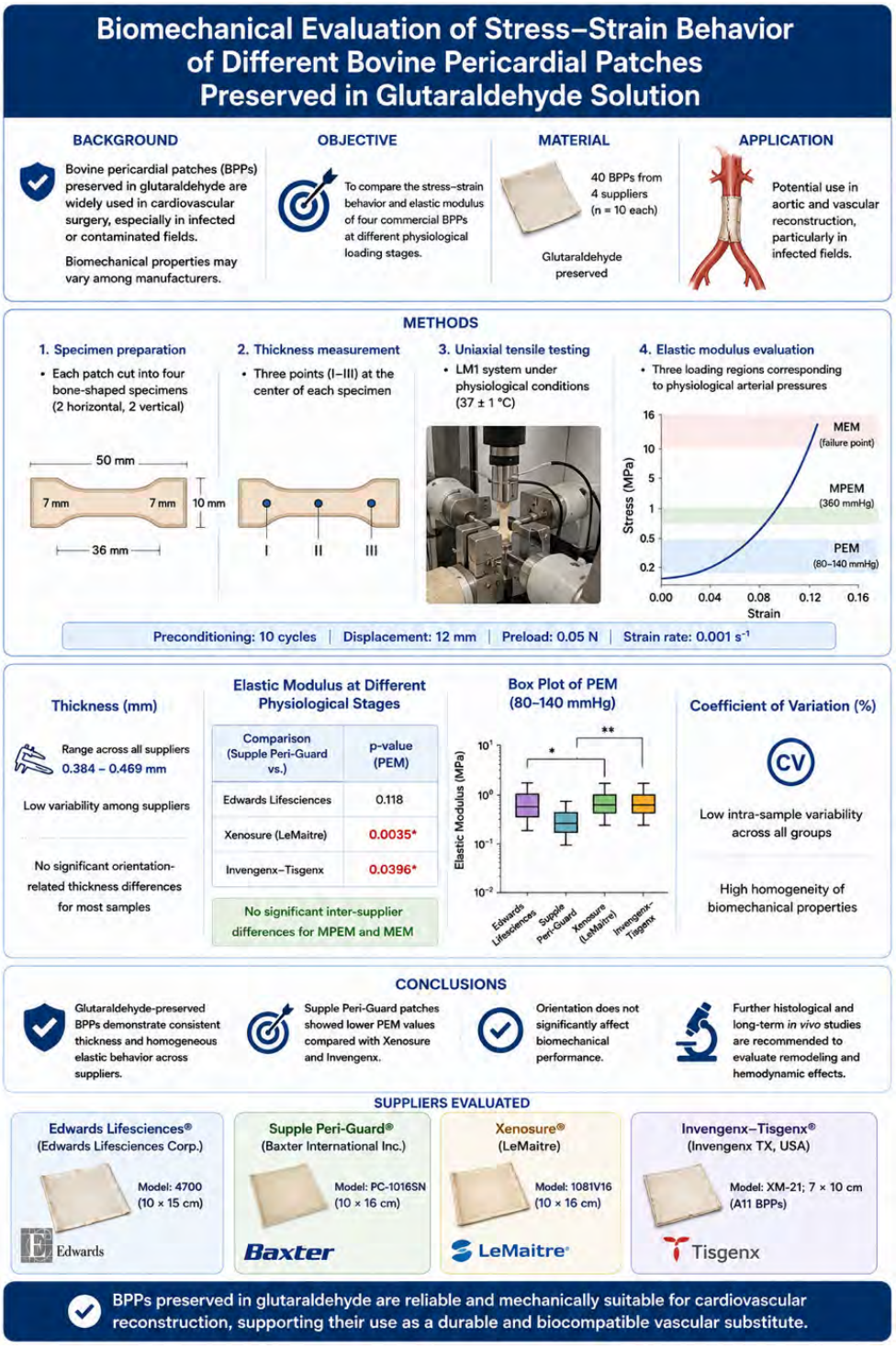


Figure 53.Graphical Abstract of failure test. the experimental design and principal findings. Forty commercially available glutaraldehyde-preserved BPPs from four manufacturers were evaluated using standardized uniaxial tensile testing. Commercial patches demonstrated comparable biomechanical behavior, low intra-sample variability, and no significant orientation-dependent differences, supporting their mechanical consistency for cardiovascular reconstruction.

The loss of energy test of BPPs from four commercial suppliers demonstrated comparable thickness and biomechanical behavior at 10% strain, with no significant intergroup differences in EDR. Although minor variability in thickness was observed, all values remained within the expected physiological range. At higher strain levels, a marked reduction in structural integrity was noted across materials, highlighting potential limitations under excessive mechanical stress. The EDR values observed fall within a clinically relevant biomechanical spectrum and may provide insight into elastic performance and tissue resilience. These findings support the overall mechanical consistency of currently available BPPs under moderate deformation, while emphasizing the need for further investigation under physiologic loading conditions. Future studies incorporating histological analysis to define the EDR threshold degeneration level and to simulate the intraoperative conditions, see the graphic abstract in **Figure 54**.

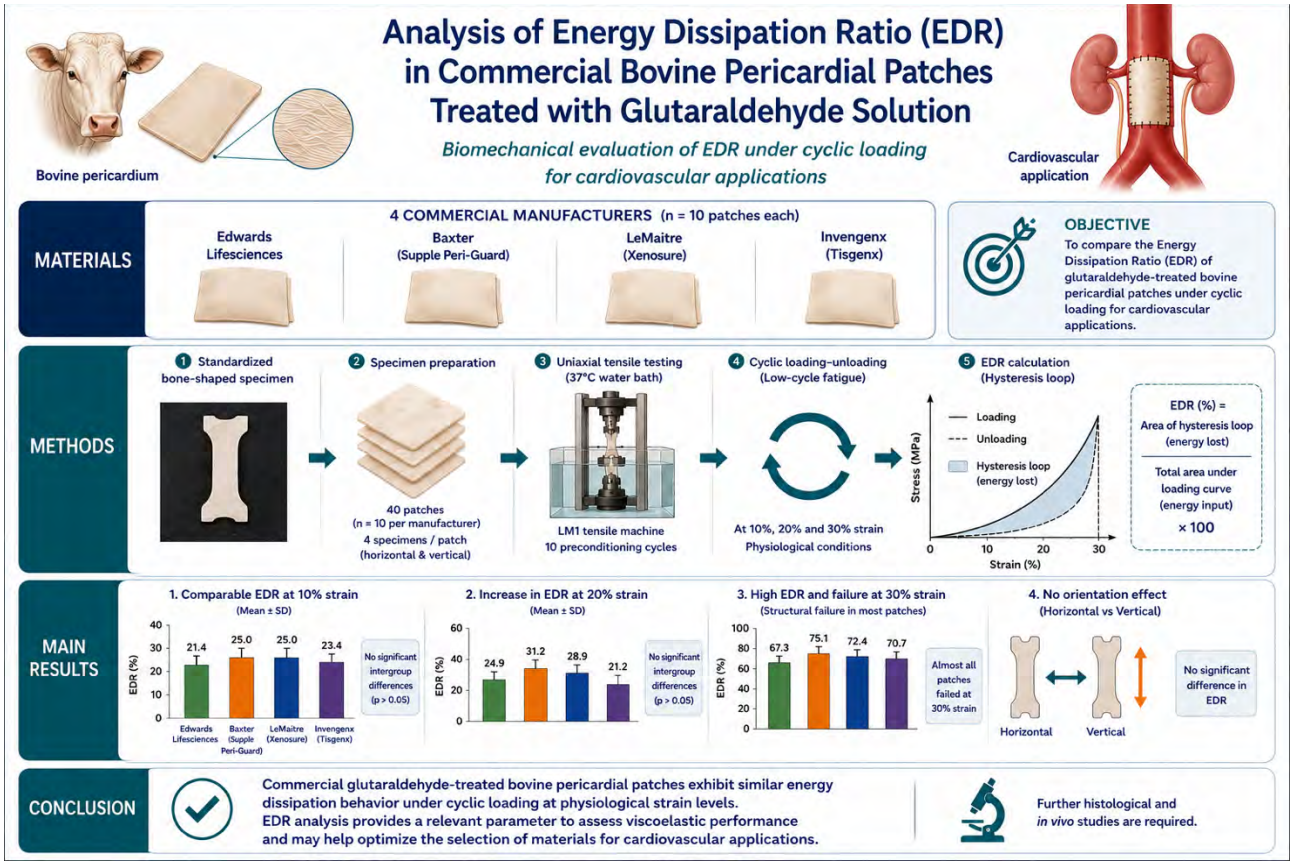


Figure 54.Graphical abstract. Commercial glutaraldehyde-preserved BPP from four manufacturers were evaluated using standardized uniaxial low-cycle fatigue testing. The EDR was calculated from stress–strain hysteresis loops. Comparable EDR values were observed at 10% strain, whereas structural failure increased at higher strain levels, supporting EDR as a useful biomechanical parameter for cardiovascular applications.

This study demonstrates that CMBPTs exhibit near-physiological strain with reduced distensibility, suggesting acceptable biomechanical performance for vascular reconstruction. BPPs showed consistent thickness, isotropic behavior, and no significant inter-supplier differences. Energy loss analysis confirmed mechanical stability under moderate strain but highlighted limitations at higher stress levels. Overall, these findings support the use of BPPs in cardiovascular surgery, although further in vivo and histological studies are required to assess long-term remodeling and hemodynamic impact.

References

Abolhoda, A., Yu, S., Oyarzun, J. R., McCormick, J. R., Bogden, J. D., & Gabbay, S. (1996). Calcification of bovine pericardium: Glutaraldehyde versus no-react biomodification. *The Annals of Thoracic Surgery*, *62*(1), 169–174. https://doi.org/10.1016/0003-4975(96)00277-9

Abramov, A., Xue, Y., Zakharchenko, A., Kurade, M., Soni, R. K., Levy, R. J., & Ferrari, G. (2023). Bioprosthetic heart valve structural degeneration associated with metabolic syndrome: Mitigation with polyoxazoline modification. *Proceedings of the National Academy of Sciences*, *120*(1), e2219054120. https://doi.org/10.1073/pnas.2219054120

Aguiari, P., Fiorese, M., Iop, L., Gerosa, G., & Bagno, A. (2016). Mechanical testing of pericardium for manufacturing prosthetic heart valves. *Interactive CardioVascular and Thoracic Surgery*, *22*(1), 72–84. https://doi.org/10.1093/icvts/ivv282

Ahmed, F., & Mohamed, N. G. (2021). TAG (Tube and Graft) Sandwich Technique: A Novel Single-Stage Scleral Reinforcement and Aqueous Drainage Tube Implantation. *Case Reports in Ophthalmological Medicine*, *2021*, 1–4. https://doi.org/10.1155/2021/6698919

Allen, D. J., DiDio, L. J., Zacharias, A., Fentie, I., McGrath, A. J., Puig, L. B., Pomerantzeff, P. N., & Zerbini, E. J. (1984). Microscopic study of normal parietal pericardium and unimplanted Puig-Zerbini pericardial valvular heterografts. *The Journal of Thoracic and Cardiovascular Surgery*, *87*(6), 845–855.

Amanuma, M., Mohiaddin, R. H., Hasegawa, M., Heshiki, A., & Longmore, D. B. (1992). Abdominal aorta: Characterisation of blood flow and measurement of its regional distribution by cine magnetic resonance phase-shift velocity mapping. *European Radiology*, *2*(6). https://doi.org/10.1007/BF00187552

Ao, S. I. & International Association of Engineers (Eds.). (2013). *The 2013 International Conference of Data Mining and Knowledge Engineering, the 2013 International Conference of Mechanical Engineering, the 2013 International Conference of Signal and Image Engineering*. IAENG.

Badran, H. M., Soltan, G., Faheem, N., Elnoamany, M. F., Tawfik, M., & Yacoub, M. (2015). Aortic biomechanics in hypertrophic cardiomyopathy. *Global Cardiology Science and Practice*, *2015*(2), 27. https://doi.org/10.5339/gcsp.2015.27

Baird, R. N., Kidson, I. G., L′Italien, G. J., & Abbott, W. M. (1977). Dynamic compliance of arterial grafts. *American Journal of Physiology-Heart and Circulatory Physiology*, *233*(5), H568–H572. https://doi.org/10.1152/ajpheart.1977.233.5.H568

Bakri, M., Lovato, F. C., Diosti, G. D. M., Salles, Y. L. S. D. G., Moreira, P. H. B., Collaço, L. M., Czeczko, N. G., Malafaia, O., & Kubrusly, L. F. (2021). COMPARATIVE ANALYSIS OF TISSULAR RESPONSE AFTER ABDOMINAL WALL REPAIR USING POLYPROPYLENE MESH AND BOVINE PERICARDIUM MESH. *ABCD. Arquivos Brasileiros de Cirurgia Digestiva (São Paulo)*, *34*(3), e1527. https://doi.org/10.1590/0102-672020200003e1527

Baldo, M. P., Cunha, R. S., Molina, M. del C. B., Chór, D., Griep, R. H., Duncan, B. B., Schmidt, M. I., Ribeiro, A. L. P., Barreto, S. M., Lotufo, P. A., Bensenor, I. M., Pereira, A. C., & Mill, J. G. (2018). Carotid-femoral pulse wave velocity in a healthy adult sample: The ELSA-Brasil study. *International Journal of Cardiology*, *251*, 90–95. https://doi.org/10.1016/j.ijcard.2017.10.075

Baldwin, M., Nagra, N. S., Greenall, G., Carr, A. J., Beard, D., Rees, J. L., Rangan, A., Merritt, N., Dritsaki, M., Hopewell, S., & Cook, J. A. (2020). Use of implantable meshes for augmented rotator cuff repair: A systematic review and meta-analysis. *BMJ Open*, *10*(12), e039552. https://doi.org/10.1136/bmjopen-2020-039552

Ballyk, P. D., Walsh, C., Butany, J., & Ojha, M. (1998). Compliance mismatch may promote graft-artery intimal hyperplasia by altering suture-line stresses. *Journal of Biomechanics*, *31*(3), 229–237. https://doi.org/10.1016/s0197-3975(97)00111-5

Belkorissat, R. A., Sadoul, C., Bouziane, Z., Saba, C., Salomon, C., Malikov, S., & Settembre, N. (2020). Tubular Reconstruction with Bovine Pericardium Xenografts to Treat Native Aortic

Infections. *Annals of Vascular Surgery*, *64*, 27–32. https://doi.org/10.1016/j.avsg.2019.10.104

Bell, V., Mitchell, W. A., Sigurðsson, S., Westenberg, J. J. M., Gotal, J. D., Torjesen, A. A., Aspelund, T., Launer, L. J., De Roos, A., Gudnason, V., Harris, T. B., & Mitchell, G. F. (2014). Longitudinal and Circumferential Strain of the Proximal Aorta. *Journal of the American Heart Association*, *3*(6), e001536. https://doi.org/10.1161/JAHA.114.001536

Bernabei, M., Margaryan, R., Arcieri, L., Bianchi, G., Pak, V., & Murzi, B. (2013). Aortic arch reconstruction in newborns with an autologous pericardial patch: Contemporary results. *Interactive CardioVascular and Thoracic Surgery*, *16*(3), 282–285. https://doi.org/10.1093/icvts/ivs510

Bertoglio, P., Garelli, E., Brandolini, J., Kawamukai, K., Antonacci, F., Ricciardi, S., Cipolli, A., Bonfanti, B., Forti Parri, S. N., Daddi, N., Dolci, G., & Solli, P. (2021). Surgical Management and Reconstruction of Diaphragm, Pericardium and Chest Wall in Mesothelioma Surgery: A Review. *Journal of Clinical Medicine*, *10*(11), 2330. https://doi.org/10.3390/jcm10112330

Biasi, G. (1996). Processed bovine pericardium as patch angioplasty for carotid endarterectomy: A preliminary report. *Cardiovascular Surgery*, *4*(5), 591–595. https://doi.org/10.1016/0967-2109(95)00086-0

Bieri, O., & Scheffler, K. (2013). Fundamentals of balanced steady state free precession MRI: Fundamentals of Balanced SSFP MRI. *Journal of Magnetic Resonance Imaging*, *38*(1), 2–11. https://doi.org/10.1002/jmri.24163

Biros, E., Gäbel, G., Moran, C. S., Schreurs, C., Lindeman, J. H. N., Walker, P. J., Nataatmadja, M., West, M., Holdt, L. M., Hinterseher, I., Pilarsky, C., & Golledge, J. (2015). Differential gene expression in human abdominal aortic aneurysm and aortic occlusive disease. *Oncotarget*, *6*(15), 12984–12996. https://doi.org/10.18632/oncotarget.3848

Blum, K. M., Zbinden, J. C., Ramachandra, A. B., Lindsey, S. E., Szafron, J. M., Reinhardt, J. W., Heitkemper, M., Best, C. A., Mirhaidari, G. J. M., Chang, Y.-C., Ulziibayar, A., Kelly, J.,

Shah, K. V., Drews, J. D., Zakko, J., Miyamoto, S., Matsuzaki, Y., Iwaki, R., Ahmad, H., … Breuer, C. K. (2022). Tissue engineered vascular grafts transform into autologous neovessels capable of native function and growth. *Communications Medicine*, *2*(1), 3. https://doi.org/10.1038/s43856-021-00063-7

Bohbot, Y., Renard, C., Manrique, A., Levy, F., Maréchaux, S., Gerber, B. L., & Tribouilloy, C. (2020). Usefulness of Cardiac Magnetic Resonance Imaging in Aortic Stenosis. *Circulation: Cardiovascular Imaging*, *13*(5), e010356. https://doi.org/10.1161/CIRCIMAGING.119.010356

Bouchet, M., Gauthier, M., Maire, M., Ajji, A., & Lerouge, S. (2019). Towards compliant small-diameter vascular grafts: Predictive analytical model and experiments. *Materials Science and Engineering: C*, *100*, 715–723. https://doi.org/10.1016/j.msec.2019.03.023

Braile-Sternieri, M. C. V. B., Goissis, G., Giglioti, A. D. F., Ramirez, V. D. A., Pereira, N. P., Vasconcellos, A., Basso-Frazzato, G. G., & Braile, D. M. (2020). In vivo evaluation of Vivere bovine pericardium valvular bioprosthesis with a new anti-calcifying treatment. *Artificial Organs*, *44*(11). https://doi.org/10.1111/aor.13718

Buxton, B. F., & Galvin, S. D. (2013). The history of arterial revascularization: From Kolesov to Tector and beyond. *Annals of Cardiothoracic Surgery*, *2*(4), 419–426. https://doi.org/10.3978/j.issn.2225-319X.2013.07.24

Cai, W.-J., Kocsis, E., Wu, X., Rodríguez, M., Luo, X., Schaper, W., & Schaper, J. (2004). Remodeling of the vascular tunica media is essential for development of collateral vessels in the canine heart. *Molecular and Cellular Biochemistry*, *264*(1/2), 201–210. https://doi.org/10.1023/B:MCBI.0000044389.65590.57

Camasão, D. B., & Mantovani, D. (2021). The mechanical characterization of blood vessels and their substitutes in the continuous quest for physiological-relevant performances. A critical review. *Materials Today Bio*, *10*, 100106. https://doi.org/10.1016/j.mtbio.2021.100106

Campion, G., Hershberger, K., Whelan, A., Conroy, J., Lally, C., & Murphy, B. P. (2021). A Biomechanical and Microstructural Analysis of Bovine and Porcine Pericardium for Use in

Bioprosthetic Heart Valves. *Structural Heart*, *5*(5), 486–496. https://doi.org/10.1080/24748706.2021.1938317

Catapano, F., Pambianchi, G., Cundari, G., Rebelo, J., Cilia, F., Carbone, I., Catalano, C., Francone, M., & Galea, N. (2020). 4D flow imaging of the thoracic aorta: Is there an added clinical value? *Cardiovascular Diagnosis and Therapy*, *10*(4), 1068–1089. https://doi.org/10.21037/cdt-20-452

Ceccopieri, C., Skonieczna, J., & Madej, J. P. (2021). Modification of a haematoxylin, eosin, and natural saffron staining method for the detection of connective tissue. *Journal of Veterinary Research*, *65*(1), 125–130. https://doi.org/10.2478/jvetres-2021-0008

Chan, B. P., & Leong, K. W. (2008). Scaffolding in tissue engineering: General approaches and tissue-specific considerations. *European Spine Journal*, *17*(S4), 467–479. https://doi.org/10.1007/s00586-008-0745-3

Chandran, P. L., Paik, D. C., & Holmes, J. W. (2012). Structural mechanism for alteration of collagen gel mechanics by glutaraldehyde crosslinking. *Connective Tissue Research*, *53*(4), 285–297. https://doi.org/10.3109/03008207.2011.640760

Chee, J., Durai, P., Wu, F., & Tiong, H. (2015). Bladder repair following iatrogenic cystotomy in irradiated small capacity bladders. *Singapore Medical Journal*, *56*(03), e49–e52. https://doi.org/10.11622/smedj.2015052

Chen, S., Xu, L., Liu, Y., Li, Q., Wang, D., Wang, X., & Liu, T. (2013). Donkey Pericardium as an Alternative Bioprosthetic Heart Valve Material. *Artificial Organs*, *37*(3), 248–255. https://doi.org/10.1111/j.1525-1594.2012.01549.x

Cheng, S., Clarke, E. C., & Bilston, L. E. (2009). The effects of preconditioning strain on measured tissue properties. *Journal of Biomechanics*, *42*(9), 1360–1362. https://doi.org/10.1016/j.jbiomech.2009.03.023

Chiquet-Ehrismann, R., Kalla, P., Pearson, C. A., Beck, K., & Chiquet, M. (1988). Tenascin interferes with fibronectin action. *Cell*, *53*(3), 383–390. https://doi.org/10.1016/0092-8674(88)90158-4

Chung, J., Lachapelle, K., Wener, E., Cartier, R., De Varennes, B., Fraser, R., & Leask, R. L. (2014). Energy loss, a novel biomechanical parameter, correlates with aortic aneurysm size and histopathologic findings. *The Journal of Thoracic and Cardiovascular Surgery*, *148*(3), 1082−1089. https://doi.org/10.1016/j.jtcvs.2014.06.021

Cocciolone, A. J., Hawes, J. Z., Staiculescu, M. C., Johnson, E. O., Murshed, M., & Wagenseil, J. E. (2018). Elastin, arterial mechanics, and cardiovascular disease. *American Journal of Physiology. Heart and Circulatory Physiology*, *315*(2), H189−H205. https://doi.org/10.1152/ajpheart.00087.2018

Concannon, J., Dockery, P., Black, A., Sultan, S., Hynes, N., McHugh, P. E., Moerman, K. M., & McGarry, J. P. (2020). Quantification of the regional bioarchitecture in the human aorta. *Journal of Anatomy*, *236*(1), 142−155. https://doi.org/10.1111/joa.13076

Costa, A., Naranjo, J. D., Londono, R., & Badylak, S. F. (2017). Biologic Scaffolds. *Cold Spring Harbor Perspectives in Medicine*, *7*(9), a025676. https://doi.org/10.1101/cshperspect.a025676

Courtman, D. W., Pereira, C. A., Kashef, V., McComb, D., Lee, J. M., & Wilson, G. J. (1994). Development of a pericardial acellular matrix biomaterial: Biochemical and mechanical effects of cell extraction. *Journal of Biomedical Materials Research*, *28*(6), 655−666. https://doi.org/10.1002/jbm.820280602

D′Ambra, L. (2012). Use of bovine pericardium graft for abdominal wall reconstruction in contaminated fields. *World Journal of Gastrointestinal Surgery*, *4*(7), 171. https://doi.org/10.4240/wjgs.v4.i7.171

Deanfield, J. E., Halcox, J. P., & Rabelink, T. J. (2007). Endothelial Function and Dysfunction: Testing and Clinical Relevance. *Circulation*, *115*(10), 1285−1295. https://doi.org/10.1161/CIRCULATIONAHA.106.652859

Di Giuseppe, M., Alotta, G., Agnese, V., Bellavia, D., Raffa, G. M., Vetri, V., Zingales, M., Pasta, S., & Pilato, M. (2019). Identification of circumferential regional heterogeneity of ascending

thoracic aneurysmal aorta by biaxial mechanical testing. *Journal of Molecular and Cellular Cardiology*, *130*, 205–215. https://doi.org/10.1016/j.yjmcc.2019.04.010

Di Lullo, G. A., Sweeney, S. M., Körkkö, J., Ala-Kokko, L., & San Antonio, J. D. (2002). Mapping the Ligand-binding Sites and Disease-associated Mutations on the Most Abundant Protein in the Human, Type I Collagen. *Journal of Biological Chemistry*, *277*(6), 4223–4231. https://doi.org/10.1074/jbc.M110709200

Dobrin, P. B. (1999). Distribution of Lamellar Deformations: Implications for Properties of the Arterial Media. *Hypertension*, *33*(3), 806–810. https://doi.org/10.1161/01.HYP.33.3.806

Donovan, D. L., Schmidt, S. P., Townshend, S. P., Njus, G. O., & Sharp, W. V. (1990). Material and structural characterization of human saphenous vein. *Journal of Vascular Surgery*, *12*(5), 531–537. https://doi.org/10.1016/0741-5214(90)90005-U

Duncan, A. C., & Boughner, D. (1998). Effect of dynamic glutaraldehyde fixation on the viscoelastic properties of bovine pericardial tissue. *Biomaterials*, *19*(7–9), 777–783. https://doi.org/10.1016/s0142-9612(97)00215-9

Duprey, A., Khanafer, K., Schlicht, M., Avril, S., Williams, D., & Berguer, R. (2010). In Vitro Characterisation of Physiological and Maximum Elastic Modulus of Ascending Thoracic Aortic Aneurysms Using Uniaxial Tensile Testing. *European Journal of Vascular and Endovascular Surgery*, *39*(6), Article 6. https://doi.org/10.1016/j.ejvs.2010.02.015

Ebert, N., McGinnis, M., Johnson, W., Kuhn, E. M., Mitchell, M. E., Tweddell, J. S., & Woods, R. K. (2021). Comparison of Patch Materials for Pulmonary Artery Reconstruction. *Seminars in Thoracic and Cardiovascular Surgery*, *33*(2), 459–465. https://doi.org/10.1053/j.semtcvs.2020.09.011

Epstein, N. (2013). A review article on the diagnosis and treatment of cerebrospinal fluid fistulas and dural tears occurring during spinal surgery. *Surgical Neurology International*, *4*(6), 301. https://doi.org/10.4103/2152-7806.111427

Erbel, R., Aboyans, V., Boileau, C., Bossone, E., Bartolomeo, R. D., Eggebrecht, H., Evangelista, A., Falk, V., Frank, H., Gaemperli, O., Grabenwöger, M., Haverich, A., Iung, B., Manolis,

A. J., Meijboom, F., Nienaber, C. A., Roffi, M., Rousseau, H., Sechtem, U., … ESC Committee for Practice Guidelines. (2014). 2014 ESC Guidelines on the diagnosis and treatment of aortic diseases: Document covering acute and chronic aortic diseases of the thoracic and abdominal aorta of the adult. The Task Force for the Diagnosis and Treatment of Aortic Diseases of the European Society of Cardiology (ESC). *European Heart Journal*, *35*(41), 2873–2926. https://doi.org/10.1093/eurheartj/ehu281

Fanous, N., Husain, S. A., Ruzmetov, M., Rodefeld, M. D., Turrentine, M. W., & Brown, J. W. (2010). Anterior pericardial tracheoplasty for long-segment tracheal stenosis: Long-term outcomes. *The Journal of Thoracic and Cardiovascular Surgery*, *139*(1), 18–25. https://doi.org/10.1016/j.jtcvs.2009.09.040

Fidalgo, C., Iop, L., Sciro, M., Harder, M., Mavrilas, D., Korossis, S., Bagno, A., Palù, G., Aguiari, P., & Gerosa, G. (2018). A sterilization method for decellularized xenogeneic cardiovascular scaffolds. *Acta Biomaterialia*, *67*, 282–294. https://doi.org/10.1016/j.actbio.2017.11.035

Foot, N. C. (1933). The Masson Trichrome Staining Methods in Routine Laboratory Use. *Stain Technology*, *8*(3), 101–110. https://doi.org/10.3109/10520293309116112

Frisch, S., Settembre, N., Belkorissat, R. A., Guerci, P., Mandry, D., AlblowI, A., Lalevee, L., Lefevre, B., & Malikov, S. (2025). Management of Infectious Aortic Aneurysms: Short- and Mid-TermOutcomes. *Annals of Vascular Surgery*, *115*, 197–205. https://doi.org/10.1016/j.avsg.2025.01.042

Fukushima, S., Uemura, M., Gotoh, K., Ujike, T., Wada, H., Miyagawa, S., Toda, K., & Sawa, Y. (2017). Xeno-pericardial patch repair of the inferior vena cava for radical resection of renal cell carcinoma with tumor thrombus. *Journal of Surgical Oncology*, *116*(6), 775–782. https://doi.org/10.1002/jso.24709

Fullybright, R. (2019). Characterization of Biological Resistance and Successful Drug Resistance Control in Medicine. *Pathogens*, *8*(2), 73. https://doi.org/10.3390/pathogens8020073

Garcia, J., Van Der Palen, R. L. F., Bollache, E., Jarvis, K., Rose, M. J., Barker, A. J., Collins, J. D., Carr, J. C., Robinson, J., Rigsby, C. K., & Markl, M. (2018). Distribution of blood flow

velocity in the normal aorta: Effect of age and gender. *Journal of Magnetic Resonance Imaging*, *47*(2), 487–498. https://doi.org/10.1002/jmri.25773

Gasser, T. C. (2021). *Vascular biomechanics: Concepts, models, and applications*. Springer.

Gilbert, T., Sellaro, T., & Badylak, S. (2006). Decellularization of tissues and organs. *Biomaterials*, S0142961206001682. https://doi.org/10.1016/j.biomaterials.2006.02.014

Girerd, X., Laurent, S., Pannier, B., Asmar, R., & Safar, M. (1991). Arterial distensibility and left ventricular hypertrophy in patients with sustained essential hypertension. *American Heart Journal*, *122*(4), 1210–1214. https://doi.org/10.1016/0002-8703(91)90941-A

Golomb, G., Schoen, F. J., Smith, M. S., Linden, J., Dixon, M., & Levy, R. J. (1987). The role of glutaraldehyde-induced cross-links in calcification of bovine pericardium used in cardiac valve bioprostheses. *The American Journal of Pathology*, *127*(1), 122–130.

Gomel, M. A., Lee, R., & Grande-Allen, K. J. (2019). Comparing the Role of Mechanical Forces in Vascular and Valvular Calcification Progression. *Frontiers in Cardiovascular Medicine*, *5*, 197. https://doi.org/10.3389/fcvm.2018.00197

Grant, C., Kfoury, E., Mukherjee, D., & Hashemi, H. (2016). The Efficacy of Patch Angioplasty for Maturation of Arteriovenous Fistulas. *Journal of Vascular Surgery*, *64*(3), 846. https://doi.org/10.1016/j.jvs.2016.06.040

Grover, V. P. B., Tognarelli, J. M., Crossey, M. M. E., Cox, I. J., Taylor-Robinson, S. D., & McPhail, M. J. W. (2015). Magnetic Resonance Imaging: Principles and Techniques: Lessons for Clinicians. *Journal of Clinical and Experimental Hepatology*, *5*(3), 246–255. https://doi.org/10.1016/j.jceh.2015.08.001

Hafeez, Y. M., Zuki, A. B. Z., Loqman, M. Y., Yusof, N., Asnah, H., & Noordin, M. M. (2004). Glycerol preserved bovine pericardium for abdominal wall reconstruction: Experimental study in rat model. *The Medical Journal of Malaysia*, *59 Suppl B*, 117–118.

Hanada, K., & Sasaki, T. (2018). Expression and purification of recombinant fibulins in mammalian cells. In *Methods in Cell Biology* (Vol. 143, pp. 247–259). Elsevier. https://doi.org/10.1016/bs.mcb.2017.08.014

Handa, K., Masai, T., Ohata, T., Sakamoto, T., & Kuratani, T. (2022). Long-term outcome of extensive mitral valve reconstruction with autologous pericardium and artificial chordae for treatment of destructive active infective endocarditis of the mitral valve. *Journal of Cardiothoracic Surgery*, *17*(1), 97. https://doi.org/10.1186/s13019-022-01851-5

Hedergott, A., Pink-Theofylaktopoulos, U., Neugebauer, A., & Fricke, J. (2021). Tendon elongation with bovine pericardium in strabismus surgery—Indications beyond Graves′ orbitopathy. *Graefe's Archive for Clinical and Experimental Ophthalmology*, *259*(1), 145–155. https://doi.org/10.1007/s00417-020-04939-7

Henry, M. J., Preventza, O., Cooley, D. A., De La Cruz, K. I., & Coselli, J. S. (2014). Left Ventricular Aneurysm Repair with Use of a Bovine Pericardial Patch. *Texas Heart Institute Journal*, *41*(4), 407–410. https://doi.org/10.14503/THIJ-13-3726

Herment, A., Lefort, M., Kachenoura, N., De Cesare, A., Taviani, V., Graves, M. J., Pellot-Barakat, C., Frouin, F., & Mousseaux, E. (2011). Automated estimation of aortic strain from steady-state free-precession and phase contrast MR images: Aortic Strain Estimation Using SSFP and PC Sequences. *Magnetic Resonance in Medicine*, *65*(4), 986–993. https://doi.org/10.1002/mrm.22678

Hess, F. (1985). History of (MICRO) vascular surgery and the development of small-caliber blood vessel prostheses (with some notes on patency rates and re-endothelialization). *Microsurgery*, *6*(2), 59–69. https://doi.org/10.1002/micr.1920060202

Ho, K. J., Nguyen, L. L., & Menard, M. T. (2012). Intermediate-term outcome of carotid endarterectomy with bovine pericardial patch closure compared with Dacron patch and primary closure. *Journal of Vascular Surgery*, *55*(3), 708–714. https://doi.org/10.1016/j.jvs.2011.10.007

Hua, X., Qian, R., Shi, K., Wei, X., Zhang, H., Qu, G., Chen, M., & Zhang, B. (2019). Effectiveness and safety of bovine pericardium patch repair for cervical anastomotic leakage after oesophagectomy for cancer. *Journal of Thoracic Disease*, *11*(9), 3808–3813. https://doi.org/10.21037/jtd.2019.09.12

Huang, X., Cai, H., & Lu, S.-Y. (2021). Iatrogenic femoral artery pseudoaneurysm surgically repaired with combined bovine pericardial roll and autologous great saphenous vein grafts. *Chinese Journal of Traumatology*, *24*(2), 75–78. https://doi.org/10.1016/j.cjtee.2020.11.001

Humphrey, J. D., & Holzapfel, G. A. (2012). Mechanics, mechanobiology, and modeling of human abdominal aorta and aneurysms. *Journal of Biomechanics*, *45*(5), 805–814. https://doi.org/10.1016/j.jbiomech.2011.11.021

Hytönen, J. P., Leppänen, O., Taavitsainen, J., Korpisalo, P., Laidinen, S., Alitalo, K., Wadström, J., Rissanen, T. T., & Ylä-Herttuala, S. (2019). Improved endothelialization of small-diameter ePTFE vascular grafts through growth factor therapy. *Vascular Biology*, *1*(1), 1–9. https://doi.org/10.1530/VB-18-0001

Ionescu, M. I., Tandon, A. P., Mary, D. A., & Abid, A. (1977). Heart valve replacement with the Ionescu-Shiley pericardial xenograft. *The Journal of Thoracic and Cardiovascular Surgery*, *73*(1), 31–42.

Iop, L., Palmosi, T., Dal Sasso, E., & Gerosa, G. (2018). Bioengineered tissue solutions for repair, correction and reconstruction in cardiovascular surgery. *Journal of Thoracic Disease*, *10*(S20), S2390–S2411. https://doi.org/10.21037/jtd.2018.04.27

Ishihara, T., Ferrans, V. J., Jones, M., Boyce, S. W., Kawanami, O., & Roberts, W. C. (1980). Histologic and ultrastructural features of normal human parietal pericardium. *The American Journal of Cardiology*, *46*(5), 744–753. https://doi.org/10.1016/0002-9149(80)90424-5

Jaworska-Wilczynska, M., Trzaskoma, P., Szczepankiewicz, A. A., & Hryniewiecki, T. (2016). Pericardium: Structure and function in health and disease. *Folia Histochemica Et Cytobiologica*, *54*(3), 121–125. https://doi.org/10.5603/FHC.a2016.0014

Jiang, S., Hu, H., Guo, C., Jiang, F., Liu, X., Tang, L., Tang, J., & Cheng, X. (2019). Thoracic tumor resection combined with SVC replacement using autologous pericardium. *World Journal of Surgical Oncology*, *17*(1), 227. https://doi.org/10.1186/s12957-019-1769-3

Johnston, D. R., Soltesz, E. G., Vakil, N., Rajeswaran, J., Roselli, E. E., Sabik, J. F., Smedira, N. G., Svensson, L. G., Lytle, B. W., & Blackstone, E. H. (2015). Long-Term Durability of

Bioprosthetic Aortic Valves: Implications From 12,569 Implants. *The Annals of Thoracic Surgery*, *99*(4), 1239–1247. https://doi.org/10.1016/j.athoracsur.2014.10.070

Kagawa, T., Yoshida, S., Shiraishi, T., Hashimoto, M., Inadomi, D., Sato, M., Tsuzuki, T., Miwa, K., & Yuasa, K. (2017). Basic principles of magnetic resonance imaging for beginner oral and maxillofacial radiologists. *Oral Radiology*, *33*(2), 92–100. https://doi.org/10.1007/s11282-017-0274-z

Karrouf, G., Zaghloul, A., & Abouelnasr, K. (2017). Repair of abdominal hernias in animals by glycerolized bovine pericardium and tunica vaginalis: A report of 22 clinical cases. *Animal Husbandry, Dairy and Veterinary Science*, *1*(1). https://doi.org/10.15761/AHDVS.1000103

Khanna, R., & Mokhtar, E. (2008). Bovine pericardium in treating large corneal perforation secondary to alkali injury: A case report. *Indian Journal of Ophthalmology*, *56*(5), 429. https://doi.org/10.4103/0301-4738.42426

Kim, H.-J., Lee, G.-W., Son, J.-W., Shin, K., Kim, H.-S., Ko, H.-C., Kim, B.-S., & Kim, M.-B. (2022). Venous Insufficiency is a Clear Provoker of Pigmented Purpuric Dermatosis. *Annals of Dermatology*, *34*(1), 34. https://doi.org/10.5021/ad.2022.34.1.34

Kim, S. Y., Hinkamp, T. J., Jacobs, W. R., Lichtenberg, R. C., Posniak, H., & Pifarré, R. (1995). Effect of an inelastic aortic synthetic vascular graft on exercise hemodynamics. *The Annals of Thoracic Surgery*, *59*(4), 981–989. https://doi.org/10.1016/0003-4975(95)00068-V

King, A. J., & Fink, G. D. (2006). Chronic Low-Dose Angiotensin II Infusion Increases Venomotor Tone by Neurogenic Mechanisms. *Hypertension*, *48*(5), 927–933. https://doi.org/10.1161/01.HYP.0000243799.84573.f8

Kleinstreuer, C., Li, Z., Basciano, C. A., Seelecke, S., & Farber, M. A. (2008). Computational mechanics of Nitinol stent grafts. *Journal of Biomechanics*, *41*(11), 2370–2378. https://doi.org/10.1016/j.jbiomech.2008.05.032

Kornhauser, S. I. (1952). Orcein and Elastic Fibers. *Stain Technology*, *27*(3), 131–134. https://doi.org/10.3109/10520295209105073

Kostyunin, A. E., Yuzhalin, A. E., Rezvova, M. A., Ovcharenko, E. A., Glushkova, T. V., & Kutikhin, A. G. (2020). Degeneration of Bioprosthetic Heart Valves: Update 2020. *Journal of the American Heart Association*, *9*(19), e018506. https://doi.org/10.1161/JAHA.120.018506

Kramer, C. M., Barkhausen, J., Bucciarelli-Ducci, C., Flamm, S. D., Kim, R. J., & Nagel, E. (2020). Standardized cardiovascular magnetic resonance imaging (CMR) protocols: 2020 update. *Journal of Cardiovascular Magnetic Resonance*, *22*(1), 17. https://doi.org/10.1186/s12968-020-00607-1

Kubota, H., Endo, H., Noma, M., Tsuchiya, H., Yoshimoto, A., Takahashi, Y., Inaba, Y., Matsukura, M., & Sudo, K. (2012). Equine pericardial roll graft replacement of infected pseudoaneurysm of the ascending aorta. *Journal of Cardiothoracic Surgery*, *7*(1), 54. https://doi.org/10.1186/1749-8090-7-54

Kuecherer, H. F., Just, A., & Kirchheim, H. (2000). Evaluation of aortic compliance in humans. *American Journal of Physiology-Heart and Circulatory Physiology*, *278*(5), H1411–H1413. https://doi.org/10.1152/ajpheart.2000.278.5.H1411

Kuralay, E. (2019). Pericardial patch closure of left atrial appendage orifice. *The Turkish Journal of Thoracic and Cardiovascular Surgery*, *27*(1), 127–129. https://doi.org/10.5606/tgkdc.dergisi.2019.14750

Laurent, S., & Boutouyrie, P. (2007). Arterial stiffness: A new surrogate end point for cardiovascular disease? *Journal of Nephrology*, *20 Suppl 12*, S45-50.

Lee, C., Lim, H.-G., Lee, C.-H., & Kim, Y. J. (2016). Effects of glutaraldehyde concentration and fixation time on material characteristics and calcification of bovine pericardium: Implications for the optimal method of fixation of autologous pericardium used for cardiovascular surgery. *Interactive CardioVascular and Thoracic Surgery*, ivw356. https://doi.org/10.1093/icvts/ivw356

Lee, J. M., & Boughner, D. R. (1985). Mechanical properties of human pericardium. Differences in viscoelastic response when compared with canine pericardium. *Circulation Research*, *57*(3), 475–481. https://doi.org/10.1161/01.RES.57.3.475

Lee, S., Levy, R. J., Christian, A. J., Hazen, S. L., Frick, N. E., Lai, E. K., Grau, J. B., Bavaria, J. E., & Ferrari, G. (2017). Calcification and Oxidative Modifications Are Associated With Progressive Bioprosthetic Heart Valve Dysfunction. *Journal of the American Heart Association*, *6*(5), e005648. https://doi.org/10.1161/JAHA.117.005648

Lehalle, B., Geschier, C., Fiévé, G., & Stoltz, J. F. (1997). Early rupture and degeneration of cryopreserved arterial allografts. *Journal of Vascular Surgery*, *25*(4), 751–752. https://doi.org/10.1016/S0741-5214(97)70305-7

Leon-Takahashi, A. M., Gomez-Pedraza, A., Cruz-Rodriguez, A., Ruiz-Molina, J. M., Padilla-Rosciano, A., & Herrera-Gomez, A. (2013). Use of Glutaraldehyde-Preserved Bovine Pericardium Patch in Vascular Repair of Portal Vein in a Patient with Pancreatic Cancer. *Indian Journal of Surgery*, *75*(S1), 247–249. https://doi.org/10.1007/s12262-012-0655-9

Leuprecht, A., Perktold, K., Prosi, M., Berk, T., Trubel, W., & Schima, H. (2002). Numerical study of hemodynamics and wall mechanics in distal end-to-side anastomoses of bypass grafts. *Journal of Biomechanics*, *35*(2), 225–236. https://doi.org/10.1016/S0021-9290(01)00194-4

Li, X., Guo, Y., Ziegler, K. R., Model, L. S., Eghbalieh, S. D. D., Brenes, R. A., Kim, S. T., Shu, C., & Dardik, A. (2011). Current Usage and Future Directions for the Bovine Pericardial Patch. *Annals of Vascular Surgery*, *25*(4), 561–568. https://doi.org/10.1016/j.avsg.2010.11.007

Liao, K. X., Seifter, E., Gong, G. F., Yellin, E. L., & Frater, R. W. (1991). Improved biocompatibility of bovine pericardium using a new method of cross linking. *ASAIO Transactions*, *37*(3), M175-176.

Liu, M., Liang, L., Sulejmani, F., Lou, X., Iannucci, G., Chen, E., Leshnower, B., & Sun, W. (2019). Identification of in vivo nonlinear anisotropic mechanical properties of ascending

thoracic aortic aneurysm from patient-specific CT scans. *Scientific Reports*, *9*(1), 12983. https://doi.org/10.1038/s41598-019-49438-w

Longo, U. G., Lamberti, A., Maffulli, N., & Denaro, V. (2010). Tendon augmentation grafts: A systematic review. *British Medical Bulletin*, *94*(1), 165–188. https://doi.org/10.1093/bmb/ldp051

Lopez-Dee, Z. P., Chittur, S. V., Patel, B., Stanton, R., Wakeley, M., Lippert, B., Menaker, A., Eiche, B., Terry, R., & Gutierrez, L. S. (2012). Thrombospondin-1 Type 1 Repeats in a Model of Inflammatory Bowel Disease: Transcript Profile and Therapeutic Effects. *PLoS ONE*, *7*(4), e34590. https://doi.org/10.1371/journal.pone.0034590

Lotz, J., Meier, C., Leppert, A., & Galanski, M. (2002). Cardiovascular flow measurement with phase-contrast MR imaging: Basic facts and implementation. *Radiographics: A Review Publication of the Radiological Society of North America, Inc*, *22*(3), 651–671. https://doi.org/10.1148/radiographics.22.3.g02ma11651

Mandal, T. K., Dhanuka, S., Choudhury, S., Mukhopadhyay, B. C., Kayal, A., Majhi, T. K., & Mondal, M. (2020). Tissue engineered indigenous pericardial patch urethroplasty: A promising solution to a nagging problem. *Asian Journal of Urology*, *7*(1), 56–60. https://doi.org/10.1016/j.ajur.2019.05.001

Mangold, M., Chaves, J. M., Blewett, C., & Williams, M. (2022). Infrarenal aortic dissection in a child after blunt trauma. *Journal of Vascular Surgery Cases, Innovations and Techniques*, *8*(2), 129–131. https://doi.org/10.1016/j.jvscit.2022.01.002

Mansour, M., Wilhite, D. R., & Rowe, J. (2018a). *Guide to ruminant anatomy: Dissection & clinical aspects*. John Wiley & Sons Inc.

Mansour, M., Wilhite, D. R., & Rowe, J. (2018b). *Guide to ruminant anatomy: Dissection & clinical aspects*. John Wiley & Sons Inc.

Mantini, C., Corradi, F., Mastrodicasa, D., Procaccini, L., Olivieri, M., Ricci, F., Cademartiri, F., Caulo, M., & De Caterina, R. (2021). A highly-detailed anatomical study of normal pericardial structures as revealed by in-vivo computed tomography and magnetic resonance

images and ex-vivo novel 3D reconstructions from Visible Human Server. *Imaging*, *13*(1), 1–12. https://doi.org/10.1556/1647.2021.00017

Massaglia, G., & Quaglio, M. (2018). Semiconducting Electrospun Nanofibers for Energy Conversion. In R. Inguanta & C. Sunseri (Eds.), *Semiconductors—Growth and Characterization*. InTech. https://doi.org/10.5772/intechopen.72817

Mavrilas, D., Sinouris, E. A., Vynios, D. H., & Papageorgakopoulou, N. (2005). Dynamic mechanical characteristics of intact and structurally modified bovine pericardial tissues. *Journal of Biomechanics*, *38*(4), 761–768. https://doi.org/10.1016/j.jbiomech.2004.05.019

Mehaffey, J. H., Perry, R. J., Pope, N. H., & Upchurch, G. R. (2016). Inferior vena cava reconstruction with tubularized bovine pericardium. *Journal of Vascular Surgery Cases*, *2*(1), 28–30. https://doi.org/10.1016/j.jvsc.2016.01.002

Mehigan, D. G., Fitzpatrick, B., Browne, H. I., & Bouchier-Hayes, D. J. (1985). Is compliance mismatch the major cause of anastomotic arterial aneurysms? Analysis of 42 cases. *The Journal of Cardiovascular Surgery*, *26*(2), 147–150.

Mehta, J. S. (2002). The sclera, the prion, and the ophthalmologist. *British Journal of Ophthalmology*, *86*(5), 587–592. https://doi.org/10.1136/bjo.86.5.587

Michel, J.-B. (2001). Contrasting Outcomes of Atheroma Evolution: Intimal Accumulation Versus Medial Destruction. *Arteriosclerosis, Thrombosis, and Vascular Biology*, *21*(9), 1389–1392. https://doi.org/10.1161/atvb.21.9.1389

Millasseau, S. C., Stewart, A. D., Patel, S. J., Redwood, S. R., & Chowienczyk, P. J. (2005). Evaluation of Carotid-Femoral Pulse Wave Velocity: Influence of Timing Algorithm and Heart Rate. *Hypertension*, *45*(2), 222–226. https://doi.org/10.1161/01.HYP.0000154229.97341.d2

Mishani, S., Belhoul-Fakir, H., Lagat, C., Jansen, S., Evans, B., & Lawrence-Brown, M. (2021). Stress distribution in the walls of major arteries: Implications for atherogenesis. *Quantitative Imaging in Medicine and Surgery*, *11*(8), 3494–3505. https://doi.org/10.21037/qims-20-614

Miura, K. (2020). Tunica intima compensation for reduced stiffness of the tunica media in aging renal arteries as measured with scanning acoustic microscopy. *PLOS ONE*, *15*(11), e0234759. https://doi.org/10.1371/journal.pone.0234759

Miyabe, M. M., Murphy, K. P., Oria, M., Duru, S., Lin, C.-Y., & Peiro, J. L. (2022). Dural substitutes for spina bifida repair: Past, present, and future. *Child's Nervous System*, *38*(5), 873–891. https://doi.org/10.1007/s00381-022-05486-8

Moon, S. J., Kim, D. H., Jo, J. K., Chung, J. H., Lee, J. Y., Park, S. Y., Kim, Y. T., Park, H. K., Choi, H. Y., & Moon, H. S. (2011). Bladder Reconstruction Using Bovine Pericardium in a Case of Enterovesical Fistula. *Korean Journal of Urology*, *52*(2), 150. https://doi.org/10.4111/kju.2011.52.2.150

Moore, M. A., & Adams, A. K. (2001). Calcification resistance, biostability, and low immunogenic potential of porcine heart valves modified by dye-mediated photooxidation. *Journal of Biomedical Materials Research*, *56*(1), 24–30. https://doi.org/10.1002/1097-4636(200107)56:1<24::AID-JBM1064>3.0.CO;2-Q

Muiznieks, L. D., Weiss, A. S., & Keeley, F. W. (2010). Structural disorder and dynamics of elastinThis paper is one of a selection of papers published in this special issue entitled "Canadian Society of Biochemistry, Molecular & Cellular Biology 52nd Annual Meeting — Protein Folding: Principles and Diseases" and has undergone the Journal's usual peer review process. *Biochemistry and Cell Biology*, *88*(2), 239–250. https://doi.org/10.1139/O09-161

Müller-Schweinitzer, E. (2009). Cryopreservation of vascular tissues. *Organogenesis*, *5*(3), 97–104. https://doi.org/10.4161/org.5.3.9495

Nabeshima, J., Mizuno, T., & Nagaoka, E. (2022). Bovine pericardial patch repair for abdominal aortic pseudoaneurysm to preserve lumbar arteries. *Interactive CardioVascular and Thoracic Surgery*, *35*(6), ivac261. https://doi.org/10.1093/icvts/ivac261

Naegeli, K. M., Kural, M. H., Li, Y., Wang, J., Hugentobler, E. A., & Niklason, L. E. (2022). Bioengineering Human Tissues and the Future of Vascular Replacement. *Circulation Research*, *131*(1), 109–126. https://doi.org/10.1161/CIRCRESAHA.121.319984

Nakamura, H., Kanai, C., & Mizuhira, V. (1977). An electron stain for elastic fibers using orcein. *The Journal of Histochemistry and Cytochemistry: Official Journal of the Histochemistry Society*, *25*(4), 306–308. https://doi.org/10.1177/25.4.858912

Narloch, J. A., & Brandstater, M. E. (1995). Influence of breathing technique on arterial blood pressure during heavy weight lifting. *Archives of Physical Medicine and Rehabilitation*, *76*(5), 457–462. https://doi.org/10.1016/S0003-9993(95)80578-8

Newman, D. L., & Greenwald, S. E. (1978). Validity of the Moens-Korteweg Equation. In R. D. Bauer & R. Busse (Eds.), *The Arterial System* (pp. 109–115). Springer Berlin Heidelberg. https://doi.org/10.1007/978-3-642-67020-6_10

Nguyen, K. P., McGilvray, K. C., Puttlitz, C. M., Mukhopadhyay, S., Chabasse, C., & Sarkar, R. (2015). Matrix Metalloproteinase 9 (MMP-9) Regulates Vein Wall Biomechanics in Murine Thrombus Resolution. *PLOS ONE*, *10*(9), e0139145. https://doi.org/10.1371/journal.pone.0139145

Noronen, K., Söderström, M., Kouhia, S., & Venermo, M. (2023). Bovine pericardial patch: A good alternative in femoral angioplasty. *Journal of Vascular Surgery*, *77*(1), 225–230. https://doi.org/10.1016/j.jvs.2022.08.010

Oliver, J. J., & Webb, D. J. (2003). Noninvasive Assessment of Arterial Stiffness and Risk of Atherosclerotic Events. *Arteriosclerosis, Thrombosis, and Vascular Biology*, *23*(4), 554–566. https://doi.org/10.1161/01.ATV.0000060460.52916.D6

Olmos-Zuñiga, J. R., Jasso-Victoria, R., Gaxiola-Gaxiola, M., Sotres-Vega, A., Hernández-Jiménez, C., Baltazares-Lipp, M., Arredondo Del Bosque, F., & Santillan-Doherty, P. (2015). Comparison of Lyophilized Glutaraldehyde-Preserved Bovine Pericardium with Different Vascular Prostheses for Use as Vocal Cords Implants: Experimental Study. *BioMed Research International*, *2015*, 1–9. https://doi.org/10.1155/2015/351862

O′Rourke, M. F., & Safar, M. E. (2005). Relationship Between Aortic Stiffening and Microvascular Disease in Brain and Kidney: Cause and Logic of Therapy. *Hypertension*, *46*(1), 200–204. https://doi.org/10.1161/01.HYP.0000168052.00426.65

Osinnski, J. N., Ku, D. N., Mukundan, S., Loth, F., & Pettigrew, R. I. (1995). Determination of wall shear stress in the aorta with the use of MR phase velocity mapping. *Journal of Magnetic Resonance Imaging*, *5*(6), 640–647. https://doi.org/10.1002/jmri.1880050605

Osler, W. (1885). The Gulstonian Lectures, on Malignant Endocarditis. *British Medical Journal*, *1*(1262), 467–470. https://doi.org/10.1136/bmj.1.1262.467

Oswal, D., Korossis, S., Mirsadraee, S., Wilcox, H., Watterson, K., Fisher, J., & Ingham, E. (2007). Biomechanical characterization of decellularized and cross-linked bovine pericardium. *The Journal of Heart Valve Disease*, *16*(2), 165–174.

Otero, J., Gómez, B., Polo, J., Mateo, C., Barreras, S., Cruz, E., De La Viña, J. L. R., & Antolín, A. (2017). Use of a lyophilized bovine pericardium graft to repair tunical defect in patients with Peyronie's disease: Experience in a clinical setting. *Asian Journal of Andrology*, *19*(3), 316. https://doi.org/10.4103/1008-682X.171572

Ovalle, W. K., & Nahirney, P. C. (Eds.). (2021). *Netter's essential histology: With correlated histopathology* (Third edition). Elsevier.

Papakostas, J. C., Avgos, S., Arnaoutoglou, E., Nassis, C., Peroulis, M., Bali, C., Papadopoulos, G., & Matsagkas, M. I. (2014). Use of the Vascu-Guard Bovine Pericardium Patch for Arteriotomy Closure in Carotid Endarterectomy. Early and Long-Term Results. *Annals of Vascular Surgery*, *28*(5), 1213–1218. https://doi.org/10.1016/j.avsg.2013.10.021

Park, C. S., Kim, Y. J., Lee, J. R., Lim, H.-G., Chang, J.-E., Jeong, S., & Kwon, N. (2017). Anticalcification effect of a combination of decellularization, organic solvents and amino acid detoxification on glutaraldehyde-fixed xenopericardial heart valves in a large-animal long-term circulatory model. *Interactive CardioVascular and Thoracic Surgery*, *25*(3), 391–399. https://doi.org/10.1093/icvts/ivx131

Pathak, C. P., Adams, A. K., Simpson, T., Phillips, R. E., & Moore, M. A. (2004). Treatment of bioprosthetic heart valve tissue with long chain alcohol solution to lower calcification potential. *Journal of Biomedical Materials Research*, *69A*(1), 140–144. https://doi.org/10.1002/jbm.a.20129

Patukale, A., Shikata, F., Marathe, S. S., Patel, P., Marathe, S. P., Colen, T., Venugopal, P., QPCR Group, Suna, J., Betts, K., Karl, T. R., Johnson, J., Versluis, K., & Alphonso, N. (2022). A single-centre, retrospective study of mid-term outcomes of aortic arch repair using a standardized resection and patch augmentation technique. *Interactive CardioVascular and Thoracic Surgery*, *35*(3), ivac135. https://doi.org/10.1093/icvts/ivac135

Peebles, C. R., Shambrook, J. S., & Harden, S. P. (2011). Pericardial disease—Anatomy and function. *The British Journal of Radiology*, *84*(special_issue_3), S324–S337. https://doi.org/10.1259/bjr/16168253

Peivandi, A. D., Martens, S., Heitplatz, B., Guseva, A., Mueller, K.-M., & Martens, S. (2022). Industrial Processing Induces Pericardial Patch Degeneration. *Frontiers in Surgery*, *9*, 881433. https://doi.org/10.3389/fsurg.2022.881433

Peng, Y. Y., Glattauer, V., & Ramshaw, J. A. M. (2017). Stabilisation of Collagen Sponges by Glutaraldehyde Vapour Crosslinking. *International Journal of Biomaterials*, *2017*, 8947823. https://doi.org/10.1155/2017/8947823

Pok, S., Stupin, I. V., Tsao, C., Pautler, R. G., Gao, Y., Nieto, R. M., Tao, Z., Fraser, C. D., Annapragada, A. V., & Jacot, J. G. (2017). Full-Thickness Heart Repair with an Engineered Multilayered Myocardial Patch in Rat Model. *Advanced Healthcare Materials*, *6*(5), 1600549. https://doi.org/10.1002/adhm.201600549

Radhakrishnan, N. (2022). Etiology of varicose veins. In *Genesis, Pathophysiology and Management of Venous and Lymphatic Disorders* (pp. 139–144). Elsevier. https://doi.org/10.1016/B978-0-323-88433-4.00022-X

Ravi, S., & Chaikof, E. L. (2010). Biomaterials for vascular tissue engineering. *Regenerative Medicine*, *5*(1), 107–120. https://doi.org/10.2217/rme.09.77

Redheuil, A., Yu, W.-C., Wu, C. O., Mousseaux, E., de Cesare, A., Yan, R., Kachenoura, N., Bluemke, D., & Lima, J. A. C. (2010). Reduced Ascending Aortic Strain and Distensibility: Earliest Manifestations of Vascular Aging in Humans. *Hypertension*, *55*(2), 319–326. https://doi.org/10.1161/HYPERTENSIONAHA.109.141275

Rodriguez, E. R., & Tan, C. D. (2017). Structure and Anatomy of the Human Pericardium. *Progress in Cardiovascular Diseases*, *59*(4), 327–340. https://doi.org/10.1016/j.pcad.2016.12.010

Rogers, I. S., Massaro, J. M., Truong, Q. A., Mahabadi, A. A., Kriegel, M. F., Fox, C. S., Thanassoulis, G., Isselbacher, E. M., Hoffmann, U., & O′Donnell, C. J. (2013). Distribution, Determinants, and Normal Reference Values of Thoracic and Abdominal Aortic Diameters by Computed Tomography (from the Framingham Heart Study). *The American Journal of Cardiology*, *111*(10), 1510–1516. https://doi.org/10.1016/j.amjcard.2013.01.306

Rose, J.-L., Lalande, A., Bouchot, O., Bourennane, E.-B., Walker, P. M., Ugolini, P., Revol-Muller, C., Cartier, R., & Brunotte, F. (2010). Influence of age and sex on aortic distensibility assessed by MRI in healthy subjects. *Magnetic Resonance Imaging*, *28*(2), 255–263. https://doi.org/10.1016/j.mri.2009.07.001

Ross, M. H., & Pawlina, W. (2016). *Histology: A text and atlas: with correlated cell and molecular biology* (Seventh edition). Wolters Kluwer Health.

Sacks, M. S., Chuong, C. J. C., & More, R. (1994). Collagen Fiber Architecture of Bovine Pericardium. *ASAIO Journal*, *40*(3). https://journals.lww.com/asaiojournal/Fulltext/1994/07000/Collagen_Fiber_Architecture_of_Bovine_Pericardium.75.aspx

Saiding, Q., Chen, Y., Wang, J., Pereira, C. L., Sarmento, B., Cui, W., & Chen, X. (2023). Abdominal wall hernia repair: From prosthetic meshes to smart materials. *Materials Today Bio*, *21*, 100691. https://doi.org/10.1016/j.mtbio.2023.100691

Sakalihasan, N., Michel, J.-B., Katsargyris, A., Kuivaniemi, H., Defraigne, J.-O., Nchimi, A., Powell, J. T., Yoshimura, K., & Hultgren, R. (2018). Abdominal aortic aneurysms. *Nature Reviews Disease Primers*, *4*(1), 34. https://doi.org/10.1038/s41572-018-0030-7

Salman, H. E., Saltik, L., & Yalcin, H. C. (2021). Computational Analysis of Wall Shear Stress Patterns on Calcified and Bicuspid Aortic Valves: Focus on Radial and Coaptation Patterns. *Fluids*, *6*(8), 287. https://doi.org/10.3390/fluids6080287

Salvi, P. (2017). *Pulse Waves: How Vascular Hemodynamics Affects Blood Pressure* (2nd ed. 2017). Springer International Publishing : Imprint: Springer. https://doi.org/10.1007/978-3-319-40501-8

Sang, C., Maiti, S., Fortunato, R. N., Kofler, J., & Robertson, A. M. (2018). A Uniaxial Testing Approach for Consistent Failure in Vascular Tissues. *Journal of Biomechanical Engineering*, *140*(6), 061010. https://doi.org/10.1115/1.4039577

Santilli, S. M., Littooy, F. N., Cambria, R. A., Rapp, J. H., Tretinyak, A. S., d'Audiffret, A. C., Kuskowski, M. A., Roethle, S. T., Tomczak, C. M., & Krupski, W. C. (2002). Expansion rates and outcomes for the 3.0-cm to the 3.9-cm infrarenal abdominal aortic aneurysm. *Journal of Vascular Surgery*, *35*(4), 666–671. https://doi.org/10.1067/mva.2002.121572

Schahab, N., Würbel, S., Busch, L., & Nickenig, G. (2025). Abdominal aortic aneurysm progression: A review of preclinical and clinical data. *Clinical Research in Cardiology*. https://doi.org/10.1007/s00392-025-02764-8

Schatzmann, L. (1998). Effect of cyclic preconditioning on the tensile properties of human quadriceps tendons and patellar ligaments. *Knee Surgery, Sports Traumatology, Arthroscopy*, *6*(0), S56–S61. https://doi.org/10.1007/s001670050224

Shinkawa, T., Anagnostopoulos, P. V., Johnson, N. C., Watanabe, N., Sapru, A., & Azakie, A. (2010). Performance of Bovine Pericardial Valves in the Pulmonary Position. *The Annals of Thoracic Surgery*, *90*(4), 1295–1300. https://doi.org/10.1016/j.athoracsur.2010.06.021

Shklover, J., McMasters, J., Alfonso-Garcia, A., Higuita, M. L., Panitch, A., Marcu, L., & Griffiths, L. (2019). Bovine pericardial extracellular matrix niche modulates human aortic endothelial cell phenotype and function. *Scientific Reports*, *9*(1), 16688. https://doi.org/10.1038/s41598-019-53230-1

SIDAWY, A. P. P. & BRUCE A. (2022). *RUTHERFORD'S VASCULAR SURGERY AND ENDOVASCULAR THERAPY.* ELSEVIER - HEALTH SCIENCE.

Simionescu, D., Simionescu, A., & Deac, R. (1993). Mapping of glutaraldehyde-treated bovine pericardium and tissue selection for bioprosthetic heart valves. *Journal of Biomedical Materials Research*, *27*(6), 697–704. https://doi.org/10.1002/jbm.820270602

Sizeland, K. H., Wells, H. C., Higgins, J., Cunanan, C. M., Kirby, N., Hawley, A., Mudie, S. T., & Haverkamp, R. G. (2014). Age Dependent Differences in Collagen Alignment of Glutaraldehyde Fixed Bovine Pericardium. *BioMed Research International*, *2014*, 1–10. https://doi.org/10.1155/2014/189197

Snell, R. S. (2007). *Clinical anatomy by systems*. Lippincott Williams & Wilkins.

Snell, Richard S. (2012). *Clinical anatomy by regions* (9th ed.). MD: Wolters Kluwer/Lippincott Williams & Wilkins.

Soletti, L., Hong, Y., Guan, J., Stankus, J. J., El-Kurdi, M. S., Wagner, W. R., & Vorp, D. A. (2010). A bilayered elastomeric scaffold for tissue engineering of small diameter vascular grafts. *Acta Biomaterialia*, *6*(1), 110–122. https://doi.org/10.1016/j.actbio.2009.06.026

Sörelius, K., Mani, K., Björck, M., Sedivy, P., Wahlgren, C.-M., Taylor, P., Clough, R. E., Lyons, O., Thompson, M., Brownrigg, J., Ivancev, K., Davis, M., Jenkins, M. P., Jaffer, U., Bown, M., Rancic, Z., Mayer, D., Brunkwall, J., Gawenda, M., … Wanhainen, A. (2014). Endovascular Treatment of Mycotic Aortic Aneurysms: A European Multicenter Study. *Circulation*, *130*(24), 2136–2142. https://doi.org/10.1161/CIRCULATIONAHA.114.009481

Spadaccio, C., Nappi, F., Al-Attar, N., Sutherland, F. W., Acar, C., Nenna, A., Trombetta, M., Chello, M., & Rainer, A. (2016). Old Myths, New Concerns: The Long-Term Effects of Ascending Aorta Replacement with Dacron Grafts. Not All That Glitters Is Gold. *Journal of Cardiovascular Translational Research*, *9*(4), 334–342. https://doi.org/10.1007/s12265-016-9699-8

Spodick, D. H. (1992). Macrophysiology, microphysiology, and anatomy of the pericardium: A synopsis. *American Heart Journal*, *124*(4), 1046–1051. https://doi.org/10.1016/0002-8703(92)90990-D

Springer, T. A., & Wang, J.-H. (2004). The Three-Dimensional Structure of Integrins and their Ligands, and Conformational Regulation of Cell Adhesion. In *Advances in Protein Chemistry* (Vol. 68, pp. 29–63). Elsevier. https://doi.org/10.1016/S0065-3233(04)68002-8

Stekelenburg, M., Rutten, M. C. M., Snoeckx, L. H. E. H., & Baaijens, F. P. T. (2009). Dynamic Straining Combined with Fibrin Gel Cell Seeding Improves Strength of Tissue-Engineered Small-Diameter Vascular Grafts. *Tissue Engineering Part A*, *15*(5), 1081–1089. https://doi.org/10.1089/ten.tea.2008.0183

Stieglmeier, F., Grab, M., König, F., Büch, J., Hagl, C., & Thierfelder, N. (2021). Mapping of bovine pericardium to enable a standardized acquirement of material for medical implants. *Journal of the Mechanical Behavior of Biomedical Materials*, *118*, 104432. https://doi.org/10.1016/j.jmbbm.2021.104432

Stone, P. A., AbuRahma, A. F., Mousa, A. Y., Phang, D., Hass, S. M., Modak, A., & Dearing, D. (2014). Prospective randomized trial of ACUSEAL versus Vascu-Guard patching in carotid endarterectomy. *Annals of Vascular Surgery*, *28*(6), 1530–1538. https://doi.org/10.1016/j.avsg.2014.02.017

Sultan, S., Acharya, Y., Soliman, O., Parodi, J. C., & Hynes, N. (2022). TEVAR and EVAR, the unknown knowns of the cardiovascular hemodynamics; and the immediate and long-term consequences of fabric material on major adverse clinical outcome. *Frontiers in Surgery*, *9*, 940304. https://doi.org/10.3389/fsurg.2022.940304

Surovtsova, I. (2005). Effects of compliance mismatch on blood flow in an artery with endovascular prosthesis. *Journal of Biomechanics*, *38*(10), 2078–2086. https://doi.org/10.1016/j.jbiomech.2004.09.004

Tai, N. R., Salacinski, H. J., Edwards, A., Hamilton, G., & Seifalian, A. M. (2000). Compliance properties of conduits used in vascular reconstruction. *Journal of British Surgery*, *87*(11), 1516–1524. https://doi.org/10.1046/j.1365-2168.2000.01566.x

Talwar, S., Das, A., Siddarth, B., Choudhary, S. K., & Airan, B. (2019). Patch materials for right ventricular outflow reconstruction: Past, present, and future. *Indian Journal of Thoracic and Cardiovascular Surgery*, *35*(1), 41–50. https://doi.org/10.1007/s12055-017-0621-z

Tanjore, H., & Kalluri, R. (2006). The Role of Type IV Collagen and Basement Membranes in Cancer Progression and Metastasis. *The American Journal of Pathology*, *168*(3), 715–717. https://doi.org/10.2353/ajpath.2006.051321

Texakalidis, P., Giannopoulos, S., Charisis, N., Giannopoulos, S., Karasavvidis, T., Koullias, G., & Jabbour, P. (2018). A meta-analysis of randomized trials comparing bovine pericardium and other patch materials for carotid endarterectomy. *Journal of Vascular Surgery*, *68*(4), 1241-1256.e1. https://doi.org/10.1016/j.jvs.2018.07.023

Thubrikar, M. (2007). *Vascular mechanics and pathology*. Springer.

Töpel, I., Uhl, C., Ayx, I., & Steinbauer, M. (2016). Xenografts in septic vascular surgery. *Gefässchirurgie*, *21*(S2), 55–58. https://doi.org/10.1007/s00772-016-0160-8

Trębacz, H., & Barzycka, A. (2023). Mechanical Properties and Functions of Elastin: An Overview. *Biomolecules*, *13*(3), 574. https://doi.org/10.3390/biom13030574

Tremblay, D., Zigras, T., Cartier, R., Leduc, L., Butany, J., Mongrain, R., & Leask, R. L. (2009). A Comparison of Mechanical Properties of Materials Used in Aortic Arch Reconstruction. *The Annals of Thoracic Surgery*, *88*(5), 1484–1491. https://doi.org/10.1016/j.athoracsur.2009.07.023

Vallerio, P., Maloberti, A., D′Alessio, I., Lista, A., Varrenti, M., Castelnuovo, S., Marone, M., Piccinelli, E., Grassi, G., Palmieri, B., & Giannattasio, C. (2019). Cardiovascular Remodeling after Endovascular Treatment for Thoracic Aortic Injury. *Annals of Vascular Surgery*, *61*, 134–141. https://doi.org/10.1016/j.avsg.2019.04.015

van Bakel, T. M. J., Arthurs, C. J., Nauta, F. J. H., Eagle, K. A., van Herwaarden, J. A., Moll, F. L., Trimarchi, S., Patel, H. J., & Figueroa, C. A. (2019). Cardiac remodelling following thoracic endovascular aortic repair for descending aortic aneurysms. *European Journal of Cardio-*

Thoracic Surgery: Official Journal of the European Association for Cardio-Thoracic Surgery, *55*(6), 1061–1070. https://doi.org/10.1093/ejcts/ezy399

Velho, T. R., Pereira, R. M., Fernandes, F., Guerra, N. C., Ferreira, R., & Nobre, Â. (2022). Bioprosthetic Aortic Valve Degeneration: A Review from a Basic Science Perspective. *Brazilian Journal of Cardiovascular Surgery*, *37*(2). https://doi.org/10.21470/1678-9741-2020-0635

Voges, I., Jerosch-Herold, M., Hedderich, J., Pardun, E., Hart, C., Gabbert, D. D., Hansen, J. H., Petko, C., Kramer, H.-H., & Rickers, C. (2012). Normal values of aortic dimensions, distensibility, and pulse wave velocity in children and young adults: A cross-sectional study. *Journal of Cardiovascular Magnetic Resonance*, *14*(1), 77. https://doi.org/10.1186/1532-429X-14-77

Vondrášek, D., Hadraba, D., Matějka, R., Lopot, F., Svoboda, M., & Jelen, K. (2018). Uniaxial Tensile Testing Device for Measuring Mechanical Properties of Biological Tissue with Stress-Relaxation Test under a Confocal Microscope. *Manufacturing Technology*, *18*(5), 866–872. https://doi.org/10.21062/ujep/192.2018/a/1213-2489/MT/18/5/866

Wagenseil, J. E., & Mecham, R. P. (2009). Vascular Extracellular Matrix and Arterial Mechanics. *Physiological Reviews*, *89*(3), 957–989. https://doi.org/10.1152/physrev.00041.2008

Walker, S., Dittfeld, C., Jakob, A., Schönfelder, J., König, U., & Tugtekin, S.-M. (2022). Sterilization and Cross-Linking Combined with Ultraviolet Irradiation and Low-Energy Electron Irradiation Procedure: New Perspectives for Bovine Pericardial Implants in Cardiac Surgery. *Thorac Cardiovasc Surg*, *70*(01), 033–042.

Walker, S., Schönfelder, J., Tugtekin, S.-M., Wetzel, C., Hacker, M. C., & Schulz-Siegmund, M. (2018). Stabilization and Sterilization of Pericardial Scaffolds by Ultraviolet and Low-Energy Electron Irradiation. *Tissue Engineering Part C: Methods*, *24*(12), 717–729. https://doi.org/10.1089/ten.tec.2018.0285

Wang, X., Chan, V., & Corridon, P. R. (2022). Acellular Tissue-Engineered Vascular Grafts from Polymers: Methods, Achievements, Characterization, and Challenges. *Polymers*, *14*(22), 4825. https://doi.org/10.3390/polym14224825

Wang, Z., & Xian, G. (2023). Impact performances of fiber reinforced polymer composites and cables: A review. *Composite Structures*, *319*, 117128. https://doi.org/10.1016/j.compstruct.2023.117128

Wanhainen, A., Van Herzeele, I., Bastos Goncalves, F., Bellmunt Montoya, S., Berard, X., Boyle, J. R., D′Oria, M., Prendes, C. F., Karkos, C. D., Kazimierczak, A., Koelemay, M. J. W., Kölbel, T., Mani, K., Melissano, G., Powell, J. T., Trimarchi, S., Tsilimparis, N., Antoniou, G. A., Björck, M., … Yeung, K. K. (2024). Editor′s Choice—European Society for Vascular Surgery (ESVS) 2024 Clinical Practice Guidelines on the Management of Abdominal Aorto-Iliac Artery Aneurysms. *European Journal of Vascular and Endovascular Surgery*, *67*(2), 192–331. https://doi.org/10.1016/j.ejvs.2023.11.002

Wanhainen, A., Verzini, F., Van Herzeele, I., Allaire, E., Bown, M., Cohnert, T., Dick, F., van Herwaarden, J., Karkos, C., Koelemay, M., Kölbel, T., Loftus, I., Mani, K., Melissano, G., Powell, J., Szeberin, Z., ESVS Guidelines Committee, de Borst, G. J., Chakfe, N., … Verhagen, H. (2019). Editor′s Choice – European Society for Vascular Surgery (ESVS) 2019 Clinical Practice Guidelines on the Management of Abdominal Aorto-iliac Artery Aneurysms. *European Journal of Vascular and Endovascular Surgery*, *57*(1), 8–93. https://doi.org/10.1016/j.ejvs.2018.09.020

Wasse, H., Huang, R., Naqvi, N., Smith, E., Wang, D., & Husain, A. (2012). Inflammation, Oxidation and Venous Neointimal Hyperplasia Precede Vascular Injury from AVF Creation in CKD Patients. *The Journal of Vascular Access*, *13*(2), 168–174. https://doi.org/10.5301/jva.5000024

Westerhof, N., Lankhaar, J.-W., & Westerhof, B. E. (2009). The arterial Windkessel. *Medical & Biological Engineering & Computing*, *47*(2), 131–141. https://doi.org/10.1007/s11517-008-0359-2

Wikkeling, T. M., Van Gijssel, S. A., Van Der Laan, M. J., Zeebregts, C. J., & Saleem, B. R. (2021). Treatment of patch infection after carotid endarterectomy: A systematic review. *Annals of Translational Medicine*, *9*(14), 1213–1213. https://doi.org/10.21037/atm-20-7531

Wolff, C. B., Collier, D. J., Shah, M., Saxena, M., Brier, T. J., Kapil, V., Green, D., & Lobo, M. (2016). A Discussion on the Regulation of Blood Flow and Pressure. In C. E. Elwell, T. S. Leung, & D. K. Harrison (Eds.), *Oxygen Transport to Tissue XXXVII* (Vol. 876, pp. 129–135). Springer New York. https://doi.org/10.1007/978-1-4939-3023-4_16

Wong, M. L., & Griffiths, L. G. (2014). Immunogenicity in xenogeneic scaffold generation: Antigen removal vs. decellularization. *Acta Biomaterialia*, *10*(5), 1806–1816. https://doi.org/10.1016/j.actbio.2014.01.028

Wymer, D. T., Patel, K. P., Burke, W. F., & Bhatia, V. K. (2020). Phase-Contrast MRI: Physics, Techniques, and Clinical Applications. *RadioGraphics*, *40*(1), 122–140. https://doi.org/10.1148/rg.2020190039

Xing, Q., Parvizi, M., Lopera Higuita, M., & Griffiths, L. G. (2021a). Basement membrane proteins modulate cell migration on bovine pericardium extracellular matrix scaffold. *Scientific Reports*, *11*(1), 4607. https://doi.org/10.1038/s41598-021-84161-5

Xing, Q., Parvizi, M., Lopera Higuita, M., & Griffiths, L. G. (2021b). Basement membrane proteins modulate cell migration on bovine pericardium extracellular matrix scaffold. *Scientific Reports*, *11*(1), 4607. https://doi.org/10.1038/s41598-021-84161-5

Xiong, J.-P., Stehle, T., Goodman, S. L., & Arnaout, M. A. (2003). Integrins, cations and ligands: Making the connection. *Journal of Thrombosis and Haemostasis*, *1*(7), 1642–1654. https://doi.org/10.1046/j.1538-7836.2003.00277.x

Xue, L., & Greisler, H. P. (2003). Biomaterials in the development and future of vascular grafts. *Journal of Vascular Surgery*, *37*(2), 472–480. https://doi.org/10.1067/mva.2003.88

Yakirevich, V. S., Abdulali, S. A., Abbott, C. R., & Ionescu, M. I. (1984). Reconstruction of the pericardial sac with glutaraldehyde-preserved bovine pericardium. *Texas Heart Institute Journal*, *11*(3), 238–242.

Yamasaki, T., Fujita, S., Kaku, Y., Katagiri, J., & Hiramatsu, T. (2018). Modified double patch repair with infarct exclusion technique for ventricular septal perforation: A case study. *Journal of Cardiothoracic Surgery*, *13*(1), 17. https://doi.org/10.1186/s13019-018-0708-7

Yamashita, H., Ozaki, S., Iwasaki, K., Kawase, I., Nozawa, Y., & Umezu, M. (2012). Tensile Strength of Human Pericardium Treated with Glutaraldehyde. *Annals of Thoracic and Cardiovascular Surgery*, *18*(5), 434–437. https://doi.org/10.5761/atcs.oa.11.01804

Yap, C. H., Saikrishnan, N., Tamilselvan, G., & Yoganathan, A. P. (2012). Experimental measurement of dynamic fluid shear stress on the aortic surface of the aortic valve leaflet. *Biomechanics and Modeling in Mechanobiology*, *11*(1–2), 171–182. https://doi.org/10.1007/s10237-011-0301-7

Yi, S., Ding, F., Gong, L., & Gu, X. (2017). Extracellular Matrix Scaffolds for Tissue Engineering and Regenerative Medicine. *Current Stem Cell Research & Therapy*, *12*(3), 233–246. https://doi.org/10.2174/1574888X11666160905092513

Yoshihara, H., & Yoshinobu, M. (2014). Effects of specimen configuration and measurement method of strain on the characterization of tensile properties of paper. *Journal of Wood Science*, *60*(4), 287–293. https://doi.org/10.1007/s10086-014-1398-y

Zhang, D., Zhu, G.-J., Wei, X.-Y., Li, B., Hu, J., Ma, W.-G., & Chen, X.-P. (2022). Repair of coronary artery ostium with a ring-shaped bovine pericardial patch. *Interactive CardioVascular and Thoracic Surgery*, *35*(5), ivac251. https://doi.org/10.1093/icvts/ivac251

Zhang, L., Wu, H., Liu, Z., Wang, X., Cheng, Y., & Wang, K. (2022). Dural repair with fat patch for idiopathic spinal cord herniation: Operative technique and a review of seven cases. *Annals of Translational Medicine*, *10*(16), 865–865. https://doi.org/10.21037/atm-22-3343

Zouhair, S., Dal Sasso, E., Tuladhar, S. R., Fidalgo, C., Vedovelli, L., Filippi, A., Borile, G., Bagno, A., Marchesan, M., De Rossi, G., Gregori, D., Wolkers, W. F., Romanato, F., Korossis, S., Gerosa, G., & Iop, L. (2020). A Comprehensive Comparison of Bovine and Porcine Decellularized Pericardia: New Insights for Surgical Applications. *Biomolecules*, *10*(3), 371. https://doi.org/10.3390/biom10030371

Zucchi, A., Silvani, M., & Pecoraro, S. (2013). Corporoplasty with small soft axial prostheses (VIRILIS I®) and bovine pericardial graft (HYDRIX®) in Peyronie's disease. *Asian Journal of Andrology*, *15*(2), 275–279. https://doi.org/10.1038/aja.2012.156